Wrocław University of Technology
Centre of Advanced Materials and Nanotechnology

Materials Science-Poland

Vol. 27 • No. 2 • 2009

Oficyna Wydawnicza Politechniki Wrocławskiej

Materials Science-Poland is an interdisciplinary journal devoted to experimental and theoretical research into the synthesis, structure, properties and applications of materials.

Among the materials of interest are:

- glasses and ceramics
- sol-gel materials
- photoactive materials (including materials for nonlinear optics)
- laser materials
- photonic crystals
- semiconductor micro- and nanostructures
- piezo-, pyro- and ferroelectric materials
- high-T_c superconductors
- magnetic materials
- molecular materials (including polymers) for use in electronics and photonics
- novel solid phases
- other novel and unconventional materials

The broad spectrum of the areas of interest reflects the interdisciplinary nature of materials research. Papers covering the modelling of materials, their synthesis and characterisation, physicochemical aspects of their fabrication, properties and applications are welcome. In addition to regular papers, the journal features issues containing conference papers, as well as special issues on key topics in materials science.

Materials Science-Poland is published under the auspices of the Centre of Advanced Materials and Nanotechnology of the Wrocław University of Technology, in collaboration with the Institute of Low Temperatures and Structural Research of the Polish Academy of Sciences and the Wrocław University of Economics.

All accepted manuscripts are placed on the Web page of the journal and are available at the address: http://MaterialsScience.pwr.wroc.pl

All published papers are placed on the Web page of the journal and are **freely accessible** at the address: http://MaterialsScience.pwr.wroc.pl

Materials Science-Poland is abstracted/indexed in: Chemical Abstracts, Materials Science Citation Index, Science Citation Index Expanded, Scopus.

Editor-in-Chief

Juliusz Sworakowski

Institute of Physical and Theoretical Chemistry
Wrocław University of Technology
Wybrzeże Wyspiańskiego 27
50-370 Wrocław, Poland
sworakowski@pwr.wroc.pl

Deputy Editor

Jan Felba

Faculty of Microsystem Electronics and Photonics
Wrocław University of Technology
Wybrzeże Wyspiańskiego 27
50-370 Wrocław, Poland
jan.felba@pwr.wroc.pl

Associate Editors

Wiesław Stręk

Institute of Low Temperature
and Structure Research
Polish Academy of Sciences
P. O. Box 1410
50-950 Wrocław 2, Poland
strek@int.pan.wroc.pl

Jerzy Hanuza

Department of Bioorganic Chemistry
Faculty of Industry and Economics
Wrocław University of Economics
Komandorska 118/120
53-345 Wrocław, Poland
hanuza@credit.ae.wroc.pl

Advisory Editorial Board

Frédéric Bernard, Dijon, France
Mikhaylo S. Brodyn, Kyiv, Ukraine
Alexander Bulinski, Ottawa, Canada
J. Paulo Davim, Aveiro, Portugal
Roberto M. Faria, São Carlos, Brazil
Andrzej Gałęski, Łódź, Poland
Reimund Gerhard, Potsdam, Germany
Paweł Hawrylak, Ottawa, Canada
Andrzej Kłonkowski, Gdańsk, Poland
Shin-ya Koshihara, Tokyo, Japan
Krzysztof J. Kurzydłowski, Warsaw, Poland
Janina Legendziewicz, Wrocław, Poland
Benedykt Licznerski, Wrocław, Poland
Jerzy Lis, Cracow, Poland
Tadeusz Luty, Wrocław, Poland
Bolesław Mazurek, Wrocław, Poland
Jan Misiewicz, Wrocław, Poland
Jerzy Mroziński, Wrocław, Poland
Krzysztof Nauka, Palo Alto, CA, U.S.A.
Stanislav Nešpůrek, Prague, Czech Republic
Marek Samoć, Wrocław, Poland
Jan Stankowski, Poznań, Poland
Jacek Ulański, Łódź, Poland
Vladislav Zolin, Moscow, Russia

The Journal is supported by the State Committee for Scientific Research

Editorial Office

Daniel Davies
Marek Łata

Printed in Poland

Drukarnia Oficyny Wydawniczej Politechniki Wrocławskiej
Zam. nr 514/2009.

Materials Science-Poland, Vol. 27, No. 2, 2009

Reducing the density of threading dislocations in GaAs epitaxial layers. Efficiency assessment of isovalent Bi doping and Pb doping

YE. BAGANOV[1*], V. KRASNOV[2], O. LEBED[3], S. SHUTOV[2]

[1]Kherson National Technical University, 24 Berislavskoye shosse, Kherson, 73008, Ukraine

[2] V. Lashkarev Institute of Semiconductor Physics, National Academy of Sciences of Ukraine,
41 Prospect Nauki, Kiev, 03028, Ukraine

[3] Kherson Marine Institute, 14 Prospect Ushakova, Kherson, 73000, Ukraine

Processes of motion of threading dislocations associated with isovalent doping of epitaxial layers were considered. An exact solution was obtained for the gliding distance of dislocations under strains. It was shown that the effectiveness of doping for reducing the density of threading dislocations in an epitaxial layer depends on the product of the surface density of the dislocations in the substrate and the lateral size of the substrate. An analysis of the effectiveness of isovalent Bi doping and standard Pb doping in reducing the density of threading dislocations in GaAs epitaxial layers and the range of applicability has been presented.

Key words: *isovalent doping; dislocations; GaAs; Bi; Pb*

1. Introduction

Dislocations are well known to increase the leakage currents and to degrade the electrophysical parameters of semiconductor devices [1, 2]. The mechanisms of the formation of dislocations in homoepitaxial layers obtained by the liquid phase epitaxy (LPE) are the inheritance of dislocations from the substrate and the difference between the lattice constants of the substrate and the doped epitaxial layer at the growth temperature [3]. Isovalent doping is one of the ways to substantially reduce the dislocation density in GaAs in comparison with the epitaxial layers grown from gallium solution melts [4–8.] The decrease in the dislocation density occurring when Ga based solution melts are replaced by Bi based melts can be explained by an increase of the threshold

---

[*] Corresponding author, e-mail: ewgb@newmail.ru

strain associated with the dislocation nucleation [4, 5]. Another explanation for the reduction in the dislocation density in GaAs epitaxial layers doped with indium is a decrease in the supersaturation of vacancies in the elastically strained layer, considerably decreasing the rate of dislocation formation due to vacancy condensation [6].

However, strains in the epitaxial layer enable threading dislocations to glide along the glide planes. The decrease in the density of threading dislocations in the epitaxial layer due to the strains was considered by Matthews, Blakeslee, and Mader [9]. Strains in epitaxial layers result in the appearance of the Peach–Koehler forces (PKF) [10] affecting threading dislocations. Under the PKF, the dislocation can be removed from the epitaxial layer to its edge by gliding resulting in the formation of edge misfit dislocations. The decrease of the number of threading dislocations due to their motion under strain has also been considered by Romanov et al. [11]. The aim of the present paper is a theoretical justification of conditions providing an effective reduction in the density of threading dislocations due to doping GaAs with Bi and Pb.

2. Mathematical model

The model proposed by Martisov [8] was used to analyse the decrease in the dislocation density in the epitaxial layers. The model is based on the balance of the PKF, the force F_1, affecting the inclined part of the threading dislocation in the epitaxial layer, and the force of linear tension of the dislocation, F_2, at the substrate/epitaxial layer interface plane, being the part of the edge misfit dislocation (Fig. 1).

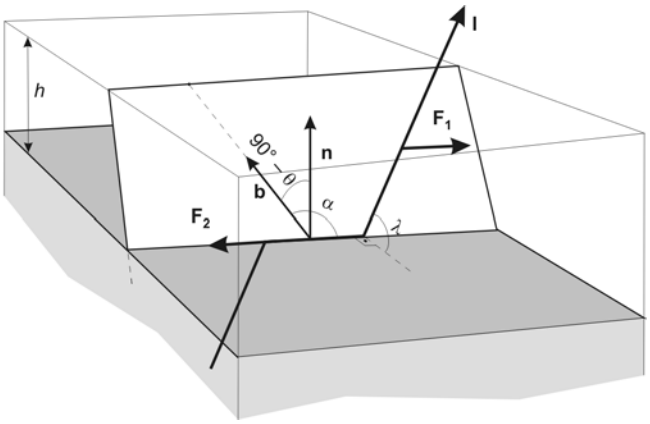

Fig. 1. Schematic diagram of the strained epitaxial layer on the substrate with a threading dislocation moving along its glide plane

The PKF arises in the strained layer and is defined by the following expression [10]:

$$dF_1 = -\mathbf{l}\times(\mathbf{b}\cdot\tau)dl \tag{1}$$

where **l** is the unit vector along the dislocation line, **b** is the Burgers vector, $\boldsymbol{\tau}$ is the tensor of stress field, and *dl* is the increment of the dislocation length, respectively.

For the analysis, it has been assumed that:

- Both the substrate and the epitaxial layer are isotropic media.
- The stresses caused by the misfit *f* of the lattice constants corresponding to the substrate and to the epitaxial layer are distributed uniformly in the substrate/epitaxial layer interface plane.
- There is no interaction between the dislocations.
- Threading dislocations in the epitaxial layer are inherited from the substrate and their density is equal to the surface density of the dislocations in the substrate.

Under these assumptions, the projection of the PKF on the slip plane and the modulus of the force of the linear tension of dislocation are defined by the following expressions [12, 13]:

$$F_1 = \frac{2G\varepsilon bh\left(1+\nu\right)}{1-\nu}\cos\lambda \tag{2}$$

$$F_2 = \frac{Gb^2}{4\pi\left(1-\nu\right)}\left(1-\nu\cos^2\alpha\right)\left(\ln\frac{h}{b}+1\right) \tag{3}$$

where G is the shear modulus, ε is the elastic stress in the epitaxial layer, b is the magnitude of the Burgers vector, h is the thickness of the epitaxial layer, ν is the Poisson ratio, λ is the angle between the slip direction and the direction in the substrate/epitaxial layer interface plane that is perpendicular to the line of intersection of the slip plane and the interface, and α is the angle between the dislocation line and the Burgers vector, respectively.

The dislocation starts to move in the slip plane when $F_1 > F_2$ and accommodates the misfit δf due to the formation of a part of the purely edge misfit dislocation. The misfit δf can be calculated as follows, assuming that dislocations do not interact [8]:

$$\delta f = qN_d Lb\cos\theta \tag{4}$$

where θ is the angle between the Burgers vector and the interface, the multiplier q takes into account the existence of equivalent slip directions and, hence, reduction of the density of the slipping dislocations along concerned direction, $q \leq 1$, N_d is the surface density of the dislocations in the substrate. Vector **n** in Fig. 1 is the normal vector to the substrate/epitaxial layer interface. The strain in the structure is calculated as follows:

$$\varepsilon = f - \delta f = f - qN_d Lb\cos\theta \tag{5}$$

Equating F_1 with F_2 (Eqs. (2) and (3)) and substituting the expression for the strain (5) in (2), the distance passed by the threading dislocation under the driving force can be calculated as follows:

$$L = \frac{1}{qN_d b\cos\theta}\left(f - \frac{b}{8\pi h(1-\nu)\cos\lambda}\left(1-\nu\cos^2\alpha\right)\left(\ln\frac{h}{b}+1\right)\right) \tag{6}$$

As follows from Eq. (6), at a certain thickness h_c of the epitaxial layer, L can be longer than the characteristic lateral size of the substrate D. Under such conditions dislocation is removed from the epitaxial layer to the edge of the structure. Equation (6) can be solved exactly, with respect to the thickness of the epitaxial layer, using the approach proposed by Braun et al. [14].

Rewriting Eq. (6) as

$$\frac{\left(f - qLN_d b\cos\theta\right)\times 8\pi(1+\nu)\cos\lambda}{\left(1-\nu\cos^2\alpha\right)}\frac{h}{b} = 1 + \ln\left(\frac{h}{b}\right) \tag{7}$$

and substituting

$$A = -\frac{\left(f - qLN_d b\cos\theta\right)\times 8\pi(1+\nu)\cos\lambda}{e\left(1-\nu\cos^2\alpha\right)}, \qquad X = \frac{h}{b}e$$

the following equation is obtained:

$$AX + \ln X = 0 \tag{8}$$

Let

$$X = \frac{1}{A}W(A)$$

with $W(A)$ being a certain function. Then Eq. (8) can be rewritten as follows:

$$\mathrm{W}(A)\mathrm{e}^{W(A)} = A \tag{9}$$

The function $W(A)$, called the Lambert W function [16], is a complex and multi-valued function with an infinite number of branches, only two of them having real values. The real branches of the Lambert W function are shown in Fig. 2. It is necessary to ascertain which of the two branches corresponds to a correct physical solution.

The absolute value of A decreases with the increase of the accommodation of misfit between the lattice constants of the substrate and the epitaxial layer due to the spreading of the dislocations. With the increase of the thickness of epitaxial layer, the projection of the PKF on the slip plane also increases. Hence, the equality of forces F_1 and F_2 is achieved at smaller residual strains in the epitaxial layer. Based on the fact that A is always negative and the value of X decreases as the absolute value of A increases, the physical solution corresponds to the positive value of dX/dA.

Using the expression for the derivative of the Lambert *W* function, which can be easily obtained by differentiation of Eq. (9)

$$\frac{dW(x)}{dx} = \frac{W(x)}{x\left(1+W(x)\right)}$$

the following expression can be obtained:

$$\frac{dX}{dA} = -\frac{1}{A^2}\frac{W^2(i,A)}{1+W(i,A)}, \qquad i = 0, -1$$

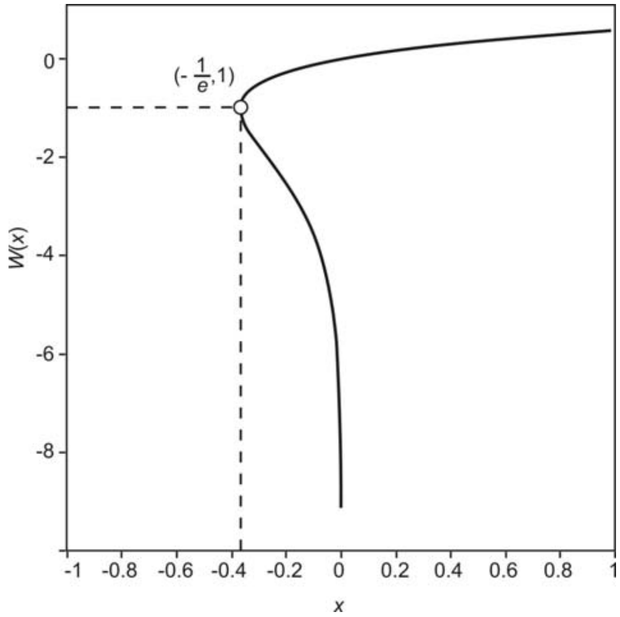

Fig. 2. The real valued Lambert *W* function with two branches, *W*(0, *x*) and *W*(–1, *x*)

As can be seen from Fig. 2, only the derivative of the function *W*(–1, *x*) is positive.

The solution of Eq. (6) with respect to the thickness of the epitaxial layer *h* can be written as follows:

$$\begin{aligned} h = -b\frac{\left(1-\nu\cos^2\alpha\right)}{\left(f-qLN_d b\cos\theta\right)\cdot 8\pi\left(1+\nu\right)\cos\lambda} \\ \times W\left(-1, -\frac{\left(f-qLN_d b\cos\theta\right)\cdot 8\pi\left(1+\nu\right)\cos\lambda}{e\left(1-\nu\cos^2\alpha\right)}\right) \end{aligned} \qquad (10)$$

The value of the critical thickness h_c is calculated as follows:

$$h_c = -b\frac{\left(1-\nu\cos^2\alpha\right)}{\left(f - qDN_d b\cos\theta\right)\times 8\pi\left(1+\nu\right)\cos\lambda} \times \mathrm{W}\left(-1, -\frac{\left(f - qDN_d b\cos\theta\right)\times 8\pi\left(1+\nu\right)\cos\lambda}{e\left(1-\nu\cos^2\alpha\right)}\right) \tag{11}$$

3. Results and discussion

Equation (11) can be applied to estimate the effectiveness of isovalent doping of GaAs by Bi and doping by Pb for the removal of threading dislocations from the inner epitaxial layer to its edge, due to the formation of edge misfit dislocations.

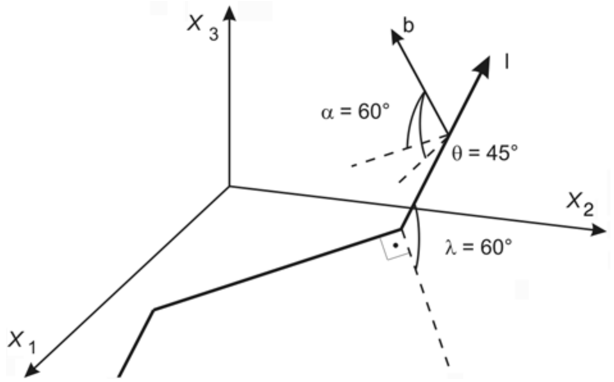

Fig. 3. Motion of the threading 60° dislocation in the strained epitaxial layer with the direction of the inclination of the dislocation line

It is known that {111} planes are the slip planes in GaAs. Consider the dislocation with 60° inclination having the direction $\mathbf{l} = 1/\sqrt{2}\,[011]$ and the Burgers vector $\mathbf{b} = a/2$ [101]. Such dislocations have been reported elsewhere [16, 17]. Then $\alpha = 60°$, $\lambda = 60°$, and $\theta = 45°$ (see Fig. 3). Since there are two independent directions of the dislocation spread, namely $\mathbf{l}_1 = 1/\sqrt{2}[011]$ and $\mathbf{l}_2 = 1/\sqrt{2}[0\bar{1}1]$ [8, 9], the value of q is 1/2.

The misfit f can be defined as [8]:

$$f = 1 - \left(\frac{1+\left(\frac{M_{\mathrm{dop}}}{M_{\mathrm{sub}}}-1\right)x}{1+\left(\frac{\rho_{\mathrm{dop}}}{\rho_{\mathrm{sub}}}-1\right)x}\right)^{1/3} \tag{12}$$

where M_{sub}, M_{dop}, ρ_{sub}, ρ_{dop} are the molar masses and the densities of materials of the substrate and the dopant, respectively, x is the molar fraction of the dopant in the substrate which can be calculated using the following expression [8]:

$$C_{\text{dop}} = \frac{N_A x}{\dfrac{M_{\text{sub}}}{\rho_{\text{sub}}}(1-x) + \dfrac{M_{\text{dop}}}{\rho_{\text{dop}}} x} \tag{13}$$

Here, C_{dop} is the concentration of the dopant in the epitaxial layer and N_A is the Avogadro number, respectively.

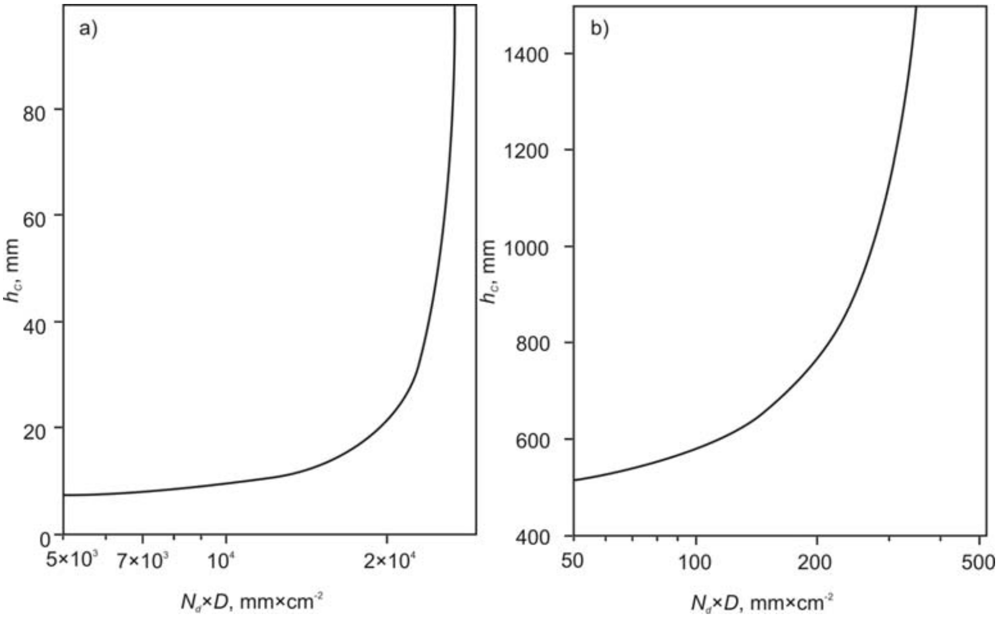

Fig. 4. Dependences of the critical thickness for dislocation removal from the epitaxial layer upon the characteristic sample size and the dislocation density in the case of doping by: a) Bi, b) Pb

Figure 4 shows how the critical thickness associated with dislocation removal (from the inner epitaxial layer to the boundary) depends on the product of two factors: the characteristic size of the sample and the density dislocation in the sample. Bi and Pb concentrations in Fig. 4 have been accepted at the highest possible level of real achievable values being 5×10^{18} cm^{-3} [18] and 4×10^{17} cm^{-3} [19] for Bi and Pb, respectively.

As follows from Fig. 4, starting from certain values of the dislocation density in the substrate and the sample size, the critical thickness of the epitaxial layer that enables removal of threading dislocations to the edge of the epitaxial layer increases dramatically. The increase in the thickness of epitaxial layers requires higher initial growth temperatures, which then leads to other defects such as point defects and impurities. It degrades the influence of the decrease of dislocation density on the electrophysical parameters of material. In this respect, the effective reduction of the threading dislocation density in the epitaxial layer at isovalent doping is only possible at certain values of A that depends on the product of DN_d.

Using the results shown in Fig. 4, the following expressions can be obtained in the case of Bi (Eq. (14)) and Pb (Eq. (15)) doping:

$$D \le \frac{2\times 10^4}{N_d} \tag{14}$$

$$D \le \frac{300}{N_d} \tag{15}$$

In Equations (14) and (15) D is expressed in millimetres and N_d in cm^{-2}.

A relatively small solubility of Pb in solid GaAs leads to a very thick epitaxial layer (hundreds of micrometers, Fig. 4b) when dislocations start to glide. That is why Pb is not an effective dopant for removing dislocations from the epitaxial layer to the edge of the structure.

The considered approach can be used for estimating the effectiveness of removing dislocations from the epitaxial layer at use compared with other methods of epitaxy. Molecular beam epitaxy (MBE) and vapour phase epitaxy (VPE) methods provide higher concentrations of isovalent doping of the epitaxial layer than LPE. Additional use of mesastructures makes it possible to decrease the value h_c considerably, up to the conventional epitaxial layer thicknesses obtained by MBE and VPE.

4. Conclusions

In this paper, an exact analytical solution is given for the critical thickness, h_c, of the epitaxial layer that permits the removal of threading dislocations from the interior of the epitaxial layer to its edge. It makes it possible to analyse the dependence of h_c on the geometrical and mechanical parameters of substrates. The critical thickness of the epitaxial layer permitting the motion of threading dislocations can be obtained by substituting $L = 0$ in Eq. (10).

The product DN_d has been shown to be the critical parameter determining the effectiveness of the dislocation removal from the epitaxial layer. Because of the absence of extreme points in the dependence $h_c\,(DN_d)$, there is no optimal combination of D and N_d which can provide the most effective removal of dislocations from thin epitaxial layers. With increasing DN_d, h_c increases monotonically.

The analysis of the dependence of the critical thickness of the epitaxial layer on the product DN_d makes it possible to quantify the isovalent doping for introducing strains in the epitaxial layers to reduce the threading dislocation density.

References

[1] SAUL R.H., J. Electrochem. Soc., 118, (1971), 793.

[2] KOVALENKO V.F., KRASNOV V.A., PROKHOROVICH A.V., Optoelectr. Poluprov. Tekh., 6 (1984), 71, (in Russian).

[3] KRESSEL H., NELSON H., *Properties and Applications of III–V Compound Films Deposited by Liquid-Phase Epitaxy, in Physics of Thin Films*, Vol. 7, G. Hass, M.H. Francombe, R.W. Hoffman (Eds.) Academic Press, New York, 1973.

[4] VASILENKO N.D., GORODNICHENKO O.K., KRASNOV V.A., Proc. 5th Int. Conf. on *Properties and Structure of Dislocations in Semiconductors*, Moscow, 57, (1986) (in Russian).

[5] KOTELEVSKIJ A.A., KRASNOV V.A., LUBJANAJA M.D., FILIPPOV N.N., *Crystallization and Crystal Properties*, Novocherkassk, Vol. 50 (1987) (in Russian).

[6] WALUKIEWICH W., Appl. Phys. Lett., 54 (1989), 2009.

[7] SOLOVJOVA E.V., MILVIDSKIJ M.G., Fiz. Tekh. Poluprov., 17 (1983), 2002 (in Russian).

[8] MARTISOV M.YU., Sov. Phys. Semicond., 26 (1992), 462.

[9] MATTHEWS W.J., BLAKESLEE A.E., MADER S., Thin Solid Films, 33 (1976), 253.

[10] PEACH M., KOEHLER J.S., Phys. Rev., 80 (1950), 436.

[11] ROMANOV E., POMPE W., MATHIS S., BELTZ G.E., SPECK J.S., J. Appl. Phys., 85 (1999), 182.

[12] MATTHEWS J.W., MADER S., LIGHT T.B., J. Appl.Phys., 41, 3800, (1970).

[13] LIU X.W., HOPGOOD A.A., USHER B.F., WANG H., BRAITHWAITE N.S.J., Semicond. Sci. Technol., 14 (1999), 1154.

[14] BRAUN K., BRIGGS M., BÖNI P., J. Cryst. Growth, 241 (2002), 231.

[15] CORLESS R.M., GONNET G.H., HARE D.E.G., JEFFREY D.J., KNUTH D.E., Adv. Comp. Math., 5 (1996), 329.

[16] MATTHEWS J.W., BLAKESLEE A.E., J. Cryst. Growth, 27 (1974), 118.

[17] EL-MASRY N.A., TARN J.C., KARAM N.H., J. Appl. Phys., 64 (1988), 3672.

[18] GANINA N.V., Phys. Chem. Sol. State, 3 (2002), 565 (in Russian).

[19] NASHELSKIY A.YA., *Single Crystals of Semiconductors*, Metallurgy, Moscow, 1978 (in Russian).

Received 5 May 2008
Revised 4 October 2008

Materials Science-Poland, Vol. 27, No. 2, 2009

Growth and characterization of an NLO material – crystal of triglycine acetate

S.S. HUSSAINI[1], N.R. DHUMANE[1], V.G. DONGRE[2], M.D. SHIRSAT[2*]

[1]Optoelectronics and Sensor Research Laboratory, Department of Physics,
Dr. Babasaheb Ambedkar Marathwada University, Aurangabad 431 004 (MS), India

[2]Department of Chemistry, University of Mumbai, Kalina Campus,
Vidyanagari, Santa Cruz (East) Mumbai 400 098 (MS), India

Triglycine acetate (TGAc), a nonlinear optical material, has been synthesized. The second harmonic generation efficiency has been determined by Kurtz's powder test and it was found to be 1.55 times more than potassium dihydrogen phosphate. The solubility studies were carried out in the temperature range 30–55 °C. Single crystals of TGAc have been grown by slow evaporation of solution at 30 °C. The cell parameters were determined by the X-ray diffraction analysis. The UV-visible absorption spectra have been recorded to study the optical transmittance in the range from 200 nm to 800 nm. The Fourier transform infrared analysis identified various functional groups present in the material. The mass spectral analysis was carried out to measure the total molecular weight of the grown crystal. Using thermogravimetric analysis the thermal behaviour was studied.

Key words: *crystal growth; nonlinear optical materials; amino acid*

1. Introduction

In last several years there has been considerable interest in growth and characterization of nonlinear optical materials (NLO) due to their important contribution in areas of optical modulation, optical switching, optical logic, frequency shifting and optical data storage. Several attempts have been made for exploration of nonlinear optical materials which found various applications in optoelectronics [1–7]. The complexes of amino acids and salts are promising materials for optical second harmonic generation (SHG) as they tend to combine the advantages of organic amino acids with those of the inorganic acids/salts. Glycine is a simple amino acid which has three polymeric crystalline forms α, β and γ. There are two types of glycine

---

[*] Corresponding author, e-mail: mdshirsat_bamu@yahoo.co.in

groups such as glycinium ions and zwitter ion. The zwitterionic structure of glycine is useful for its optical activity [8].

Many NLO crystals grown by mixing amino acids with various organic and inorganic acids have been reported in the literature [9–11]. However, to the best of our knowledge, there is no report on the growth and characterization of TGAc single crystal (mixing glycine with acetic acid). Moreover, our objective was to grow a single crystal of TGAc with enhanced nonlinearity as compared to reported single crystals of this kind. In the present investigation, the synthesized salt – triglycine acetate (TGAc) – was subjected to SHG test and found to possess nonlinearity higher than potassium dihydrogen phosphate (KDP) and many other crystals of amino acids. The bulk single crystal of TGAc was grown by the method of slow evaporation of solution and characterized by various techniques.

2. Experimental

Triglycine acetate was synthesized by adding three moles of glycine of high purity (Kemphasol, 99%) and one mol of annalar grade glacial acetic acid in deionized water. The synthesized salt was purified by repeated crystallization. The solubility test was carried out at constant temperature baths (CTB) (30 ºC, 35 ºC, 40 ºC, 45 ºC, 50 ºC and 55 ºC) stabilized with the accuracy of ±0.01 °C. We observed temperature increase of solubility (Fig. 1). The saturated solution was prepared at 30 °C to grow the single crystal by the slow evaporation technique.

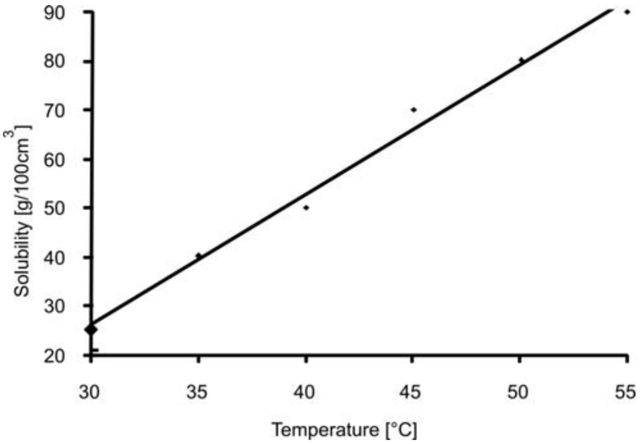

Fig. 1. Solubility curve of TGAc in water

After obtaining the saturation, the prepared solution was filtered with Whatmann filter paper and the solution was placed for slow evaporation at the room temperature. The seed crystals were harvested from the solution after eight days and a suitable seed was selected. The supersaturated solution of TGAc was prepared in 500 cm^3 of deionized water at 30 ºC and kept at this temperature for slow evaporation. After 24 h the selected seed was suspended in the solution. A colourless crystal, harvested after 25 days, was subjected to various characterizations. The photograph of a crystal is shown in Fig. 2.

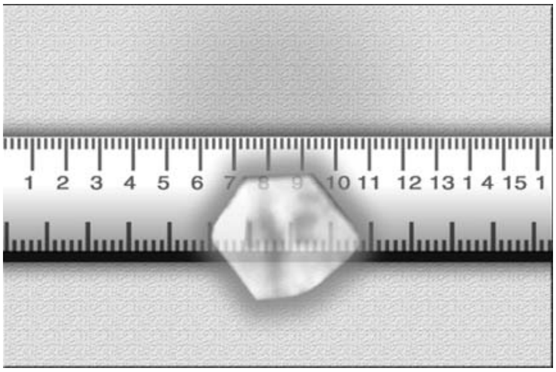

Fig. 2. Photograph of a TGAc crystal

3. Results and discussion

3.1. X-ray diffraction analysis

The single crystal XRD analysis of grown crystals was carried out using the ENRAF NONIUS CAD4 automatic X-ray diffractometer and the collected cell parame-

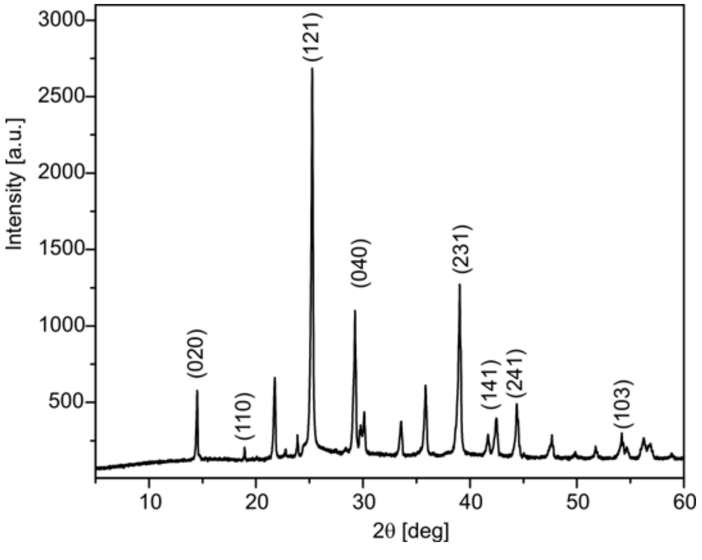

Fig. 3. Powder X-ray spectrum of TGAc

ters are $a = 5.1021$ Å, $b = 11.9704$ Å, $c = 5.4617$ Å and $\alpha = \gamma = 90°$, $\beta = 111.7665°$, the cell volume $V = 309.7863$ Å^3. The powdered sample of the grown crystal was also subjected to powder X-ray diffraction analysis using Panalytical, XPert PRO powder X-ray diffractrometer employing CuK$_\alpha$ radiation ($\lambda = 1.5418$ Å).

The peaks observed in the X-ray diffraction spectrum were analysed and the lattice parameters were calculated by the least square fit method. The data obtained by the powder X-ray diffraction analysis is in accordance with the single crystal X-ray diffraction data. It is clear that for the crystal $a \neq b \neq c$, $\alpha = \gamma = 90°$ and $\beta \neq 90°$, which ensures that the grown TGAc crystal is of monoclinic structure. The powder X-ray diffraction pattern is shown in Fig. 3.

3.2. Fourier transform infrared (FTIR) analysis

The IR spectrum of grown TGAc crystal was recorded in the solid state as KBr dispersion using Perkin-Elmer Spectrum-one FT-IR spectrometer (Fig. 4).The spectrum exhibited a characteristic N–H stretching absorption band in the high frequency range between 2787 and 3093 cm^{-1}. The peak at 2787 cm^{-1} is attributed to C–H stretching mode vibration [12].

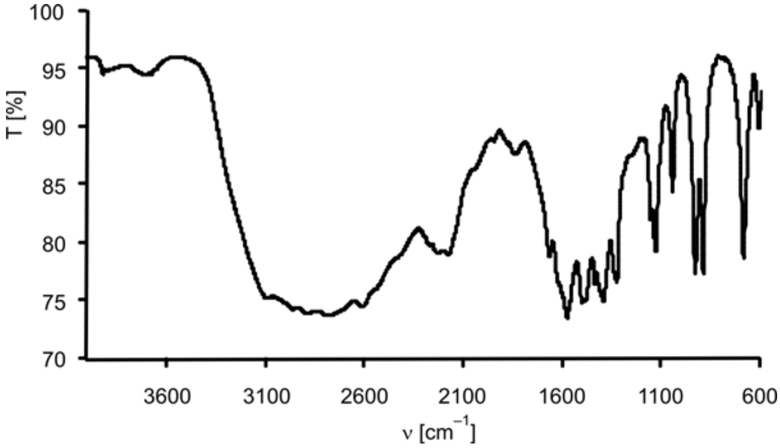

Fig. 4. FT-IR spectrum of TGAc

The absorption band at 1665 cm^{-1} corresponds to C=O stretching mode. The bands between 1574 and 1434 cm^{-1} were due to the asymmetric and symmetric stretching modes of COO$^-$ groups. The bands at 1324 cm^{-1} and 1045 cm^{-1} can be attributed to the presence of COOH groups and stretching vibrations (involving carbon and nitrogen of amino groups), respectively. The torsional vibration of amino group lies between 500 and 556 cm^{-1}. The absorption band between 930 and 1152 cm^{-1} was assigned to asymmetric coupled vibration of acetate and glycine.

3.3. UV-visible spectra

The UV-vis absorption spectrum of TGAc in solution (0.1 mg/cm^3 in methanol) was recorded using a Perkin Elmer Lambda 35 UV spectrophotometer. The UV spectrum (Fig. 5) was recorded between 200 to 800 nm; the absorbance was evident below 250 nm. It is assigned to electronic excitation in the COO$^-$ group of glycine. A complete transparency between 230 and 800 nm is interesting, as it is very much required for NLO applications of this crystal [13].

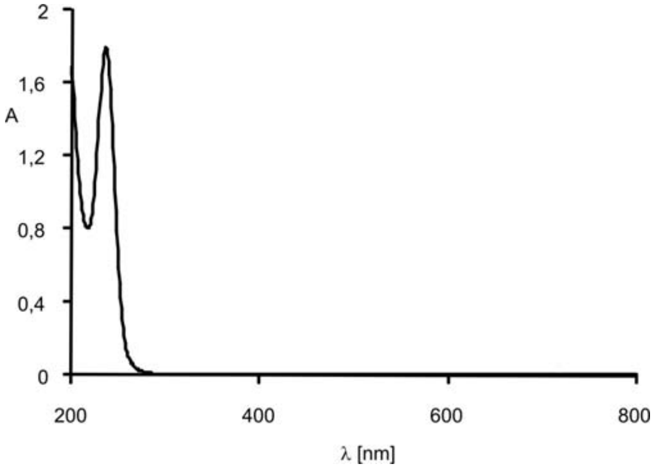

Fig. 5. UV-visible absorption spectra

3.4. SHG efficiency test

The Kurtz's Perry technique was employed to test the strength of SHG efficiency of the TGAc crystal by passing the output of an Nd:YAG laser. The laser input pulse

Table 1. Comparison of SHG efficiencies of promising amino acid family crystals

Compound	SHG efficiency
KDP(reference) [10]	1
L-arginine phosphate monohydrate [14]	1.49
L-threonium acetate [10]	1.14
L-alanine [10]	0.2
L-alanine acetate [10]	0.3
L-arginine chloride [10]	0.2
L-arginine bromide [10]	0.3
L-arginine tetrefluroborate [10]	0.54
Triglycine acetale (present paper)	1.55

of 3 mJ with the repetition rate of 10 Hz and the pulse width of 8 ns was used. The photomultiplier tube was used as a detector. The SHG signals of 920 mV and 1430 mV were obtained through KDP and TGAc samples, respectively. Thus, the SHG efficiency of TGAc is 1.55 times higher than that of KDP. A comparison of SHG efficiencies of promising amino acids family crystals is shown in Table 1.

3.5. Thermal studies

The melting point of fine powder of the material was measured as 248±1 °C. The thermogravimetric analysis (TGA) of the triglycine acetate crystal was carried out using TG Q-500 thermogravimetric analyzer at the heating rate of 25 °C/min to 800 °C in a nitrogen inert atmosphere (Fig. 6).

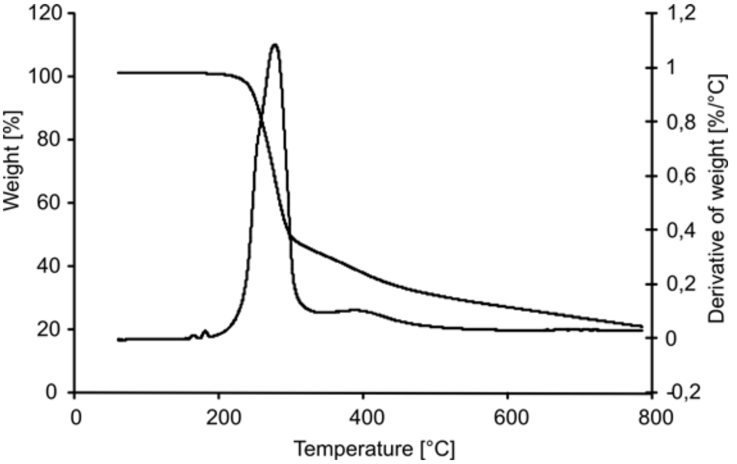

Fig. 6. Thermogram of thermogravimetric analysis

The spectrum shows that there is small weight loss around 180 °C. The material starts decomposing near temperature of 248 °C, which is melting point of the TGAc crystal. The weight loss of 73.25% of 7.432 mg of sample was observed in the temperature range from 248 °C to 306.36 °C. Thereafter residue remains up to of 800 °C. It is clear that the crystal is thermally stable up to 248 °C.

3.6. Mass spectroscopy

The mass spectrum of TGAc was recorded using a thermo-electron LCQ advantage (San Jose, CA, USA) ion trap mass spectrometer. The source voltage was 5 kV and the capillary temperature 375 °C. Nitrogen was used both as a sheath and auxiliary gas. The mass (*m*) to charge (*z*) ratio was scanned across the range of *m*/*z* from 152 to 400. The mass spectrum is shown in Fig. 7.

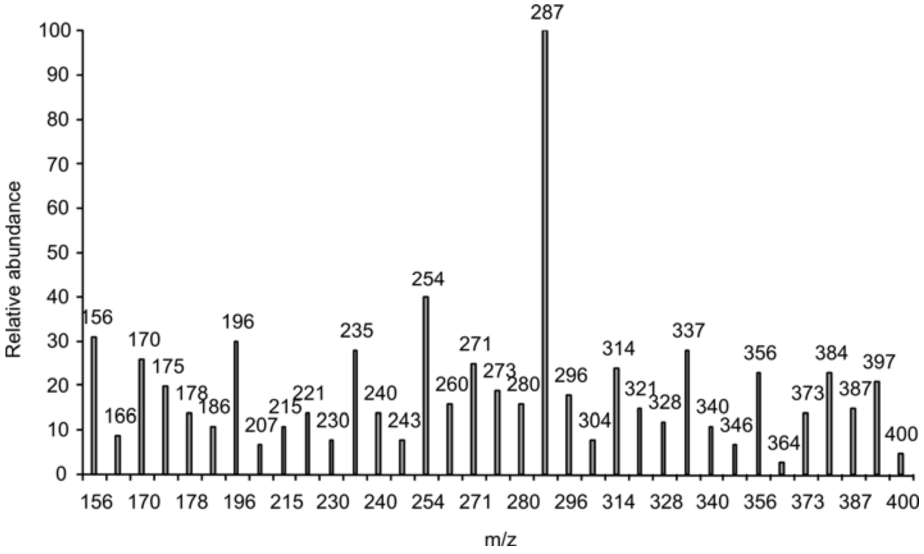

Fig. 7. Mass spectrum of a TGAc crystal

The mass spectrum of TGAc showed a protonated molecular adduct ion peak at $m/z = 287$ (M + 2H)·$[(NH_2CH_2COOH)_3CH_3COOH + 2H]^+$. The loss of NH_2CH_2 moiety from the molecular ion (285 amu) gives the peak at m/z 255, while the parent ion at m/z 287 undergoes dissociation to form daughter ion at m/z 237 by the loss of $–CO_2$ moiety along with four carboxylic protons. The loss of carboxylic group (–COOH) from the parent ion gives a product ion at $m/z = 242$. The peak at $m/z = 210$ can be assigned to the contamination of the impurity: diglycine acetate $(NH_2CH_2COOH)_2$ $·CH_2COOH$.

4. Conclusions

A single crystal of triglycine acetate (TGAc) was successfully grown using the slow evaporation technique. The X-ray diffraction analysis confirmed the monoclinic structure of the crystal. The minimum absorption in the entire visible region and lower cut off wavelength near 230 nm indicates its applicability NLO material. Various functional groups have been identified by the FTIR spectral analysis. The Kurtz powder test confirmed that SHG efficiency of TGAc is higher than that of KDP and many other crystals of amino acid family. The thermogravimetric analysis confirms the thermal stability of the TGAc up to 248 °C. The mass spectral analysis provides the additional confirmation for formation of this compound.

Acknowledgements

The authors are thankful to the University Grants Commission New Delhi, India, for providing financial assistance. The authors are very grateful to Dr. Babu Varghese, SAIF, Indian Institute of Technology, Chennai, India, for the single crystal XRD, and Dr. P.K. Das, Indian Institute of Science, Bangalore, India, for the SHG test.

References

[1] DHUMANE N.R., HUSSAINI S.S., NAVARKHALE V.V., SHIRSAT M.D., Cryst. Res. Technol., 41 (2006), 897.

[2] HUSSAINI S.S., DHUMANE N.R., RABBANI G., KARMUSE P., DONGRE V.G., SHIRSAT M.D., Cryst. Res. Technol., 42 (2007), 1110.

[3] HUSSAINI S.S., DHUMANE N.R., DONGRE V.G., SHIRSAT M.D., Optoelectr. Adv. Mater. Rapid Comm., 2 (2008), 108.

[4] HUSSAINI S.S., DHUMANE N.R., DONGRE V.G., GHUGHARE P., SHIRSAT M.D., Optoelectr. Adv. Mater. Rapid Comm., 2 (2007), 707.

[5] SURESH KUMAR B., RAJENDIRAN BABU K., Cryst. Res. Technol., 42 (2007), 607.

[6] MALLIK T., KAR T., BOCELLI G., MUSATTI. A., Cryst..Res. Technol., 41 (2006), 280.

[7] RAMESH BABU R., VIJAYAN N., GOPALAKRISHANAN R., RAMASAMY P., Cryst. Res. Technol., 41 (2006), 405.

[8] AMBUJAM K., RAJARAJAN K., SELVAKUMAR S., VETHA POTHEHER I., JOSEPH G.P., SAGAYARAJ P., J. Cryst. Growth., 286 (2006), 440.

[9] MOHAN KUMAR R., RAJAN BABU D., JAYARAMAN D., JAYAVEL R,, KITAMURA K., J. Cryst Growth., 275 (2005), e1935.

[10] RAMESH KUMAR G., GOKUL RAJ S., MOHAN R., JAYAVAL R., J. Cryst. Growth., 283 (2005), 193.

[11] MURALIDHARAN R., MOHAN KUMAR R., JAYAVAL R., RAMASAMY, P., J..Cryst. Growth., 259 (2003), 321.

[12] SILVERSTEIN R.M., BASSLER G.C, MORRILL T.C., *Spectrometric Identification of Organic Compounds*, Wiley, New York, 1981.

[13] RAJENDRAN K.V., JAYARAMAN D., JAYAVEL R., RAMASAMY P., J. Cryst. Growth., 254 (2003), 461.

[14] MADHAVAN J., ARUNA S, PRABHA K., PACKIUM J.J., JOSEPH G.P., SELVAKUMAR S., SAGAYARAJ P., J. Cryst. Growth., 293 (2006), 409.

Received 6 June 2008
Revised 1 September 2008

Materials Science-Poland, Vol. 27, No. 2, 2009

Dielectric relaxation and ac conductivity of WO_3 added $(Na_{1/2}Bi_{1/2})TiO_3$ ceramic

K. PRASAD[1*], K. KUMARI[1], K. P. CHANDRA[2], K. L. YADAV[3], S. SEN[4]

[1]Materials Research Laboratory, University Department of Physics,
T. M. Bhagalpur University, Bhagalpur 812 007, India

[2]Department of Physics, S.M. College, T. M. Bhagalpur University, Bhagalpur 812 001, India

[3]Department of Physics, Indian Institute of Technology, Roorkee 247 667, India

[4]National Metallurgical Laboratory, Jamshedpur 831 007, India

Ceramic samples of WO_3 added $(Na_{1/2}Bi_{1/2})TiO_3$ were prepared using a high-temperature solid-state reaction method. X-ray diffraction analyses indicate the formation of a single-phase orthorhombic structure. The apparent particle size and lattice strain are estimated using the Williamson–Hall plot. Dielectric studies revealed the relaxor behaviour and addition of WO_3 shifted phase transition temperature as well as depolarization temperature of $(Na_{1/2}Bi_{1/2})TiO_3$ to higher side. ac impedance plots were used to analyse the electrical behaviour of samples in function of frequency at various temperatures. The ac impedance studies revealed the presence of the grain boundary effect and evidence of a negative temperature coefficient of resistance. Cole–Cole analysis indicated a non-Debye type dielectric relaxation. The ac conductivity obeys the universal power law. The pair approximation type correlated barrier hopping model explains the universal behaviour of the s exponent. The apparent activation energy of the conduction process and density of states at the Fermi level have been discussed.

Key words: *$(Na_{1/2}Bi_{1/2})TiO_3$; impedance spectroscopy; dielectric relaxation; ac conductivity*

1. Introduction

In recent years, a number of perovskite ABO_3-type lead-free materials have been studied for their possible use in electronic applications. To date, lead-based compounds such as $Pb(Zr,Ti)O_3$, $PbTiO_3$, $Pb(Mg_{1/3}Nb_{2/3})O_3$, etc. have been widely used for multilayer capacitor, pyroelectric and/or piezoelectric applications. However, a need of lead-free materials has been felt worldwide for environmental protection. Recently, the legislation on waste electrical/electronic equipment (WEEE) and a re-

---

[*]Corresponding author, e-mail: k.prasad65@gmail.com; k_prasad65@yahoo.co.in

striction of hazardous substances (RoHS) has been issued by the European Union. The use of hazardous substances such as lead in electrical parts has been prohibited since 2006. To meet this requirement, the search for alternative environment-friendly lead-free materials for these applications has become the current trend. Sodium bismuth titanate, $(Na_{1/2}Bi_{1/2})TiO_3$ (NBT) is considered to be an excellent candidate as a key material of lead-free piezoelectric ceramic, which shows strong ferroelectric properties [1–7]. NBT belongs to perovskite family with rhombohedral symmetry at ambient temperature having a Curie temperature, T_m = 320 °C, and large remanent polarization, P_r = 38 μC/cm^2.

Furthermore, it has been reported that the NBT-based composition modified with $BaTiO_3$ [8,9], $Ba(Zr,Ti)O_3$ [10], $Ba(Cu_{1/2}W_{1/2})O_3$ [11], $SrTiO_3$ [12], $NaNbO_3$ [13], $MnCO_3$ [14], La_2O_3 [15,16], CeO_2 [16,17], Bi_2O_3-Sc_2O_3 [18], $LiTaO_3$ [19], ZrO_2 [20], etc. showed improved electrical as well as electromechanical properties. In addition, NBT exhibits an anomaly in its dielectric properties as a result of low temperature phase transition from a ferroelectric to an antiferroelectric phase at about 200 °C, which is termed the depolarization temperature T_d. Thus T_d is an important factor in NBT and NBT-based ceramics, in view of their practical uses, because the piezoelectric response disappears above T_d. It has also been seen that additives such as $SrTiO_3$, $BaTiO_3$, $(K_{1/2}Bi_{1/2})TiO_3$, etc. show better piezoelectric properties while the T_d is greatly reduced [11, 21]. Besides, it has been found that the addition of WO_3 improves the electrical properties of a similar perovskite system [22, 23]. A recent study on dielectric properties of the 2.5 wt. % WO_3 added $(Na_{1/2}Bi_{1/2})TiO_3$ system showed a remarkable shift in T_m as well as T_d to higher values [24].

Accordingly, in the present work, structural, microstructural, dielectric and impedance studies of 2.5 wt. % WO_3 added $(Na_{1/2}Bi_{1/2})TiO_3$ (abbreviated hereafter NBT -WO_3) ceramic are presented. An attempt has also been made to understand the mechanism of charge transport and the role of grain and grain boundaries on the electrical properties of NBT-WO_3 using complex impedance spectroscopy. The apparent activation energy of the conduction process and density of states at the Fermi level in the system are also evaluated.

2. Experimental

Polycrystalline samples of 2.5 wt. % WO_3 added $(Na_{1/2}Bi_{1/2})TiO_3$ were obtained from AR-grade (99.9%, pure) chemicals (Na_2CO_3, Bi_2O_3, TiO_2 and WO_3) using the solid-state reaction technique. The details of the sample preparation conditions have been discussed elsewhere [24]. The calcination and sintering conditions were kept at 1050 °C for 4 h and 1090 °C for 3 h, respectively. Completion of the reaction and the formation of the desired compound were checked by X-ray diffraction method. The weight of the sample was monitored before and after heat treatments. The maximum difference was about 1.12 mg for the total 10 g of the sample. Therefore, the composition of the sample was considered to be the same as the initial one. The XRD data were collected on calcined powder with an X-ray diffractometer (Siemens D500) at room temperature, using CoK_{α} radiation (λ = 1.7902 Å), over a wide range of Bragg angles (20° ≤ 2θ ≤ 80°) with the scanning rate of 2 deg·min^{-1}. The microstructure of the sintered NBT-WO_3 sample was taken on the fractured surface using a computer controlled scanning electron microscope (JEOL-JSM840A). The frequency dependent electric permittivity (ε), electrical impedance (Z), phase angle (θ) and loss tangent ($\tan\delta$) were measured at various temperatures using a computer-controlled LCR Hi-Tester (HIOKI 3532-50), Japan, on a symmetrical cell of type Ag|ceramic|Ag, where Ag is a conductive paint coated on either side of the pellet. ac conductivity data were obtained from impedance data, using the relation $\sigma_{ac} = t/(SZ')$, where Z' is the real part of impedance, t and S are the thickness and area of the sample, respectively.

3. Results and discussion

Figure 1 shows the X-ray diffraction (XRD) profile of NBT-WO_3 at room temperature. A standard computer program, 'PowdMult' [25], was utilized for the XRD profile analysis. A good agreement between the observed and calculated interplane spacing and no trace of any extra peaks due to constituent oxides were found, thereby suggesting the formation of a single-phase compound having an orthorhombic structure.

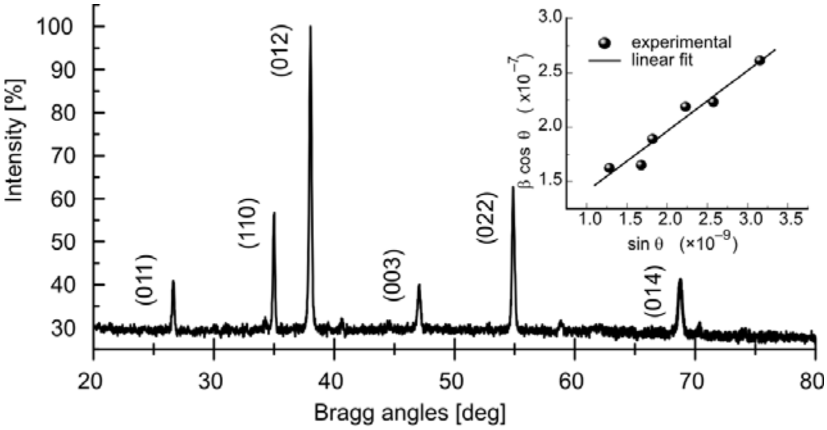

Fig. 1. Indexed X-ray diffraction pattern of NBT WO_3 at room temperature. Inset: the Williamson–Hall plot

The lattice parameters were found to be: a = 3.808(8) Å, b = 4.764(4) Å and c = 6.722(2) Å, with an estimated error of ±10^{-3} Å. The unit cell volume was estimated to be 121.99 Å^3. The apparent particle size and lattice strain of NBT-WO_3 were estimated by analyzing the X-ray diffraction peak broadening, using the Williamson–Hall approach [26]:

$$\beta\cos\theta = 2\frac{\Delta\xi}{\xi}\sin\theta + \frac{K\lambda}{D} \tag{1}$$

where D is the apparent particle size, β is the diffraction peak width at half intensity (FWHM) and $\Delta\xi/\xi$ is the lattice strain and K is the Scherrer constant (0.89). The term $K\lambda/D$ represents the Scherrer particle size distribution. The lattice strain can be estimated from the slope of the plot $\beta\cos\theta$ in function of $\sin\theta$, and the apparent particle size can be estimated from the intersection of this line at $\sin\theta = 0$. Linear least squares fitting to $\beta\cos\theta/\lambda - \sin\theta/\lambda$ data provided the values of the intercept and slope of the plot. A Gaussian model was applied to estimate the diffraction peak width at a half intensity.

$$I = I_0 + \frac{A}{\beta\sqrt{\frac{\pi}{2}}}\exp\left(-2\left(\frac{\theta-\theta_c}{\beta}\right)^2\right) \tag{2}$$

where A and θ_c are the area and centre of the curve, respectively. The inset of Fig. 1 illustrates the Williamson–Hall plot for NBT-WO_3. The apparent particle size and lattice strain are estimated, respectively, to be of the order of 104 nm and 0.0056.

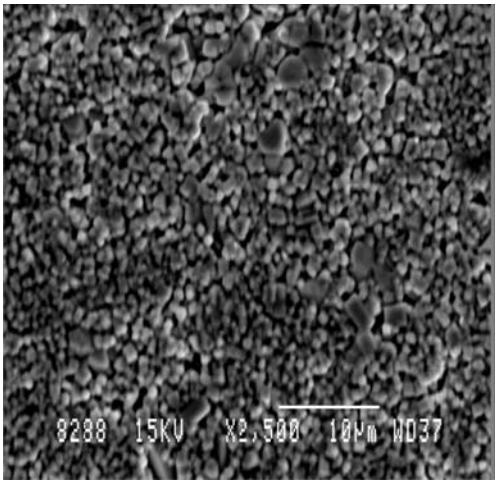

Fig. 2. SEM micrograph of NBT-WO_3 at 10 μm magnification

Figure 2 shows the SEM micrograph of NBT-WO_3 at 10 μm magnification. Grain shapes are clearly visible, indicating the existence of polycrystalline microstructure. Grains of unequal sizes appear to be distributed throughout the sample. The average grain size was estimated to be about 2.5 μm. The ratio of the grain size to apparent particle size of NBT-WO_3 is found to be of the order of 24.

Figure 3 presents the temperature dependences of ε and $\tan\delta$ at three representative frequencies for NBT-WO_3 system. It can be seen that the temperature of maximum relative permittivity (T_m) shifted to a higher temperature (from 440 °C at 1 kHz to 465 °C at 100 kHz) and ε_m decreased from 3139 at 1 kHz to 1001 at 100 kHz with the increase in frequency. Also, the plots show the diffuse phase transition (DPT) around 10 °C and a strong frequency dispersion, which indicates the relaxor behavior in NBT-WO_3. Besides, it is important to note that the addition of WO_3 to NBT shifts T_m as well as T_d to higher temperature by more than 100 °C which is desirable for piezoelectric applications. The room temperature value of ε and $\tan\delta$ at 1 kHz were found to be 424 and 0.18, respectively.

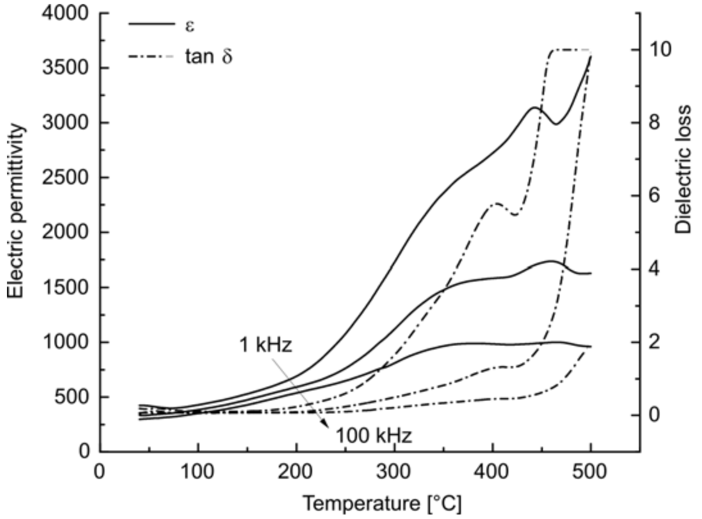

Fig. 3. Temperature dependences of ε and $\tan\delta$ of NBT-WO_3 at 1, 10 and 100 kHz

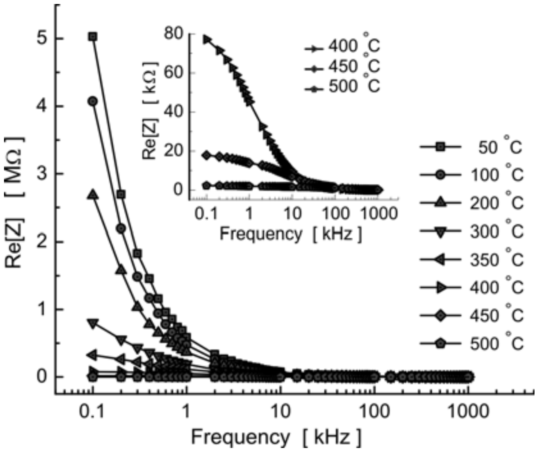

Fig. 4. Dependences of the real part of impedance of NBT-WO_3 on frequency at various temperatures. The inset shows an enlarged view at 400 °C, 450 °C and 500 °C

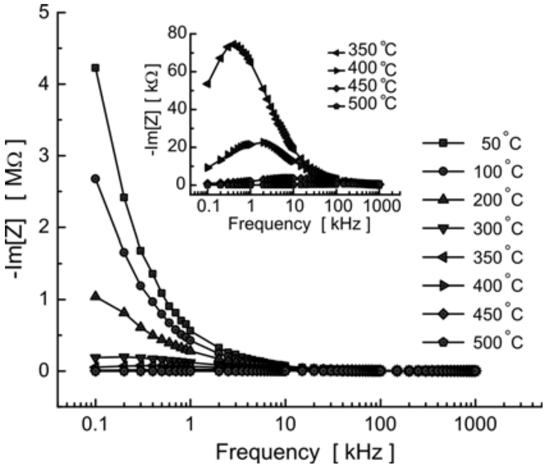

Fig. 5. Dependences of the imaginary part of impedance of NBT-WO$_3$ on frequency at various temperatures. The inset shows an enlarged view at 350–500 °C

Figures 4, 5 and their insets show the dependences of the real (Z') and imaginary (Z'') parts of impedance on frequency at various temperatures. The value of Z' decreases with increasing temperature as well as with increasing frequency which shows that NBT-WO$_3$ has the negative temperature coefficient of resistance (NTCR). This indicates an increase in the ac conductivity with the increase in temperature and frequency. The loss spectrum (Fig. 5) is characterized by some important features in the pattern such as the appearance of a peak ($Z''_{\max}$), asymmetric peak broadening (inset of Fig. 5) and the decrease of values of $Z''_{\max}$ which shift to higher temperatures with the increasing frequency. The asymmetric broadening of peaks in frequency explicit plots of Z'' suggests that there is a spread of relaxation times, i.e. the existence of a temperature dependent electrical relaxation phenomenon in the material.

Figure 6 shows the complex impedance plots at various temperatures in a logarithmic scale. It is observed that the impedance data at room temperature do not take the shape of a semicircle but rather resemble a straight line, suggesting the insulating behaviour of NBT-WO$_3$. It can also be seen that with the increase in temperature the slope of the lines decreases, and the lines bend towards the real (Z') axis. Also, at 300 °C a single semicircle, and at 400 °C and above two semicircles could be obtained with different values of resistance for grain (R_b) and grain boundary (R_{gb}). This indicates the increase in conductivity of the sample with the increase of temperature. Hence, the grain and grain boundary effects could be separated at these temperatures. It can also be observed that the peak maxima of the plots decrease and the frequency for the maximum shifts to higher values with the increase in temperature. Furthermore, it can be seen that the Cole–Cole plots (inset of Fig. 6) are not represented by a full semicircle, and the centre of the arc lies below the real (Z') axis, which suggests that the dielectric relaxation is of non-Debye type in NBT-WO$_3$. This may be due to the presence of distributed elements in the material-electrode system [27].

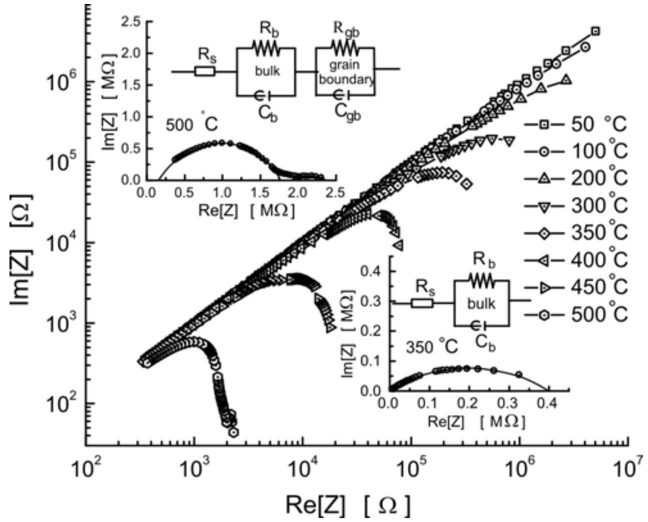

Fig. 6. Complex impedance plots of NBT-WO_3 at various temperatures in a logarithmic scale. The inset shows the Cole–Cole plots at 350 °C and 500 °C with the appropriate, equivalent electrical circuit

It is believed that the correlation among the Debye relaxators may start developing via formation of nanopolar clusters of Na-TiO_3 and Bi-TiO_3. Since the relaxation times of the relaxators within polar clusters are distributed over a wide spectrum at higher temperatures, their responses to an external field are in a different time domain. This results in the deviation from the Cole–Cole plots [28–30]. The first semicircle (which may be ascribed to a parallel combination of bulk resistance R_b and capacitance C_b), in a high frequency region corresponds to the intragranular behaviour of the material or bulk properties. The second semicircle (which may be attributed to a parallel combination of grain boundary resistance, R_{gb} and capacitance, C_{gb}), in a low frequency region represents the grain boundary contribution. It is obvious that the conductivities of grains and grain boundaries may be different, owing to different underlying processes, and thereby relax in different frequency regions. In such a case, the equivalent circuits (inset of Fig. 6) can be represented as a series network of parallel *RC* elements [27]. The impedance can then be expressed as:

$$Z^* = (R_b^{-1} + j\omega C_b)^{-1} + (R_{gb}^{-1} + j\omega C_{gb})^{-1} \quad (3)$$

The values of R_b and R_{gb} could directly be obtained from the intercept of the ends of the semicircle on the Z' axis whose temperature dependences are shown in Fig. 7. It can be seen that the values of R_b and R_{gb} decrease with the increase of temperature, which clearly indicates the NTCR character of NBT-WO_3 and supports Fig.4. The capacitances (C_b and C_{gb}) due to these effects can be estimated using the relation:

$$\omega_{\max} RC = 1 \quad (4)$$

where $\omega_{\max}$ (= $2\pi f_{\max}$) is the angular frequency at the maximum of the semicircle. Figure 7 shows the temperature dependences of C_b and C_{gb} obtained from the Cole–Cole plots at various temperatures. The decrease in the value of R_b of NBT-WO$_3$ is associated with an increase in conductivity with the increase in temperature. Also, a decrease in the R_{gb} values with the increment of temperature suggests the lowering of the barrier towards the mobility of charge carriers aiding electrical conduction at higher temperatures [30]. Besides, these curves do not coincide with the origin; rather they start from ~350 Ω. Therefore, a series resistance R_s =350 Ω should be added to the LCR circuit representation (inset of Fig. 6) of the sample.

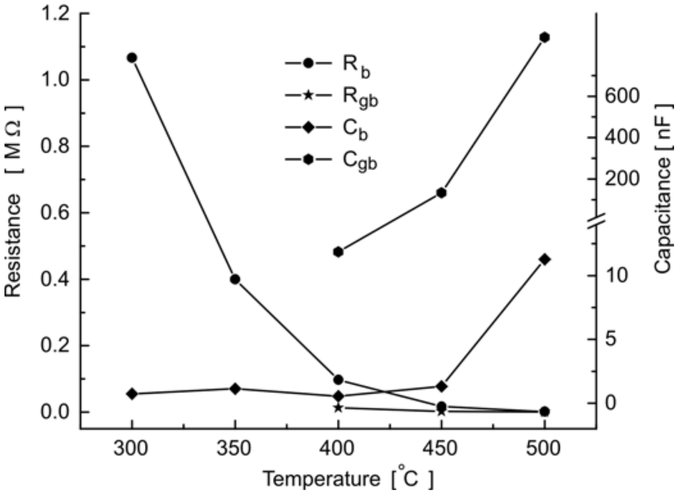

Fig. 7. Temperature dependences of R_b, R_{gb}, C_b and C_{gb} of NBT-WO$_3$

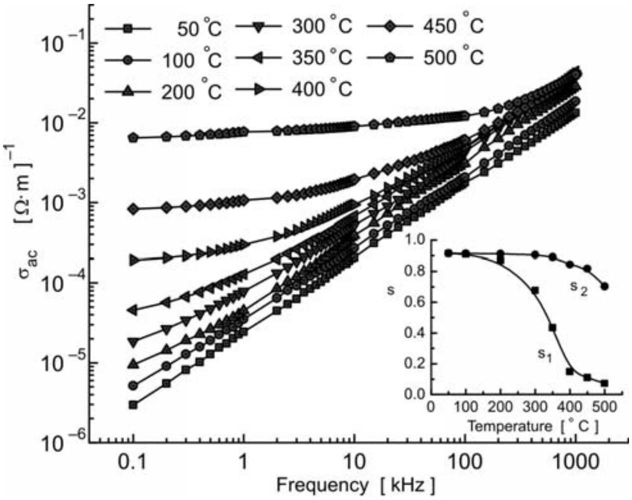

Fig. 8. Dependences of ac conductivity on frequency at various temperatures of NBT-WO$_3$. Inset: Temperature dependence of index *s*

Figure 8 shows the log–log dependences of electrical conductivity on frequency at various temperatures. The pattern of the conductivity spectrum shows dispersion throughout the chosen frequency range. The frequency dependence of the ac conductivity at room temperature obeys the universal power law [31]:

$$\sigma_{ac} = A\omega^{S} \tag{5}$$

whereas above room temperature this dependence follows the double power law of type [32]:

$$\sigma_{ac} = A_1\omega^{S_1} + A_2\omega^{S_2} \tag{6}$$

where A, A_1 and A_2 are the temperature dependent constants, and s, s_1 and s_2 are the temperature as well as frequency dependent parameters. Such dependence is associated with displacement of carriers which move within the sample by discrete hops of the length R between randomly distributed, localized sites. The values of the indices s_1 and s_2 can be obtained from the slopes in the low and high frequency regions, respectively. The inset of Fig. 8 shows the temperature dependences of s_1 and s_2. It can be seen that the values of both s_1 and s_2 are always lower than 1, and decrease with the increase of temperature. Furthermore, the value of s_1 approaches zero at higher temperatures, indicating that dc conductivity dominates at higher temperatures in the low frequency region and obeys Jonscher's power law [33]:

$$\sigma_{ac} = \sigma(0) + A\omega^{S_2} \tag{7}$$

where $\sigma(0)$ is the frequency independent part of the conductivity. The model based on correlated hopping of electrons over a barrier [34] predicts a decrease in the value of the index with the increase in temperature, and it was found to be consistent with the experimental results. Therefore, the electrical conduction in the system could be considered due to the short-range translational type hopping of charge carriers [30, 32, 35]. This indicates that the conduction process is thermally activated. The exponent s_i (i = 1 or 2) and binding energies are related by:

$$s_i = 1 - \frac{6k_BT}{W_m} \tag{8}$$

A decrease of W_m upon temperature increase was observed. The characteristic decrease in slopes (s_1 and s_2) with the increase of temperature is due to the decrease in binding energy [35].

Figure 9 shows the dependence of ac conductivity on T^{-1}. A linear least squares fit of $\ln\sigma_{ac}$–$10^3/T$ data in the higher temperature region gives the value of the apparent activation energy of the conduction process. It has been observed that the value of the activation energy (0.019 eV at 1 kHz) decreases with the increase in frequency. It can be seen that the ac conductivity is almost insensitive in the low temperature region, irrespective of the operating frequencies. Also, the onset temperature shifts to a higher temperature with the increase in frequency. A low value of the activation energy obtained could be attributed to the influence of an electronic contribution to the conductivity in which the transport of carriers may occur through hopping between localized states in a disordered manner. Also, the increase in conductivity with temperature may be explained based on the assumption that within the bulk, the oxygen vacancies, due to the loss of oxygen, are usually created during sintering and the charge compensation, which may leave behind free electrons, making them n-type.

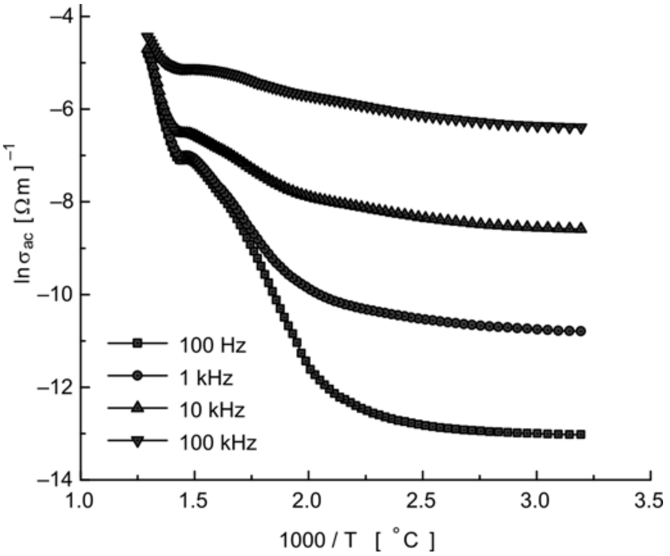

Fig. 9. Dependence of ac conductivity of NBT-WO_3on inverse of temperature at various frequencies

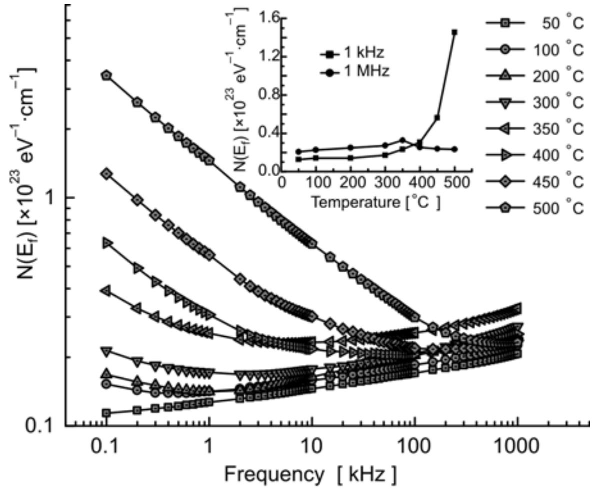

Fig. 10. Frequency dependence of $N(E_f)$ in NBT-WO_3 at various temperatures.
Inset: Temperature dependences of $N(E_f)$ at 1 kHz and 1 MHz

The hopping conduction mechanism is generally consistent with the existence of a high density of states in the materials having a band gap similar to that of a semiconductor. Due to localization of charge carriers, formation of polarons takes place and the hopping conduction may occur between the nearest neighbouring sites. The ac conductivity data were used to evaluate the density of states at the Fermi level $N(E_f)$ using the dependence [36]:

$$\sigma_{ac}(\omega) = \frac{\pi}{3} e^2 \omega k_B T \left(N(E_f) \right)^2 \alpha^{-5} \left(\ln \frac{f_0}{\omega} \right)^4 \tag{9}$$

where e is the electronic charge, f_0 the photon frequency and α is the localized wave function, assuming $f_0 = 10^{13}$ Hz, $\alpha = 10^{10}$ m^{-1} at various operating frequencies and temperatures. Figure 10 shows the frequency dependence of $N(E_f)$ at different temperatures. As can be seen the value of $N(E_f)$ increases with the increase in operating frequency at low temperatures showing a minimum (from 100 °C onwards) which shift towards higher frequencies with the increasing temperature. The inset of Fig. 10 shows the variation of $N(E_f)$ with temperature at two representative frequencies: 1 kHz and 1 MHz. It is found that the value of $N(E_f)$ increases with the increase in temperature at low frequencies, while it shows a maximum at 350 °C at 1 MHz. The reasonably high values of $N(E_f)$ suggest that the hopping between the pairs of sites dominate the mechanism of charge transport in NBT-WO_3.

4. Conclusion

Polycrystalline samples of 2.5 wt. % WO_3 added $(Na_{1/2}Bi_{1/2})TiO_3$, prepared by a high-temperature solid-state reaction technique, were found to have a single-phase perovskite-type orthorhombic structure. Impedance analyses indicated the presence of grain and grain boundary effects. The dielectric relaxation in the system was found to be of non-Debye type. The ac conductivity was found to obey the universal power law. The pair approximation type correlated barrier hopping (CBH) model accurately describes the mechanism of charge transport in NBT-WO_3 system.

References

[1] GOMAH-PETTRY J.R., SAÏD S., MARCHET P., MERCURIO J.P., J. Eur. Ceram. Soc., 24 (2004), 1165.
[2] XU Q., CHEN S., CHEN W., WU S., ZHOU J., SUN H., LI Y., Mater. Chem. Phys., 90 (2005), 111.
[3] BUHRER C.F., J. Chem. Phys., 36 (1962), 798.
[4] SUCHANICZ J., ROLEDER K., KANIA A., HANDEREK J., Ferroelectrics, 77 (1988), 107.
[5] ROHLEDER K., SUCHANICZ J., KANIA A., Ferroelectrics, 89 (1989), 1.
[6] HOSONO Y., HARADA K., YAMASHITA Y., Jpn. J. Appl. Phys., 40 (2001), 5722.
[7] SUCHANICZ J., KUSZ J., BHÖM H., DUDA H., MERCURIO J.P., KONIECZNY K., J. Eur. Ceram. Soc., 23 (2003), 1559.
[8] TAKEDA H., AOTO W., SHIOSAKI T., Appl. Phys. Lett., 87 (2005), 102104.

[9] WANG X.X., TANG X.G., CHAN H.L.W., Appl. Phys. Lett., 85 (2004), 91.

[10] PENG C., LI J-F., GONG W., Mater. Lett., 59 (2005), 1576.

[11] CHU B.J., CHEN D.R., LI G.R., YIN Q.R., J. Eur. Ceram. Soc., 22 (2002), 2115.

[12] GUO Y., KAKIMOTO KEN-ICHI, OHSATO H., Solid State Commun., 129 (2004), 279.

[13] LI Y.M., CHEN W., ZHOU J., XU Q., GU X.Y., LIAO R.H., Physica B, 365 (2005), 76.

[14] NAGATA H., TAKENAKA T., J. Eur. Ceram. Soc. 21 (2001), 1299.

[15] HERABUT A., SAFARI A., J. Amer. Ceram. Soc. 80 (1997), 2954.

[16] WANG X.X., CHAN H.L.W., CHOY C.L., Appl. Phys. A 80 (2005), 333.

[17] LI Y., CHEN W., XU Q., ZHOU J., WANG Y., SUN H., Ceram. Int., 33 (2007), 95.

[18] TAKENAKA T., NAGATA H., Jpn. J. Appl. Phys., 30 (1991), 2236.

[19] GUO Y., KAKIMOTO K-I., OHSATO H., Mater. Lett., 59 (2005), 241.

[20] LILY, KUMARI K., PRASAD K., CHOUDHARY R.N.P., J. Alloys Comp., 453 (2008), 325.

[21] ZHAO S., LI G., DING A., WANG T., YIN Q., J. Phys. D: Appl. Phys., 39 (2006), 2277.

[22] UEDA I., Jpn. J. Appl. Phys., 11 (1972), 450.

[23] ZHONG N., DONG X., SUN D., DU H., YANG H., Mater. Sci. Eng. B, 106 (2004), 263.

[24] PRASAD K., KUMARI K., LILY, CHANDRA K.P., YADAV K.L., SEN S., Solid State Commun., 144 (2007), 42.

[25] *PowdMult, An interactive powder diffraction data interpretation and indexing program*, ver. 2.1, School of Physical Science, Flinders University of South Australia, Bedford Park, S. A. 5042, Australia.

[26] SURYANARAYANA C., GRANT NORTON M., *X-Ray Diffraction A Practical Approach*, Plenum Press, New York, 1998.

[27] *Impedance Spectroscopy Emphasizing Solid Materials and Systems*, J.R. Macdonald (Ed.), Wiley, New York, 1987.

[28] BONNEAU P., GARNIER O., CALVARIN G., HUSSON E., GAVARRI J.R., HEWAT A.W., MORREL A., J. Solid State Chem., 91 (1991), 350.

[29] LILY, KUMARI K., PRASAD K., YADAV K.L., J. Mater. Sci., 42 (2007), 6252.

[30] PRASAD K., LILY, KUMARI K., CHANDRA K.P., YADAV K.L., SEN S., Appl. Phys. A., 88 (2007), 377.

[31] MOTT N.F., DAVIS E.A., *Electronic Processes in Non-Crystalline Materials*, Oxford University Press, London, 1979.

[32] FUNKE K., Prog. Solid State Chem., 22 (1993), 111.

[33] JONSCHER A.K., Nature, 267 (1977), 673.

[34] ELLIOTT S.R., Philos. Mag. B, 37 (1978), 553.

[35] PRASAD K., KUMARI K., LILY, CHANDRA K.P., YADAV K.L., SEN S., Adv. Appl. Ceram., 106 (2007), 241.

[36] SHARMA G.D., ROY M., ROY M.S., Mater. Sci. Eng. B, 104 (2003), 15.

Received 19 June 2008

Materials Science-Poland, Vol. 27, No. 2, 2009

Electrical properties of tin phthalocyanine-based heterostructures: $SnPcCl_2$/GaP, $SnPcCl_2$/InP and $SnPcCl_2$/GaAs

M.M. EL-NAHASS[1], A.M. FARID[1], H.H. AMER[2], K.F. ABDEL-RAHMAN[1*], H.A.M. ALI[1]

[1]Faculty of Education, Ain Shams University, Cairo, Egypt

[2]National Centre for Radiation Research and Technology, Nasr City, Cairo, Egypt

Electrical characteristics of organic/inorganic, $SnPcCl_2$/GaP, $SnPcCl_2$/GaAs and $SnPcCl_2$/InP (Pc standing for phthalocyanine) heterojunctions were studied. Current density–voltage (*J*–*V*) characteristics showed thermionic emission conduction at relatively low voltages followed by a space charge limited conduction mechanism at relatively high voltages. The capacitance–voltage (*C*–*V*) characteristics indicated that the devices have an abrupt nature. Various parameters have been determined from the *J*–*V* and *C*–*V* analysis for the three devices.

Key words: *phthalocyanines; organic/inorganic heterojunction*

1. Introduction

A considerable interest in electrical and optical properties of organic molecular semiconductors reflects their increasingly widespread use in organic and hybrid organic-inorganic (OI) devices [1]. When organic semiconductors are deposited onto inorganic semiconductor substrates such as Si or InP, a rectifying energy barrier is formed at the OI interface [2]. Transport of charge across the energy barrier is limited by various mechanisms.

Organic semiconductors like phthalocyanines have been intensively studied with regard to their electrical and photoconduction properties [3]. Phthalocyanines are generally p-type semiconductors and have the advantage of being sufficiently stable under chemical and thermal treatment. They can be easily vacuum deposited, find application in gas sensors and various organic optoelectronic devices such as solar cells, light-emitting diodes as hole transport layers [6–9] in high purity thin films without

---

[*]Corresponding author, e-mail: elrahman99@hotmail.com

decomposition [4, 5]. Electronic devices with phthalocyanines as the active materials can be fabricated on a wide variety of substrates [5]. Phthalocyanines have attracted a lot of attention in view of their possible applications in organic-inorganic structures. They are expected to open up new areas of research in optoelectronic materials, because they make it possible to include and exploit in a single system the specific light absorption characteristics of the organic molecules as well as the good carrier mobility of the inorganic materials [10, 11]. Recently, efforts have been exerted to combine the desired properties of inorganic and organic layers in optoelectronic junctions. Takada et al. [12] have demonstrated an example of the formation of CuPc/TiO heterostructure; these junctions were found to exhibit 40 times higher photoconductivity than a single layer of CuPc. Recently, Lee et al. [13] have fabricated PbTe/CuPc heterojunctions.

Among various phthalocyanines, tin phthalocyanine dichloride ($SnPcCl_2$) has received less attention than others. The object of this paper is to investigate the electrical characteristics of $SnPcCl_2$/GaP, $SnPcCl_2$/GaAs and $SnPcCl_2$/InP heterojunctions. In particular, the voltage properties of the different substrates were investigated in a controlled-light environment, in order to test the response of the heterojunctions to illumination and to total darkness. Also, capacitance-voltage measurements were carried out in the dark in order to characterize these cells.

2. Experimental

The films were fabricated using tin phthalocyanine dichloride ($SnPcCl_2$) which had been purchased from the ACROS Organics Company, USA. Gallium phosphide (GaP), gallium arsenide (GaAs) and indium phosphide (InP) single crystals were used as substrates in order to fabricate different organic/inorganic diodes. The substrates were cleaned and etched before the device fabrication. The substrates were rinsed in distilled water, ethyl alcohol and acetone for 2 min, and then in distilled water for 1 min. The substrates were then etched for 45 s in aqueous solution of H_2O_2 and H_2SO_4. After etching, the substrates were washed for 1 min in distilled water and then dried with nitrogen. All surface treatments were chosen such that they would not attack the underlying semiconductor but would rather only affect the surface region.

After surface cleaning, the samples were mounted inside the vacuum chamber of an Edward 306 evaporator unit. A thin film of $SnPcCl_2$ with a thickness of 325 nm was then deposited onto the clean surface of the substrates by thermal evaporation. The evaporation was carried out by sublimation of the $SnPcCl_2$ powder from a quartz crucible source heated with a tungsten coil in the vacuum of 10^{-4} Pa with the deposition rate of 2.5 $nm\cdot s^{-1}$. The substrate temperature was kept at 300 K during the deposition. The OI devices were completed by vacuum deposition of an ohmic Au contact using a suitable mask placed in contact with the top of the $SnPcCl_2$ layer. The other ohmic contact was made to the back wafer surface, also by vacuum deposition of Ag. A typical heterojunction is shown in Fig. 1a.

In the present paper, the electrical characteristics of $SnPcCl_2$/GaP, $SnPcCl_2$/GaAs and $SnPcCl_2$/InP hetrerojunctions were examined by using current density–voltage (*J–V*) measurements in the dark. The current flowing through the device was determined using a stabilized power supply and a high impedance electrometer (Keithley 617 A).

Also, capacitance–voltage (*C–V*) measurements were performed at a frequency of 1 MHz using a computerized (*C–V*) system, consisting of a 410 *C–V* meter, controlled via interface with a 4108 *C–V* connected to a personal computer.

3. Results and discussion

3.1. Dark *J–V* characteristics

J–V characteristics at room temperature for the three fabricated diodes structures; Au/$SnPcCl_2$/GaP/Ag, Au/$SnPcCl_2$/GaAs/Ag and Au/$SnPcCl_2$/InP/Ag, are shown in Fig. 1b. The differences in the behaviour of these devices result from a significant difference between the inorganic substrates and the nature of the OI interface. The rectification ratio for Au/$SnPcCl_2$/GaP/Ag at 1.4 V was found to be about 100 and this value was higher than those obtained for the other diodes.

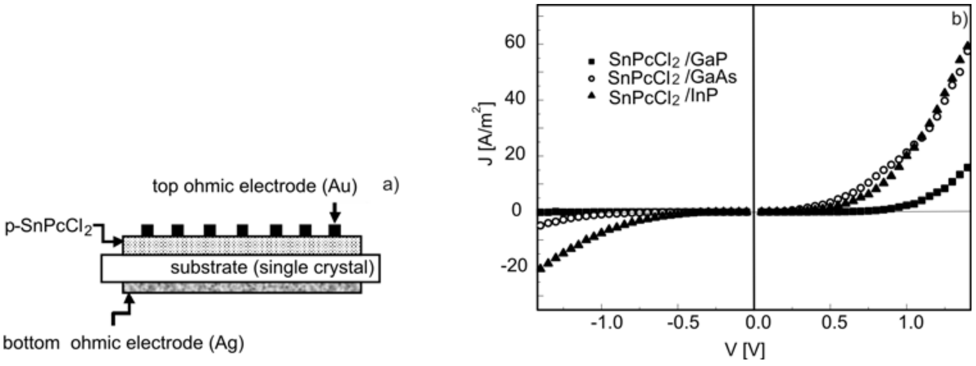

Fig. 1. Typical schematic diagram of p-$SnPcCl_2$/n-substrate (GaP or GaAs or InP), heterojunction (a), and *I–V* characteristics at room temperature for p-$SnPcCl_2$/n-GaP, p-$SnPcCl_2$/n-GaAs and p-$SnPcCl_2$/n-InP contact barrier diodes

J–V characteristics for various heterojunction devices under a forward bias at several temperatures ranging from 293 to 373 K are shown in Fig. 2. As observed from the figure, the current density increases exponentially with the applied voltage and then deviates from the exponential due to the effect of series resistance on the system. So, the forward current can be classified into two regions according to the applied voltage. In the first region (low voltage, $V < 0.5$ V), the *J–V* characteristics of the devices follow the dependence characteristic of thermionic emission theory for conduction across the junction, which can be expressed by the following equation [14]

$$J = J_s \exp\left(\frac{qV}{nk_B T}\right) - 1 \tag{1}$$

where J_s is the reverse saturation current density, q is the electronic charge, n is the diode quality factor, which accounted for the extent of the non-ideality of the diode and k_B is the Boltzmann constant.

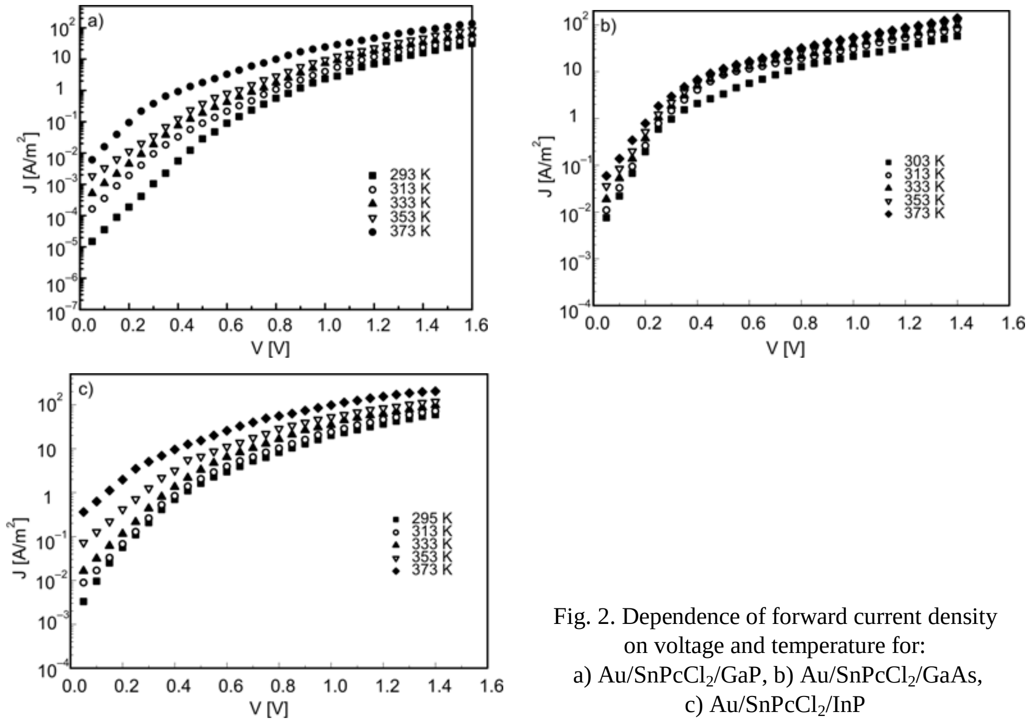

Fig. 2. Dependence of forward current density on voltage and temperature for: a) Au/SnPcCl$_2$/GaP, b) Au/SnPcCl$_2$/GaAs, c) Au/SnPcCl$_2$/InP

The saturation current density, J_s, is given by [14]:

$$J_s = A^* T^2 \exp\left(-\frac{\phi_B}{k_B T}\right) \tag{2}$$

where A^* is the effective Richardson constant, and ϕ_B is the Schottky barrier height of the diode. Applying this theory, the values of the diode quality factor n and the reverse saturation current density J_s have been calculated and collected in Table 1. The value of n is greater than unity which can be attributed to the recombination of the electrons and holes in the depletion region [15]. The potential barrier ϕ_B has been calculated by employing the same theory and is compiled in Table 1. It is observed that the Schottky barrier effect disappears when the applied voltage is 0.63, 0.58 and 0.26 V in SnPcCl$_2$/GaP, SnPcCl$_2$/InP and SnPcCl$_2$/GaAs devices, respectively. Beyond these, the current density is mainly contributed from the bulk resistance of SnPcCl$_2$ layer. The SnPcCl$_2$/GaAs and SnPcCl$_2$/InP devices exhibit smaller contact barrier heights than that obtained for the SnPcCl$_2$/GaP heterojunction device, as seen from Table 1. The relatively small OI barrier heights are found to arise from a high density of states at the inorganic substrate surface [16].

Table 1. Electrical parameters derived from the analysis of *J–V* characteristics

Sample	n	J_s [A/m^2]	ϕ_B [eV]
Au/SnPcCl$_2$/GaP/Ag	2.34	7.476×10^{-6}	0.63
Au/SnPcCl$_2$/InP/Ag	2.75	7.895×10^{-4}	0.58
Au/SnPcCl$_2$/GaAs/Ag	1.81	2.5×10^{-3}	0.26

In the second region (relatively high voltage, $V > 0.5$ V), the conduction may be attributed to the space charge limited currents in the organic layer. It is observed that the current density shows a power dependence of voltage of the type $J \propto V^m$ for the three devices as seen in Fig. 3. The calculated value of m is higher than 2, as seen in Table 2, thus this power dependence shows that the forward biased current is a space charge limited current (SCLC) dominated by an exponential distribution of traps.

Table 2. The parameters derived from the *J–V* analysis in the SCLC region

Parameter	SnPcCl$_2$/GaP	SnPcCl$_2$/GaAs	SnPcCl$_2$/InP
m	6.24	2.6	3.14
T_t [K]	1538	485	631.3
μ, [m^2·s^{-1}·V^{-1}]	8.19×10^{-9}	4.35×10^{-12}	3.53×10^{-11}
N_t [m^{-3}]	1.75×10^{21}	1.85×10^{21}	2.28×10^{21}
P_0 [J^{-1}·m^{-3}]	8.26×10^{40}	2.76×10^{41}	2.61×10^{41}
E_r [eV]	0.34	0.29	0.23

The current density in this region is given by [16]:

$$J = q\mu N_V \left(\frac{\varepsilon}{eP_0 k_B T_t}\right)^l \frac{V^{l+1}}{d^{2l+1}} \tag{3}$$

where μ is the hole mobility, N_V is the effective density of states at the valence band edge, taken as 10^{27} m^{-3} [17], ε is the permittivity of the SnPcCl$_2$ taken as 3.214×10^{-11} F·m^{-1} [18], P_0 is the trap concentration per unit energy range at the valence band edge, l is the ratio between the temperature parameter T_t and the ambient temperature. The parameter T_t is the characteristic temperature of the exponential trap distribution, tabulated in Table 2 for the three junctions. The total concentration of traps is given by:

$$N_t = P_0 k_B T_t \tag{4}$$

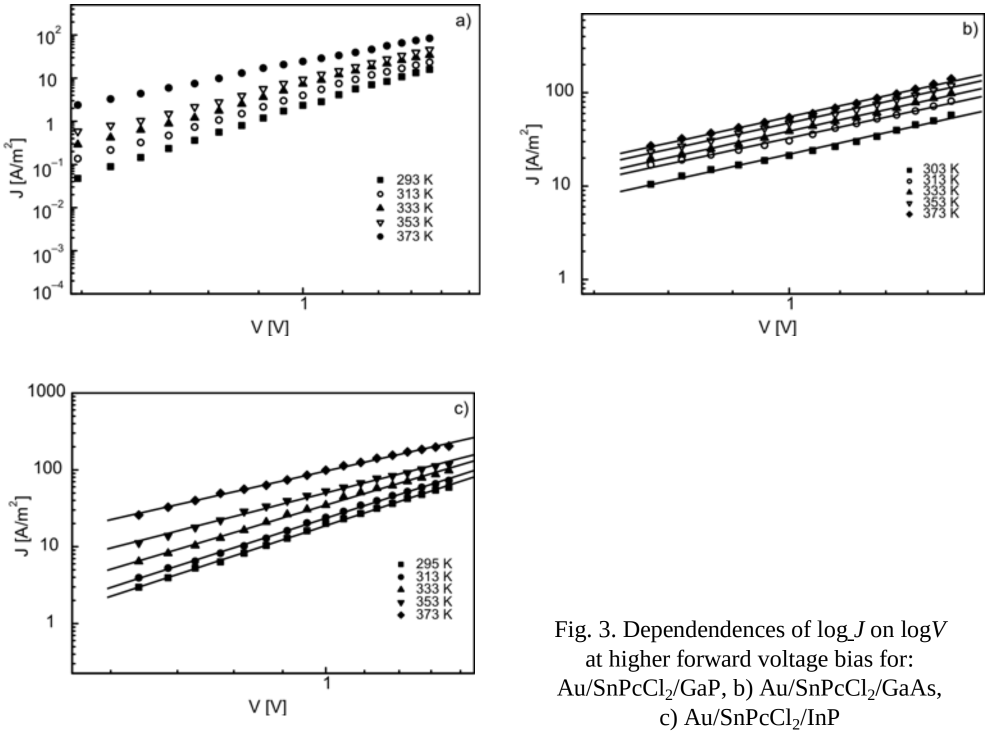

Fig. 3. Dependendences of log *J* on log*V* at higher forward voltage bias for: Au/SnPcCl$_2$/GaP, b) Au/SnPcCl$_2$/GaAs, c) Au/SnPcCl$_2$/InP

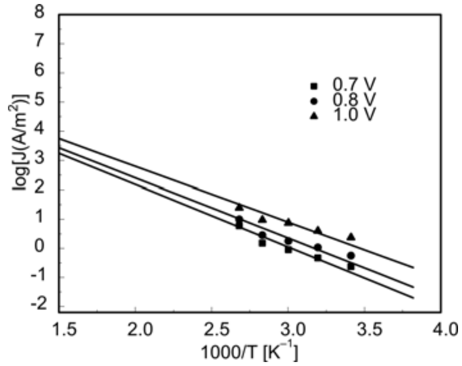

Fig. 4. Dependences of log*J* on 1000/*T* in SCLC for SnPcCl$_2$/GaP device

The value of N_t can be obtained from the variation of the current density with the temperature in the SCLC region. As shown in Fig. 4, the dependences of log*J* on 1000/T for the SnPcCl$_2$/GaP heterojunction are straight lines. The same behaviour was also obtained for the other two devices. The slope of these lines is given by [17, 19]:

$$\frac{d\left(\log J\right)}{d\left(\dfrac{1}{T}\right)} = T_t \log \frac{\varepsilon V}{e d^2 N_t} \tag{5}$$

The value of μ, has been calculated from the intercept of the line in Fig. 4 given by [5]:

$$\log J_0 = \log \frac{q\mu N_V V}{d} \tag{6}$$

The values of μ, N_t and P_0 have been calculated for the three heterojunctions (Table 2). The electrical parameters derived from the *J–V* analysis in the SCLC region, are consistent with the values reported for some other metal phthalocyanines (MPc's).

The measured reverse-bias characteristics of $SnPcCl_2$/GaP, $SnPcCl_2$/GaAs and $SnPcCl_2$/InP heterojunctions at various temperatures are shown in Fig. 5. A relatively bias dependence of the reverse current is observed which could be due to the recharging of trapping states within the junction region [20].

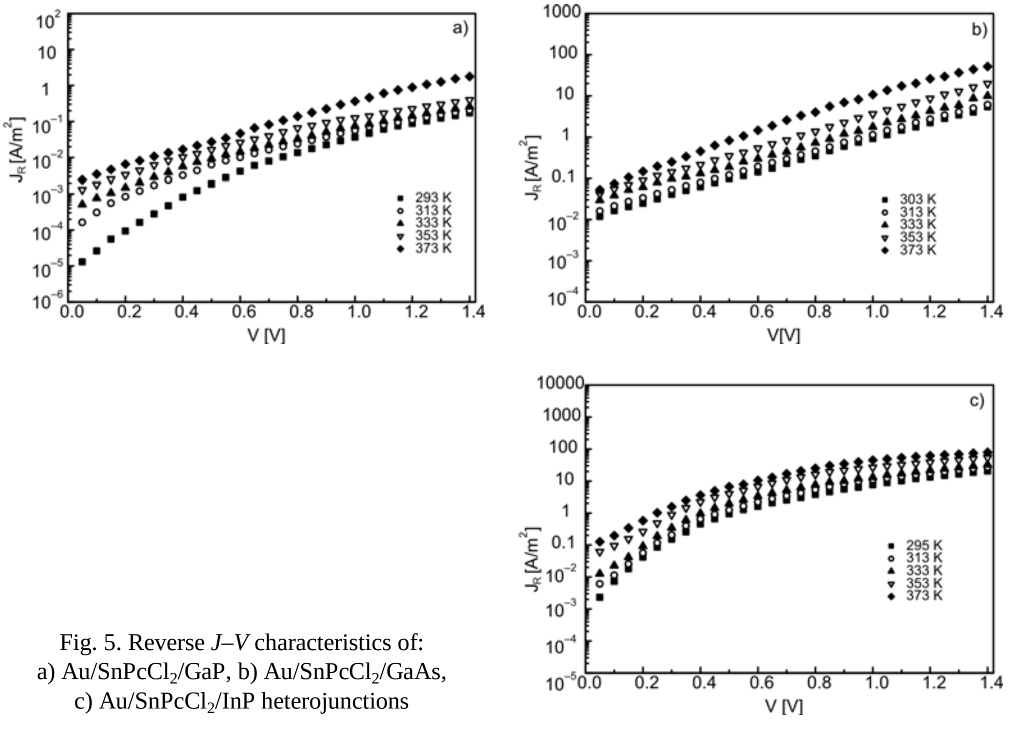

Fig. 5. Reverse *J–V* characteristics of:
a) Au/$SnPcCl_2$/GaP, b) Au/$SnPcCl_2$/GaAs,
c) Au/$SnPcCl_2$/InP heterojunctions

Figure 6 shows the temperature dependences of the reverse current of $SnPcCl_2$/GaP, $SnPcCl_2$/GaAs and $SnPcCl_2$/InP heterojunctions. ln(J_R) was plotted in function of 1000/T at various reverse-bias voltages. As the Arrhenius plots appear to exhibit a thermally activated behaviour, it is reasonable to assume that the reverse current can be expressed as [21]

$$J_R(T) = \alpha \exp\left(-\frac{E_r}{k_B T}\right) \tag{7}$$

where E_r is the activation energy. The calculated values of E_r for the three junctions are tabulated in Table 2.

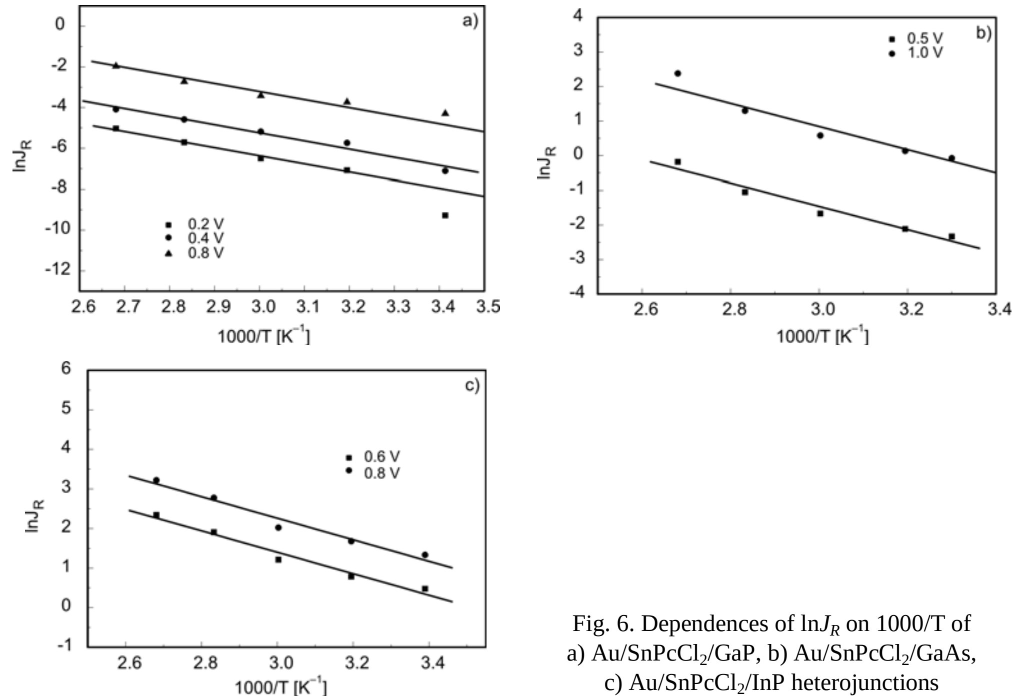

Fig. 6. Dependences of lnJ_R on 1000/T of a) Au/SnPcCl$_2$/GaP, b) Au/SnPcCl$_2$/GaAs, c) Au/SnPcCl$_2$/InP heterojunctions

3.2. Capacitance–voltage characteristics

The capacitance of the heterojunctions (Au/SnPcCl$_2$/GaP, Au/SnPcCl$_2$/GaAs and Au/SnPcCl$_2$/InP) were measured at 1 MHz and at various temperatures. Figure 7 shows the dependence of $1/C^2$ with the voltage across the junctions. It is clear from the figure that the capacitances of the samples increase with the increase in temperature. Also, the values of C^{-2} on V varies linearly with the applied voltage, indicating that the junctions have an abrupt nature and the voltage dependence is [22]:

$$C^{-2} = \frac{2(V_d - V)(\varepsilon_1 N_1 + \varepsilon_2 N_2)}{qA^2 \varepsilon_0 \varepsilon_1 \varepsilon_2 N_1 N_2} \tag{8}$$

where V_d is the built-in voltage, ε_i is the electric permittivity and N_i is the donor (or acceptor) concentration; $i = 1$ or 2 denotes the two semiconductors that form the junction.

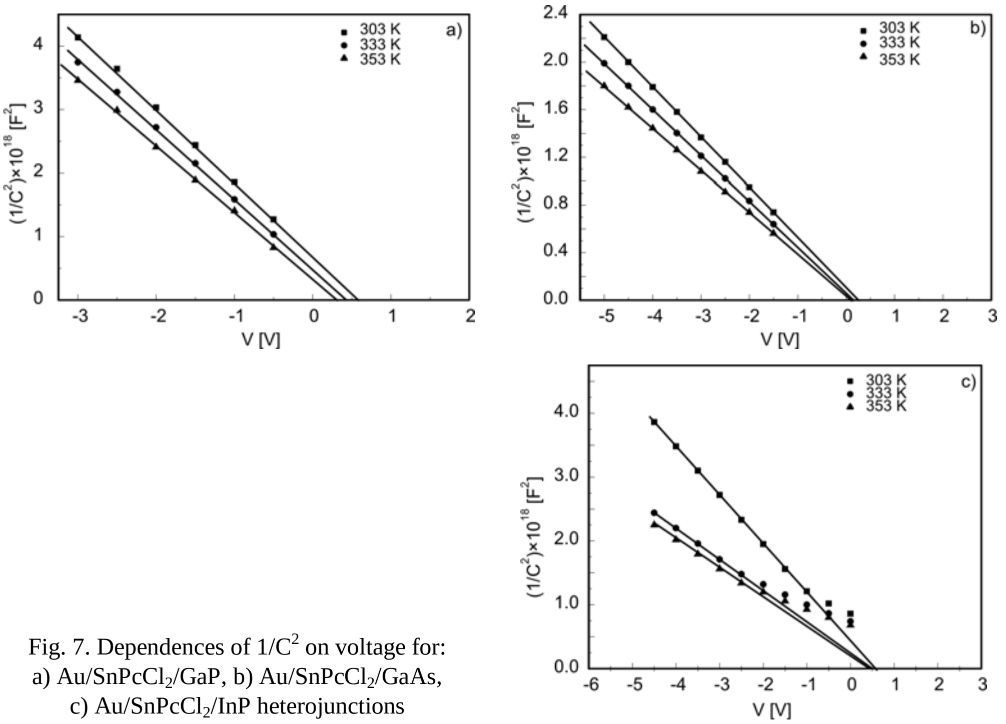

Fig. 7. Dependences of 1/C^2 on voltage for:
a) Au/SnPcCl$_2$/GaP, b) Au/SnPcCl$_2$/GaAs,
c) Au/SnPcCl$_2$/InP heterojunctions

Table 3. Electrical parameters calculated from the *C–V* measurements for SnPcCl$_2$/GaP, SnPcCl$_2$/InP and SnPcCl$_2$/GaAs devices

Heterojunction	Temperature					
	303 K		333 K		353 K	
	Parameter					
	V_d [V]	N [m^{-3}]	V_d [V]	N [m^{-3}]	V_d [V]	N [m^{-3}]
SnPcCl$_2$/GaP	0.58	7.33×10^{20}	0.42	7.74×10^{20}	0.30	8.07×10^{20}
SnPcCl$_2$/InP	0.55	5.52×10^{19}	0.50	8.13×10^{19}	0.46	9.59×10^{19}
SnPcCl$_2$/GaAs	0.25	9.12×10^{20}	0.15	9.92×10^{20}	0.09	1.08×10^{21}

Equation (8) can be reduced to [23]:

$$C^{-2} = \frac{2\left(V_d - V\right)}{q\varepsilon_0\varepsilon N A^2} \tag{9}$$

where ε is the electric permittivity of SnPcCl$_2$, A is the effective area of the device and N is the free carrier concentration. The built-in voltages of the junctions were calculated by extrapolating the $1/C^2$ curve to $V = 0$ and from the slope of the straight lines the values of N can be determined. The calculated values of V_d and N are compiled in Table 3. It can be seen from these tables that the built-in voltage decreases with the increase in temperature, while the carrier concentration increases with the increase in temperature.

4. Conclusion

The electrical characteristics of OI semiconductor diodes $SnPcCl_2$/GaP, $SnPcCl_2$/GaAs and $SnPcCl_2$/InP have been studied. Thermionic emission conduction in the low voltage range has been identified from the forward bias current density –voltage (J–V) measurements at various temperatures for the three devices. The contact barrier height for the $SnPcCl_2$/GaP heterojunction device is larger than those obtained for the $SnPcCl_2$/GaAs and $SnPcCl_2$/InP devices. At higher voltages, a space charge limited current (SCLC) controlled by an exponential trapping distribution above the valence band edge has been observed. Some electrical parameters, derived from the J–V analysis in the SCLC region, are consistent with the values reported for some other metal phthalocyanines. The C–V measurements showed that the heterojunctions have an abrupt nature. The built-in potential V_d decreases with the increase in temperature, while the carrier concentration N increases with the increase in temperature.

References

[1] VEAREY-ROBERTS A.R., EVANS D.A., Appl. Phys. Lett., 86 (2005), 072105.
[2] SO F.F., FORREST S.R., J. Appl. Phys., 63 (1988), 442.
[3] ABDEL-MALIK T.G., ABDEL-LATIF R.M., Thin Solid Films, 305 (1997), 336.
[4] GOULD R.D., SHAFAI T.S., Superfic., 9 (1999), 226.
[5] SAMUEL M., MENON C. S., UNNIKRISHNAN N. V., Mater. Sci.-Poland, 25 (2007), 177.
[6] PEUMANS P., BULOVIC V., FORREST S.R., Appl. Phys. Lett., 76 (2000), 2650.
[7] ZHOU X., PFEIFFER M., BLOCHWITZ J., WERNER A., NOLLAU A., FRITZ T., LEO K., Appl. Phys. Lett., 78 (2001), 410.
[8] NEWTON M.I., STARKE T.K.H., WILLIS M.R., MCHALE G., Sensors Act. B, 67 (2000), 307.
[9] KWONG C.Y., DJURISIC A.B., CHUI P.C., LAM L.S.M., CHAN W.K., Appl. Phys. A, 77 (2003), 555.
[10] PEISERT H., SCHWEIGER T., KNUPFER M., GOLDEN M.S., FINK J., J. Appl. Phys., 88 (2000), 1535.
[11] RIAD A.S., Thin Solid Films, 370 (2000), 253.
[12] TAKADA J., AWAJI H., KOSHIOKA M., NEVIN W.A., J. Appl. Phys., 75 (1994), 4055.
[13] LEE H.Y., KANG Y.S., JANG M.S., TANAKA H., KAWAI T., J. Korean Phys. Soc., 37 (2000), 475.
[14] MORGAN D.V., ALIYU Y., BUNCE R.W., Phys. Stat. Sol. (a), 133 (1992), 77.
[15] SHARMA G.D., SANGODKAR S.G., ROY M.S., Mat. Sci. Eng. B, 41 (1996), 222.
[16] FORREST S.R., KAPLAN M.L., SCHMIDT P.H., J. Appl. Phys., 60 (1986), 2406.
[17] SHARMA G.D., GUPTA S.K., ROY M.S., Thin Solids Films, 333 (1998), 176.

[18] EL-NAHASS M.M., ABD-EL-RMAN K.F., AL-GHAMDI A.A., ASIRI A.M., Physica B, 344 (2004), 398.
[19] GOULD R.D., J. Phys. D, 9 (1986), 1785.
[20] BAYHAN H., OZDEN S., Turk. J. Phys., 29 (2005), 371.
[21] CZERWINSKI A., SIMOEN E., POYAI A., CLAEYS C., J. Appl. Phys., 94, (2003), 1218.
[22] RIAD A.S., DARWISH S., AFIFY H.H., Thin Solid Films, 391 (2001), 109.
[23] DARWISH S., EL ZAWAWI I.K., RIAD A.S., Thin Solid Films, 485 (2005), 182.

Received 23 June 2008
Revised 3 November 2008

Materials Science-Poland, Vol. 27, No. 2, 2009

Characterisation and preparation of sonochemically synthesised silver–silica nanocomposites

S. ASKARI, R. HALLADJ[*], B. NASERNEJAD

Chemical Engineering Department, Amirkabir University of Technology,
P.O. Box 15875-4413, Hafez Ave., Tehran, Iran

Properties of nanoparticles differ from those of bulk phase or individual molecules. The metal form of these particles shows chemical and physical properties that can be used in fields such as optics, optoelectronics and catalysis. Silver nanoparticles can be used as an antimicrobial agent in wound dressings and as surface coatings, e.g., catheters. In this work, silver nanoparticles were deposited on silica submicrospheres using ultrasounds. A mixture of silver nitrate solution with silica submicrospheres was sonificated under an atmosphere of argon gas in order to eliminate oxygen and decrease both the cavitational threshold as well as the intensity of the ultrasounds. Duration of irradiation was varied between 90 and 180 min at a the frequency of 24 kHz.The resulting silver–silica nanocomposites were characterized with Fourier transform infrared (FTIR), high resolution transmission electron microscopy (HR-TEM), scanning electron microscopy (SEM), energy dispersive X-ray analysis (EDAX) and X-ray florescence (XRF). The results of SEM micrographs show submicrospheres of silver-silica nanocomposites, with the 16–64 nm size distribution. Furthermore, HR-TEM micrographs show that the particle size distribution does not depend on time of irradiation. The particle size distribution of silver nanocomposite in all samples was approximately 4–30 nm. EDAX and FTIR measurements show that, with increasing $AgNO_3$ concentration, the percentage of deposited silver on silica increases. XRF patterns show that the amount of silver deposited on silica can be increased by increasing the ultrasound power.

Key words: *energy dispersive X-ray analysis; high resolution transmission electron microscopy (HR-TEM); scanning electron microscopy; silver nanocomposite; sonochemical treatment*

1. Introduction

Nanoparticles of noble metals have been extensively studied due to their potential applications in microelectronics, and their optical, electronic and catalytic properties [1, 2]. There is particular interest in nanoparticulate Ag, due to its ability to act as both an electron sink as well as a redox catalyst. Antimicrobial properties of silver were

---

[*] Corresponding author, e-mail: halladj@aut.ac.ir

well known to the ancient Egyptians and Greeks, for example Hippocrates mentions silver as a treatment for ulcers [3]. Silver nanoparticles can be used as an antimicrobial agent in applications such as wound dressings and as surface coatings e.g., catheters [4, 5]. Silver has been shown to inhibit energy production by inhibiting the respiratory chain of *E. coli* [6].

In order to obtain high performance materials, it is of paramount importance that particle size and structure be controlled [7, 8]. One significant approach is to synthesize them in the presence of a porous solid such as alumina, silica, or zeolite. Mesoporous solids, due to their small pore size, high opening pore volume, and large internal surface area, have found great utility. Different techniques for improving the formation of metal particle loaded mesoporous composites have been developed [9, 10] but recently there has been a rapid increase in the application of unconventional methods. Different than other traditional chemical methods, sonochemistry is based on acoustic cavitation, that is, the formation, growth and collapse of bubbles in a liquid [11]. Being a sound wave, ultrasounds are transmitted through any substance, be it solid, liquid or gas, which possesses elastic properties. For liquid and gases, particle oscillation takes place in the direction of the wave, and produces longitudinal waves. This causes the layer of liquid or gas closest to the ultrasound source to be displaced, which then causes other neighbouring layers to be displaced in an iterative manner, thus the layers become compressed. This is the compression cycle of the process. When some layers are compressed, others are expanded. This is called the rarefaction cycle of the process. Besides the variation in the positions of molecules, when an ultrasound wave travels through a liquid or gas, there is a variation in pressure. At the point where the layers are crowded together (i.e., where the molecules are compressed), the pressure is higher than normal at the given instant, whereas in the region where the layers are furthest apart (i.e. the rarefaction region), the pressure is lower than normal. This pressure is called the applied acoustic pressure. The total pressure, P in the liquid is given by: [12]

$$P = P_h + P_a \tag{1}$$

In this equation, P_h, is the ambient pressure (usually hydrostatic) in the liquid. If a sufficiently large negative pressure P_c is applied to the liquid (here it will be the acoustic pressure on rarefaction, $P_c = P_h - P_a$) such that the average distance between the molecules exceeds the critical molecular distance, the liquid breaks down and cavities will be created (bubble formation). These cavities may grow in size until the maximum of the negative pressure has been reached (bubble growth). The total collapse of the bubbles, due to enormous energies involved, produces a shock wave.

The adiabatic process associated with an implosive collapse generates localized hot spots with transient temperatures of about 5000 K and pressures of 181.8 MPa [13]. The chemical effects of ultrasounds are attributed to the cavitation producing strong reactants from aqueous solutions, thereby reducing metal salts *in situ*.

The use of ultrasound in liquid–solid systems for the preparation of nanostructure of metals, especially in the presence of porous solid, however, is rarely reported in the literature [14]. In this paper, we report on the ultrasound-assisted preparation of Ag/SiO_2 nanocomposites, their microstructure characterizations, and we also study the effects of such parameters as ultrasound power, concentration of $AgNO_3$ and irradiation time on the particle size of nanocomposites, and the amount of silver deposited on silica by this method.

2. Experimental

Pieces of the mesoporous silica (1 g) were immersed into aqueous solutions containing metal ionic precursor (say, 0.2, 0.3, 0.4 and 0.5 g $AgNO_3$). The liquid–solid mixture (about 100 cm^3in total) charged in the conical flask, was placed in the water pool and irradiated with ultrasounds at the frequency of 24 kHz. Ultrasonic irradiation was accomplished by using an ultrasonic processor UP200H with 186 to 480 W/cm^2 output power. During irradiation, the flask was purged with Argon gas to eliminate oxygen and to decrease both the cavitational threshold and the intensity of the ultrasound power. A water flow was used to cool the glass vessel in the bath. Then the mesoporous silica containing $AgNO_3$ was irradiated with ultrasounds for 90 to 180 min. Each solid sample was washed with distilled water and dried at 100 °C for 30–40 min.

The structures of the as-prepared composites were characterized mainly by the Fourier transform infrared (FTIR), high resolution transmission electron microscopy (HR-TEM), scanning electron microscopy (SEM), energy dispersive X-ray analysis (EDAX) and X-ray florescence (XRF).

3. Results and discussion

The presence of silver, silicon and oxygen in the coated materials was examined with EDAX. The EDAX spectrum was also used to obtain a quantitative estimate of the silver content and the Ag/Si ratio. Figure 1 shows this silver silica nanocomposite EDAX spectrum.The silver content in the sample was about 4.48 wt. %.

The SEM spectra of the sample are shown in Fig. 2. Due to the limit of the resolution, only large silver nanocomposites can be seen. The particle size distribution of silver nanocomposites is 16–64 nm, which is shown in Fig. 3. More than 16% of the particles have the diameter of approximately 44–46 nm.

The effect of increasing the irradiation time, for 90, 120, 150 and 180 min, on the particle size is demonstrated by the HR-TEM spectrum in Fig. 4. HR-TEM is used to study small particles, due to its higher resolution. The size distributions and the shape of the metal nanoparticles were obtained from HR-TEM micrographs. HR-TEM measurements were performed with a Philips model EM208.

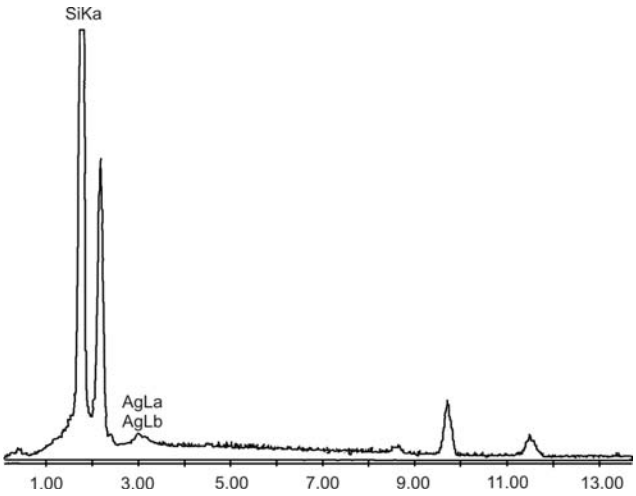

Fig. 1. The EDAX spectrum of silver silica nanocomposite

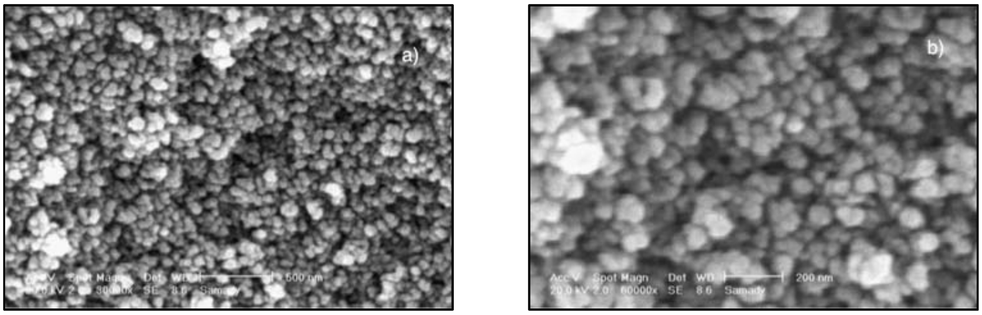

Fig. 2. Scanning electron micrographs of silver silica nanocomposite
with magnification: a) 30000×, b) 60000×

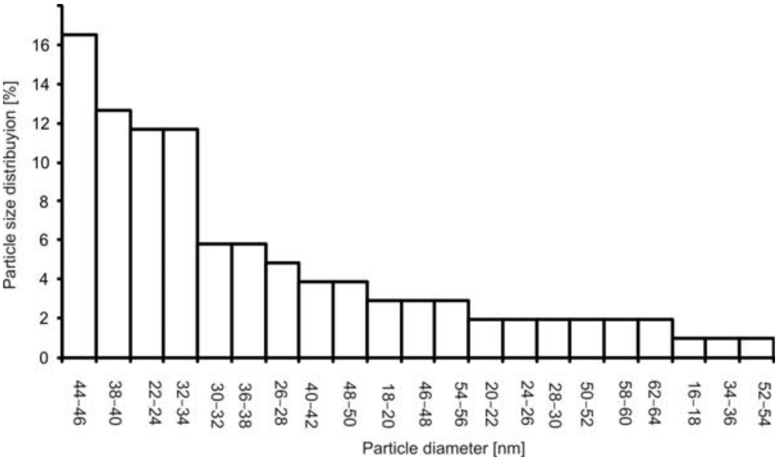

Fig. 3. Particle size distribution of silver nanocomposite

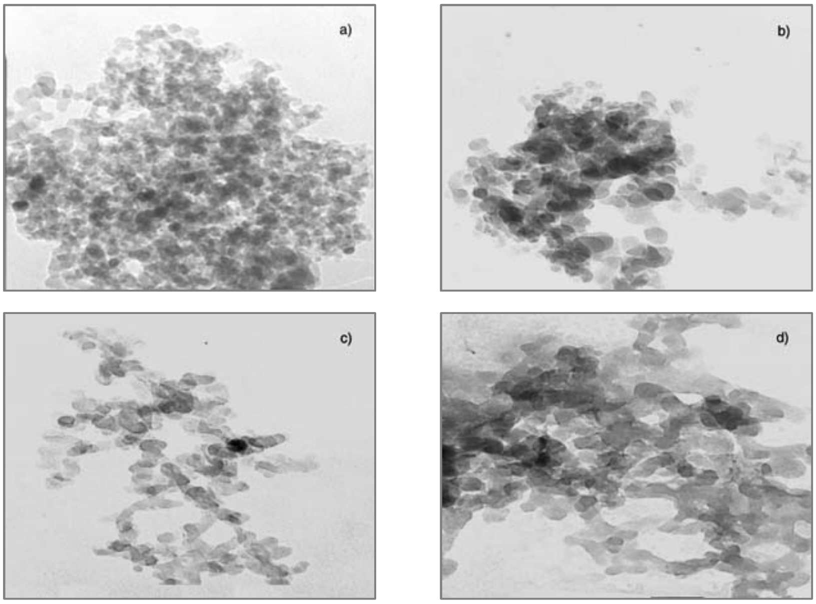

Fig. 4. HR-TEM micrographs of silver silica nanocomposites with irradiation time:
a) 90 min, b)120 min, c)150 min, d)180 min

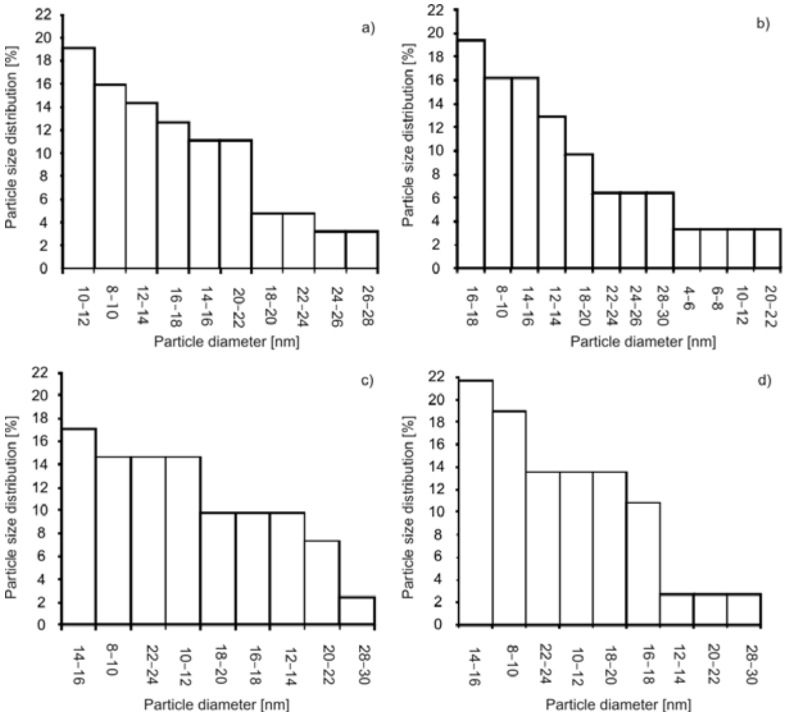

Fig. 5. Particle size distributions of samples with various irradiation times:
a) 90 min, b) 120 min, c) 150 min, d)180 min

The particle size distributions of the obtained samples of silver nanocomposites are shown in Fig. 5. The particle size distribution in all samples is about 4–30 nm. Thus there is no significant difference between the particle size distributions of samples having different irradiation times, but increasing the irradiation time does prevent agglomeration of particles.

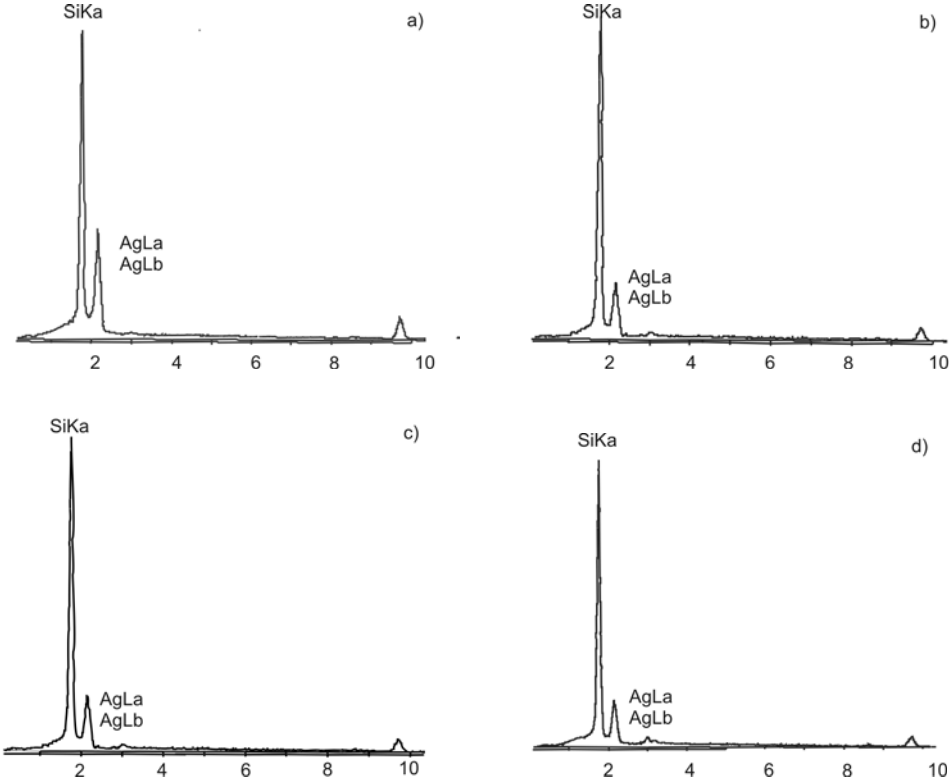

Fig. 6. The EDAX spectra of silver silica nanocomposites with various $AgNO_3$ concentrations: a) 0.2 g/100 cm^3, b)0.3 g/100cm^3, c) 0.4 g/100cm^3, d) 0.5 g/100cm^3

Effects of $AgNO_3$ concentration (0.2- 0.3- 0.4- 0.5 g/100 cm^3) on the deposition of Ag particles on silica are demonstrated by EDAX spectra in Fig. 6. Also, Figure 7 shows that the percentage of deposited silver on silica increases as the $AgNO_3$ concentration increases.

FTIR spectra, shown in Fig. 8, confirm the presence of silver on silica spheres. FTIR absorption is used in order to assess the extent of interaction between the metal and the surface. This interaction drastically changes the nature of the coated material. The comparison between silica spectra with different silver nanocomposite spectrum confirms this result. One of the main changes between these spectra is a decrease in the intensity of the peaks in the broad, 1000–1100 cm^{-1} range, for the surface -deposited samples. This range corresponds to the asymmetric stretching (AS) vibration mode of the Si–O–Si bridge of the siloxane link [15]. Also, a relatively strong peak at 810 cm^{-1}, corresponding to the symmetric stretching of the Si–O–Si group, is decreased in intensity. This result might be explained as follows. During a sonochemical reaction, the energy produced during bubble collapse is sufficient to rupture the strained surface Si–O–Si bonds. This activates the surface of the silica spheres, producing better adhesion of the formed silver nanoparticles.

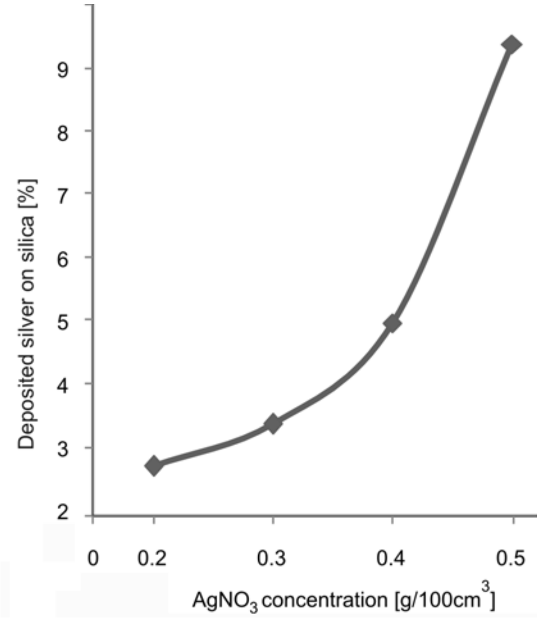

Fig. 7. Effect of $AgNO_3$ concentration on the percentage of deposited silver on silica

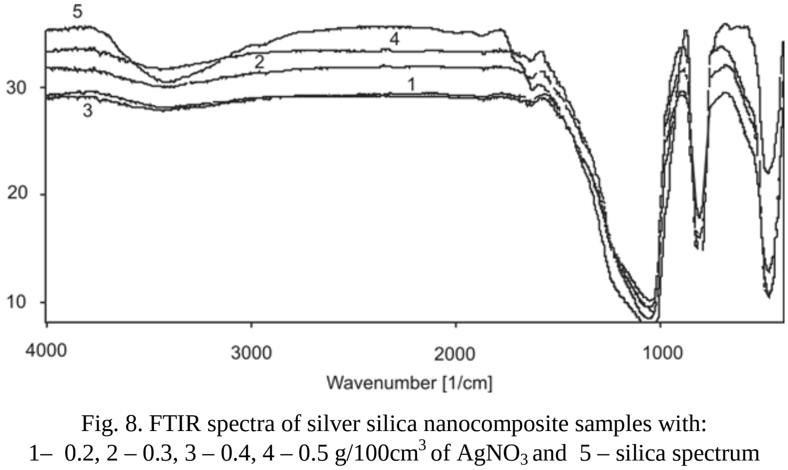

Fig. 8. FTIR spectra of silver silica nanocomposite samples with: 1– 0.2, 2 – 0.3, 3 – 0.4, 4 – 0.5 g/100cm^3 of $AgNO_3$ and 5 – silica spectrum

Table 1. The effect of ultrasound power

Ultrasound power [W/cm^2]	Silica content [wt. %]
480	96.64
368	97.6
276	98.15
186	98.56

Finally, the effect of ultrasound power was investigated by the XRF analysis. The result is shown in Table 1. As the ultrasound power is increased from 186 to 480 W/cm^2, the percentage of silica is decreased and therefore the percentage of deposited silver on silica is increased.

4. Conclusions

Nanosized silver-silica nanocomposite with a 16–64 nm size distribution is obtained by ultrasound power using a basic aqueous solution containing Ag^+ ions. The importance of bubbling Argon gas prior to and during the sonication lies in the elimination of oxygen gas and in the decrease both of the the cavitational threshold as well as the intensity of the ultrasound power. Scanning electron microscopy (SEM) and energy dispersive X-ray analysis (EDAX) were used to characterize the resulting silver–silica nanocomposite. The weight percentage of silver deposited on submicrospheres silica ranges from 2.96 to 9.37. The effect of increasing irradiation time on the particle size was investigated by HR-TEM. The particle size distribution of silver nanocomposite in all samples is about 4–30 nm. Thus, there is no significant difference between the particle size distributions of samples having different irradiation times, but increasing the irradiation time does prevent agglomeration of particles. The effect of $AgNO_3$ concentration on the deposition of Ag particles on silica is shown by the EDAX spectra and Fourier transform infrared (FTIR) analysis. The percentage of deposited silver on silica increases as the $AgNO_3$ concentration increases. Finally, we can say that the advantages of this process are its simplicity, effectiveness and short preparation time, as compared with other methods which take a minimum of 14.15 to 24 h.

References

[1] HAPERIN W.P., Rev. Mod. Phys., 58(1986), 533.
[2] SURYANARAYANA C., Int. Mater. Rev., 40 (1995), 41.
[3] HIPPOCRATES, *On Ulcers*, 400 B.C.E.; Translated by Francis Adams.
[4] RUSSUL A.D., HUGO W.B., Prog. Med. Chem., 31(1994), 351.
[5] SILVER S., FEMS Microbiol. Rev., 27 (2003), 341.
[6] BRAGG P.D., RAINNIE D.J., Can. J. Microbiol., 20 (1973), 883.
[7] FUJIMOTO T., TERAUCHI S., UMEHARA H., KOJIMA I., HENDERSON W., Chem. Mater., 13 (2001), 1057.

[8] NIEDERER J., ARNOLD A., HOLDERICH W., SPLIETHOF B., TESCHE B., REETZ M., BOENNEMAN H., Topics in Catal., 18 (2002), 3.

[9] MORRIS C., ANDERSON M., STROUD R., MERZBACHER C., ROLISON D., Science, 284 (1999), 622.

[10] WIRNSBERGER G., STUCKY G., ChemPhysChem., 1 (2000), 89.

[11] SUSLICK K., PRICE G., Annu. Rev. Mater. Sci., 29 (1999), 295.

[12] MASON T.J., LORIMER J.P., *Applied Sonochemistry: Uses of Power Ultrasound in Chemistry and Processing*, Wiley, Weinheim, Germany2002.

[13] SUSLICK K., Science, 247 (1990), 1439.

[14] OKITSU K., YUE A., TANABE S., MATSUMOTO H., Bull. Chem. Soc. Jpn., 75(2002), 449.

[15] POUCHERT C.J., *The Aldrich Library of Infrared Spectra*, 1981.

[16] CHEN S.W., HUANG K., STEARNS J.A., Chem. Mater., 12 (2000), 540.

[17] CHEN W., ZHANG J., CAI W., Scripta Mater., 48 (2003), 1061.

[18] HUDSON M., SEQUEIRA C., *Multifunctional Mesoporous Inorganic Solids*, Kluwer, Dordrecht, 1993.

[19] BRONSTEIN L.M., POLARZ S., SMARSLY B., ANTONIETTI M., Adv. Mater., 13(2001), 1333.

[20] HYEON T., FANG M., SUSLICK K.S., J. Am. Chem. Soc., 118 (1996), 5942.

[21] TANEV P.T., CHIBWE M., Nature., 368 (1994), 321.

[22] CAO X., KOLTYPIN Y., KATABI G., FELNER I., GEDANKEN A., J. Mater. Res., 12 (1997), 405.

[23] CREIGHTON J.A., EADON D.G., J. Chem. Soc. Faraday. Trans., 37 (1991), 3537.

[24] RAMESH S., KOLTYPIN Y., GEDANKEN A., J. Mater. Res., 12 (1997), 3271.

Received 26 July 2008
Revised 10 November 2008

Materials Science-Poland, Vol. 27, No. 2, 2009

Preparation and characterization of yttria stabilized zirconia minispheres by the sol-gel drop generation method

J. JUDES*, V. KAMARAJ

Department of Ceramic Technology, Anna University, Chennai – 600025, India

Near-net-shaped zirconia minispheres were prepared by a novel processing technique based on the sol-gel method. Yttrium was used as a stabilizing agent. Formation of minispheres was achieved in a setting solution by drop generation. The impact of the stabilizing agent on sintering conditions was analysed in detail. The spheres were crystallized into tetragonal phase at 472 °C, and the tetragonal phase was retained up to 900 °C. Maximum theoretical density (97%) was achieved for spheres sintered at 900 °C. Sintering temperatures higher than 900 °C led to the formation of monoclinic phase and reduction in density. The grain size and crystallite size were identified as 0.8 μm and 24 nm, respectively. The phase identification, density variation, chemical decomposition, functional group specification and microstructural features of the dried and sintered final product were also studied

Key words*: sol-gel method; zirconia minispheres; sintering; X-ray diffraction; thermal analysis*

1. Introduction

Ball milling is the most common and effective method for commutation into a range of finer particle sizes. The comminution occurs by compression, impact and shear (friction) between the moving grinding media and the particles. The rate of grinding increases inversely with the radius of the ball. However, grinding media should have high density in addition to uniformity in shape and size, in order to perform the effective particle fracture. The conventional powder compaction method has its limitations in the production of fine milling media, such as the variety of sizes, density and non-uniformity in shape, since slight change in processing parameter leads to structural changes. In order to overcome these limitations, in the present study, a novel processing technique based on the sol-gel method was adapted to produce near-net-shaped prototype zirconia minispheres.

---

*Corresponding author, e-mail: taj_judes@yahoo.com

Among various monolithic ceramics, yttria stabilized tetragonal zirconia polycrystalline ceramics (Y-TZP) have been regarded as a potential structural material. Its unique combination of high strength, fracture toughness and chemical inertness makes it indispensable for a use as milling media [1]. Small grain structure is required to produce a high strength zirconia minispheres that can be obtained by the addition of yttria with 5 mol %, which also sets the crystal structure in tetragonal phase [2]. The stabilization of tetragonal zirconia has been attributed to structural similarity of the larger yttrium ion radius, compared with the zirconium ion radius, and based on the formation of oxygen vacancies resulting from the presence of these trivalent cations [3]. Crystalline structures and catalytic properties of zirconia are generally dependent on the synthesis and thermal treatment. Thus, the sol-gel method was chosen to control the process at the molecular level: it produces nanocrystalline zirconia and also avoids impurities. Various methods had been attempted for preparing spheres, such as drop generation, spray pyrolysis, emulsion evaporation, emulsion water extraction, emulsion ion extraction. Among the above methods, drop generation is found to be very economical and effective. The paper describes the preparation of yttria stabilized zirconia minispheres by the sol-gel drop generation route. The characterization studies reveal the structural and physical properties of yttria stabilized zirconia minispheres.

2. Experimental

Various potential sol precursors were investigated and characterised for the preparation of zirconia minispheres, the optimum being an aqueous sol made from hydrolysed zirconium oxalate ($ZrO(COO)_2$) [4]. The starting material used for the preparation of zirconium oxalate sol was zirconium oxy-chloride octahydrate ($ZrOCl_2{\cdot}8H_2O$). 1 M concentration of zirconium-oxy chloride and oxalic acid ($(COOH)_2.2H_2O$) taken in 1: 0.7 vol. ratio to obtain a transparent sol. The stabilizing (sintering) agent yttrium nitrate hexahydrate ($Y(NO_3)_3{\cdot}6H_2O$) of 5 mol % was added. The concentration was chosen based on the formation of spheres in the setting solution and the retention of shape after sintering. The formation of zirconium oxalate can be expressed as

$$ZrOCl_2{\cdot}8H_2O + (COOH)_2{\cdot}2H_2O \rightarrow ZrO(COO)_2 + 2HCl + 10H_2O \quad (1)$$

The sol thus obtained was kept at room temperature for a very short time to achieve gelation. The viscosity of the gel increases with time. The required viscosity and fluidity were obtained by adding polyvinyl alcohol (PVA) of 35 wt. %. At the suitable viscosity, the mixed sol was added drop by drop to the sphere container (a 500 ml beaker filled with 400 ml of ammonia solution) for the formation of uniform minispheres. The spheres were dried at 40 °C and then sintered in stages from 300 °C to 1500 °C in steps of 200 °C for 5 h at the heating rate of 10 °C/min. Vasylkiv [5] observed that the crystallization stage was shifted to higher temperatures as the heating rate was increased, and a slow heating rate delivers a much better final density of zirconia spheres [5]. In contrast with earlier studies Wang [4] found that the weight loss was almost the same for all heating rates. Zirconium oxalate ($ZrO(COO)_2$) was decomposed to zirconia when the sintering temperature was increased

$$ZrO(COO)_2 \longrightarrow ZrO_2 + CO + CO_2 \qquad (2)$$

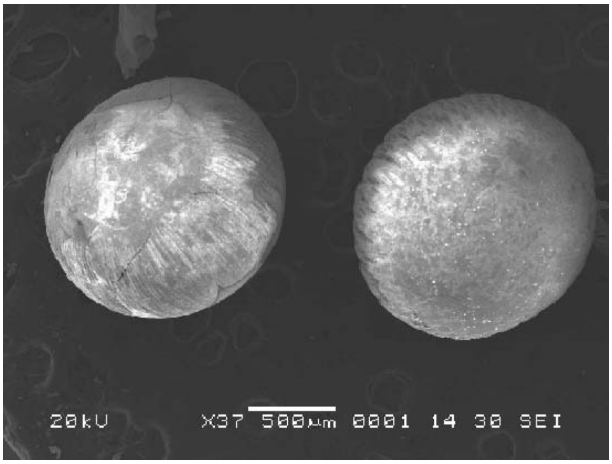

Fig. 1. SEM micrograph of zirconia minispheres sintered at: 1500 °C (left) and 900 °C (right)

Figure 1 shows the SEM micrograph of zirconia spheres sintered at 1500 °C and 900 °C. Microcracks are evident on the surface of spheres sintered at 1500 °C. pH during the sol-gel processing of ZrO_2 had no influence on the thermal stability of t-ZrO_2 product [6].

3. Results and discussion

3.1. Thermal analysis

Thermogravimetric analysis (TGA, Perkin Elmer) and differential thermal analysis (DTA, Netzsch STA409PC) studies (Fig. 2) were carried out to analyse the weight loss and phase transitions of dried spheres (heating rate was 10 $°C\cdot min^{-1}$ in air). TGA shows three major stages of weight losses. The first stage weight loss of around 11.54% up to 150 °C corresponds to the loss due to residual ammonia and dehydration of the samples. The second stage of weight loss of around 6.88% is observed between 150 °C and 230 °C, and corresponds to the release of nitrates. The third weight loss of 12.77% is due to: (i) the decomposition of oxalate with the simultaneous binder removal process; and (ii) the elimination of CO and CO_2 molecules in the 260–428 °C temperature range. The liberation of chlorine may take place at around 512 °C.

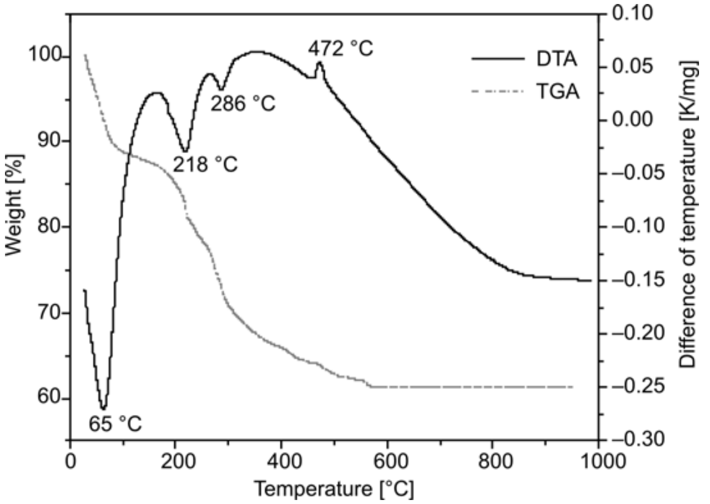

Fig. 2. TGA/DTA curves for the zirconia minispheres dried at 40 °C

A residue weight of 59.13% was found for the spheres sintered at 1500 °C. The porosity details were estimated from the shrinkage data, assuming that there was no further shrinkage above 1500 °C. However, it is quite possible that some porosity remained at this temperature and that these porosity values were underestimated [7, 8]. Variations in percentage weight loss, shrinkage and porosity with the gradual increase in temperature have been studied in detail (Table 1).

Table 1. Weight losses, linear shrinkage, estimated porosities, densities and average crystallite sizes of minispheres with the sintering temperature

Temperature [°C]	Shrinkage [%]	Weight loss [%]	Porosity [%]	Density of sintered spheres [g/cm^{-3}]	Percentage of theoretical density [%]	Average crystallite size [nm]
300	29.79	29.87	67.62	n/a	n/a	n/a
500	38.69	34.32	51.35	5.01	82.13	09.87
700	44.73	37.34	33.63	5.72	93.77	17.32
900	47.99	38.97	20.36	5.89	96.56	24.17
1100	49.01	39.48	15.48	5.85	95.90	30.19
1300	51.33	40.64	2.81	5.82	95.41	49.62
1500	51.79	40.87	~0.0	5.81	95.25	54.32

The DTA showed one exothermic and three distinct endothermic peaks. The endothermic peak around 64 °C is due to the dehydration of the sample and loss of residual ammonia: as observed in the TGA curve. The second endothermic peak around 216 °C is due to the decomposition of nitrate. The endothermic peak around 288 °C is attributed to the decomposition of oxalate. The liberation of chlorides was not observed in the DTA curve, which may be due to smooth release of the same. The exothermic peak around 472 °C is due to the crystallization of zirconia in tetragonal phase, which is connected with the phase change from amorphous zirconia to a metastable tetragonal phase [9, 10]. It is believed that the dopants are uniformly distributed on the pore surface of the zirconyl oxalate gel structure. During sintering, the dopant ions are substituted for zirconium ions in the crystal structure, which favours the formation of tetragonal phase (t phase) and subsequently facilitates transformation toughening. Gradual elevation in the DTA curve beyond 900 °C indicates a possible tetragonal to monoclinic phase transformation.

3.2. X-ray powder diffraction analysis

X-ray diffraction studies (XRD, Philips PW-1730 X-ray unit, CuK$_\alpha$ radiation) were carried out in order to determine the crystal structure and phase identification of spheres sintered in the range 300–1500 °C (Fig. 3).

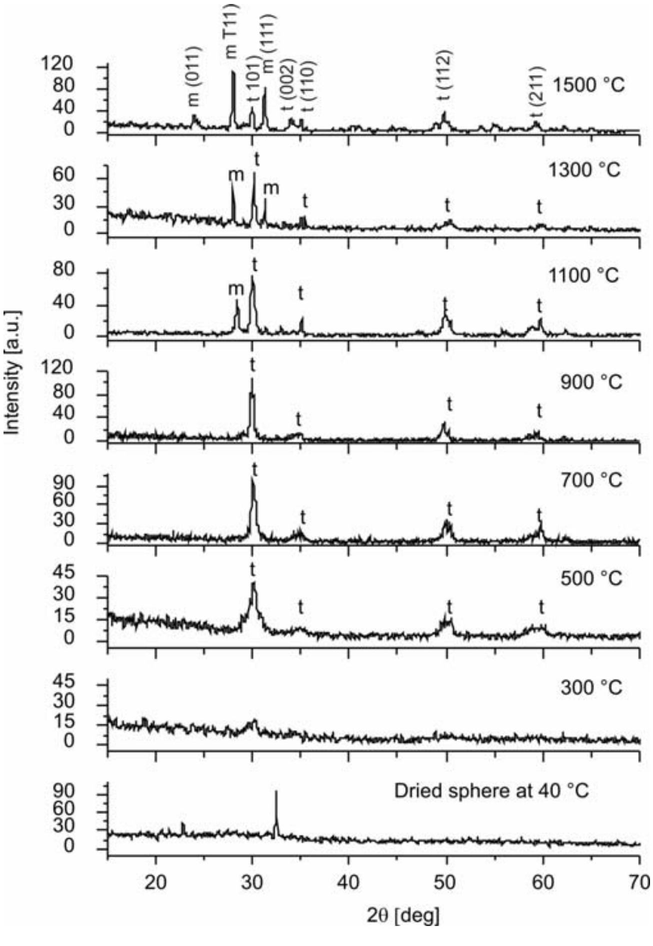

Fig. 3. XRD patterns of zirconia minispheres after heat treatment at various temperatures (t – tetragonal, m – monoclinic)

It was observed that the spheres sintered at 300 °C were amorphous in nature. The metastable zirconia spheres crystallized into tetragonal phase at 470 °C and retained the tetragonal phase up to 900 °C. The intensities of the tetragonal diffraction peaks were found to vary with the sintering temperature. Transformation toughening depends directly on the t phase content and therefore materials containing 100% of the tetragonal phase can be extremely tough. The role of stabilization of the t phase of zirconia by yttrium ions shows that the presence of these ions reduce the overcrowding of the oxygen around the zirconium ions, and hence relieve the strain energy associated with it. On further rise in temperature, tetragonal to monoclinic phase transformation occurs at 1100 °C. The fraction of monoclinic phase (m-ZrO_2) in zirconia is only 0.29 at 1300 °C. Srinivasan et al. observed that the tetragonal phase forms first from the amorphous phase and that the tetragonal crystals grow subsequently [11–13]. The sphere sintered at 1500 °C is dominated by the monoclinic phase with 0.41 fractions. The decrease in the t-phase content on increase of sintering temperature may indicate the sluggishness of the diffusion of yttria into zirconia.

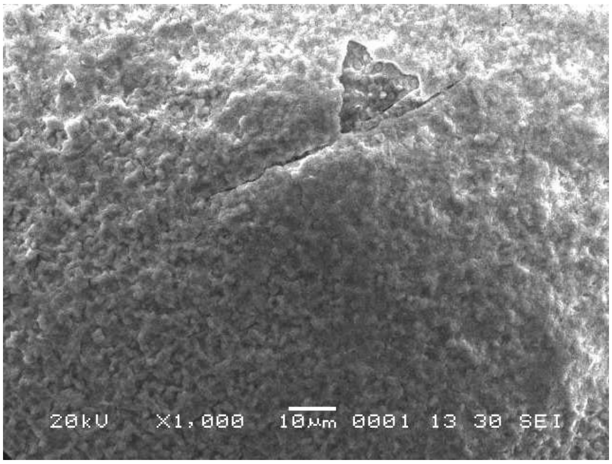

Fig. 4. SEM micrograph of zirconia minispheres sintered at 1500 °C with a microcrack

From the earlier investigations [14, 15], it is evident that partially stabilized zirconia with a mixture of m and t phases was observed for the compositions with up to 11 mol % of yttria, even for firing temperatures of up to 1500 °C. The t-phase in yttria stabilized spheres is metastable and might be due to compressive stress developed during sintering. When the tetragonal material reverts back to the monoclinic phase, the transformation results in microcracking which weakens the strength of spheres [16]. The microcrack is evident from the SEM micrograph (Fig. 4) of yttria stabilized zirconia spheres sintered at 1500 °C. The grain size is found to be around 1.4 µm from the microstructural evidence. It has been observed that the average grain size increases from 0.8 to 1.4 µm with an increase in the sintering temperature from 900 °C to

1500 °C. This influences the internal tensile stress produced, due to the thermal expansion of zirconia. When the grain size is above the critical level, the internal stress is equal to the stress required for transformation. Thus, zirconia grain growth and the internal tensile stress are responsible for tetragonal to monoclinic transformation at temperatures above 900 °C. The average crystallite size of 5 mol % yttria stabilized zirconia minispheres is determined by the diffraction line, using the Scherer and Warren equation [17]. The crystallite size increases from 10 to 54 nm when the sintering temperature is increased from 500 °C to 1500 °C (Table 1). The increased crystallite size of zirconia spheres is evident in the XRD spectrum by the decrease in width of the dominant tetragonal spectral lines. It was found that the reduction of the crystallite size to the nanometre regime can result in the stabilization of high-temperature phases.

3.3. FTIR characterization

The vibrational frequencies of all possible functional groups for the minispheres dried at 40 °C in the region 4000–400 cm^{-1} were studied by considering the FTIR spectrum (Fig. 5).

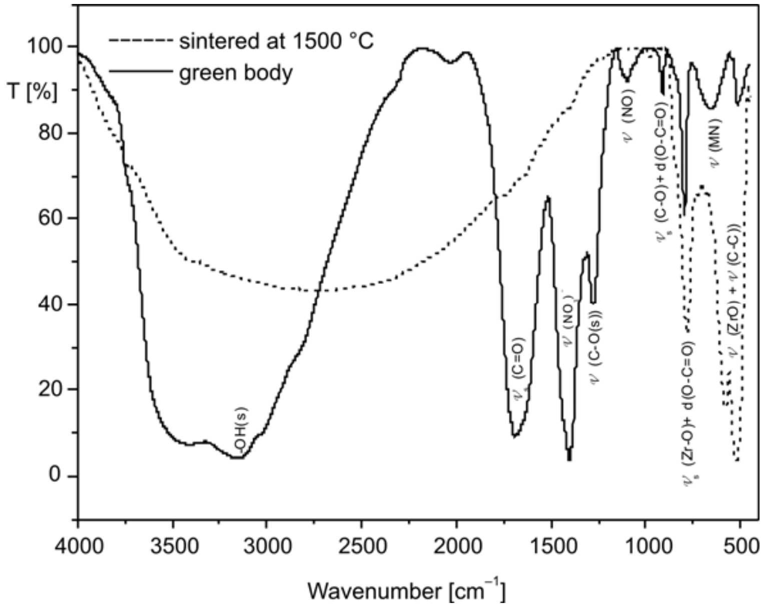

Fig. 5. FTIR spectrum of zirconia minispheres dried (40 °C) and sintered (1500 °C)

The peaks at 795 cm^{-1} and 517 cm^{-1} are prominent, which confirms the presence of Zr–O vibration. The appearance of the peak at 1402 cm^{-1} illustrates the presence of nitrates in the dried oxalate spheres. The peak at 3152 cm^{-1} shows the presence of OH stretching mode. The peaks at 910 cm^{-1}, 1096 cm^{-1}, 1279 cm^{-1} and 1689 cm^{-1} are related to the volatile compounds (O–C=O, NO, C–O and C=O groups). It has been reported that the oxalate ion has a quadridentate structure with the zirconium ion [18]. It is clear that the addition of yttrium ions does not affect the structure of the zirconyl oxalate. The results obtained in the present study are in good agreement with the results of previous reports [19, 20].

3.4. Density measurements

The density of spheres was determined by using a specific gravity bottle. The density variations with the sintering temperature are listed in Table 1. The theoretical density (TD) is calculated according to the theory of Ingel and Lewis [21]. The density of spheres increases with the sintering temperature. It reaches a maximum value of 5.89 gm/cm^3 (*TD* = 96.56%) for spheres sintered at 900 °C. On further increase in sintering temperature, the density of the spheres is found to be reduced, which may be due to the volume expansion that takes place during the phase transformation, from tetragonal to monoclinic phase, as well as the formation of microcracks.

4. Conclusion

Sol-gel derived yttria stabilized zirconia minispheres were successfully fabricated by the drop generation method. Formation of zirconium oxalate sol has been shown to be a good starting route for the preparation of yttria stabilized zirconia minispheres. Amorphous phase exists below 300 °C and the tetragonal phase is formed at 470 °C. The ideal sintering temperature for the production of sol-gel derived yttria doped zirconia minispheres was identified as 900 °C, which has the fully stabilized tetragonal phase with 97% of theoretical density. The minimum composition required for the fully tetragonal microstructure clearly depends on the sintering temperature and the grain size produced. Further increase in the sintering temperature above 900 °C leads to the phase transformation and a reduction in density. The presence and periodic removal of volatile compounds were observed by DTA and thermogravimetric analysis, which was confirmed by FTIR studies. Zirconia minispheres were extensively characterised in order to establish a correlation between physical and structural properties with the sintering temperature.

References

[1] RUIZ L., READEY M.J., J. Am. Ceram. Soc., 79 (1996), 2331.
[2] SETTU T., *Studies on preparation and characterization of tetragonal zirconia polycrystals by sol-gel method*, Ph. D. Thesis, Anna University, Chennai, India, 1995.
[3] PANDOFELLI V.C., RODRIGUES J.A., STEVENS R., J. Mater. Sci., 26 (1991), 5327.
[4] WANG J.A., VALENZUELA M.A., Catalysis Today, 68 (2001), 21.
[5] VASYLKIV O., SAKKA Y., J. Am. Ceram. Soc., 83 (2000), 2196.
[6] WANG H.C., LIN K.L., J. Mater. Sci., 26 (1991), 2501.

[7] PULLAR R.C., TAYLOR M.D., BHATTACHARYA A.K., J. Eur. Ceram. Soc., 21 (2001), 19.

[8] FULRATH R.M., PARK J.A., *Ceramic Microstructures*, Wiley, New York, 1968.

[9] KUNDA P., PAL D., SEN S., J. Mater. Sci., 23 (1988), 1539.

[10] MERCERA P.D.L., VAN OMMEN J.G., DOESBURG E.B.M., BURGGRAAF A.J., ROSS J.R.H., Appl. Catal., 57 (1990), 127.

[11] NAUER M., *Microstructure et superplasticite de Zircones Yittriées* These No. 996, Departement des Materiux, Ecole Polytechnique Fédérale de Lausanne, Switzerland, 1992.

[12] SRINIVASAN R., RICE L., DAVIS B.H., J. Am. Ceram. Soc., 73 (1990), 3528.

[13] SRINIVASAN R., DAVIS B.H., CAVIN O.B., HUBBARD R., J. Am. Ceram. Soc., 75 (1992), 1217.

[14] RAMADASS N., MOHAN S.C., RAVINDRA REDDY S., SRINIVASAN R., SAMDANI G., Mater Sci. Eng., 60 (1983), 65.

[15] SCOTT H.G., J. Mater. Sci., 10 (1975), 1527.

[16] GARVIE R.C., HANNINK R.H., PASCOE R.T., Nature, 258 (1975), 703.

[17] DING J., TSUZUKI T., MCCORMICK P. Nanostruct. Mater., 8 (1997), 75.

[18] ETIENNE J., LARBOT A., GRIZRAD C., COT.L., ALARY.I.A., J.Non-Cryst. Solids., 125 (1990), 224.

[19] KHARITONOV Y.Y., ZAITSEV L.M., BOCHKAREW G.S., EVSTAFEVA O.N., Russ. J. Inorg. Chem., 9 (1964), 876.

[20] GANGADEVI T., SUBBA RAO M., NARAYANAN KUTTY T.R., Ind. J. Chem., A19 (1980), 303.

[21] INGEL R.P., LEWIS III D., J. Am. Ceram. Soc., 69(4) (1986), 325.

Received 31 July 2008
Revised 16 November 2008

Materials Science-Poland, Vol. 27, No. 2, 2009

Hydrosodalite ion exchange in saturated $Ca(OH)_2$ solution

D. VAIČIUKYNIENE[*], K. BALTAKYS, A. KANTAUTAS

Faculty of Chemical Technology, Kaunas University of Technology,
Radvilenų str. 19, 50254 Kaunas, Lithuania

The possibility of substituting Na^+ ions contained in pure hydrosodalite crystal structure with Ca^{2+} ions in saturated $Ca(OH)_2$ solution has been examined in the temperature range from 25 °C to 95 °C. It was found that temperature strongly influences the hydrosodalite ion exchange: upon increasing temperature only by 5 °C (from 25 to 30 °C) Ca^{2+} the time required for Ca^{2+} ions to be incorporated within the hydrosodalite crystal structure is reduced by the factor of 3. With the increase of temperature from 45 °C to 65 °C almost all the Ca^{2+} ions, initially contained in the $Ca(OH)_2$ solution, become incorporated in the hydrosodalite structure after 5 min However, high temperature has an adverse effect on the sorption process (Ca^{2+} ions will not be incorporated within the hydrosodalite structure before 10 min have elapsed). Partly reversible ion exchange reactions of hydrosodalite are characteristic at temperatures higher than 30 °C). The structure of hydrosodalite crystals remains stable when performing ion exchange reactions at 25–95 °C temperature.

Key words: *hydrosodalite; ion exchange*

1. Introduction

Zeolites form a group of minerals of a micro-porous structure containing hydrated aluminosilicates of alkaline metals and alkaline earth ones. Their crystal lattices are composed of $[Si(Al)O_4]^{4-}$ tetrahedrons [1]. An important property of zeolites is the capacity of their chemical composition to vary with regard to crystal radii (form and size), pore size and their configuration. A rather easy chemical modification of zeolites creates broad possibilities to perform controlled changes to the structure and to the properties. These parameters can be altered by synthesis, by ion exchange or by other methods [2–5]. Thus, zeolites display an unusually broad application range in industry and agriculture, where they are used for water softening, ammonia removal

---

[*] Corresponding author, e-mail: danute.palubinskaite@ktu.lt

from waste water, concentration removal of radioactive isotopes from radioactive waste. Besides, zeolites are used for nuclear waste transportation. Radiation has no influence on zeolite stability [6, 7].

Gualtieri and Aprea [8] investigated the possibility of substituting of Na^+ ions with K^+ ions in the structure of hydrosodalite crystals. The chemical formula of hydrosodalite with K^+ ions is $K_6[AlSiO_4]_6·7.8H_2O$. It is obtained from $Na_6[AlSiO_4]_6·8H_2O$, which is a synthetic modification of natural sodalite containing additional water molecules. It should be noted that the symmetry of the hydrosodalite changes after insertion of K^+ ions.

By exploiting ion exchange with nitrate solutions of appropriate metals for 24 h, Kendrick, Dann et al. [9, 10] from $Na_6[AlSiO_4]_6·$ $8H_2O$ obtained hydrosodalites of alkaline and earth-alkaline metals having the formula $M_6[AlSiO_4]6·8H_2O$ (M = Li, Na, K, Mg, Ca, Sr). Alkaline or alkaline–earth metal ion substituted hydrosodalites possess a cubic sodalite lattice with the space group *P*43*n*; its parameters vary from 0.88 to 0.92 nm. Reference [11] presents relevant data regarding the possibility of realizing hydrosodalite ion exchange using different cations, such as Cd^{2+}, Cu^{2+} Zn^{2+}, Ag^{2+}, and Pb^{2+}.

There have been few references in the established literature to the question of ion exchange in zeolites, especially with regard to the substitution of Na^+ ions with Ca^{2+} ions. This has much relevance, because zeolites having calcium ions are quite universally applied in concrete technologies [12, 13].

The aim of the paper was to investigate the possibility of substituting Na^+ ions contained in pure hydrosodalite crystal structure with Ca^{2+} ions in saturated $Ca(OH)_2$ solution.

2. Materials and methods

Pure hydrosodalite was synthesized from reagents: NaOH (Delta Chem., Czech Rep.), $Al(OH)_3$ (POCh S.A., Poland); amorphous $SiO_2·nH_2O$ (Krasny Khimik Sankt Petersburg, Russia; loss on ignition – 23.5 %). The molar ratios of the starting materials $Na_2O:Al_2O_3:SiO_2:H_2O$ – 2:1:2:10 were chosen based on the results of previous experiments [14, 15]. Low-temperature (105 °C) zeolite synthesis was performed in the unstirred suspension: isothermal curing was of 2 h duration. The final product was filtered, dried at ca. 60 °C and sieved through a 80 μm mesh sieve.

Ion exchange reactions were performed in an unstirred suspension: 100 cm^3 of saturated $Ca(OH)_2$ solution obtained from 98% CaO (POCh S.A., Poland) was filled up with 2 g of zeolite. The experiments were repeated three times, from which the average ion concentrations were evaluated. The sediments in the solution were observed to carbonize and to form $CaCO_3$, which remains in the synthesis products in all investigated cases. It is known [16] that the concentration of Ca^{2+} ions decreases when the temperature of the solution increases. Thus, as the temperature increased from 25 °C to 95 °C, the corresponding concentration decreased from 0.81 to 0.50 g/dm^3. Ion exchange experiments at 25, 30, 45, 65 and 95 °C lasted 60 min.

The concentration of sodium and calcium ions in the solution was determined (with 97% accuracy) by the atomic absorption spectroscopy with the aid of a Perkin-Elmer Analyst 4000 spectrometer. Each calculation was made 3 times; the data declined no more than 3.5 % from the mean value. After ion exchange, the hydrosodalite was characterized by instrumental as well as chemical analysis methods.

The X-ray powder diffraction data were collected with a DRON-6 X-ray diffractometer, having the Bragg–Brentano geometry, using Ni-filtered CuK$_\alpha$ radiation and a graphite monochromator, operating at 30 kV and with the emission current of 20 mA. The step-scan covered the angular range 2–70 ° (2θ) in steps of $2\theta = 0.02$ °.

Simultaneous thermal analyses (STA: differential scanning calorimetry – DSC and thermogravimetry – TG) were also employed for measuring the thermal stability and phase transformation of products. The heating rate was 15 °C/min, and the temperature ranged from 30 °C up to 1000 °C under the air atmosphere. The test was carried out on a Netzsch instrument STA 409 PC Luxx: ceramic sample handlers, and crucibles of Pt–Rh were used.

IR spectra were recorded with a Perkin Elmer FT-IR System spectrometer. For the IR analysis, 1 mg of the substance was mixed with 200 mg of KBr and compressed in a forming press under vacuum.

3. Results and discussion

Ion exchange reactions in pure hydrosodalite occur in the same way both, at 25 °C and at 30 °C, since the shapes of the curves describing the Ca^{2+} ion concentration in the solution are similar (Fig. 1). It should be noted that at 25 °C the equilibrium amount (0.49 g/dm^3) of Ca^{2+} ions is incorporated in the hydrosodalite crystal lattice within 30 min of sorption because after this time its change is rather small (0.51 g/dm^3 in 1 h) (Fig. 1, curve 1).

Moreover, at 30 °C, when the Ca^{2+} ion concentration in the initial solution was 0.68 g/dm^3, it decreased to 0.45 g/dm^3 after 5 min of sorption (Fig. 1, curve 2). The concentration of Ca^{2+} ions after 1 h decreased by the factor of 3 and was equal to 0.24 g/dm^3. Clearly, temperature strongly influences the ion exchange processes in hydrosodalite: if the temperature is increased by 5 °C, the time required for inserting the Ca^{2+} ions into the hydrosodalite crystal structure is reduced by the factor of 3 (from 30 min to 10 min).

In order to investigate the influence of temperature on the ion exchange capacity, the tests were performed at higher temperatures. At 45 °C and 65 °C, the Ca^{2+} ions were incorporated into the hydrosodalite crystal structure much faster than at 25 °C or 30 °C. After first 5 min of the ion exchange, the Ca^{2+} ion concentration in the solution was 0.006 g/dm^3 (at 45 °C) and 0.002 g/dm^3 (at 65 °C), i.e., nearly all the Ca^{2+} ions were incorporated into the hydrosodalite structure (Fig. 2, curves 1, 2).

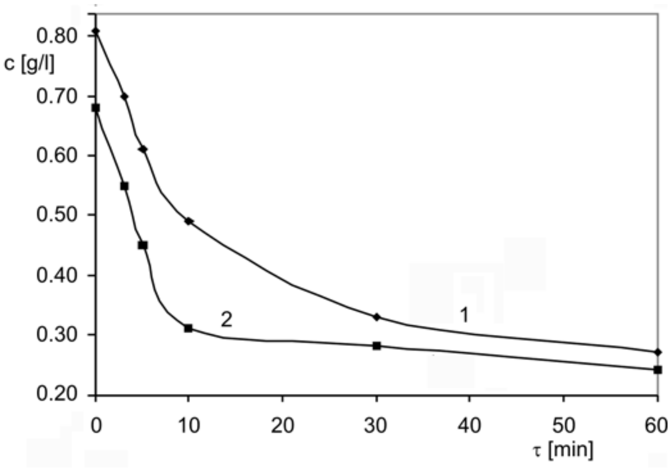

Fig. 1. Time dependence of Ca^{2+} concentration in solution at 25 °C (1) and 30 °C (2)

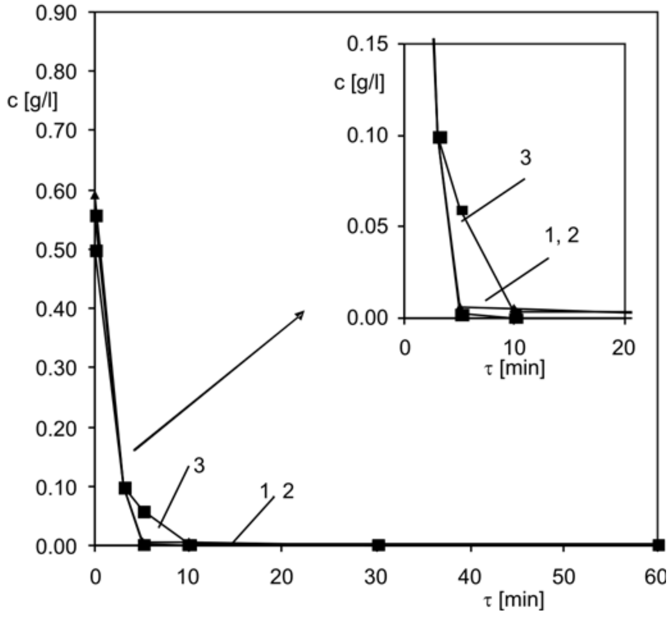

Fig. 2. Time dependence of Ca^{2+} concentration in solution at: 45 °C (1), 65 °C (2), and 95 °C (3)

The results demonstrate also that high temperatures adversely affect the sorption. At 95 °C, the reactions of ion exchange were observed to be slower than those at lower temperatures, because the equilibrium amount of Ca^{2+} ions was incorporated in the hydrosodalite structure only after 10 min (Fig. 2, curve 3). The main reason for this is that the considered temperature (namely 95 °C) is close to the formation temperature of hydrosodalite itself. Thus, the duration time does affect essentially the ion exchange, its largest part occurs during the first 3–5 min of each experiment.

It was determined that during Ca^{2+} ion adsorption, Na^+ ion desorption proceeded simultaneously. However, at 25 °C desorption of Na^+ ions was almost unchanged: after 3 min the concentration increased only up to 0.0125 g/dm^3 and remained constant during the experiment (Fig. 3, curve 1).

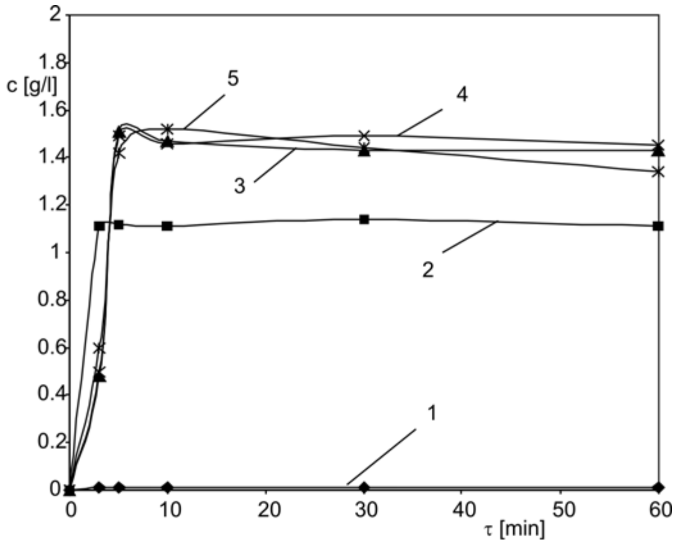

Fig. 3. Time dependence of Na^+ concentration in solution at:
25 °C (plot 1), 30 °C (plot 2), 45 °C (plot 3), 65 °C (plot 4), 95 °C (plot 5)

At higher temperatures, 30 °C, 45 °C, 65 °C and 95 °C, Na^+ ion desorption was more intense. At 30 °C (Fig. 3, curve 2), 1.11 g/dm^3 of sodium ions desorbed from hydrosodalite into the solution after 3 min. Similarly, the concentration of sodium ions in the solution also increased at higher temperatures: after 5 min, the amount of Na^+ ions increased from 1.42 to 1.51 g/dm^3. It can be stated that the equilibrium amounts of Na^+ ions enter from hydrosodalite crystal structure to the solution in 3–5 min.

It was noticed that the quantity of sodium ions desorbed from hydrosodalite structure is higher than that of incorporated Ca^{2+} ions. This was confirmed by chemical analysis which showed that pure hydrosodalite contained: SiO_2 – 34.5%, Al_2O_3 – 31.0%, Na_2O – 16.2%. After ion exchange the Na_2O zeolite composition was: SiO_2 – 34.5%, Al_2O_3 – 31.0%, Na_2O – 8.62%, CaO – 1.97%.

The obtained results were confirmed by structure examinations. The general composition of hydrosodalite is expressed by the formula $Na_{6+x}(SiAlO_4)_6(OH)_x{\cdot}nH_2O$. The ratio $(6 + x):x:n$ denotes the number of sodium ions, hydroxyl anions and water molecules per a unit cell, respectively. One unit cell equals two β cages. The β cages of the hydrosodalite contain Na^+ cations for the compensation of the negative charge and may host OH^- ions and H_2O molecules. Some sodium cations can be compensated by OH^- anions and these sodium cations can be easily removed by washing hydrosodalite in water. The structure of hydrosodalites is dynamical with respect to the guest molecules in β cages. Sodalite β cages connected by six and four rings, in the centre one β cage in detail displaying the Si–O–Al bond angles, the 4 positions of the Na^+ cations, and the oxygen atoms of 4 water molecules embedded in this cage. Because of this, the kinetic curves of Ca^{2+} adsorption and Na^+ desorption are different, e. g. hydrosodalite adsorbs about 0.55 g/dm^3 Ca^{2+} ions and desorbs about 1.5 g/dm^3 Na^+ ions. It is reasonable to presume that in the hydrosodalite structure some of the desorbed Na^+ cations are compensated by host OH^- ions and H_2O molecules.

In order to determine whether a reversible ion exchange reaction is characteristic of hydrosodalite, the samples after sorption were placed in distilled water. It was determined that Ca substituted hydrosodalite is stable in water at temperatures up to 25 °C (Table 1). In the 65 – 95 °C temperature range, Ca^{2+} ions from the zeolite enter to the liquid phase and achieve their highest concentration (0.222 g/dm^3). During the investigation of hydrolysis isothermal dynamics of this zeolite with prolonged duration the amount of Ca^{2+} ions in the solution was noticed to decrease gradually due to $CaCO_3$ formation and sedimentation.

Table 1. The amount of Ca^{2+} ions in solution, g/dm^3

Duration [min]	Temperature [°C]				
	25	30	45	65	95
5	0	0.028	0.125	0.222	0.222
10	0	0	0.037	0.074	0.074
30	0	0	0.019	0.037	0.037
60	0	0	0.005	0.037	0.009

Figure 4 presents the results of X-ray diffraction analyses of hydrosodalite before and after sorption and desorption. The curves show that the diffraction peaks with interplanar distances (*d*) at 0.628, 0.363, 0.281, 0.256, 0.290, 0.174 nm are characteristic of hydrosodalite. The structure of hydrosodalite crystals was observed to be stable because the shape of the X-ray diffraction patterns (Fig. 4, curve 2) did not change when the duration of the experiment was prolonged up to 60 min.

It is important to note that the temperature of the ion exchange process has no effect on hydrosodalite mineral composition (Fig. 5). The peaks of the X-ray diffraction patterns were similar when the temperature varied in the 25 °C to 95 °C range of, i.e., hydrosodalite was predominant.

DSC analysis shows that hydrosodalite is predominant in the products: the endothermic peaks at 130, 143, ~275 °C are characteristic of hydrosodalites (Fig. 6).

$CaCO_3$ decomposes at 755 °C, while the peak at 866 °C corresponds to the transformation of zeolite into anhydrous nepheline $NaAlSiO_4$ (Fig. 6b).

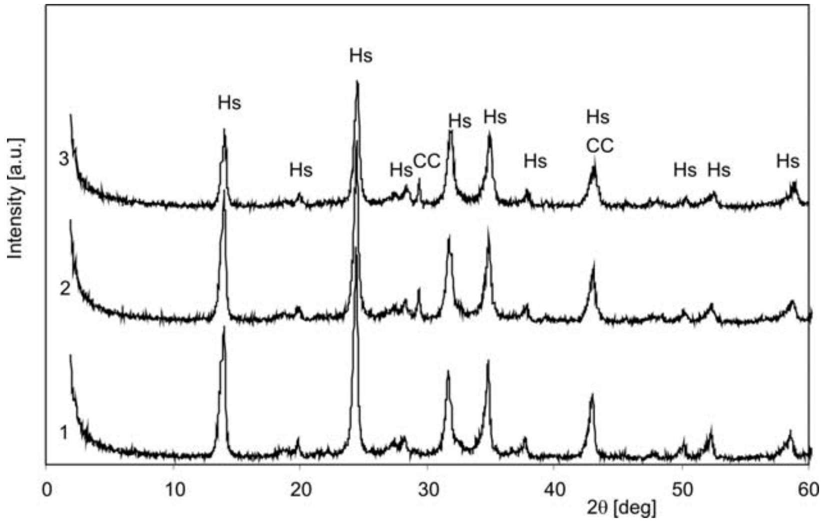

Fig. 4. X-ray diffraction patterns of hydrosodalite, ion exchange carried out at 65 °C for 60 min: 1 – pure hydrosodalite; 2 – after sorption; 3 – after desorption; Hs – hydrosodalite; CC – calcium carbonate

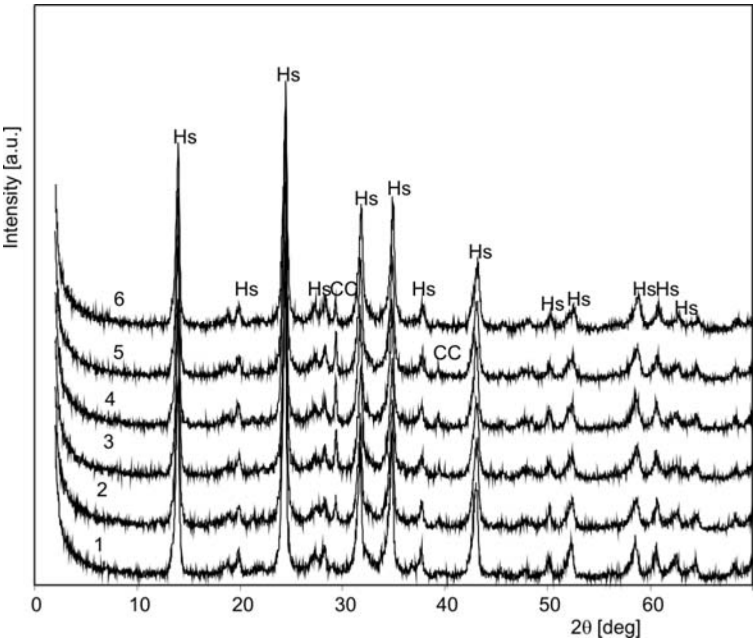

Fig. 5. X-Ray diffraction patterns of hydrosodalite, ion exchange carried out in 60 min, at various temperatures: 1 – pure hydrosodalite, 2 – 25 °C; 3 – 30 °C; 4 – 45 °C; 5 – 65 °C, 6 – 95 °C; Hs – hydrosodalite; CC – calcium carbonate

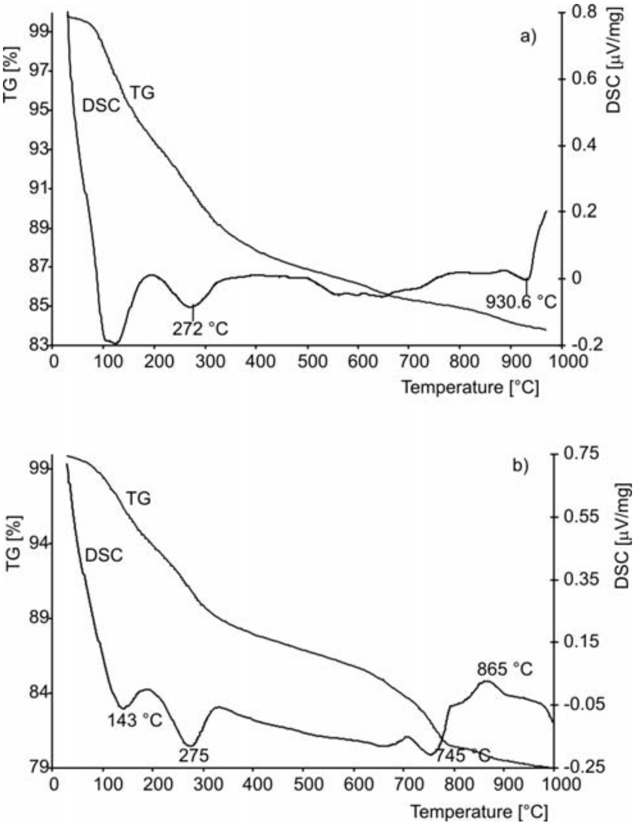

Fig. 6. The results of thermal analyses of hydrosodalite (a) and hydrosodalite after ion exchange carried out at 65 °C for 60 min (b)

Hydrosodalite gradually lost mass in all temperature ranges. Pure hydrosodalite shows lower loss on ignition (16.24%) compared with hydrosodalite after ion exchange (20.99%).

The results of IR spectroscopy analysis (Fig. 7) confirmed the data obtained by X-ray diffraction and thermal analyses. In the IR spectrum of the sample strong absorption band at 3442 cm^{-1} represents the frequencies of hydroxyl groups bound with hydrogen bonds. A narrow absorption band at 3638 cm^{-1} is attributed to water molecule hydroxyl groups that bound with the frame oxygen or with sodium cations. The above-mentioned peak dominates in pure hydrosodalite and disappears after sorption (Fig. 7, curve 2). The absorption band at 1667 cm^{-1} is attributed to deformation vibration of water molecules. A broad absorption band at 979 cm^{-1} is attributed to frequencies of (Si, Al)–O bond in tetrahedron along lines that bind [(Si, Al)O$_4$]$^{4-}$ tetrahedron oxygen atoms with central Si or Al atom. The characteristic hydrosodalite absorption bands are as follows: 987 cm^{-1} – asymmetric atomic vibration, 731, 701, 662 cm^{-1} – symmetrical atomic vibration, – 458, 428 cm^{-1} Si(Al)–O deformation vibration. Multiplicity of IR curve (Fig. 7, curve 2) of Ca^{2+} substituted hydrosodalite is altered

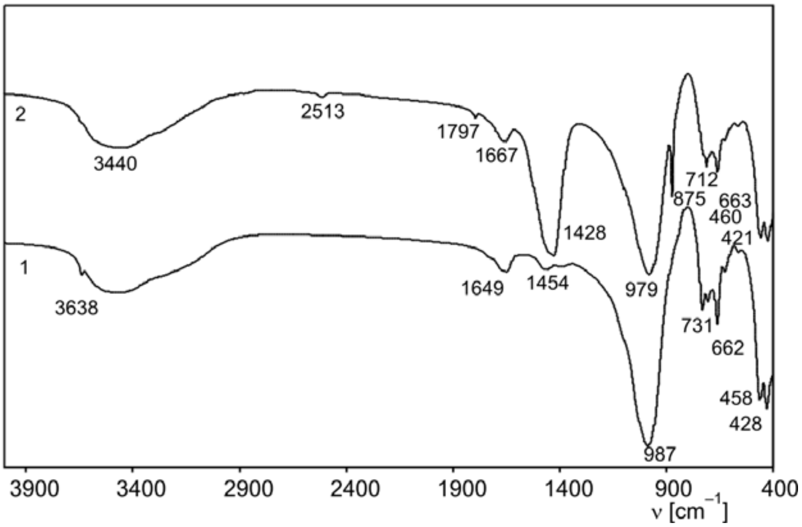

Fig. 7. The IR spectra of hydrosodalite (1) and hydrosodalite after ion exchange carried out at 65 °C for 60 min (2)

instead of three peaks of pure hydrosodalite two peaks at 712, 663 cm^{-1} occurred in the 731, 701, and 662 cm^{-1}. Bands at 2513; 1797; 1428 and 875 cm^{-1} are characteristic of $CaCO_3$.

4. Conclusion

Temperature has a large effect on the process of hydrosodalite ion exchange: upon increasing the temperature by only 5 °C (from 25 to 30 °C), the time required for inserting the Ca^{2+} ions into the hydrosodalite crystal structure is reduced by a factor of 3 (namely from 30 min to 10 min).

At higher temperatures (45 °C and 65 °C), the equilibrium amount of absorbed Ca^{2+} ions from saturated $Ca(OH)_2$ solution also increased: after 5 min of sorption almost all Ca^{2+} ions contained in the solution were incorporated into the structure of hydrosodalite. Meanwhile, high temperature that is close to the temperature of formation of hydrosodalite has a an adverse influence on the sorption process, since the equilibrium amount of Ca^{2+} ions incorporated hydrosodalite structure only after 10 min.

Partly reversible ion exchange reactions of hydrosodalite occur at a higher temperatures (at least 30 °C).

The structure of hydrosodalite crystals was determined to be stable in the 25–95 °C temperature under conditions of ion exchange reactions ($Na^+ \leftrightharpoons Ca^{2+}$).

References

[1] BREKK D., *Molecular Sieve Zeolites*, Mir, Moscow, 1976 (in Russian).
[2] http://www.elega.lt (in Lithuanian).
[3] WONG CHEONG W., TAK YIN AU L., TELLEZ ARISO C., LUN YEUNG K., J. Membr. Sci., 191 (2001), 143.
[4] ŠTUOPYS A., SASNAUSKAS K., PALUBINSKAITE D., Sci. Life, 10 (1996), 18 (in Lithuanian).
[5] MOTYČKA J., JARAUSCH M., *Application of non-metallics in environmental protection and agriculture*, Unido, Pilsen, 1991.
[6] EL-KAMASH A. M., EL-NAGGAR M. R., EL-DESSOUKY M. I., J. Hazardous Mater., 136 (2006), 310.
[7] GOÑI S., GUERRERO A., LORENZO M. P., J. Hazardous Mater., 137 (2006), 1608.
[8] GUALTIERI A. F., APREA P., Microporous Mesoporous Mater., 96 (2006), 276.
[9] KENDRICK E., DANN S., J. Solid State Chem., 177 (2004), 1513.
[10] MATTHEW E., BRENCHLEY T., MARK T., Zeolites, 14, (1994), 682.
[11] EIDEN-ASSMANN S., Mater. Res. Bull., 37 (2002), 875.
[12] GRUTZECK M., KWAN S., DICOLA M., Cement Concr. Res., 34 (2004), 949.
[13] PERRAKI TH., KAKALI G., KONTOLEON F., Microporous Mesoporous Mater., 61 (2003), 205.
[14] PALUBINSKAITE D., KANATUATAS A., Chem. Technol., 38 (2005), 35 (in Lithuanian).
[15] SASNAUSKAS K., PALUBINSKAITE D., SASNAUSKAS V., Chem. Technol., 10 (1999), 12 (in Lithuanian).
[16] BUTT J. M., RASHKOVICH L. N., The setting of bindings in higher temperatures (in Russian), Stroijizdat, Moscow, 1965.

Received 31 March 2008
Revised 30 September 2008

Materials Science-Poland, Vol. 27, No. 2, 2009

Slip casting process for the manufacture of tubular alumina microfiltration membranes

C. FALAMAKI[1,2*], M. BEYHAGHI[1]

[1]Ceramics Department, Materials and Energy Research Center, P.O. Box 14155-4777, Tehran, Iran

[2]Chemical Engineering Department, Amirkabir University of Technology,
P.O. Box 15875-4413, Tehran, Iran

A thorough investigation of the slip casting process for the manufacture of tubular alumina microfiltration membranes is presented. For this means an initial powder of an average particle size of 2 μm and broad size distribution (up to 10 μm) for imparting initial large pores during the slip casting process was used. The dispersing ability of sodium carboxymethylcellulose (Na-CMC) and Tiron ($C_6H_4O_8S_2Na_2 \cdot H_2O$) for slips containing 40, 50 and 60 wt. % of alumina was studied. It was shown that Na-CMC is not able to act as a proper dispersant. The kinetics of the slip casting process and time dependences of cast two-dimensional profile were investigated in function of slip concentration. The effect of sintering temperature on the pore microstructure of the final products was investigated. In all cases, the cross sections of the tubular membranes consisted of two regions: an inner thick section, consisting of relatively large pores, and a thin outer section, consisting of smaller pores. This phenomenon was attributed to Na-CMC migration during drying prior to sintering. The ratio of the thicknesses of the two sections depended on the slip concentration and sintering temperature. The average permeable pore size, based on dry nitrogen permeability experiments, was in the range of 0.13–0.24 μm. The controlled use of partial binder migration during cast drying for the production of graded microfilter membranes was addressed.

Key words: *slip casting; alumina; membrane; Na-CMC; Tiron*

1. Introduction

Ceramic membranes have attracted increasing interest in academic and industrial sectors during the last two decades. Most scientific reports concerning ceramic membrane processing discuss flat membrane preparation and far fewer have reported on the manufacture of tubular membranes. The latter include extrusion [1, 2] and centrifugal casting methods [3, 4]. Slip casting is a conventional ceramic processing method, widely used for the production of dense alumina tubular sintered bodies, mostly tradi-

---

[*]Corresponding author, e-mail: c.falamaki@aut.ac.ir

tional ceramics [5]. However, there has been no reported research on the application of the latter method to the manufacture of microfilter membranes. This is while slip casting is considered a relatively simple and economical industrial processing route for the production of ceramic bodies and is applied to the manufacture of tubular microfilter membranes by the industrial sector. The present investigation discloses for the first time a systematic approach to study the slip casting process for the manufacture of alumina tubular microfilters.

In conventional alumina slip casting, submicron powder is usually used [5, 6]. This is for guaranteeing slip stability during casting (avoiding particle sedimentation and flocculation). Slip cast bodies obtained by such powders generally result in low permeability of the sintered final products. Using larger particle sizes enhances permeability by introducing initial larger pores. In order to investigate this more comprehensively, the initial powder used in this study consisted of a wide range of particle sizes, from submicron to ten microns with an average around 2 μm.

In this work, high purity alumina sintered microfilters were considered. Sodium carboxymethylcellulose (Na-CMC) was used as dispersant in the first attempt. This was performed according to the existing reports claiming the effectiveness of Na-CMC in slip casting of high purity alumina, acting as a deflocculant, binder and fluxing agent with low residual sodium upon burnout, albeit for sub-micron powders [7, 8]. The sedimentation, zeta potential and rheological behaviour of the slips in function of Na-CMC content and solid loading for the powder used in this work are presented in the first part. Furthermore, the effect of adding a polyvalent organic salt (Tiron, $C_6H_4O_8S_2Na_2{\cdot}H_2O$) for improving significantly the slip stability was investigated. This is while existing reports on alumina slips sedimentation behaviour have considered only the effect of one additive as a dispersant [9–14]. To the best of the authors knowledge, few reports have been published concerning the stabilization of alumina slips and which consider both the dispersant as well as the binder [15]. Slip casting was performed on slips containing both Tiron (as a dispersant) and Na-CMC (as a binder and a fluxing agent). The effect of slip solid loading on the slip casting process (two-dimensional cast profile in function of time and slip solid loading) is presented in the second part of this study. In the third part, the effect of slip concentration and sintering temperature on the characteristics of the final sintered microfilter membranes (microstructure, porosity, nitrogen permeability, effective permeable pore size) were investigated.

Finally, the controlled use of partial binder migration during cast drying for the production of graded microfilter membranes was addressed.

2. Experimental

A Martoxide alumina powder (MR42, 99.8 wt. % of α-alumina) was used. The average particle diameter was 2 μm. The particle size distribution was as follows: $0.3 < d_{10} < 0.6$ μm, $1.5 < d_{50} < 2.5$ μm and $3.0 < d_{90} < 5.0$ μm. The specific surface area was 2.5 $m^2 \cdot g^{-1}$. The impurities were as follows: $Na_2O \leq 0.10$, $CaO \leq 0.05$, $Fe_2O_3 \leq 0.04$ and $SiO_2 \leq 0.06$ wt. %. Na-CMC from Merck was used for several purposes (dispersant, binder, sintering aid). It had the viscosity of around 75 Pa·s at 25 °C when dissolved in distilled water to get a 2 wt. % aqueous solution. Tiron from Acros Co. was used as a dispersant.

Slips containing 40, 50 and 60 wt. % of alumina with Na-CMC alone (N slips) or Na-CMC and Tiron (TN slips) were prepared according to the following procedure: For the N slips, first appropriate quantities of alumina in distilled water were milled in a fast mill for 15 min (first step). Afterwards, appropriate quantities of Na-CMC as aqueous solution (1 wt. %) were added and the resulting mixture was fast milled for 5 min. For the TN slips, Tiron was also added in the first step as 0.0017 g per 1 g of alumina powder. The latter optimum proportion was taken according to ref. [16]. Stable slips for the slip casting processes were produced using a Na-CMC content of 0.05 g per 100 g of alumina for the 40 and 60 wt. % of alumina concentrations.

Sedimentation tests were performed using test tubes filled with 10 cm^3 of the slips. The height of the sediment after 24 h was measured for each case. All the sediment tests were repeated after a time interval of more than 2 months, to ensure that the observed results were not affected by gross errors. The data presented further in the text are the average results.

For the production of tubular green compacts by slip casting, appropriate molds (hydrated calcium sulfate) were prepared. An Iranian plaster of Paris (industrial grade, > 95 wt. % α-hemihydrate calcium sulfate) was used. The ratio of water to plaster of Paris was chosen to be 3/4. After they had formed, the molds were dried for 3 days at 47 °C. The internal diameter of the tubular void was 50 mm.

The slip casting process was performed as follows: the mold was initially filled with the slip (TN slips). As the air-slip interface fell under 5 mm, the mold was gently filled with distilled water. Water was added to avoid crack creation of the upper sections which otherwise were not in contact with the slip. The bottom of the mold was made impermeable by installing a PTFE disk. The slip casting process duration was between 1 and 70 min. The cast compacts were taken out of the mold after 24 h and dried at room temperature for 48 h. Afterwards, they were dried at 70 °C in an oven for 1 h and consecutively put into an electric furnace for sintering. The heating rate applied was 10 °C min^{-1} and the soaking time was 2 h. The sintered samples were fabricated from green compacts with slip casting times of 20 and 5 min for the slips of concentrations 40, 50 and 60 wt. %, respectively. The sintering temperatures were 1375, 1400 and 1450 °C, respectively.

The density of the sintered product was measured according to ASTM C-373-88 (Archimedes' principle). The densities of the dried cast compacts were also measured. As it was not possible to apply the above standard test (because dried casts disintegrated in contact with water), a special method was applied. The dry weight of several segments of the dried cast was measured. Then, the latter were covered gently with a thin layer of vacuum grease, and the weight of the added grease was measured. In the last step, the surface coated segment weights of the submerged segments were measured. From the above data, the buoyancy force due to the volume of water displaced could be evaluated and corresponded to the total volume of the segment. As a result, the density and porosity of the initial dry cast segments could be readily calculated.

Microstructure evaluation was performed using an XL30 (Philips) instrument. XRD diffraction patterns were taken using a PW3710 (Philips) instrument. Dry N_2 gas permeability measurements were performed using a patented setup [17] in accordance with the ASTM F 316 standard. Circular segments with an approximate projected radius of 10 mm were cut out of the sintered tubular membrane supports. The effective permeable pore diameter was calculated from the permeability measurements for the Knudsen and Poiseuille flow regimes. The mathematical details may be found elsewhere [16]. Zeta-potential measurements were performed using a Malvern zeta sizer 3000 HAS instrument. Rheological measurements (duplicate) were performed using a Brookfield DV III apparatus. Surface porosity was evaluated using Oracle 2 software through analysis of the SEM pictures.

3. Results and discussion

3.1. Slip characterization

The sedimentation heights of the slips containing Na-CMC (N slips) in function of the slip alumina concentration and the quantity of additive added are shown in Fig. 1. As the amount of solid content was different for the test tubes filled with 10 cm^3 of the 40, 50 and 60 wt. % slips, the heights have been normalized for a constant mass of alumina equal to 8.672 g (corresponding to the solid content of the test tube filled with the 40 wt. % slip). The first interesting observation is that by increasing the slip concentration, the packing of the sediment improves. Considering the right hand asymptotes at high CMC concentrations, it is observed that the sediment height of the 60 wt. % slip decreases by ca. 30 % with respect to the 40 wt. % slip. The better particle arrangement at high solids loading is attributed to an intensified steric effect. At high slip solid concentrations, the particles collide more frequently into each other and fewer hydrated layers around each particle are expected [18]. In such circumstances, organic layers of Na-CMC induce a steric effect, eventually acting as a lubricant, preventing particle adhesion due to van der Waals forces.

The second remarkable observation, based on Fig. 1 is that there exists a distinct minimum in the dependence of the height on Na-CMC concentration at each slip concentration. Referring to Fig. 2, it is observed that for the 60 wt. % of alumina slip, viscosity steadily increases with the increase in Na-CMC content in the range of 0.0167 to 0.025 g/100 g of alumina. It should be stated that the slips did exhibit a shear thinning behaviour. Nonetheless, the ratio shear stress/shear rate was approximately constant in the range of the shear rate 0–200 s^{-1} used in this study.

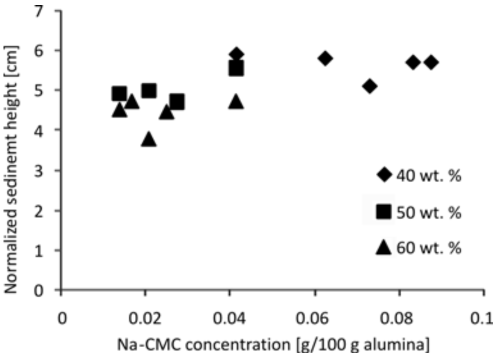

Fig. 1. Sediment height in function of slip and Na-CMC concentration for N slips

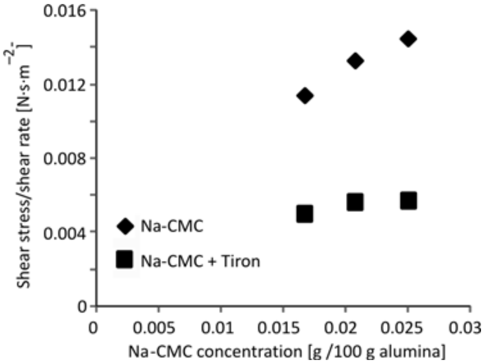

Fig. 2. Shear stress/shear rate in function of Na-CMC content for the N and TN slips

On the other hand, according to Fig. 1, the minimum sediment height (highest packing) corresponds to the Na-CMC content of 0.02075 g/100 g of alumina. Such a behaviour might be explained as follows: if the Na-CMC content lies between 0.0167 to 0.02075 g/100 alumina, more additive is adsorbed on the particles, inferring a higher absolute value of zeta-potential (Fig. 3). More additive does not increase particle charge but, instead, enhances flocculation as a result of bridging effects due to hydrogen bonds [7]. The result is an increase in viscosity, from 0.02075 to 0.025 g Na-CMC/100 alumina content. For 0.0167–0.02075 g Na-CMC/100 g of alumina content, an increase in viscosity is still observed which, at first sight, does not seem to be in concordance with the increase in the zeta-potential observed. This is attributed to the high solid loading of the slip. At high slip concentrations, due to frequent collisions, particles approach each other near their "sphere of influence" [19]. Any increase in the zeta potential in this case results in more interaction (repulsion) between particles, due to a larger sphere of influence. Consequently, any shear stress applied to the slip is accompanied with an increased momentum transfer between particles, due to their strong interaction. Therefore, for concentrated slips, the zeta potential increase may result in an increase in viscosity.

The shift of the minima towards higher values for less concentrated slips, as shown in Fig. 1, may be explained as follows. The amount of Na-CMC added to slip at the minimum for the 60 wt. % slip is 0.02075 g Na-CMC per 100 g of alumina. The corresponding zeta potential is –14.96 mV. For a lower slip concentration, e.g. 50 wt. % of alumina, the minimum sediment height corresponds to 0.0275 g Na-CMC per 100 g of alumina. The corresponding zeta potential was measured to be –36.75 mV. The higher value of the zeta potential at the minimum for the 50 wt. % slip shows that more Na-CMC could be adsorbed on the surface of the alumina particles compared with the 60 wt. % slip. A possible explanation for such a phenomenon is that adsorption of Na-CMC molecules on the surface of alumina particles may be restricted due to steric hindrance at high solid concentrations. In other words, the higher the solid concentration, the smaller is the amount adsorbed and, as a corollary, the smaller the absolute value of the zeta potential.

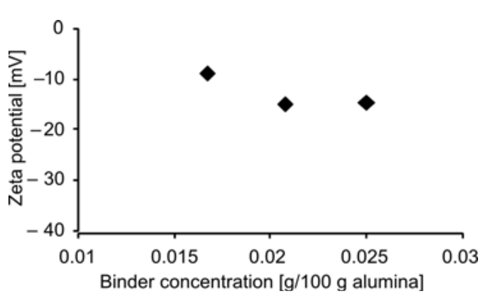

Fig. 3. Zeta potential in function of Na-CMC concentration for the N slips (60 wt. % of alumina slip)

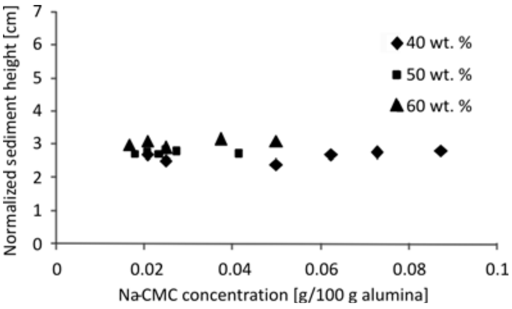

Fig. 4. Sediment height in function of slip and Na-CMC concentration for the TN slips

Although Na-CMC imparted significant dispersion to the slips, the rate of sedimentation in the test tubes was appreciably high (sediment observed after 1 h). It should be recalled that for “membrane support” manufacturing purposes, we have intentionally used an alumina powder with ca. 10 wt. % particles of the diameter in the range 3–5 μm to obtain a porous support of a sufficient high permeability (see ref. [16] for more explanation).To this effect, Tiron was added to the slips before the addition of Na-CMC to try to enhance the slip stability. The sedimentation behaviour is illustrated in Fig. 4. It is observed that Tiron could significantly increase slip stability (the sediment heights being significantly smaller with respect to N slips). It should be noted that any sediment was observable only after 12 h. The authors of the present work do not attribute any specific extremum to the curves in Fig. 4. The zeta-potential of the 60 wt. % slip has a constant value of –31.37±3.21 mV in the Na-CMC concentration range 0.0167–0.025 g/100 g of alumina. The viscosity dependence of the corresponding slips on Na-CMC is shown in Fig. 2. Tiron addition results in a substantial viscosity reduction. Comparing Figs. 4 and 1, it is observed that the trend in slip stability change versus slip alumina concentration has been reversed. The general explanation is the reduction of steric effects in the case of Tiron addition. The particles’ surface is totally covered with Tiron and Na-CMC does not appreciably physically adsorb on the Tiron layer. In other words, Na-CMC is present mainly in the aqueous solution and its main effect is to increase the viscosity of the solution (as observed in Fig. 2). Considering the 50 wt. % slip, although the zeta potential is lower than its counterpart for the N slip, the better slip stability is attributed to fewer bridging effects due to the absence of physically adsorbed Na-CMC on the particles.

3.2. Investigation of the slip casting process

Figures 5–7 show the dependences of the tubular cake thickness during slip casting on the sediment height at various slip casting times for the slips containing 40, 50 and 60 wt. % of alumina. The Na-CMC concentration was 0.05 g per 100 g of alumina. Tiron concentration was 0.0017 g per 1 g of alumina.

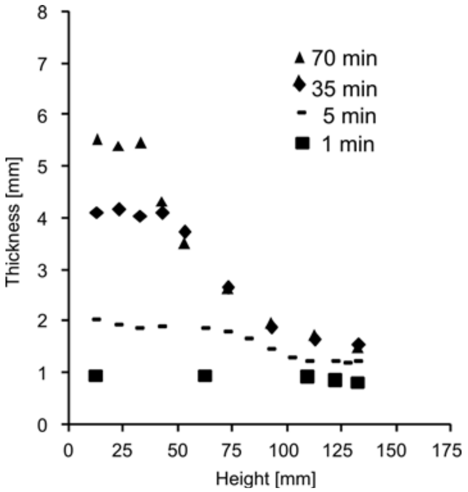

Fig. 5. Thickness in function of height for various slip casting times for the 40 wt. % of alumina slips

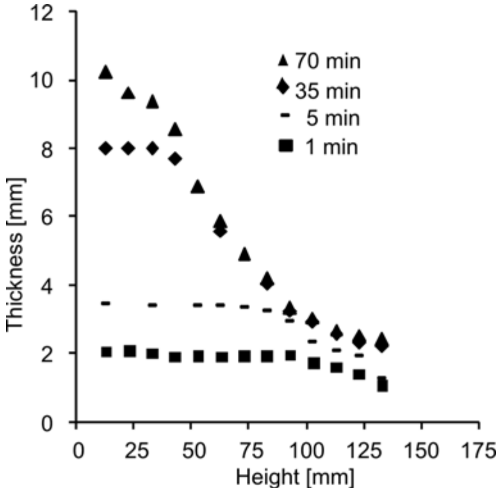

Fig. 6. Thickness in function of height for various slip casting times for the 50 wt. % of alumina slips

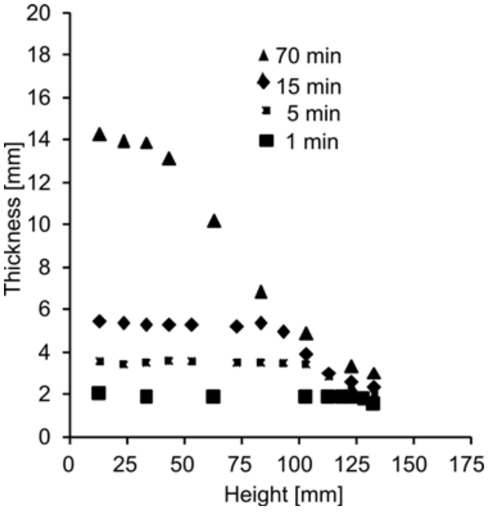

Fig. 7. Thickness in function of height for various slip casting times for the 60 wt. % of alumina slips

A common phenomenon takes place for all the slip concentrations used. At each instant of the slip casting process, the cast may be considered as consisting of two distinct regions: a zone of constant thickness and a zone of variable thickness. By simple visual inspection of the cast after draining the slip, a zone of constant glittering aspect could be observed which corresponds to the constant thickness zone. The reason for the production of such an approximately "constant thickness" cast in the lower section of the tubular cast may be attributed to the slip sectioning into two distinct zones at all slip casting times: A lower zone of approximately constant concentration and an upper zone of high dilution.

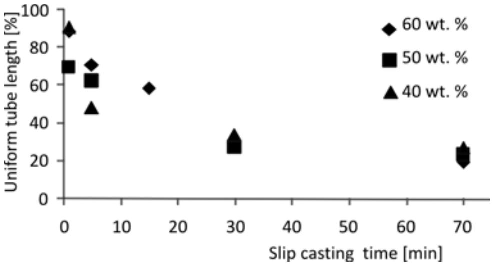

Fig. 8. Uniform tube length in function of slip casting time for various slip concentrations

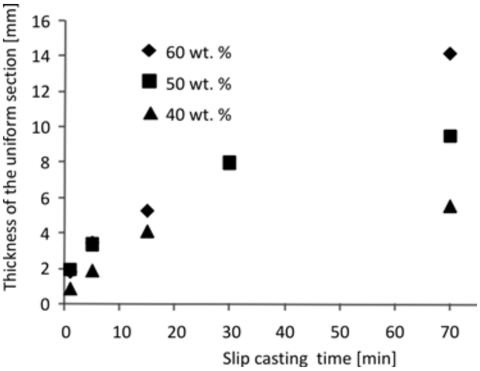

Fig. 9. Uniform tube thickness in function of slip casting time and slip concentration

For all the slip concentrations under consideration, the length of the constant thickness zone decreases with the slip casting time. It should be noted that the length of the constant thickness zone was determined from Figs. 5–7 by finding the point at which the change in the thickness is most abrupt, with respect to the increasing sediment height. Figure 8 shows the uniform tube length in function of the slip casting time for various slip concentrations. It is observed that the rate of length decrease is initially high, and then reduces at longer slip casting periods. The initial period of the decreasing rate decreases with increasing slip concentration. Actually the former rate is approximately constant during most of the slip casting process in the case of 60 wt. % slips.

Figure 9 shows the uniform tube thickness in function of slip casting time and slip concentration. At early times of the casting process, thickness could be correlated with the slip casting time through the following well known equation [20]:

$$L = Kt^{0.5} \tag{1}$$

where L is the thickness [mm], K a constant [mm·min$^{-0.5}$] and t is the time of the slip casting [min]. The value of K depends on the slip initial concentration and has been calculated to be 0.646, 1.148 and 1.195 mm·min$^{-0.5}$ for the 40, 50 and 60 wt. % slip concentrations, respectively.

It is noteworthy to consider the rate of water suction by the mold for each slip concentration used. Slip concentrations of 40 and 50 wt. % of alumina result in approximately similar water suction by the molds (Fig. 10). The reasonable reproducibility of the process for the 40 wt. % of alumina slip may be observed referring to the same figure. A slight discrepancy between the two curves for the 40 wt. % slip is due mainly to the difference of the two molds. Generally, it is impossible to fabricate two identical molds as far as the slip casting behaviour of the molds is concerned. The

60 wt. % slip, on the other hand, results in a significantly reduced rate of water suction. This is attributed to a more packed cast structure for the latter slip concentration.

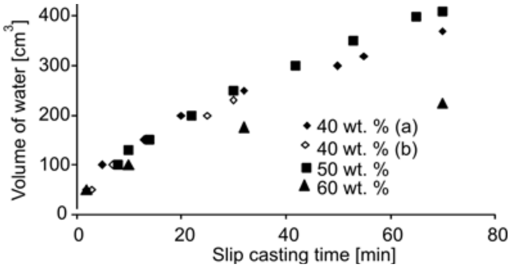

Fig. 10. Amount of water added in function of slip casting time and slip concentration

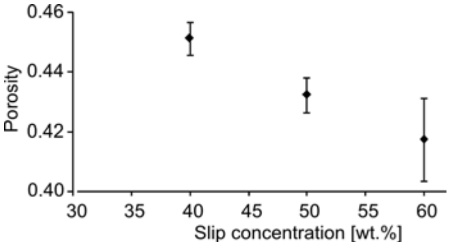

Fig. 11. Porosity of the dried casts in function of slip concentration

Considering Fig. 11, it may be easily observed that the porosity of the dried casts is a function of the slip concentration: the higher the slip concentration, the lower the porosity. The reason for this phenomenon will be explained in the next section.

3.3. Sintered membrane characterization

It should be mentioned that only the “constant thickness” portion of the sintered tubular membranes was investigated. Figures 12a, b show the SEM pictures of the cross section of the inner and outer boundary surfaces of a membrane sintered at 1400° C using a 60 wt. % slip. As far as particle size distribution is concerned no significant difference between the surfaces is observed.

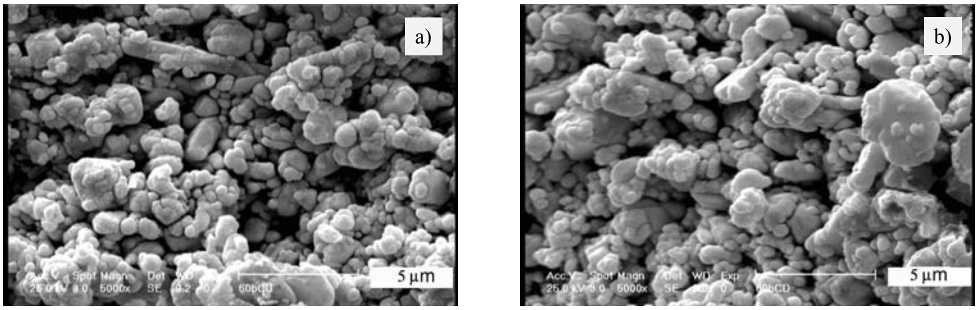

Fig. 12. Cross sections of the inner (left) and outer (right) layers of a sintered sample at 1400 °C using a 60 wt. % slip

The result is the same for the membranes sintered at the same temperature but using different slip concentrations. Generally, no significant particle size gradient exists across the cross section of the membranes. Nonetheless, the outer surfaces consisted of relatively small particles. These surfaces belong to a very thin layer which is the result of small particle migration at the very beginning of the slip casting process. Such a phenomenon is well known in the processing of ceramics by slip casting [21] and has been referred to as the "clogging effect". The latter phenomenon occurs due to the smaller inertia of smaller particles and a high fluid velocity from the slip towards the mold at the very first stage of the slip casting process. The lower the slip concentration, the greater is the freedom of smaller particles to reach the slip–mold interface. Accordingly, the outer surface of the membrane corresponding to the 40 wt. % slip was observed to have smaller particles in comparison with the particles on the surface of the membrane corresponding to the 60 wt. % slip (Fig. 13).

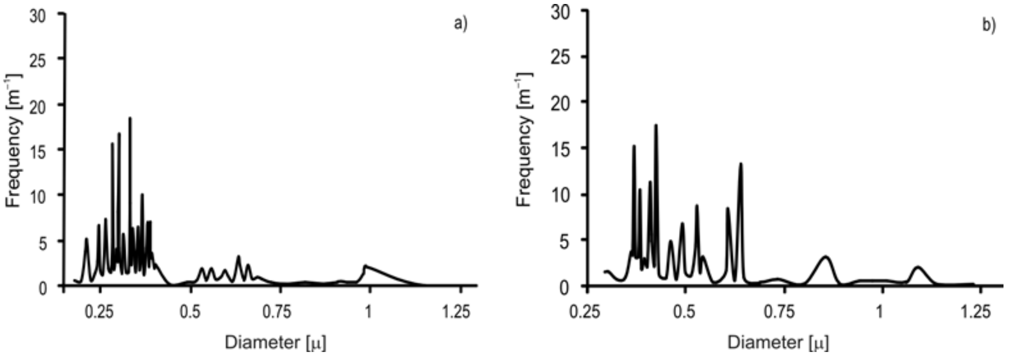

Fig. 13. Outer surface particle size distribution for a sintered membrane using 40 wt. % (a) and 60 wt. % (b) slip at 1400 °C

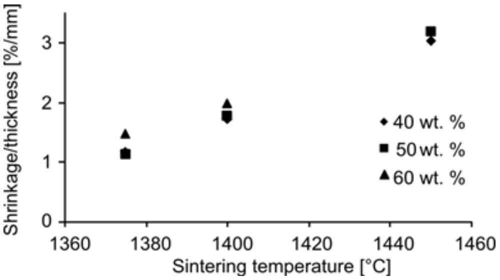

Fig. 14. Ratio of radial shrinkage over thickness for the sintered membranes in function of the sintering temperature and slip concentration

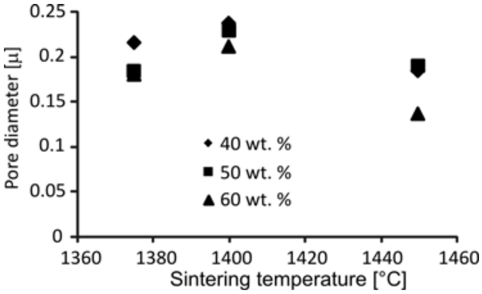

Fig. 15. Average permeable pore diameter of the sintered membranes in function of sintering temperature and slip concentration

Figure 14 shows the ratio of the radial shrinkage to the final thickness of the tubular membranes in function of slip concentration and sintering temperature. Division by the thickness had been performed to cancel out the effect of different initial thicknesses of the slip cast membranes. The values corresponding to the 60 wt. % slip are significantly larger than the values corresponding to the other slip concentrations (the temperature of 1450 °C has been omitted intentionally and will be explained later). The 50 wt. % slip shows a small deviation from the 40 wt. % slip between 1375 °C to 1400 °C. The deviation is even higher at 1450 °C.

Table 1 summarizes the arithmetic average values of porosity of the sintered products for various slip concentrations and sintering temperatures. It is observed that porosity undergoes an abrupt decrease between 1400 °C and 1450 °C. The latter change increases with increasing slip concentration.

Table 1. Average porosity [%] of the sintered products in function of the slip concentration and sintering temperature

Slip concentration [wt. %]	Sintering temperature [°C]		
	1375	1400	1450
40	39	38	30
50	39	40	23
60	40	40	19

The trends presented above may be partially explained referring to Fig. 11. The total length of the error bar at each point corresponds to twice the standard deviation, calculated data obtained from at least 4 experiments. The larger the slip concentration, the higher is the green body density. Increasing the slip concentration from 40 to 60 wt. %, a 6% increase in the raw density is observed. It is the opinion of the authors of this work that the sole 6% difference in the raw density may not cause a 33% difference in density at 1450 °C between the membranes corresponding to 40 and 60 wt. % slips. Sintering behaviour depends upon packing structure, green density, coordination number and particle size distribution [22]. We presume that increasing the slip concentration in the range of 40–60 wt. % of alumina results in a higher homogeneity of the slip during non-agitated slip-casting. In other words, due to more frequent particle collisions at higher slip loadings, a better level of mixing of the particles takes place. This results in a broader particle size distribution throughout the slip and in the cast cake [23]. The enhanced lubricating effect at higher solid loadings, due to less hydrated layers around each particle, also improves particle packing during the slip casting process.

Table 2. Knudsen permeability and slope of the ratio permeability/average pressure drop in the Poiseuille region for the sintered membranes

Sintering temperature [°C]	Slip concentration [wt. %]	Knudsen permeability×10^5 [$m^3 \cdot s^{-1} \cdot Pa^{-1} \cdot m^{-2}$]	Poiseuille regime slope×10^{11} [$m^3 \cdot s^{-1} \cdot Pa^{-2} \cdot m^{-2}$]
1375	40	1.99	4.69
1400	40	1.69	4.36
1450	40	0.83	1.66
1375	50	2.24	4.51
1400	50	1.89	4.64
1450	50	0.98	0.19
1375	60	1.81	3.57
1400	60	1.73	4.01
1450	60	1.59	2.38

The experimental estimates of the Knudsen permeability and slope of the permeability/average pressure drop in the Poiseuille region are summarized in Table 2. The relevant average permeable pore diameters have been calculated and are shown in Fig. 15. For all slip concentrations, an increase in pore the diameter between 1375 °C and 1400 °C and a decrease between 1400 °C and 1450 °C is observed. The 60 wt. % slip results in smaller pores throughout the whole temperature range. Generally, all calculated pore diameters lie in the lower extreme for inorganic microfilter membranes ($0.13 < d < 0.24$ μm). The explanation for this will become apparent in the text below, and upon consideration of some important additional issues which shall now be introduced.

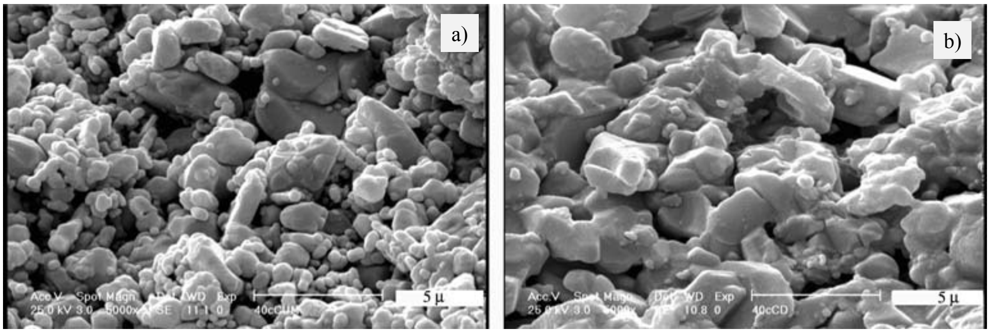

Fig. 16. Micrographs of the middle (left) and inner (right) parts of the cross section of a membrane sintered at 1450 °C using a 40 wt. % slip

As mentioned in the beginning of this section, no appreciable particle size gradient could be observed throughout the entire cross section of the membranes. However, for all the membranes produced, a clear gradient in “pore diameter” across the outer layers could be observed. Figures 16a, b show the micrographs of the middle part and inner layer of the cross section of a membrane sintered at 1450 °C using a 40 wt. % slip. It is clearly observed that the outer layer has undergone appreciable sintering in comparison with the middle layer. SEM analysis of other samples showed that the latter phenomenon is more intense for the membranes produced using higher slip concentrations. The inner and outer surface of a membrane sintered at 1375 °C for a 50 wt. % slip are shown in Fig. 17a, b. It is clearly observed that the outer side has undergone more densification, has smaller pores and also less surface porosity.

All these observations might be explained as follows: The porosity profile across the cross sections of the outermost layers is a result of binder migration during the drying step. The outer surfaces are subject to faster drying. This results in the “concentration” of the dissolved Na-CMC near the outer side of the tubular casts. Actually Na-CMC solidifies near the outer side. As this material is also a sintering aid (it produces active sodium oxide at high temperature), it causes the outer part of the cast to sinter faster. The latter effect is more intense for the casts produced with higher slip solid loadings because, as demonstrated before, higher slip concentrations produce denser initial casts. Generally, this phenomenon might be of great use in producing graded membranes if used in a controlled manner. The difference in the sintering rate of adjacent layers may result in high stresses between them, especially during the intermediate stages of sintering [16]. In our case, it was observed that the cast pertaining to the 60 wt. % slips underwent longitudinal macrocracks at 1450 °C. This is why the shrinkage of the latter sample was not reported in Fig. 14.

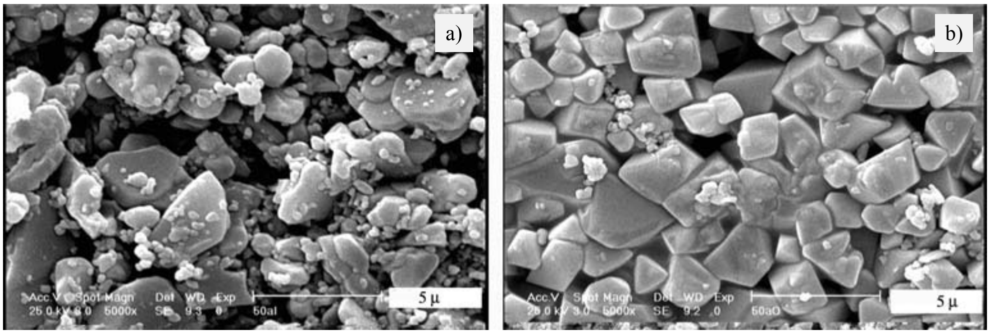

Fig. 17. Inner (left) and outer (right) surfaces of a membrane sintered at 1375 °C using a 50 wt. % slip

The explanations given above elucidate why the calculated microfilter pore diameters are significantly small: they correspond mostly to the denser, outer layers (compare Figs. 17a and b). The thickness of the latter layer for the membranes produced using 40 wt. % slips was approximately 100, 250 and 470 µm at the sintering temperatures 1375, 1400 and 1450 °C, respectively.

Referring again to Fig. 15, it is observed that a clear pore size enlargement occurs in the 1375–1400 °C temperature range. This is attributed to "pore enlargement" of the inner layers during the initial stages of sintering. Initial pore enlargement during the initial sintering stage of alumina green compacts has been reported and discussed in detail by several researchers [24–26]. It is observed that increasing the sintering temperature up to 1450 °C results in a decrease in the pore size, due to significant densification, especially for the outer layers.

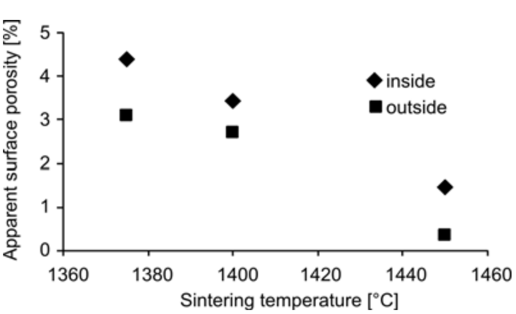

Fig. 18. Apparent surface porosity for the inside and outside surfaces of the sintered membranes fabricated using a 40% slip in function of the sintering temperature

As outlined in the literature (see for example Ref. [16]), the apparent surface porosity is of importance especially if the microfilter is to be coated further for the production of ultra- and nanofilters. Therefore, we report the latter parameter for the inside and outside surfaces of the sintered membranes produced using a 40 % slip (Fig. 18). It is observed that the apparent surface porosity decreases approximately linearly as the sintering temperature increases. The outside surface has less porosity with respect to the inner surface at all temperatures.

4. Conclusions

The manufacture of tubular alumina ceramic microfilter membranes by the slip casting method is a rather complicated process. As the final sintered membranes should have reasonable permeability, the average particle size of the initial slip should be larger than that used for conventional slip casting for the production of fully sintered bodies. It was shown in the first part of this work that Na-CMC cannot act as a proper dispersant for stabilizing such alumina slips. The addition of another dispersant, such as Tiron, is indispensable in order to obtain stable slips.

Based on the detailed study performed on the slip casting process, the thickness and two-dimensional profile of the casts, in function of time and slip concentration, are predictable within the ranges of 40-60 wt. % of alumina, and 0–70 min slip casting times.

As far as the membrane characteristics of the final sintered body are concerned, the optimum slip concentration was found to be 40 %. Higher solid loading results in a lower permeability and a smaller effective permeable pore size of the final product. The optimum sintering temperature range is 1375–1400 °C. Within the latter range, the average permeable pore size increases. Higher temperatures result in excessive total and outer layer surface porosity reduction and the creation of macrocracks, especially for high slip concentrations. It is noteworthy to mention that industrial slip casting is generally performed with concentrated slips (typically having a solidity of more than 50 wt. %) in order to minimize water consumption. Therefore, we did not investigate further slips of concentrations lower than 40 wt. %.

In all cases, the cross sections of the tubular membranes consisted of two regions: an inner thick section consisting of relatively large pores and high porosity, and an outer, thin section, consisting of smaller pores and lower porosity. This phenomenon was attributed to binder migration during drying prior to sintering. The ratio of the thicknesses of the two sections depended on the slip concentration and the sintering temperature. The average pore sizes of the membranes were calculated to be within the 0.13–0.24 μm range, and their dependences on the slip concentration and sintering temperature was determined.

Generally, binder migration should be minimized in order to avoid unwanted macrocracks (especially longitudinal) and prematurely high sintering of the outer layers of the cast. The results of our experiments strongly suggest that proper control the "binder migration" phenomenon may be profitably used for the production of functionally graded membranes and is worth further investigation.

References

[1] KHEMAKHEM S., BEN AMAR R., BEN HASSEN R., LARBOT A., BEN SALAH A., COT L., Ind. Ceram., 24 (2004), 207.

[2] ISMAGILOV Z.R., SHKRABINA R.A., KORYABKINA N.A., KIRCHANOV A.A., VERINGA H., PEX P., React. Kinet. Catal. Lett., 60 (1997), 225.

[3] NIJMEIJER A., HUISKES C., SIBELT N.G.M., KRUIDHOF H., VERWEIJ H., Am. Ceram. Soc. Bull. 77 (1998), 95.

[4] KIM K.H., CHO S.J., YOON K.J., KIM J.J., HA J., CHUN D.II, J. Membrane Sci., 199 (2002), 69.

[5] BANNO T., SANO S.and ODA K., , J. Am. Ceram. Soc., 81 (1998), 2933.

[6] CESARINO III J., AKSAY I.A., J. Am. Ceram. Soc., 71 (1988), 1062.

[7] RUYS A.J., SORREL C.C., Am. Ceram. Soc. Bull. 69 (1990), 828.

[8] RUYS A.J., SORRELL C.C., Am. Ceram. Soc. Bull., 75 (1996), 66.

[9] HIDBER P.C., GRAULE T.J., GAUCKLER L.J., J. Eur. Ceram. Soc., 17 (1997), 239.

[10] EVANKO C.R., DZOMBAK D.A., NOVAK J.W.Jr., Coll. Surf. A: Physicochem. Eng. Asp., 110 (1996), 219.

[11] BRISCOE B.J., KHAN A.U., LUCKHAM P.F., J. Eur. Ceram. Soc., 18 (1998), 2141.

[12] SINGH B.P., MENCHAVEZ R., TAKAI C., FUJI M., TAKAHASHI M., J. Coll. Interf. Sci., 291 (2005), 181.

[13] JIANG L., GAO L., Mat. Chem. Phys., 80 (2003), 157.

[14] TSETSEKOU A., AGRATIOTIS C., MILIAS A., J. Eur. Ceram. Soc., 21 (2001), 363.

[15] KHAN A.U., BRISCOE B.J., LUCKHAM P.F., Coll. Surf. A: Phys. Eng. Asp., 161 (2000), 243.

[16] FALAMAKI C., VEYSIZADEH J., J. Membrane Sci., 280 (2006), 899.

[17] FALAMAKI C., AGHAIE A.and ARDESTANI N.R., J. Eur. Ceram. Soc., 21 (2001), 2267.

[18] TARI G., FERREIRA J.M., LYCKFELDT O., J. Eur. Ceram. Soc., 18 (1998), 479.

[19] RICHARDSON D.W., *Modern Ceramic Engineering: Properties, Processing, and Use in Design*, Marcel Dekker, New York, 1992, p. 447.

[20] FALAMAKI C., NAIMI M., AGHAIE A., J. Eur. Ceram. Soc., 26 (2006), 949.

[21] FERREIRA J.M., J. Eur. Ceram. Soc., 18 (1998), 1161.

[22] LINIGER E.G., RAJ R., J. Am. Ceram. Soc., 71 (1988), C-408.

[23] IGA T., J. Ceram. Soc. Japan, 104 (1996), 1143.

[24] FALAMAKI C., AFARANI M.S., AGHAIE A., J. Eur. Ceram. Soc., 24 (2004), 2285.

[25] ZHENG J.and REED J.S., J. Am. Ceram. Soc., 72 (1989), 810.

[26] WHITTEMORE O.J., SIPE J.J., Powder Techn., 9 (1974), 159.

Received 18 May 2008
Revised 21 January 2009

Materials Science-Poland, Vol. 27, No. 2, 2009

Influence of antimony oxide on the dielectric properties of barium strontium titanate based ceramics

C. ZHANG[*], Y. QU

Key Laboratory for Advanced Ceramics and Machining Technology of Ministry of Education,
Tianjin University, Tianjin 300072, P. R. China

The dielectric properties of Sb_2O_3 doped $(Ba_{0.992-x}Sr_xDy_{0.008})TiO_{3.004}$ ceramics fabricated by a solid state route with various Sb_2O_3 contents and Sr/Ba ratios were investigated. The XRD patterns confirm the samples to be multiphase compounds composed of perovskite major phase and $Ba_4Ti_{13}O_{30}$, $Ba_6Ti_{17}O_{40}$, Ti_7O_{13} secondary phases. The average lattice constant indicates that Sb^{3+} ions initially occupy the A-sites and then enter the B-sites serving as acceptor dopants. The Curie temperature decreases as the Sb_2O_3 content increases and as the Sr/Ba ratio increases also. The thermal stability of the electric permittivity increases as the Sb_2O_3 concentration increases but decreases as the Sr/Ba ratio increases. The resistivity and ac standing voltage decrease as the Sr/Ba ratio decreases. The Sb_2O_3 doped $(Ba_{0.992-x}Sr_xDy_{0.008})TiO_{3.004}$ ceramics with high permittivity, low dielectric loss, high ac standing voltage and low temperature coefficient of capacitor are obtained for applications in environment friendly capacitors.

Key words: *barium strontium titanate; doping effects; dielectrics; capacitors*

1. Introduction

Barium titanate ceramics has been used extensively as capacitor dielectrics for the past few decades [1]. Barium strontium titanate ($Ba_{1-x}Sr_xTiO_3$, hereafter referred to as BST) as a solid solution composed of barium titanate and strontium titanate has received intensive attention due to its high electric permittivity, low dissipation factor and adjustable Curie temperature [2–6]. Doping effects of various oxides on barium strontium titanate ceramics have also been reported [7, 8]. Incorporating rare earth oxides into the perovskite structure is an effective way to improve dielectric properties of barium strontium titanate ceramics. According to Huang [9], Dy_2O_3-doped BST capacitor ceramics possess a high permittivity (ε = 5245), low dielectric loss (tanδ

---

[*] Corresponding author, e-mail: zhch1234581@hotmail.com

= 0.0026) and high dc breakdown voltage (E_b = 5.5 MV/m). Zhao et al. [10] also reported that significantly new properties (ε = 3658, tanδ = 0.0093, $\Delta\varepsilon/\varepsilon$ = 14.1%) were obtained in Y_2O_3 and Dy_2O_3 doped BST ceramics.

Many rare earth elements are confirmed to act as donors in $BaTiO_3$ perovskite structure within a certain doping concentration. According to Kim [11], Y_2O_3 initially entered the A sites (< 1.0 mol %) in Ba excess $BaTiO_3$ ceramics and then occupied the B sites (>1.0 mol %) as acceptors. With the increase in the Sm_2O_3 doping content in $BaTiO_3$ ceramics, the following two defect reactions occurred successively and then another phase belonging to $P6_322$ space group appeared [12]:

$$2\mathrm{Sm_2O_3} + 4\mathrm{TiO_2} \rightarrow 4\mathrm{Sm}^{\bullet}_{\mathrm{Ba}} + 4\mathrm{Ti}_{\mathrm{Ti}} + 12\mathrm{O}_{\mathrm{O}} + \mathrm{O_2} + 4\mathrm{e}' \tag{1}$$

$$2\mathrm{Sm_2O_3}+6\mathrm{TiO_2} \rightarrow 4\mathrm{Sm}^{\bullet}_{\mathrm{Ba}}+6\mathrm{Ti}_{\mathrm{Ti}}+18\mathrm{O}_{\mathrm{O}}+2\mathrm{V}''_{\mathrm{Ba}} \tag{2}$$

The substitution characteristics of Dy_2O_3 in barium titanate ceramics are similar to those of Y_2O_3. The substituting mechanism can be expressed as follows [13]:

$$x\mathrm{Dy}^{3+} + \mathrm{BaTiO_3} \rightarrow (\mathrm{Ba}^{2+}_{1-x}\mathrm{Dy}^{3+}_{x})[\mathrm{Ti}^{4+}_{1-x}(\mathrm{Ti}^{4+}\cdot\mathrm{e})_x]\mathrm{O_3} + x\mathrm{Ba}^{2+} \tag{3}$$

$$x\mathrm{Dy}^{3+} + \mathrm{BaTiO_3} \rightarrow \mathrm{Ba}^{2+}_{1-x/2}\mathrm{Dy}^{3+}_{x}(\mathrm{Ti}^{4+}_{1-x/2})\mathrm{O_3} + (x/2)\mathrm{Ba}^{2+} + (x/2)\mathrm{Ti}^{4+} \tag{4}$$

Antimony oxide is one of the common additives in $BaTiO_3$ based ceramics with positive temperature coefficient of resistance (PTCR). The effects of Sb_2O_3 addition on the PTCR properties of BST ceramics have been investigated [14]. Unfortunately, there have been few reports concerning the effects of antimony oxide on the dielectric properties of BST ceramics. In the previous work, we have studied the dielectric properties of Sb_2O_3 doped $(Ba_{0.992-x}Sr_xY_{0.008})TiO_{3.004}$ ceramics [15]. In this study, we continue to prepare the Sb_2O_3 doped $(Ba_{0.992-x}Sr_xDy_{0.008})TiO_{3.004}$ dielectrics by solid state reaction technique. The purpose of this paper is to investigate the influence of antimony oxide on the structural and the dielectric properties of $(Ba_{0.992-x}Sr_xDy_{0.008})TiO_{3.004}$ ceramics, as well as to provide a class of fine capacitor ceramics possessing high electric permittivity, low dielectric loss, high breakdown voltage and low temperature coefficient of the capacitor.

2. Experimental

The chemical compositions of the specimens are shown in Table 1. High purity $BaCO_3$ (>99.0%), $SrCO_3$ (>99.0%), TiO_2 (>98.0%) and Dy_2O_3 (>99.0%) powders, used as raw starting materials, were weighed, ball-milled, dried and calcined at 1080 °C for 2 h. The calcined powders were mixed with Sb_2O_3 (>99.0%), reground, dried and added with 5 wt. % polyvinyl alcohol (PVA) as a binder for granulation. The granulated powders were sieved through a 40 mesh screen and then pressed into pellets (Φ12 mm×2 mm) under 250 MPa. Sintering was conducted in air at 1300 °C for 2 h. For dielectric measurement, both flat surfaces of the specimens were coated with silver paste. Finally, the painted samples were fired at 610 °C for 10 min.

Table 1. Chemical compositions of the specimens

Sample	Composition
A1	$(Ba_{0.732}Sr_{0.26}Dy_{0.008})TiO_{3.004}$
A2	$(Ba_{0.732}Sr_{0.26}Dy_{0.008})TiO_{3.004}$+0.4 wt. % Sb_2O_3
A3	$(Ba_{0.732}Sr_{0.26}Dy_{0.008})TiO_{3.004}$+0.8 wt. % Sb_2O_3
A4	$(Ba_{0.732}Sr_{0.26}Dy_{0.008})TiO_{3.004}$+1.2 wt. % Sb_2O_3
A5	$(Ba_{0.732}Sr_{0.26}Dy_{0.008})TiO_{3.004}$+1.6 wt. % Sb_2O_3
A6	$(Ba_{0.732}Sr_{0.26}Dy_{0.008})TiO_{3.004}$+2.0 wt. % Sb_2O_3
B1	$(Ba_{0.612}Sr_{0.38}Dy_{0.008})TiO_{3.004}$+1.6 wt. % Sb_2O_3
B2	$(Ba_{0.672}Sr_{0.32}Dy_{0.008})TiO_{3.004}$+1.6 wt. % Sb_2O_3
B3	$(Ba_{0.872}Sr_{0.12}Dy_{0.008})TiO_{3.004}$+1.6 wt. % Sb_2O_3
B4	$(Ba_{0.952}Sr_{0.04}Dy_{0.008})TiO_{3.004}$+1.6 wt. % Sb_2O_3
B5	$(Ba_{0.972}Sr_{0.02}Dy_{0.008})TiO_{3.004}$+1.6 wt. % Sb_2O_3

The phases of the specimens were confirmed by X-ray diffraction (Rigaku D/max 2500 V/pc) with CuK_α radiation. The surface morphologies of the specimens were studied using a scanning electron microscope (PhilipXL30 ESEM). The electric permittivities of ceramic bodies were measured with a YY 2811 Automatic LCR Meter 4425 at 1kHz in an environment chamber with controlled temperature from –25 °C to 90 °C. And the ac standing voltages were measured with a high voltage device (CJ-2677A) at 50 Hz after the pellets had been coated with 1 mm diameter point electrodes to prevent the surface discharges.

3. Results

Figures 1–3 show the XRD patterns of $(Ba_{0.732}Sr_{0.26}Dy_{0.008})TiO_{3.004}$ ceramics with various Sb_2O_3 contents. As indicated in Fig. 1, all these samples are multiphase compounds with $Ba_{1-x}Sr_xTiO_3$ as the major phase. XRD profiles focusing on the (103)/(310) and (113)/(311) diffraction peaks are presented in Fig. 2. The (103) and (310) peaks are separated from each other for sample A1 and A2, whereas the two peaks are merged together for samples A4 and A6. The XRD peak corresponding to (113) and (311) plane exhibits a split only for sample A1. It is revealed that at room temperature the structure of major phase changes from tetragonal to cubic as the Sb_2O_3 content increases. The patterns in the 2θ range from 20° to 30° are recorded in Fig. 3. It was found that in addition to the perovskite phase, the orthorhombic compound $Ba_4Ti_{13}O_{30}$

(space group *Cmca*(64)) is precipitated as a secondary phase in samples A1 and A2. As the Sb_2O_3 content increases, the monoclinic compound $Ba_6Ti_{17}O_{40}$ (space group *C*2/*c*(15)) and the triclinic compound Ti_7O_{13} (space group $\overline{I}1(2)$) are formed consecutively in samples A4 and A6. There is no phase containing Sb, even in samples A6, implying that the dopants have entered the perovskite structure but have not contributed to the formation of secondary phases.

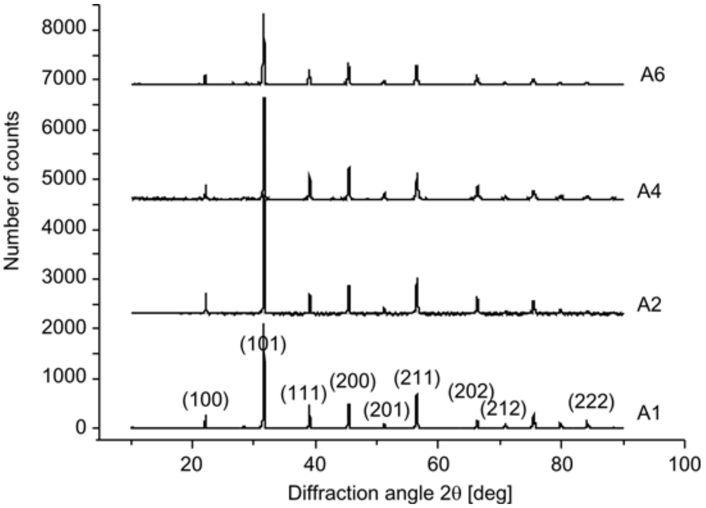

Fig. 1. XRD patterns of $(Ba_{0.732}Sr_{0.26}Dy_{0.008})TiO_{3.004}$ ceramics with various Sb_2O_3 contents; 2θ in the range 10–90°

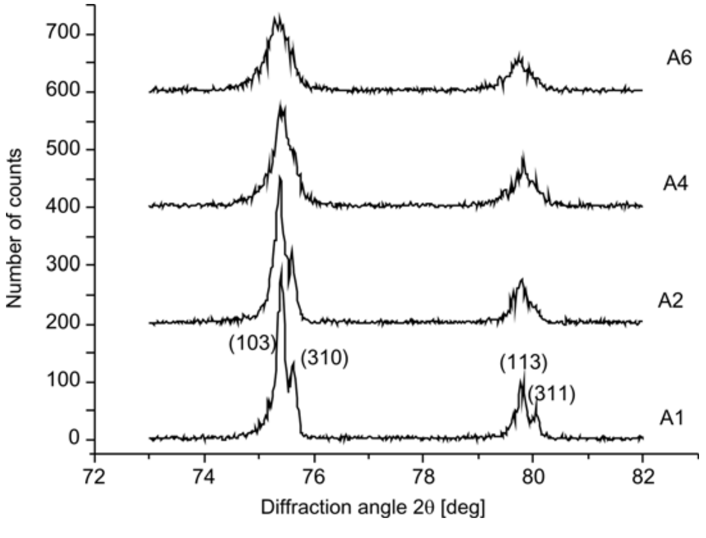

Fig. 2. XRD patterns of $(Ba_{0.732}Sr_{0.26}Dy_{0.008})TiO_{3.004}$ ceramics with various Sb_2O_3 contents; 2θ in the range 73–82°

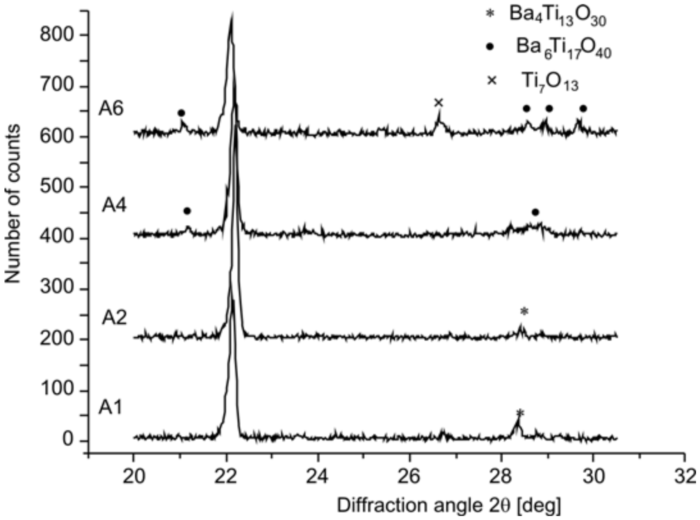

Fig. 3. XRD patterns of $(Ba_{0.732}Sr_{0.26}Dy_{0.008})TiO_{3.004}$ ceramics with various Sb_2O_3 contents; 2θ in the range 20–30.5°

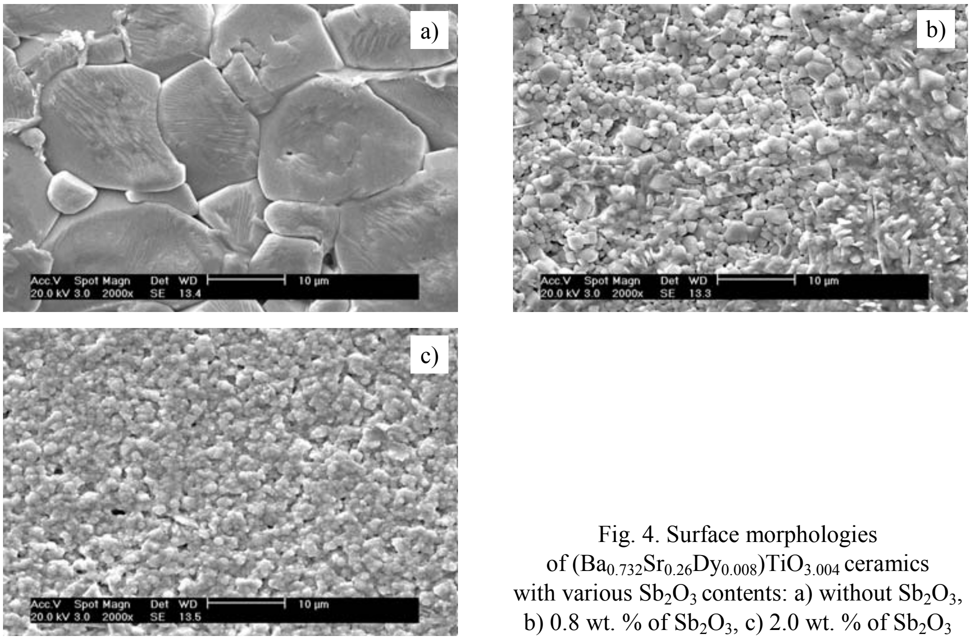

Fig. 4. Surface morphologies of $(Ba_{0.732}Sr_{0.26}Dy_{0.008})TiO_{3.004}$ ceramics with various Sb_2O_3 contents: a) without Sb_2O_3, b) 0.8 wt. % of Sb_2O_3, c) 2.0 wt. % of Sb_2O_3

The surface morphologies of $(Ba_{0.732}Sr_{0.26}Dy_{0.008})TiO_{3.004}$ ceramics with various Sb_2O_3 contents are shown in Fig. 4. It appears that all the samples exhibit a dense and uniform microstructure. The average grain size is decreased as the content of Sb_2O_3 is increased.

The structural and dielectric parameters of sintered specimens with different Sb_2O_3 contents at room temperature are shown in Table 2. It is obvious that the average lattice constant $(a^2c)^{1/3}$ where a and c are lattice parameters of the tetragonal cell decreases initially and then increases as the Sb_2O_3 content increases. The electric permittivity increases, reaches a maximum and then decreases as the Sb_2O_3 doping content increases. The dielectric loss increases at the beginning and then decreases dramatically with the increase of Sb_2O_3 content before it gets saturated. The Curie temperature decreases as the added Sb_2O_3 content increases.

Table 2. Structural and dielectric parameters of sintered specimens with various Sb_2O_3 contents

Sample	a [nm]	c [nm]	$(a^2c)^{1/3}$ [nm]	ε	tanδ	T_c [°C]
A1	0.39485	0.40115	0.39694	3295	0.009	45
A2	0.39534	0.40006	0.39691	9055	0.024	30
A3	–	–	–	6733	0.007	5
A4	0.39304	0.40140	0.39581	2498	0.007	–24
A5	–	–	–	2252	0.007	<–25
A6	0.39463	0.40156	0.39693	2054	0.007	<–25

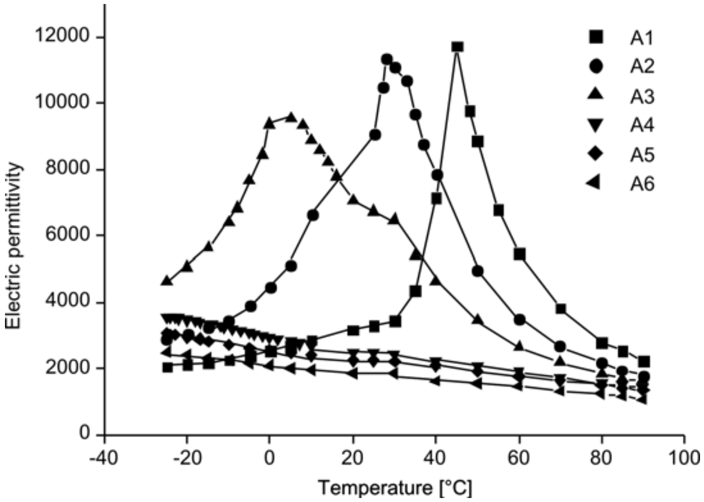

Fig. 5. Temperature dependences of electric permittivities of A1–A6 samples at 1 kHz

Figure 5 shows the temperature dependence of the electric permittivity of $(Ba_{0.732}Sr_{0.26}Dy_{0.008})TiO_{3.004}$ ceramics with various Sb_2O_3 contents. It is obvious that the permittivity of the samples is significantly suppressed as the Sb_2O_3 content increases, which is consistent with our previous findings with respect to Sb_2O_3 doped $(Ba_{0.732}Sr_{0.26}Y_{0.008})TiO_{3.004}$ system. In particular, the peak value decreases rapidly from 11 730 to 3550 for samples A1 and A4, respectively. Furthermore, at low Sb_2O_3 doping concentration (<0.8 wt. %) the curves are characterized by narrow peaks which imply high values of the temperature coefficient of capacitor (TCC). When the level of Sb_2O_3 addition reaches 2.0 wt. %, the curve becomes flat and a low TCC over a wide temperature range from –25 °C to 85 °C can be obtained.

Table 3. Dielectric parameters of sintered specimens with various Sr to Ba ratios

Sample	ε	tanδ	ρ [MΩ·mm]	E_b [kV/mm]	*Tc* [°C]
B1	1415	0.002	3941	5.3	<–25
B2	1600	0.003	3597	5.1	<–25
B3	2501	0.006	1130	4.4	–15
B4	3237	0.009	608	4.2	5
B5	3248	0.009	607	4.2	8

The dielectric parameters of sintered specimens with various Sr/Ba ratios at room temperature are shown in Table 3. It is evident that the Curie temperature increases with the decrease in the Sr/Ba ratio, which is consistent with many other reports [1, 16]. The resistivity and ac standing voltage decrease as the Sr/Ba ratio decreases and due to the shift of the Curie temperature towards room temperature, the electric permittivity as well as the dielectric loss increase as the Sr/Ba ratio decreases.

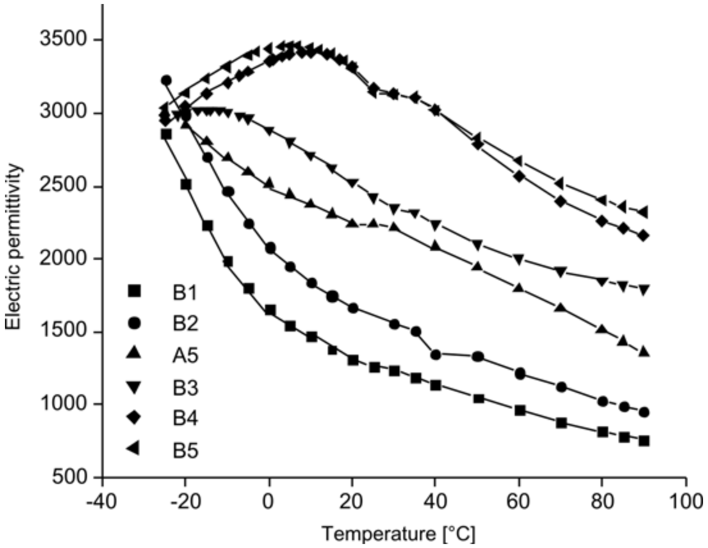

Fig. 6. Temperature dependences of electric permittivities for B1–B5 and A5 sample

Figure 6 shows the temperature dependences of the electric permittivity of ceramics with various Sr/Ba ratios. It can be seen that the curves for samples B4 and B5 are much broader than those for samples B1 and B2. This indicates that the thermal stability of the electric permittivity for samples increases with the decrease in the Sr/Ba ratio.

4. Discussion

As shown in Table 2, the average lattice constant $(a^2c)^{1/3}$ decreases initially and then increases as the Sb_2O_3 content increases. This demonstrates that Sb^{3+} ions (0.076 nm) first substitute the bigger Ba^{2+} ions (0.161 nm) or Sr^{2+} ions (0.144 nm) and then replace the smaller Ti^{4+} ions (0.061 nm). Thus the substitution characteristic of Sb_2O_3 in $(Ba_{0.732}Sr_{0.26}Dy_{0.008})TiO_{3.004}$ ceramics is similar to that of Sb_2O_3 in Y-doped BST dielectrics [15]. When Sb^{3+} ions occupy the A sites and serve as donor dopants, the defect reaction is as follows:

$$\mathrm{Sb_2O_3} \rightarrow 2\mathrm{Sb}_\mathrm{A}^{\bullet} + V_A^{"} + 3\mathrm{O_O} \tag{5}$$

With the increase of Sb_2O_3 concentration, Sb^{3+} ions begin to enter B sites and serve as acceptor dopants. The defect reaction can be expressed as follows:

$$\mathrm{Sb_2O_3} \rightarrow 2\mathrm{Sb}_\mathrm{B}' + V_\mathrm{O}^{\bullet\bullet} + 3\mathrm{O_O} \tag{6}$$

The above models are similar to those proposed by Sasaki et al. [17] for $BaTiO_3$ thin films with high Sb doping concentration:

$$\mathrm{Sb_2O_3} + 3\mathrm{TiO_2} \rightarrow 2\mathrm{Sb}_\mathrm{Ba}^{\bullet} + 3\mathrm{Ti_{Ti}} + 9\mathrm{O_O} + \mathrm{V}_\mathrm{Ba}'' \tag{7}$$

and/or

$$\mathrm{Sb_2O_3} + 2\mathrm{BaO} \rightarrow 2\mathrm{Sb}_\mathrm{Ti}' + 2\mathrm{Ba_{Ba}} + 5\mathrm{O_O} + \mathrm{V}_\mathrm{O}^{\bullet\bullet} \tag{8}$$

The substitution for A site or B site with any of the Sb^{3+} ions leads to a shorter distance between the central ion and its nearest neighbours of the octahedron, thus the movement of the central ion is confined which weakens the spontaneous polarization of the grain lattice, and consequently, the Curie temperature decreases as the Sb_2O_3 content increases. The charged vacancies caused by A site and B site substitution give rise to the local deformation of the perovskite unit cells which also causes the reduction of the Curie temperature. It is well known that the electric permittivity and dielectric loss near the phase transition region usually exhibit high values. Therefore, the shift of the Curie temperature is expected to be the main reason for variation of the electric permittivity and dielectric loss.

The influence of Sb_2O_3 addition on the temperature dependence of the permittivity is caused by the weakening of ferroelectricity which is attributed to the replacement reaction of Sb^{3+} ions for the host cations in the perovskite lattice.

As shown in Fig. 6, the lower Sr/Ba ratio is, the flatter the temperature variation curve becomes. The broadening of the curve is attributed to the disorder in the arrangement of cations at the A site which leads to a microscopic heterogeneity in the composition, and thus results in a continuous phase transition of different tiny regions. A considerable decrease in the ac standing voltage shown in Table 3 is ascribed to the increasing proportion of tiny regions which undergo the transitions between tetragonal and cubic phases at room temperature. In other words, it is basically because of the shift of the Curie temperature towards the room temperature as the Sr/ Ba ratio decreases. Due to its high permittivity ($\varepsilon = 3248$), acceptable dielectric loss ($\tan\delta = 0.009$), high ac standing voltage ($E_b = 4.2$ kV/mm) and low TCC (< ±25%), the sample B5 is promising for applications in environment friendly capacitors.

5. Conclusions

Dielectric ceramics based on Sb_2O_3 doped $(Ba_{0.992-x}Sr_xDy_{0.008})TiO_{3.004}$ were prepared through a conventional solid state reaction technique and their dielectric properties were investigated. The doping content of Sb_2O_3 and the Sr/Ba ratio were both varied. XRD patterns confirmed these ceramics to be multiphase compounds with perovskite major phase. The average lattice constant indicates that Sb^{3+} ions first substitute the A site ions and then replace the B site ions. The Curie temperature decreases as the Sb_2O_3 content and Sr/Ba ratio increase. The temperature dependence of the electric permittivity increases as the Sb_2O_3 concentration increases but decreases with the increase in the Sr/Ba ratio. Sintered samples with high Sb_2O_3 doping level and low Sr/Ba ratio in the Sb_2O_3 doped $(Ba_{0.992-x}Sr_xDy_{0.008})TiO_{3.004}$ system exhibit more satisfactory dielectric properties compared with previous ceramics .

Acknowledgement

This work was supported by the Chinese Doctor Foundation of National Ministry of Education (Grant No. 20040056055).

References

[1] Fu C.L., Yang C.R., Chen H.W., Wang Y.X., Hu L.Y., Mater. Sci. Eng. B, 119 (2005), 185.
[2] Jeon J.H., Hahn Y.D., Kim H.D., J. Eur. Ceram. Soc., 21 (2001), 1653.
[3] Wei X.Y., Yao X., Mater. Sci. Eng. B, 99 (2003), 74.
[4] Abdelkefi H., Khemakhem H., Vélu G., Carru J.C., Mühll R.V., J. Alloys Compd., 399 (2005), 1.
[5] Alexandru H.V., Berbecaru C., Ioachim A., Nedelcu L., Dutu A., Appl. Surf. Sci., 253 (2006), 354.
[6] Ioachim A., Toacsan M. I., Bancium.G., Nedelcu L., Dutu A., Antohe S., Berbecaru C., Georgescu L., Stoica G., Alexandru H.V., Thin Solid Films, 515 (2007), 6289.
[7] Li R.X., Cheng J.R., Meng Z.Y., Wu W.B., J. Mater. Sci.-Mater. Electron., 17 (2006), 587.
[8] Liu S.J., Zenou V.Y., Sus I., Kotani T., Schilfgaarde M., Newman N., Acta Mater., 55 (2007), 2647.

[9] HUANG X.Y., GAO C.H., CHEN X.C., ZHENG X.L., HUANG G.J., LIU H.P., J. Rare Earths, 22 (2004), 226.
[10] ZHAO C., HUANG X.Y., GUAN H., GAO C.H., J. Rare Earths, 25 (2007), 197.
[11] KIM J.H., YOON S.H., HAN Y.H., J. Eur.Ceram. Soc., 27 (2007), 1113.
[12] LI Z.C., ZANG H., ZOU X., BERGMAN B., Mater. Sci. Eng. B, 116 (2005), 34.
[13] MIAO H.Y., DONG M., TAN G.Q., PU Y.P., J. Electroceram., 16 (2006), 297.
[14] KIM I.H., LEE H.W., KIM Y.M., KIM H.J., UR S.C., Mater. Lett., 60 (2006), 3027.
[15] ZHANG C., QU Y.F., MA S.C., Mater. Sci. Eng. B, 136 (2007),118.
[16] PATIL D.R., LOKARE S.A., DEVAN R.S., CHOUGULE S.S., KANAMADI C.M., KOLEKAR Y.D., CHOUGULE B.K., Mater. Chem. Phys., 104 (2007), 254.
[17] SASAKI Y., FUJII I., MATSUI T., MORII K., Mater. Lett., 26 (1996), 265.

Received 15 June 2008
Revised 31 March 2009

Materials Science-Poland, Vol. 27, No. 2, 2009

Oxidation of activated carbon fibre and its adsorption of amylase

Y. LI[1*], S. HU[2]

[1]Department of Logistic Services Administration,
North University of China, Taiyuan 030051, P.R. China

[2]The Graduate School, North University of China, Taiyuan 030051, P. R. China

Activated carbon fibre was oxidized by combustion of nitrocellulose and oxidation with nitric acid to introduce the nitrogen and oxygen groups on its surface. The pore structure and chemical groups were investigated by nitrogen adsorption and FTIR. The result showed that the pore structure and surface morphology were not much affected but amide and hydroxyl groups could be introduced after oxidation. The adsorption capacity of amylase was markedly increased, and the hydrolysis activity of starch was maintained after 3 runs.

Key words: *activated carbon fibre; surface modification; adsorption; amylase; hydrolysis*

1. Introduction

Porous carbons have been widely used as adsorbents, catalyst/catalyst supports, electronic materials and energy storage materials due to their high surface area and large pore volume [1]. The advantages of activated carbon fibre are the smaller fibre diameter which minimizes diffusion limitations and allows rapid adsorption /desorption, more concentrated pore size distribution. The novel porous carbon has been widely used in separation, purification and catalytic processes.

Activated carbon fibres display a better adsorption capacity for small molecules and a higher storage capacity/volume for hydrogen. They have also been used as electrode materials in high performance electric double-layer capacitors [4]. Not only the pore structure but also the surface chemical composition of the activated carbon fibre significantly influence its adsorption capacity, catalytic activity or its catalyst support performance. Heteroatoms on the surface of the activated carbon fibre determine its surface chemical properties and play a significant role in device applications. The two most important heteroatoms are oxygen and nitrogen which affect the surface acidic, basic and hydrophilic properties of activated carbon fibres [5–7].

---

[*]Corresponding author, e-mail: LiY@nuc.edu.cn

Chemical oxidation of activated carbon fibre is a frequently used method to introduce heteroatoms onto its surface. Various reagents have been used as oxidizers: concentrated nitric or sulfuric acid, sodium hypochlorite, permanganate, bichromate, hydrogen peroxide, transition metals, ozone-based gas mixtures, etc. Among various oxidation treatments, oxidation of nitric acid is the most widely used method for increasing the total acidity that is produced from wet oxidation treatment [8]. Recently, it was reported that the oxygen- and nitrogen-containing groups on activated carbon fibre surface could be introduced by nitrocellulose combustion oxidation at 300 °C [9], the modified activated carbon fibre showed higher adsorption capacities for ammonia and carbon disulfide.

It is well known that carbon possesses good biocompatibility [10]. Enzymes as biocatalysts with high specificity, high catalytic efficiency and bio-degradability, are widely applied in industrial process and medical sciences, because they can increase the rate of chemical reaction by lowering the activation energy. Enzyme immobilization on a support may improve its thermal behaviour, it may be repeatedly and continuously used and simplify the separation of enzymes from reaction media, thus, the recovery of enzyme and purification of the final products become more reliable, simple and efficient [11].

α-Amylases belong to an enzyme group widely used in food, paper, textile, distillery, fermentation and brewing industries. The hydrolysis of starch to products with low molecular weight, catalyzed by α-amylase (1,4- α-d glucan glucanohydrolase) is one of the most important commercial enzymatic processes [12]. The immobilization of α-amylase was investigated by many researchers. For example, α-amylase was immobilized on zirconia or alumina via adsorption and exhibited higher activity [13, 14], it was covalently immobilized on phthaloyl chloride-containing amino group functionalized glass beads forming amide bonds between amino groups on protein and acid chloride groups on the glass surface [15]. α-amylase was also immobilized in modified ordered mesoporous silicas through the reaction of free –CHO (following alkylamine and glutaraldehyde procedures) with $–NH_2$ of enzyme for hydrolysis of starch, thermal and pH stability of the immobilized enzyme was improved [16]. Although activated carbon fibre displayed developed pore structure, it has not been widely used as an enzyme support because its surface chemical property was generally hydrophobic, its oxygen and nitrogen content was very small, and it could not interact strongly with enzymes. Thus it is necessary to investigate the properties of modified activated carbon fibre as an enzyme support material. Activated carbon fibre was treated by nitrocellulose combustion and nitric acid oxidation to modify its surface chemical composition, and the adsorption of amylase and hydrolysis for starch were investigated and discussed.

2. Experimental

Oxidation of activated carbon fibre. Commercially viscose-based activated carbon fibre (designated as ACF-0), activated at 850 °C with steam, was supplied by Zichuan Carbon Fiber Limited Company, Qinhuangdao (P.R. China). Firstly, the ACF-0 was dried at 120 °C for 2 h to remove the adsorbed steam and organic molecules, then, it was impregnated with nitrocellulose acetone solution and the loading amount was fixed at 1 wt. % of nitrocellulose at room temperature for 4 h. Finally, the impregnated activated carbon fibre was heated to 300 °C for 30 min in air and labelled as ACF-NC. ACF-0 was impregnated in 5 M nitric acid for 12 h, then, it was leached with distilled water until pH of approximately 7 has been attained. Finally, it was dried at 80 °C and designated as ACF-HNO_3.

Characterization of activated carbon fibres. Nitrogen adsorption isotherms were performed at 77.4 K with a Micromeritics ASAP 2010 analyzer. The surface area was calculated using the Brunauer–Emmett–Teller (BET) model. The pore volume, pore size distribution and the average pore diameter were determined by the density function theory. Before nitrogen adsorption measurements, the activated carbon fibres were outgassed at 300 °C for 15 h. Infrared spectra were recorded on a Nicolet Impact 380 FT-IR spectrometer using KBr pellets. Scanning electron micrographs were obtained on a JEM-3010 using a copper grid type sample holder. Before observation, the samples were sputtered with gold for 2 min in order to avoid charging.

Adsorption of amylase and hydrolysis of starch. In the adsorption experiments, 1 g of activated carbon fibre was mixed with equal volumes of 0.1 M phosphate buffer and α-amylase solution. It was shaken at room temperature for 1 h and then filtered. The adsorbed amount of α-amylase was obtained as the difference between the hydrolysis capacity of the original enzyme solution with that of the filtrate.

The hydrolysis activities of free and the immobilized enzymes were examined in a batch reactor. 1 wt. %, 2 wt. % and 5 wt. % starch solution was prepared by dissolving soluble starch in distilled water and the pH was adjusted to 4.7 by 0.1 M HCl. Then 1 g of activated carbon fibre containing α-amylase was placed in a test vial. Subsequently, 100 cm^3 of starch solution was added and the system was incubated in a water bath with constant shaking at 40 °C. 1 cm^3 of solution was drawn each 10 min to determine the amount of hydrolyzed maltose. The reaction was stopped by adding 1 cm^3 of 3,5-dinitrosalicylic acid reagent. Incubation was also performed in a boiling water bath for 5 min. The amount of reducing sugar (maltose) was determined spectrophotometrically at 540 nm.

3. Results and discussion

3.1. Pore structures of activated carbon fibres

The specific surface areas and pore volumes of the ACF-0, ACF-NC and ACF-HNO_3 are 651 m^2/g, 696 m^2/g and 682 m^2/g, 0.35 cm^3/g, 0.38cm^3/g and 0.36 m^3/g, respectively, indicating the ACF-NC and ACF-HNO_3 have a more developed pore structure.

Figure 1 shows the nitrogen adsorption isotherms and pore size distributions of ACF-0, ACF-NC and ACF-HNO_3. The nitrogen isotherms were planar at the relative pressure higher than 0.1 which suggested that the activated carbon fibres mainly had micropores. The ACF-NC has a wider pore size distribution, especially in the 0.7–0.8 nm range than that of ACF-0. It implies that not only the carbon of external surface but the micropore surface are oxidized during the combustion of nitrocellulose. The pore size distribution of ACF-HNO_3 was slightly wider than that of ACF-0.

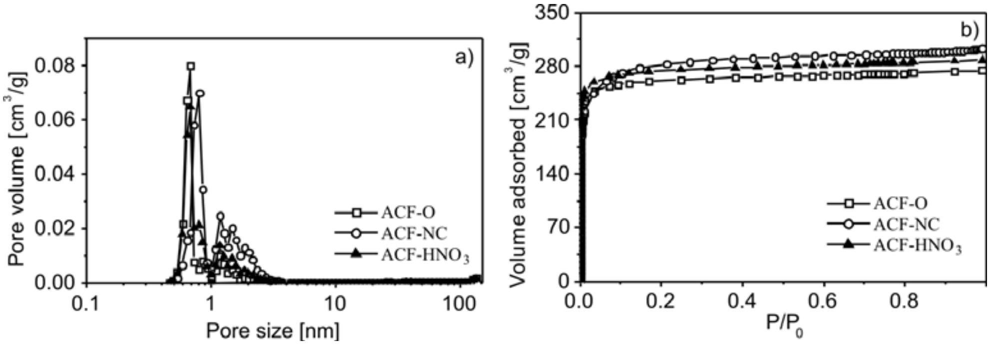

Fig. 1. The nitrogen adsorption isotherms (a)
and pore size distribution (b) of ACF-0, ACF-NC and ACF-HNO_3

Thus specific surface area, micropore volume and pore diameter of activated carbon fibre all increase slightly after combustion of nitrocellulose or oxidation of nitric acid.

3.2. Surface functional groups of activated carbon fibres

The elemental compositions of activated carbon fibre before and after oxidation are listed in Table 1. The carbon content markedly decreased and the oxygen content significantly increased after oxidation, the hydrogen and nitrogen contents also slightly increased.

Table 1. Elemental compositions [wt. %] of samples

Sample	C	H	N	O
ACF-0	83.63	2.87	2.01	11.48
ACF-HNO_3	79.44	3.01	2.12	15.43
ACF-NC	69.43	3.27	2.34	24.95

In order to investigate the change of surface acidicity and basicity, the Boehm method was used [17]. The differences of the surface functionalities on basic ACFs and acidically treated ACFs determined by the Boehm titration are listed in Table 2.

Oxidation with HNO_3 introduces a large number of carboxylic groups; nitrocellulose oxidation can form phenolic and basic groups.

Table 2. Surface functionalities of ACFs by the Boehm titration [molecule/nm^2]

Sample	Phenol	Lactone	Carboxyl	Acidic groups	Basic groups
ACF	0.58	0.28	0.02	0.88	0.12
ACF-HNO_3	0.31	0.64	0.44	1.39	0.06
ACF-NC	0.83	0.07	0.00	0.90	0.87

The FT-IR spectra of ACF samples are shown in Fig. 2. For the ACF-NC, the asymmetry of the peak ranging from 3000 cm^{-1} to 3400 cm^{-1} indicates strong hydroxyl interaction and the presence of overlapping N–H bands. The peak at 1700 cm^{-1} may be attributed to overlapping of N–H in-plane bending and the conjugated –C=O modes [18]. The two correlative peaks at 1456 cm^{-1} and 1395 cm^{-1} indicate the -C=O belonged to the carbonate groups [18]. Moreover, there are a number of overlapping bands appearing between 1400 cm^{-1} and 1000 cm^{-1}, which indicate the presence of C-O-C, C-O-N or >C-N groups. A wider and stronger peak at 3460 cm^{-1} corresponds to the hydroxyl for ACF-HNO_3.

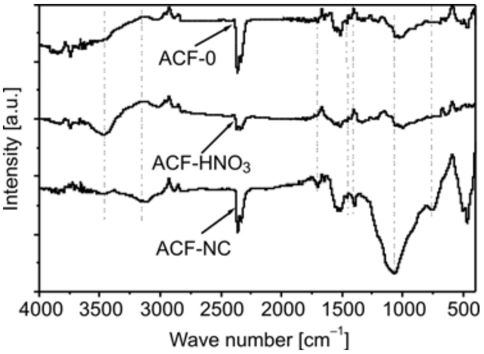

Fig. 2. The FT-IR spectra of: ACF-0, ACF-NC and ACF-HNO_3

FT-IR spectra show that ACF-NC, unlike ACF-0, contains functional groups primarily consisting of phenolic hydroxyls, imide and ethers. The spectra also show that ACF-HNO_3 has more surface hydroxyl groups that does ACF-0.

3.3. The SEM morgraphology of samples

The SEM images of activated carbon fibres are shown in figure 3. The surface of ACF-0 looks smooth, the spots on the surface are the adsorbed dirt. The least dirt was found on the surface of ACF-HNO_3; most of the dirt was leached during nitric acid impregnation. This also shows that the nitric acid oxidation does not damage the fibre surface.

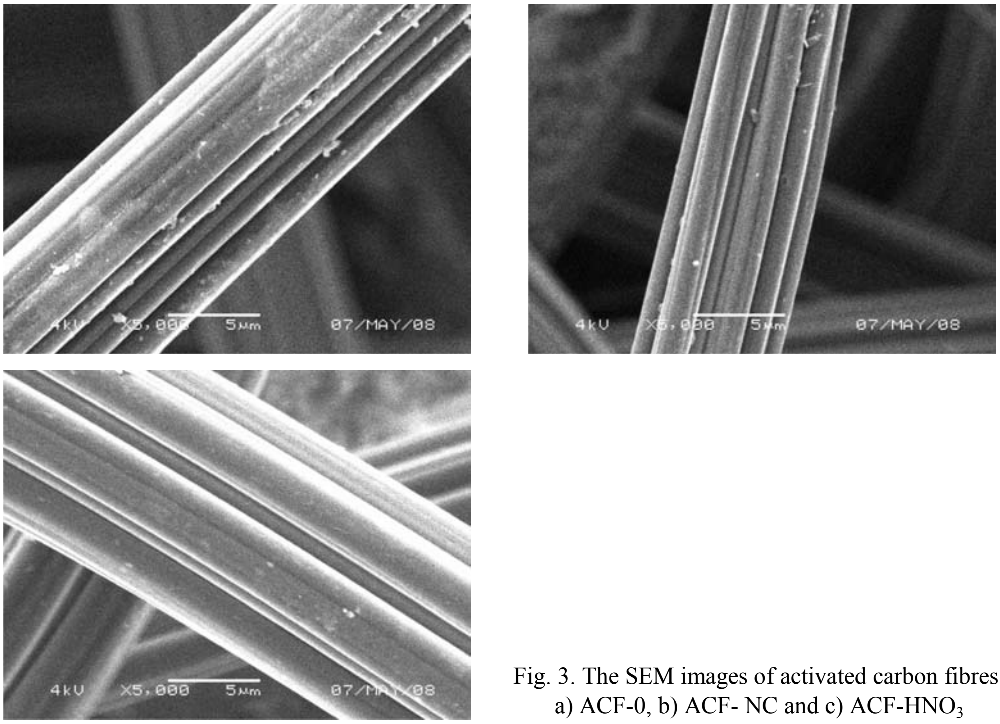

Fig. 3. The SEM images of activated carbon fibres: a) ACF-0, b) ACF- NC and c) ACF-HNO_3

The surface of ACF-NC was less contaminated than that of ACF-0, some impurities were washed during impregnation of nitrocellulose; this suggests that all nitrocellulose had been completely combusted. By comparing the SEM images, the activated carbon fibre surface was not destroyed after oxidation with nitric acid and combustion of nitrocellulose. This proves that it is a simple method to introduce nitrogen/oxygen atoms on the surface of activated carbon fibre, and one in which no damage occurs to the surface.

3.4. Adsorption of amylase and hydrolysis of starch

The adsorption capacities of α-amylase on ACF-0, ACF-NC ACF-HNO_3 are 2.0 mg/g, 9.9 mg/g and 7.9 mg/g, respectively. Because the pore structures of ACFs were similar, the surface oxygen- and nitrogen-containing groups are the only markedly affected factor characterizing the α-amylase adsorption, especially the phenolic hydroxyls, which could form a hydrogen-bond with the $–NH_2$ of an α-amylase molecule.

Compared with free α-amylase, the hydrolysis activity of α-amylase immobilized on ACF-0, ACF-NC and ACF-HNO_3 was decreased to 20%, 48% and 34%, respectively. This suggests that active sites of α-amylase were affected by the activated carbon fibre pore structure, which could change the interaction between the α-amylase and starch molecule. In addition, the immobilized α-amylase molecule was fixed on the pore channel and the mass transfer was also restricted, so the apparent hydrolysis activity was decreased.

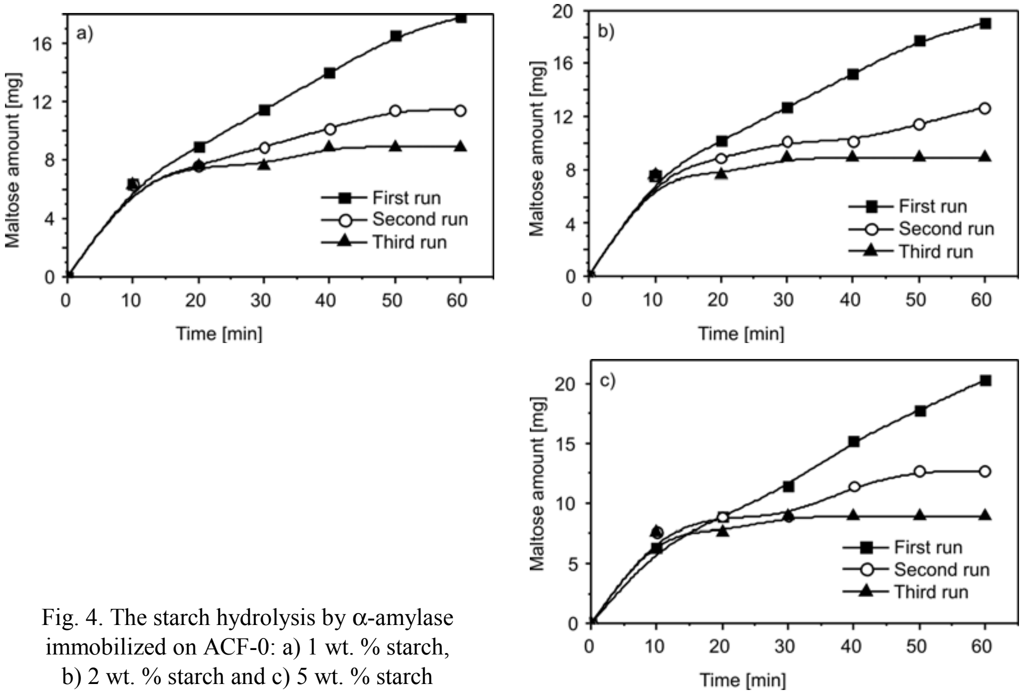

Fig. 4. The starch hydrolysis by α-amylase immobilized on ACF-0: a) 1 wt. % starch, b) 2 wt. % starch and c) 5 wt. % starch

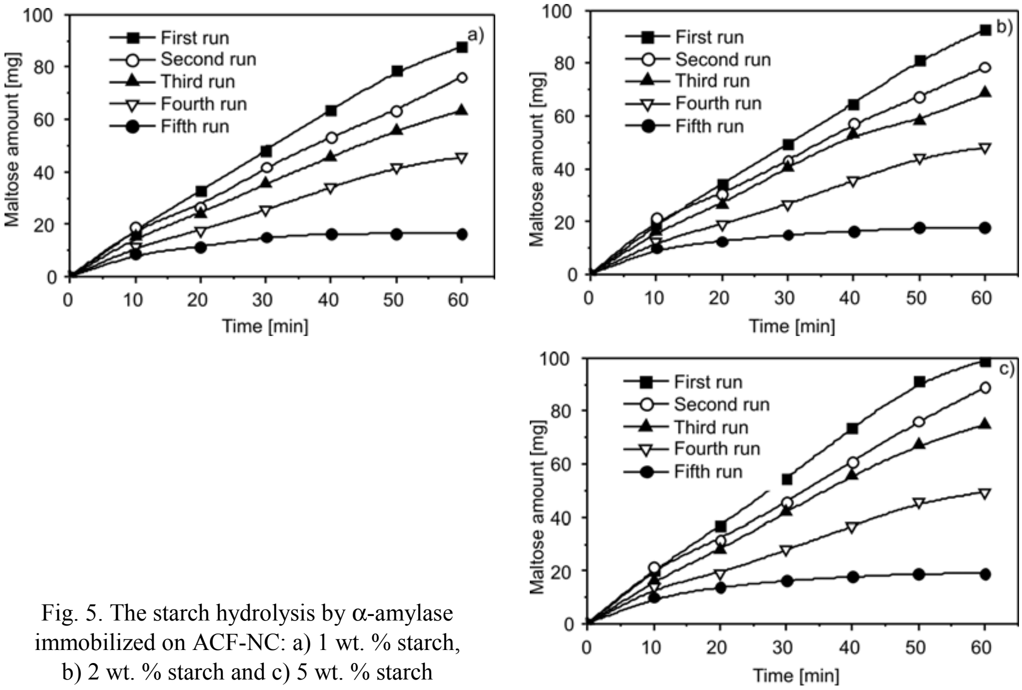

Fig. 5. The starch hydrolysis by α-amylase immobilized on ACF-NC: a) 1 wt. % starch, b) 2 wt. % starch and c) 5 wt. % starch

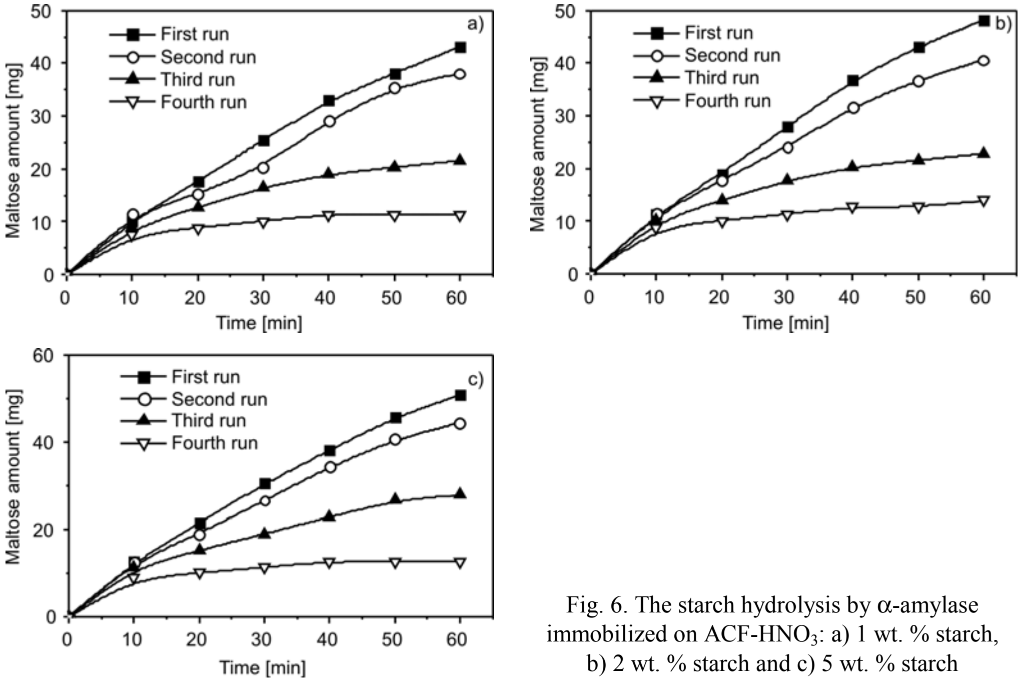

Fig. 6. The starch hydrolysis by α-amylase immobilized on ACF-HNO_3: a) 1 wt. % starch, b) 2 wt. % starch and c) 5 wt. % starch

The results of starch hydrolysis by immobilized α-amylase are shown in Figs. 4–6. The amount of maltose hydrolyzed by α-amylase immobilized on same ACF was independent of the starch concentration. Maltose was also hydrolyzed by α-amylase: the results show that if immobilization occurs on the same ACF, the quantities of hydrolyzed maltose and hydrolyzed starch remain the same. This suggested that the starch concentration was sufficient. The greater the quantity of amylase immobilized on ACF, the higher was the amount of hydrolyzed maltose. As for the ACF-0, the quantity of hydrolyzed maltose was 20 mg after 60 min for the first run; it decreased to 12 mg in the second run and to 8 mg in the third run. As for the ACF-NC, the amount of hydrolyzed maltose was 100 mg after 60 min for the first run; the adsorbed amylase maintained higher hydrolysis activity after three runs. Its activity decreased after a fourth run, and the maltose amount was then 50 mg. As for the ACF-NC, the amount of hydrolyzed maltose was 50 mg after 60 min for the first run; the adsorbed amylase maintained higher hydrolysis activity after two runs. Its activity decreased after 3 runs, and the maltose amount was then 20 mg.

The most important advantage of the immobilized enzyme was its reusability. The surface groups of activated carbon fibre also affected the desorption behaviour of α-amylase. Most of the α-amylase immobilized on ACF-0 would be desorbed during the hydrolysis, and the retained activity of α-amylase immobilized on ACF-0 was 10% after 2 runs. However, α-amylase immobilized on ACF-NC and ACF-HNO_3 exhibited more than 24% and 14% activity (relative to free α-amylase) after 4 runs and 3 runs, respectively. This indicated that there existed a strong interaction between α-amylase and the surface groups of ACF-NC and ACF-HNO_3.

4. Conclusion

Activated carbon fibre could be oxidized by nitric acid and nitrocellulose combustion to modify its surface chemical property. The carbon content of activated carbon fibre markedly decreased and the oxygen content significantly increased after oxidation. The hydrogen and nitrogen content also increased to a certain degree. The Boehm titration and FTIR results indicated that the oxidation with HNO_3 introduces a large number of carboxylic groups; while the nitrocellulose oxidation could form phenolic and basic groups (amide). The adsorption was increased 5 times and 3.5 times, respectively. Immobilized amylase showed higher hydrolysis activity for starch after 3 runs.

References

[1] RADOVIC L.R., MORENO-CASTILLA C., RIVERA-UTRILLA J., *Carbon Materials as Adsorbents in Aqueous Solutions*, [in:] L.R. Radovic (Ed.), *Chemistry and Physics of Carbon*, Marcel Dekker, New York, 2001, p. 227.
[2] TANG D.Y., ZHENG Z., LIN K., LUAN J.F., ZHANG J.B., J. Hazard. Mater., 143 (2007), 49.
[3] LEE Y.S., KIM Y.H., HONG J.S., SUH J.K., CHO G.J., Catal. Today., 120 (2007), 420.
[4] XU B., WU F., CHEN S., ZHANG C.Z., CAO G.P., YANG Y.S., Electrochim. Acta, 52 (2007), 4595.
[5] KIM B.K., RYU S.K., KIM B.J., PARK S.J., J. Colloid. Interf. Sci., 302 (2006), 695.
[6] ODA H., YAMASHITA A., MINOURA S., OKAMOTO M., MORIMOTO T., J. Power Sources, 158 (2006), 1510.
[7] EL-SAYED Y., BANDOSZ T.J., Langmuir, 21 (2005), 1282.
[8] SHIM J.W., PARK S.J., RYU S.K., Carbon, 39 (2001), 1635.
[9] SHEN W.Z., WANG H., GUO Q.J., LIU Y.H., ZHANG Y.L., Coll. Surf. A., 308 (2007), 20.
[10] Carbon Soc. Jap., Introduction of New Carbon Materials, Realize Inc. Press, 1996.
[11] BAJPAI A.K., BHANU S., Coll. Polym. Sci., 282 (2003), 76.
[12] TANYOLAC D., YURUKSOY B.I., OZDURAL A.R., Biochem. Eng. J., 2 (1998), 179.
[13] RESHMI R., SANJAY G., SUGUNAN S., Catal. Commun., 8 (2007), 393.
[14] RESHMI R., SANJAY G., SUGUNAN S., Catal. Commun., 7 (2006), 460.
[15] KAHRAMAN M.V., BAYRAMOGLU G., KAYAMAN-APOHAN N., GUNGOR A., Food Chem., 104 (2007), 1385.
[16] PANDYA P.H., JASRA R.V., NEWALKAR B.L., BHATT P.N., Micropor. Mesopor. Mater., 77 (2005), 67.
[17] BOEHM H.P., Carbon, 32 (1994), 759.
[18] BINIAK S., SZYMANSKI G., SIEDLEWSKI J., SWIATKOWSKI A., Carbon, 35 (1997), 1799.

Received 1 July 2008
Revised 30 October 2008

Materials Science-Poland, Vol. 27, No. 2, 2009

Hydrothermal synthesis of aqueous nano-TiO_2 sols

S. MAHATA, D. KUNDU[*]

Sol-Gel Division, Central Glass and Ceramic Research Institute,
196, Raja S. C. Mullick Road, Kolkata 700 032, India

A poorly crystalline nano-anatase precursor with the crystallite sizes of about 3.5 nm was prepared via reprecipitation of nano-anatase at pH = 7.0 from a highly transparent sol obtained by acidic peptization of hydrous titania precipitates, hydrolysed product of titanium isopropoxide. The weakly agglomerated nano-anatase precursor has been used for preparing well crystalline nano-TiO_2 sols by hydrothermal treatment at pH = 9.5 using a weak base, NH_4OH. The crystallite size gradually grew with increasing temperature and reached 7.6 nm (X-ray) at 175 °C after 4 h of hydrothermal treatment. The sizes of particles were mostly in the range 5–15 nm. The hydroxyl content in the nano-TiO_2 decreased with increasing hydrothermal temperature of treatment and supported a gradual growth of nano-TiO_2 as evident from the X-ray and TEM.

Key words: *nano-TiO_2 sol; peptization; hydrothermal treatment*

1. Introduction

Crystalline TiO_2 nanopowders find various photocatalytic applications [1–3]. Synthesis of TiO_2 powder via hydrothermal treatment of amorphous hydrous titania or its peptized sol (poorly crystalline) is a common approach. The literature mainly covers the formation of crystalline polymorphs under various experimental conditions [4–10]. On the contrary, very little attention has been paid to the *in situ* fabrication of aqueous nano-TiO_2 sol via a hydrothermal process [6] although it is known that handling of aqueous nano-TiO_2 sol will be much easier compared to dry nanopowder. An aqueous TiO_2 dispersion showed a maximum stability at pH = 10–11 where a maximum negative zeta potential was found indicating the maximum stability of the dispersion due to electrostatic repulsion [11]. *In situ* fabrication of nano-TiO_2 dispersion has been reported in basic solutions via hydrothermal treatment of poorly crystalline nano-TiO_2 sol obtained by peptization of amorphous hydrous titania by tetrabutylammonium hydroxide (TBNOH) [6].

---

[*] Corresponding author, e-mail: debtosh@cgcri.res.in

It has been shown that amorphous hydrous titania obtained by hydrolysis of titanium alkoxide in aqueous solution during peptization with either acids (HCl and HNO_3) or strong bases like tetraalkylammonium hydroxide (TANOH) transformed into titania sol containing poorly crystalline nano-TiO_2 particles [5]. Nano-TiO_2 obtained by acid peptization showed a relatively high degree of crystallinity compared to that obtained in the base petization process [5, 6]. The hydrothermal treatment of the peptized sols generates well crystalline nano-TiO_2 powders and the particle sizes of the hydrothermally treated nano-TiO_2 obtained from acid peptized sols were smaller than that obtained from base peptized ones [5]. Moreover, the application of the TBNOH peptized and hydrothermal sol for deposition of coatings may occlude TBN^+ which needs higher decomposition temperature for its removal as observed for the coprecipitation synthesis of $CoFe_2O_4$ [12]. In view of this, we report a hydrothermal synthesis of the *in situ* fabrication of aqueous nano-TiO_2 sol by separating poorly crystalline nano-TiO_2 from acid peptized sol and its subsequent hydrothermal treatment in basic solution using NH_4OH.

2. Experimental

Titanium isopropoxide (TTIP) technical grade (Sigma, Aldrich), 1-propanol (Qualigens, 99%), HNO_3 (69%, GR, Merck, India), ammonia solution (25%, GR, Merck, India) and distilled water were used for the preparation of nano-TiO_2 by the hydrothermal method. TTIP (0.5 M) solution in 1-propanol was prepared and to this solution distilled water was added under stirring keeping very high H_2O:TTIP mole ratio of 450. Hydrous titania precipitates were kept under stirring for 30 min and then filtered. The precipitate thus obtained was either directly treated hydrothermally in water or peptized with HNO_3 keeping the H^+/Ti mole ratio of 1.75 and wt. % TiO_2 of 0.5. The peptization of the resulted precipitate under stirring at room temperature generated a slightly bluish coloured transparent sol. pH of the sol was adjusted to 7.0 by adding 1 M NH_4OH under stirring and then the sol was filtered. The precipitate was then thoroughly washed with distilled water till the presence of NO_3^- ions in the filtrate was detected. The precipitate was then redispersed under stirring in aqueous solution of NH_4OH having the pH of 9.5 maintaining the wt. % equivalent TiO_2 of 0.5 and 2.0. The dispersion was kept overnight and finally pH was readjusted to 9.5 prior to hydrothermal treatment. All the hydrothermal treatment was carried out with ca. 420 g of suspension under stirring condition (400 rpm) in a 2 dm^3 Teflon lined autoclave under autogenic pressure. The heating rate of ca. 2 °C/min was used for achieving the final temperature of hydrothermal treatment and a natural cooling of the autoclave was maintained for all the experiments. Translucent titania sols were centrifuged at 8000 rpm. However, very little was found at the bottom. The sol was then kept at 50 °C in a Petri dish for drying. A thick paste was formed during drying and acetone was added to it followed by drying at 50 °C. It was then ground mildly in acetone and again dried at 50 °C. The process was repeated for 2–3 times and finally the dried powder was obtained.

X-ray diffraction (XRD) patterns of the powders were recorded with a Philips make diffractometer (Model: PW-1730). DTA and TGA of the powders were carried out using Shimadzu thermal analyzer (Models: DA-50 and TA-50). Transmission electron microscopic (TEM) measurements were carried out with a Jeol 2010 TEM. The samples for TEM study were prepared by adding a drop of diluted sols on carbon coated grids placed on tissue paper followed by drying at 50 °C.

3. Results and discussion

Hydrolysis rate of titanium alkoxide resulting in an amorphous powdery precipitate is very fast. However, the deliberate addition of water into alcoholic solution of titanium alkoxide generated various products depending on the amount of water, concentration of alkoxide and nature of alkyl group [13] indicating the extent of polymerization is different. The powdery precipitate obtained after hydrolysis of TTIP in the present study was X-ray amorphous. The hydrothermal treatment of the amorphous powder in distilled water showed the formation of mainly anatase with the presence of little amount of brookite (Fig. 1).

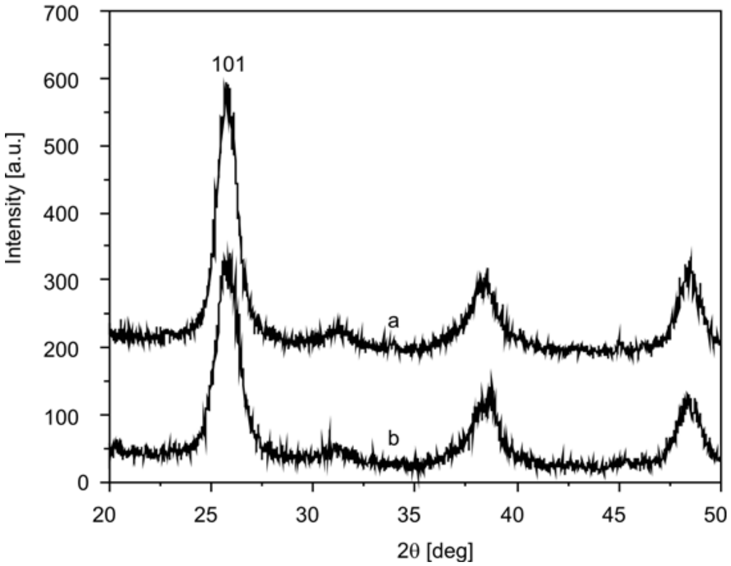

Fig. 1. X-ray diffraction patterns of the powders obtained after hydrothermal treatment of 0.5 wt. % slurry for 4 h at 175 °C (a) and 150 °C (b)

The particles were separated out from the mother liquid. As expected, higher temperature of hydrothermal treatment favours better crystallization. On the other hand, the amorphous precipitate under acid peptization at room temperature gradually converted to a slightly bluish coloured highly transparent sol indicating the formation of very small particles.

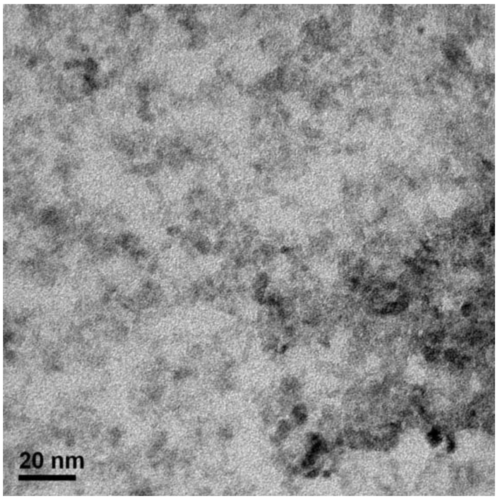

Fig. 2. TEM photograph of nano-TiO_2 present in a peptized sol

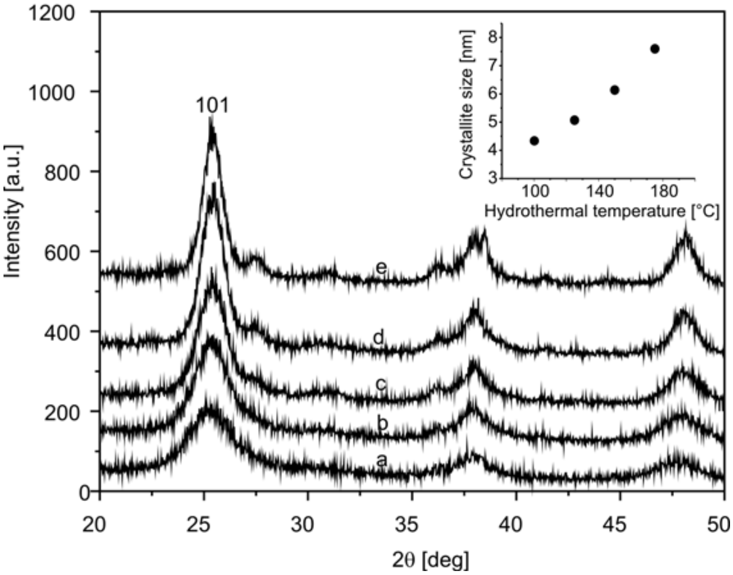

Fig. 3. X-ray diffraction patterns of the powders obtained from the 0.5 wt. % equivalent TiO_2 containing peptized sol (a) and after hydrothermal treatment of 0.5 wt. % equivalent TiO_2 containing suspension using reprecipitated anatase precursor at pH = 9.5 for 4 h at 100 °C (b), 125 °C (c), 150 °C (d) and 175 °C (e). Inset shows the corresponding crystallite size of hydrothermally treated samples

TEM photograph (Fig. 2) shows the formation of very small TiO_2 particles in the peptized sol. X-ray diffraction pattern of the powder obtained from the sol shows the formation of poorly crystalline nano-anatase (Fig. 3) with the particle size of about 3.5 nm as determined from Scherrer's equation. The formation of anatase and rutile during peptization of amorphous hydrous titania precipitate with H^+/Ti ratio of 1.0 and 4.0, respectively has been reported [4,14]. It is believed that during the peptization process the aggregated TiO_6 octahedra in the amorphous phase gradually break down via protonation of the –Ti–O–Ti– bonds. The protonated surface Ti–OH recombine with –OH groups of other TiO_6 octahedra to form –Ti–O–Ti– bridge bonds and the structural rearrangement causes transformation of amorphous to crystalline state. The structural rearrangement of the TiO_6 octahedra through edge sharing leads to formation of anatase from an amorphous phase under peptization with H^+/Ti mole ratio of 1.75. It is known that basic solution favours the formation of anatase through edge sharing of TiO_6 octahedra both in peptization as well as in hydrothermal processes [5]. It has been shown that the crystallization of TiO_2 from an amorphous precipitate during peptization was very poor in the case of basic peptization process (TBNOH and TENOH) compared to acid (HNO_3) peptization [5, 6]. Thus a relatively fine crystalline nano-anatase obtained by acid peptization is expected to produce fine crystalline nano-anatase at a relatively lower hydrothermal temperature under basic condition. The reprecipitation is expected to generate weakly agglomerated nano-anatase particles which were subsequently used as an intermediate precursor for hydrothermal treatment in basic aqueous medium for *in situ* fabrication of nano-TiO_2 sol.

Figure 3 shows the X-ray diffraction pattern of powders obtained after hydrothermal treatment at various temperatures. The increase of temperature is expected to increase crystallization. This is clearly evident from the diffraction patterns. Moreover, it is evident that increasing temperature favours the formation of small amounts of rutile along with major anatase phase. TiO_2 obtained at 100 °C was purely anatase. The rutile formation was started at 125 °C and the amount of rutile gradually increased with the increase of temperature of hydrothermal treatment. The formation of pure anatase at 200 °C under hydrothermal condition of the sol under basic solution (using TBNOH) has been reported [5]. However, the appearance of very slight amount of rutile along with the major anatase phase at 240 °C indicates that the higher temperature favours the formation of rutile [5]. The calculated crystallite size using Scherrer's equation gradually increases with increasing hydrothermal temperature as shown in the inset of Fig. 3. The crystallite size of nano-anatase obtained after hydrothermal treatment at 175 °C was about 7.6 nm whereas that of the nano-anatase present in the peptized sol was about 3.5 nm.

Figure 4 shows particle morphology of the nano-TiO_2 after hydrothermal treatment. It is clear from the TEM picture that well crystalline particles of the sizes mostly in the range of 5–15 nm have been formed and remained dispersed in the mother liquid as a translucent sol. Figure 5 shows the TGA of the samples hydrothermally treated at 100 °C and 175 °C for 4 h. The TG curves show a sharp weight loss up to about 130 °C and subsequent gradual weight loss up to 800 °C. The initial weight loss is due to the dehydration of adsorbed water. An endothermic peak observed at about

63 °C in the DTA supports the weight loss. The weight loss after about 450 °C is negligible. A similar result was observed for hydrothermally synthesized TiO_2 nanopowders from the amorphous hydrated titania obtained by hydrolysis of TTIP [7]. It has been observed that a higher weight loss in the temperature range 130°–450 °C for 100 °C sample (5.06%) compared to 175 °C sample (3.7%) indicates the presence of high amounts of Ti–OH in 100 °C hydrothermally treated sample. The better crystallization at higher temperature as evident from X-ray results supports the decreased weight loss due to Ti–OH.

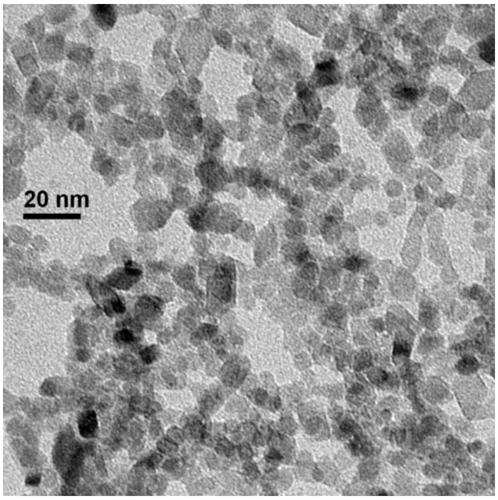

Fig. 4. TEM photograph of nano-TiO_2 present in the sol obtained after hydrothermal treatment of 0.5 wt. % equivalent TiO_2 containing slurry using reprecipitated anatase precursor at pH = 9.5 for 4 h at 175 °C

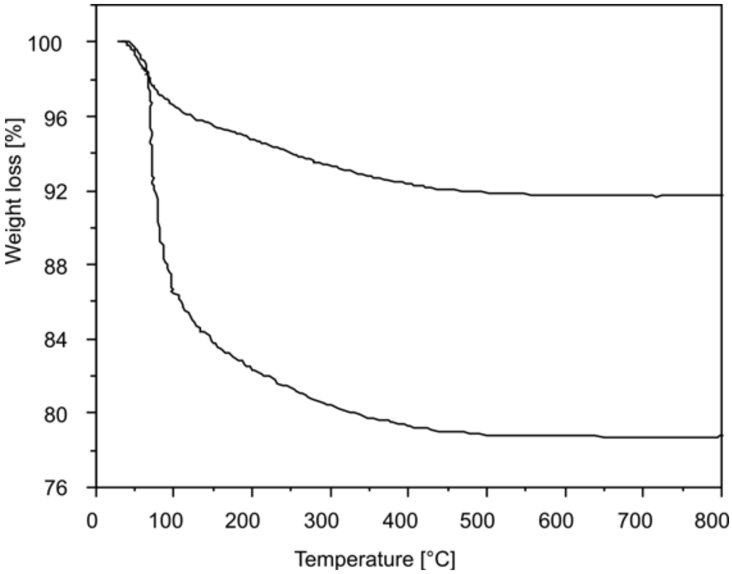

Fig. 5. TGA of TiO_2 powders obtained after hydrothermal treatment at 175 °C (top) and 100 °C (bottom) for 4 h

It has been shown by Chen et al. that the optical absorbance of TiO_2 dispersion in aqueous solution showed a maximum value in the pH range of 10–11 while a maximum negative zeta potential was found in this pH range [11]. This clearly suggests the maximum stability of the dispersion in this pH range due to a very strong electrostatic repulsive force. The optical absorbance in the acidic solution (pH from 2 to 6) was very low, indicating the instability of the TiO_2 dispersion though the zeta potential was negative ($pH > 4$) and positive ($pH < 4$). A similar hydrothermal result of TBNOH peptized titania sol was reported by Yung et al. [6] and explained based on a strong electrostatic repulsive force due to large negative zeta potential ($pH = 10$). Weakly agglomerated nanoanatase as a precursor and the development of a strong electrostatic repulsive force among the nano-TiO_2 particles were probably responsible for the *in situ* fabrication of nano-TiO_2 sol via hydrothermal treatment of the suspension at $pH = 9.5$ in the present study.

The increase of wt. % equivalent TiO_2 from 0.5 wt. % to 2 wt. % in the suspension for hydrothermal treatment also produces nano-TiO_2 sol. The calculated crystallite size was about 7.4 nm which is almost the same as observed in case 0.5 wt. % TiO_2 containing sol indicating that growth is almost independent of the concentration of TiO_2 at least in the present investigation. Thus weakly agglomerated nano-anatase precursor obtained by reprecipitation of the acidic peptized sol and subsequent hydrothermal treatment at $pH = 9.5$ using NH_4OH was found to be suitable for the fabrication of nano-TiO_2 sol. These sols may be suitable for the deposition of crystalline TiO_2 coatings at low temperatures as ammonia can be removed easily.

4. Summary

Aqueous poorly crystalline nano-anatase sols have been prepared via peptization in acidic medium of the amorphous hydrous titania precipitate obtained by hydrolysis of titanium isopropoxide. The nano-anatase thus produced has been reprecipitated at $pH = 7$ and used as intermediate precursor for *in situ* fabrication of well crystalline nano-TiO_2 sols in the basic solution (9.5) using a weak base, NH_4OH under hydrothermal. The hydrothermal treatment of the basic aqueous suspension of weakly agglomerated nano-anatase showed the formation of nano-TiO_2 sol. A gradual growth of nano-anatase with increasing hydrothermal temperature has been observed. The sol contains well crystalline nano-TiO_2 particles having the size mostly in the range 5-15 nm after hydrothermal treatment at 175 °C for 4 h. The weakly agglomerated nanoanatase as precursor and the development of strong electrostatic repulsive force among the nano-TiO_2 powders were responsible for the *in situ* fabrication of nano-TiO_2 sol via hydrothermal treatment. The reprecipitation of the poorly crystalline nano-TiO_2 sol generates an intermediate precursor which is suitable for the hydrothermal preparation of well crystalline aqueous nano-TiO_2 sol at $pH = 9.5$ using NH_4OH.

Acknowledgement

Financial support from the Department of Science and Technology (DST, SERC), Govt. of India in the form of a project (No. SR/S3/ME/06/2002-SERC-Engg) is thankfully acknowledged. The authors are grateful to Dr. H. S. Maiti, Director of the Central Glass and Ceramic Research Institute for his constant encouragement.

References

[1] RINCON A.G., PULGARIN C., Appl. Catal. B: Environmental, 51 (2004), 283.
[2] SO C.M., CHENG M.Y., YU J.C., WONG P.K., Chemosphere, 46 (2002), 905.
[3] MATTHEWS R.W., J. Catal., 122 (1988), 549.
[4] ARUNA S.T., TIROSH S., ZABAN A., J. Mater. Chem., 10 (2000), 2388.
[5] YANG J., MEI S., FERREIRA J.M.F., J. Amer. Ceram. Soc., 83 (2000), 1361.
[6] YANG J., MEI S., FERREIRA J.M.F., J. Mater. Res., 17 (2002), 2197.
[7] HAYASHI H., TORII K., J. Mater. Chem., 12 (2002), 3671.
[8] KOLEN'KO Y.V., BURUKHIN A.A., CHURAGULOV B.R., OLEYNIKOV N.N., Mater. Lett., 57 (2003), 1124.
[9] BACSA R.R., GRATZEL M.L., J. Amer. Ceram. Soc., 79 (1996), 2185.
[10] ERDURAL B.K., YURUM A., BAKIR U., KARAKUS G., J. Nanosci. Nanotechnol., 8 (2008), 878.
[11] CHEN X., CHENG H., MA J., Powder Technol., 99 (1998), 171.
[12] PAIKE V.V., NIPHADKAR P.S., BOKADE V.V., JOSHI P.N., J. Amer. Ceram. Soc., 90 (2007), 3009.
[13] YOLDAS B.E., J. Mater. Sci., 21 (1986), 1087.
[14] ZHANG R., GAO L., Mater. Res. Bull., 36 (2001), 1957.

Received 14 July 2008

Materials Science-Poland, Vol. 27, No. 2, 2009

Room-temperature ferromagnetism in Fe-doped $Na_{0.5}Bi_{0.5}TiO_3$ crystals

Y. WANG[1], G. XU[1], L. YANG[2], Z. REN[1],
X. WEI[1], W. WENG[1], P. DU[1], G. SHEN[1], G. HAN[1*]

[1]State Key Laboratory of Silicon Materials, Department of Materials Science and Engineering,
Zhejiang University, Hangzhou 310027, PR China

[2]Shandong Research and Design Institute of Industrial Ceramics, Zibo 255031, PR China

Fe-doped $Na_{0.5}Bi_{0.5}TiO_3$ crystals were synthesized and studied by X-ray diffraction, X-ray spectroscopy, scanning electron microscopy, high-resolution transmission electron microscopy, and magnetic property measurement system. Room-temperature ferromagnetism was observed in Fe-doped $Na_{0.5}Bi_{0.5}TiO_3$ crystals. It was found that the magnetism of $Na_{0.5}Bi_{0.5}TiO_3$ crystals can be controlled by the Fe dopant concentration. The magnetism of the Fe-doped $Na_{0.5}Bi_{0.5}TiO_3$ crystals develops from diamagnetism to ferromagnetism and paramagnetism on increasing the Fe doping concentration from 0 to 10 mol %. The results presented in this study may provide new insights to the problem of synthesizing more single-phase multiferroic materials which will hopefully lead to rich and fascinating fundamental physics.

Key words: *ferroelectrics; magnetic materials; Fe-doped $Na_{0.5}Bi_{0.5}TiO_3$ crystals*

1. Introduction

A new class of materials, in which both electrical and magnetic ordering can coexist, the so-called multiferroic materials have many potential applications including a new type of memory devices based on the combination of ferromagnetism and ferroelectricity [1, 2]. Despite recent surge of worldwide interest in multiferroic materials, very few such materials exist in nature, or have been synthesized in the laboratory [3–5] because the usual atomic-level mechanisms driving ferromagnetism and ferroelectricity are mutually exclusive [6]. Therefore, it has been considered a major challenge to synthesize more multiferroic materials possessing both ferroelectric and ferromagnetic properties at room temperature [7].

It is well known that semiconductors have been successfully converted into diluted magnetic semiconductors [8] (DMS) by doping with transition-metal elements

---

[*] Corresponding author, e-mail: hgr@zju.edu.cn

(Fe, Ni, Co, etc.), and DMS have been considered as key functional components of many spin-based semiconductor devices [9, 10]. The method to obtain room temperature ferromagnetism by doping semiconductors with transition metal atoms (Fe, Co, Ni, etc.) has offered an alternative approach to achieve room temperature ferromagnetism in ferroelectric materials. For instance, the ferromagnetism in $PbTiO_3$ doped with Fe and Mn has been studied [11, 12]. Our group has successfully synthesized a Fe-doped $PbTiO_3$ ferroelectric material showing ferromagnetism at room temperature [13]. Bismuth sodium titanate $Na_{0.5}Bi_{0.5}TiO_3$ (abbreviated to NBT) has been considered to be an excellent candidate as a key material of lead-free ferroelectric materials [14, 15], and here we report that the room-temperature ferromagnetism is also observed in Fe-doped $Na_{0.5}Bi_{0.5}TiO_3$ crystals. The Fe doping concentration was defined as the molar ratio of Fe/ (Fe+Ti) in the form of Fe^{3+} ions.

2. Experimental

The chemical reagents were bismuth nitrate ($Bi(NO_3)_3{\cdot}5H_2O$), titanium(IV) sulfate [$Ti(SO_4)_2$], iron nitrate [$Fe(NO_3)_3{\cdot}9H_2O$] and sodium hydroxide (NaOH). All the chemicals were analytical grade purity and were used as-received without further purification.

The hydrothermal process included the following steps: 0.005 mol of $Bi(NO_3)_3$, 0.01 mol of $Ti(SO_4)_2$, and an appropriate amount of $Fe(NO_3)_3$ were dissolved in 30 cm^3 of diluted HNO_3 (10%) to form aqueous solutions. Then, NaOH solution was slowly added to the above solution to coprecipitate Ti^{4+}, Bi^{3+} and Ni^{2+} ions by constant stirring. The precipitate was filtered, and washed with distilled water to remove NO_3^-, SO_4^{2-} and Na^+ ions. Then, the precipitate was mixed with 6 M NaOH solution under constant magnetic stirring for 5 min. The suspension solution was poured into a stainless-steel Teflon-lined autoclave for hydrothermal treatment. The autoclave was sealed and maintained at 200 °C for 12 h. Finally, it was cooled down to room temperature. The obtained products were filtered, washed several times with distilled water and absolute ethanol, and then dried at 90 °C for 4 h for characterization.

X-ray diffraction was performed on an ARL XTRA X-ray diffractometer with high-intensity CuK_α radiation. The EDS spectroscopy pattern was performed on an X-ray energy dispersion spectrometer (GENENIS4000). Scanning electron microscope (SEM) images were obtained from a HITACHI S-4800 device. Magnetic measurement was carried out using a quantum design superconducting quantum interference device (SQUID, MPMS XL-5).

3. Results and discussion

Figure 1a shows the X-ray diffraction patterns of the Fe-doped $Na_{0.5}Bi_{0.5}TiO_3$ samples with various Fe doping concentrations. All XRD patterns can be indexed to a pure phase of well-crystallized $Na_{0.5}Bi_{0.5}TiO_3$ with a perovskite structure, suggesting that doping of Fe ions up to 10% did not introduce any impurity phase to the system.

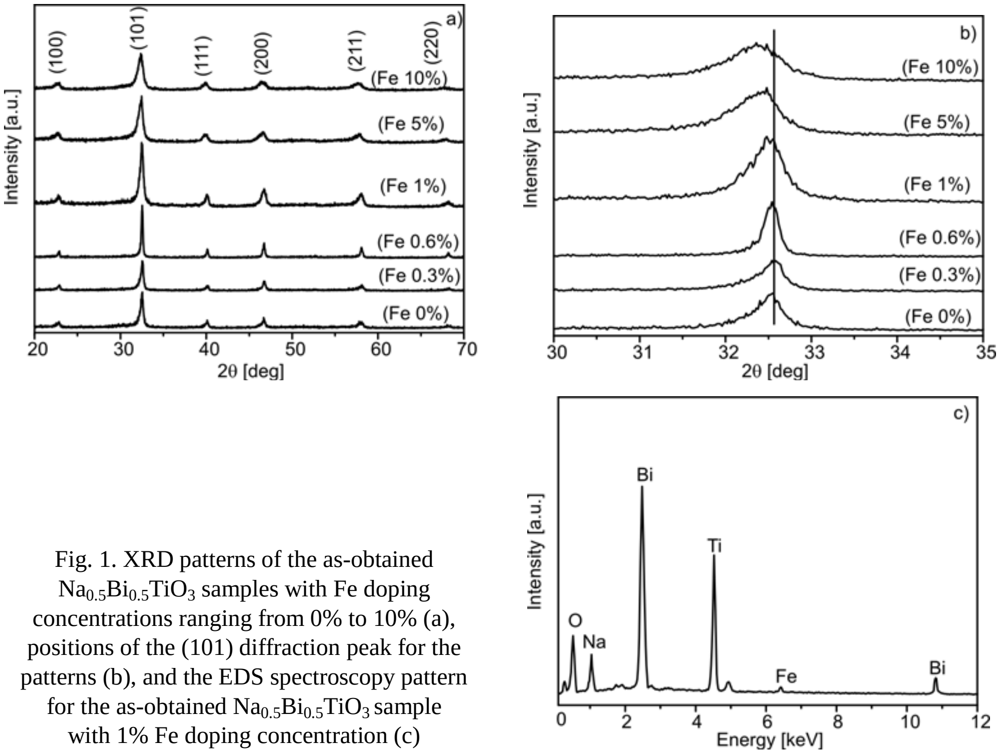

Fig. 1. XRD patterns of the as-obtained $Na_{0.5}Bi_{0.5}TiO_3$ samples with Fe doping concentrations ranging from 0% to 10% (a), positions of the (101) diffraction peak for the patterns (b), and the EDS spectroscopy pattern for the as-obtained $Na_{0.5}Bi_{0.5}TiO_3$ sample with 1% Fe doping concentration (c)

Fe doping does not affect the crystalline structure of the parent compound NBT which is important for preserving the ferroelectric properties in Fe-doped $Na_{0.5}Bi_{0.5}TiO_3$. An enlarged comparison of the location of (101) diffraction peaks in the range of 30°–35° (Fig. 1b) shows that the peak position of the sample slightly shifts toward a lower 2θ value in the case of the Fe doping, indicating that the lattice parameter a of $Na_{0.5}Bi_{0.5}TiO_3$ is enlarged, due to the larger radius of Fe^{3+} cations with respect to Ti^{4+} cations. Energy dispersive X-ray (EDS) patterns obtained from the prepared samples (Fe 1%) clearly show the existence of Fe in the obtained samples (Fig. 1c). Therefore, according to the above results, it is reasonable to conclude that the doped Fe ions had been effectively incorporated into the crystal structure of $Na_{0.5}Bi_{0.5}TiO_3$.

In Figure 2, the magnetizations of the as-prepared Fe-doped $Na_{0.5}Bi_{0.5}TiO_3$ samples at room temperature are shown. The dependence of magnetization of pure $Na_{0.5}Bi_{0.5}TiO_3$ phase is an anti-S type curve, suggesting its intrinsic diamagnetism. When the Fe doping is at the level as low as 0.3%, there is no obvious difference in the curve. As the concentration of doped Fe approaches 0.6%, the curve gradually transits into a weak S-type hysteresis, indicating the emergence of ferromagnetic long-range ordering in Fe-doped $Na_{0.5}Bi_{0.5}TiO_3$. Remarkably, a typical hysteresis for ferromagnetic materials is observed with Ms ~ 0.005emu/g (ca. $0.05u_B$/Fe) and the coercive field of ca. 100 Oe, indicating that the Fe-doped $Na_{0.5}Bi_{0.5}TiO_3$ (1% doping concentration) samples do become ferromagnetic even at room temperature. By increasing the doping concentration of Fe from 1% to 10% in $Na_{0.5}Bi_{0.5}TiO_3$, the paramagnetic component becomes strong. The linearization in *M–H* curves gradually increases, and the variation trend of the curves is similar to that of Fe-doped $PbTiO_3$ and Mn-doped ZnO [13, 16]. It could be attributed to the competition between ferromagnetic and paramagnetic contributions to the magnetism of the samples.

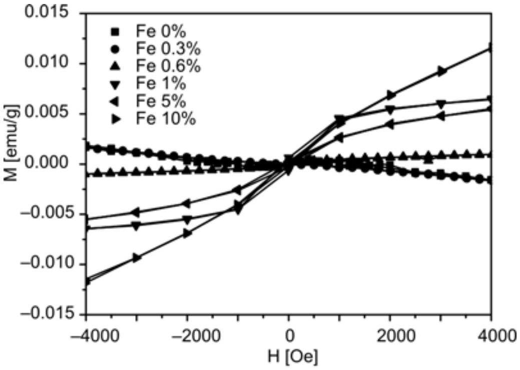

Fig. 2. *M–H* curve of the as-obtained $Na_{0.5}Bi_{0.5}TiO_3$ samples with Fe doping concentration ranging from 0% to 10% at room temperature

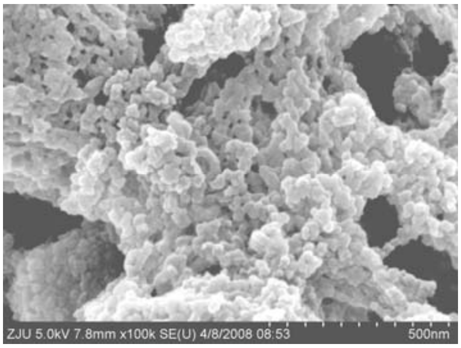

Fig. 3. SEM image of the Fe-doped $Na_{0.5}Bi_{0.5}TiO_3$ crystals with 1% Fe doping concentration

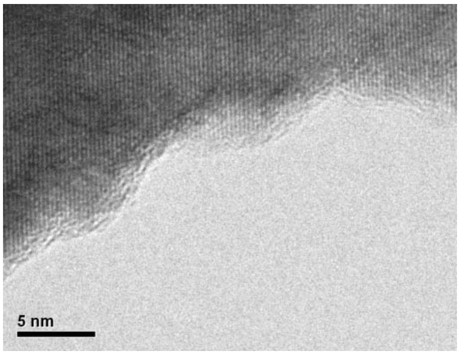

Fig. 4. High-resolution TEM image of Fe-doped $Na_{0.5}Bi_{0.5}TiO_3$ crystals with 1% Fe doping concentration

As shown in Fig. 2a, pure $Na_{0.5}Bi_{0.5}TiO_3$ shows diamagnetism, doping with Fe is the cause of its ferromagnetism (in the case of 1% concentration). One should carefully consider the possibility that secondary phase formation is possible. Although a secondary phase was not detectable in our XRD, it might exist in the samples. Firstly, one can consider what known ferromagnetic impurity phases are possible. A metallic Fe cluster is ferromagnetic at room temperature, but it is impossible for it to form in the the process under consideration here. Moreover, nearly all of the possible Fe-based oxides are antiferromagnetic, such as FeO and Fe_2O_3. The exception to this is Fe_3O_4. However, even if Fe_3O_4 were responsible for the ferromagnetic behaviour, a further increase up to 10% in the Fe doping concentration would presumably enhance the corresponding ferromagnetism. Instead, the opposite behavior is observed. Therefore, the observed ferromagnetism is considered to be an intrinsic property of Fe-doped $Na_{0.5}Bi_{0.5}TiO_3$. As shown in Figs. 3, 4, in SEM and high-resolution TEM images of the Fe-doped $Na_{0.5}Bi_{0.5}TiO_3$ no elemental Fe or Fe-contained nanoparticles or clusters can be found, confirming that Fe ions had been doped into the $Na_{0.5}Bi_{0.5}TiO_3$ lattice.

An *F*-center exchange (FCE) mechanism can be employed to explain the ferromagnetism in Fe-doped $Na_{0.5}Bi_{0.5}TiO_3$ crystals, proposed by Coey et al. in the case of Fe-doped SnO_2 thin films [17]. In addition, Fe^{3+} ion is paramagnetic. Thus, the competition between ferromagnetic and paramagnetic components will lead to the observed variations in Fig.2.

4. Conclusions

Room-temperature ferromagnetism was successfully observed in Fe-doped $Na_{0.5}Bi_{0.5}TiO_3$ crystals. The magnetism of Fe-doped $Na_{0.5}Bi_{0.5}TiO_3$ crystals can be controlled by the Fe doping concentration, exhibiting diamagnetism, ferromagnetism, and paramagnetism. The results presented in this study may provide new insights into the problem of synthesizing more single-phase multiferroic materials, which will hopefully lead to rich and fascinating fundamental physics.

Acknowledgement

This work was supported by the National Science Foundation of China (No. 50452003).

References

[1] Hur N., Park S., Sharma P.A., Ahn J.S., Guha S.S., Cheong S.W., Nature, 429 (2004), 392.
[2] Kimura T., Kawamoto S., Yamada I., Azuma M., Takano M., Tokura Y., Phys. Rev. B., 67 (2003), 180401.
[3] Aken B.B.V., Palstra T.T.M., Filippetti A., Spaldin N.A., Nat. Mater., 3 (2004), 164.
[4] Kimura T., Goto T., Shintani H., Ishizaka K., Arima T., Tokura Y., Nature, 426 (2003), 55.
[5] Fiebig M., Lottermoser T., Fröhlich D., Goltsev A.V., Pisarev R.V., Nature, 419 (2002), 818.
[6] Spaldin N.A., Fiebig M., Science, 309 (2005), 391.
[7] Eerenstein W., Mathur N.C., Scott J.F., Nature, 442 (2006), 759.
[8] Ohno H., Science, 281 (1998), 951.
[9] Wolf S.A., Awschalom D.D., Buhrman R.A., M.Daughton J., Molnar S., Roukes M.L., Science, 294 (2001), 1488.
[10] Ohno H., Chiba D., Matsukura F., Omlya T., Abe E., Dietl T., Ohno Y., Nature, 408 (2000), 944.
[11] Stoupin S., Chattopadhyay S., Bolin T., Segre C.U., Solid State Commun., 144 (2007),46.
[12] Palkar V.R., Malik S.K., Solid State Commun., 134 (2005), 783.

[13] REN Z.H., XU G., WEI X., HOU X.H., LIU Y., SHEN G., Appl. Phys. Lett., 91 (2007), 063106.
[14] HERABUT A., DAFAN A., J. Am. Ceram. Soc., 80 (1997), 2954.
[15] HAGIYEV M.S., ISMAIZADE I.H., ABIYEV A.K., Ferroelectrics, 56 (1984), 215.
[16] RAMACHANDRAN S., NARAYAN J., PRATER J.T., Appl. Phys. Lett., 88 (2006), 242503.
[17] COEY J.M.D., DOUVALIS A.P., FITZGERALD C.B., VENKATESAN M., Appl. Phys. Lett., 84 (2004), 1332.

Received 19 July 2008
Revised 30 October 2008

Materials Science-Poland, Vol. 27, No. 2, 2009

Controllable synthesis of ZnO nanostructures by a simple solution route

J. WANG[1,2*], S. HE[1], S. ZHANG[1], Z. LI[1], P. YANG[1], X. JING[1], M. ZHANG[1], Z. JIANG[2]

[1]College of Material Science and Chemical Engineering,
Harbin Engineering University, Harbin 150001, P R China

[2]College of Chemical Engineering, Harbin Institute of Technology, Harbin 150001, P.R. China

Flower-shaped ZnO nanostructures, composed of ZnO nanorods, and sphere-shaped ZnO nanoclusters, composed of ZnO nanosheets, were synthesized by reacting zinc acetate dehydrate with sodium hydroxide and polyethylene glycol-20000 (PEG-20000) at 180 °C for 4 h in solution. The thickness of individual nanosheets is about 40–60 nm. The nanorods are of hexagonal shape with sharp tips, and have basic diameters of ca. 450–550 nm. The ZnO nanostructures were characterized by scanning electron microscropy, transmission electron microscopy, X-ray diffraction, Fourier transform infrared, and Raman scattering measurements. The results demonstrated that the synthesized products are single crystalline with wurtzite hexagonal phase, the sphere-shaped ZnO grew in the [100] direction and the flower-shaped ZnO grew in the [001] direction.

Key words: *nanostructure; zinc oxide; optical properties; self-assembly*

1. Introduction

Controllable synthesis of semiconductors with nanostructures in terms of size and shape has been strongly motivated as their properties can be tailored by shape and size and novel applications can be investigated dependent on their structural properties [1–4]. Among various semiconductor nanostructures, a variety of ZnO nanostructures have been investigated, showing them to be one of the richest families of nanostructures [5]. ZnO is a key technological material that finds uses in a large number of applications in nanoelectronics, piezoelectric devices, optoelectronics, chemical sensors. ZnO has three key advantages. First, ZnO is a semiconductor with a direct wide band gap of 3.37 eV and a large exciton binding energy (60 eV). Second, because of its noncentral symmetry (wurtzite structure), ZnO is highly piezoelectric, which is a key property in building electromechanically coupled sensors and transducers. Finally, ZnO is a bio-safe and biocompatible material, and hence can be used for biomedical applications.

---

[*]Corresponding author, junwang@hrbeu.edu.cn

A variety of ZnO nanostructures have been reported in the literature, for instance, nanowires [6, 7], nanorods [8, 9], nanobelts [10], nanotubes [11], hexagonal nanocolumns [12], nanobows, nanorings, nanosprings [13, 14], nanostars [15], nanoflowers [16], microspheres and cages [17], aligned nanonails and nanopencils [18], nanosheet networks and hexagonal nanodisks [19]. In this study, we investigated a controllable synthesis of single-crystalline sphere-shaped ZnO and flower-shaped ZnO by a simple solution route.

2. Experimental

Zinc acetate dihydrate, sodium hydroxide and PEG-20000 were used as the source materials for the synthesis of ZnO, which was carried out at 180 °C in solution. All of the chemicals were purchased from the Tian Jin City Tian Xin Refined Chemical Corporation and used without further purification. Equivalent volumes of zinc acetate dihydrate (0.5 M) and sodium hydroxide (5 M) were mixed to obtain solution A. 1 g of PEG-20000 was dissolved in 4 ml of water by sonication to obtain solution B which was then added to 5 cm^3 of solution A to obtain solution C. 55 cm^3 of distilled water was added to solution C under stirring at room temperature to obtain solution D, Solution D was divided into two portions, and poured into Teflon tubes A and B, respectively. The Teflon tube A was immediately transferred to a Teflon-lined stainless steel autoclave, which was then heated at 180 °C for 4 h in an electric oven. The Teflon tube B was first kept at room temperature for 12 h, and then transferred to a Teflon-lined stainless steel autoclave, which was then heated at 180 °C for 4 h in an electric oven. ZnO crystalline powders were separated from the solution by filtration, washed with distilled water and dried. The ZnO samples obtained from tubes A and B were labelled A_1 and A_2, respectively.

General morphologies were identified using scanning electron microscopy (SEM). The SEM samples were made by dipping a copper grid into the suspension of ZnO powder in ethanol and dried at room temperature. The structure and crystal phases were determined by an X-ray powder diffractometry (XRD) with CuK_α radiation ($\lambda = 1.54178$ Å), with the Bragg angle ranging from 20° to 80°. The quality and composition of the synthesized sphere-shaped ZnO nanostructures were characterized by the Fourier transform infrared (FTIR) spectroscopy in the range of 400–4000 cm^{-1}. Optical properties were analyzed by the Raman scattering.

3. Results and discussion

3.1. Structural characterization of the sphere-shaped ZnO nanostructures

Figure 1 shows general scanning electron morphologies of synthesized samples. Figures 1a, b show the low magnification SEM images and Fig. 1c presents the high magnification images of the grown products of A_1. The images clearly show the flower-shaped structures that are composed of hexagonal nanorods. The magnified image shows that flower-shaped structures are composed of hundreds of nanorods in the range of 450–550 nm with the length of 2–4 µm.

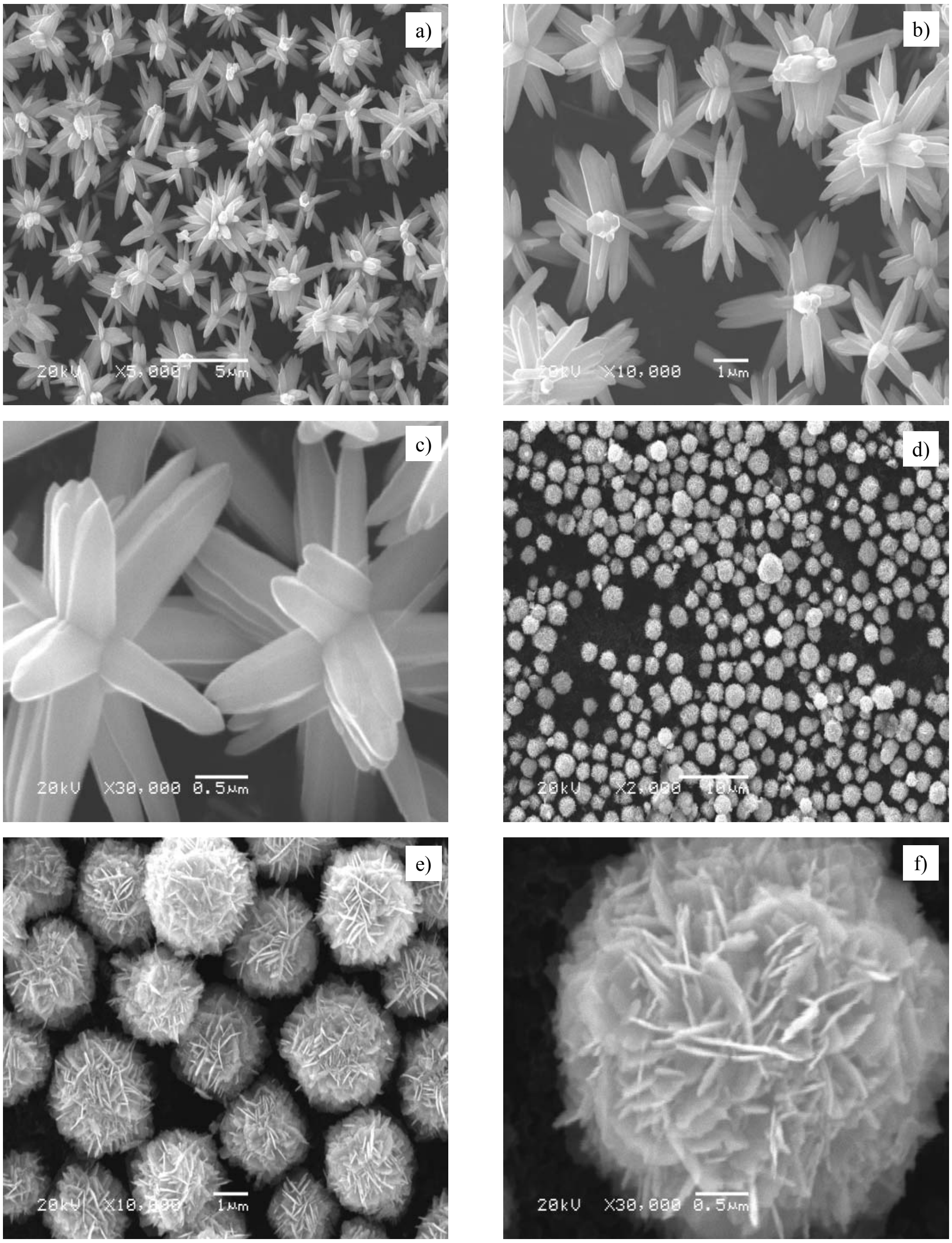

Fig. 1. SEM images of ZnO: a) overall product morphology of A_1, b) detailed views on average sized flowers of A_1, c) detailed view on an individual flower of A_1, d) overall product morphology of A_2, e) detailed views on average sized spheres of A_2, f) detailed view on an individual sphere of A_2

All the nanorods are seen to have originated from a single centre exhibiting flower-shaped morphologies. Figures 1d, e show low magnification SEM images, and Fig. 1f shows high magnification images of the grown products of A_2. The images clearly revealed that the sphere-shaped structures are formed by the accumulation of several hundred ZnO nanosheets. The size of each full array of a sphere-like structure is in the range of 3–4 µm.

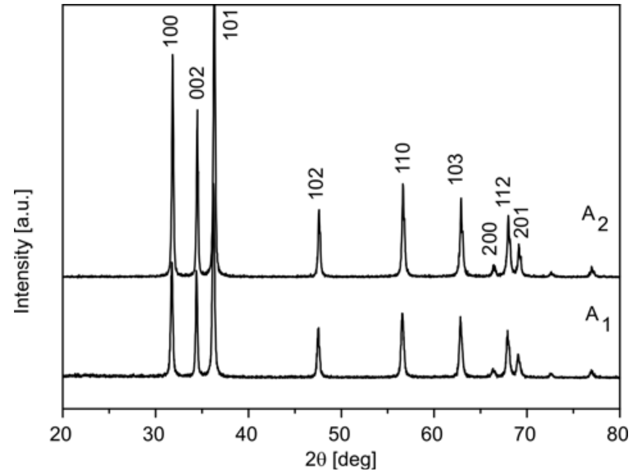

Fig. 2. Typical XRD pattern of the synthesized nanostructure: the indexed peaks correspond to the wurtzite hexagonal phase

Figure 2 presents the X-ray diffraction pattern of the synthesized powder. All of the indexed peaks are well matched with the bulk ZnO which confirmed that both A_1 and A_2 have wurtzite hexagonal structures. No other peaks related to impurities were detected in the spectra within the detection limit, which indicated that the synthesized powders are pure ZnO.

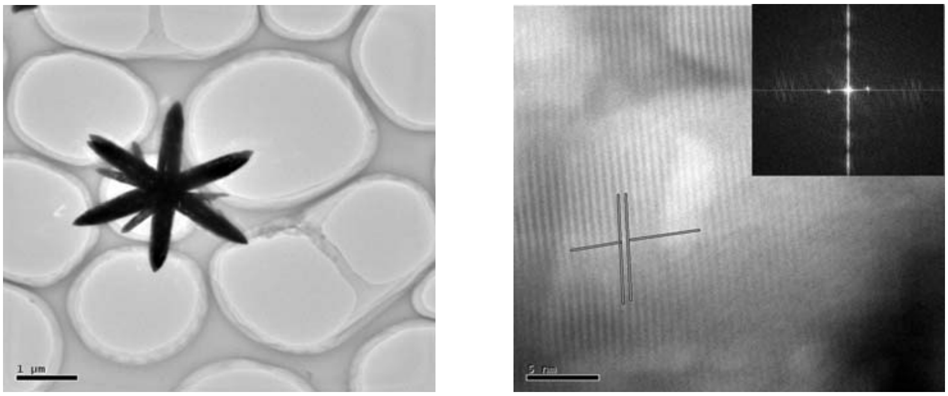

Fig. 3. Low magnification TEM image of the grown ZnO nanorods (a), HRTEM image showing the difference between two lattice fringes (b), being ca. 0.281 nm. The corresponding FT pattern (inset) is consistent with the HRTEM observation

Figure 3a shows a low magnification TEM image of the ZnO nanorods grown in the flower-shaped structures. The presence of ZnO nanorods is clearly evident from this image. The corresponding FFT pattern obtained from the shown nanorods confirmed that the synthesized products grew in the [001] direction. Figure 3b shows the HRTEM image of a nanorod. The lattice fringes between two adjacent planes is about 0.52 nm, being equal to the lattice constant of the ZnO, further indicating that the obtained structure is a wurtzite hexagonal phase and predominantly grown along the *c*-axis [001]. The corresponding FFT pattern (inset in Fig. 3b) is consistent with the HRTEM observation [20].

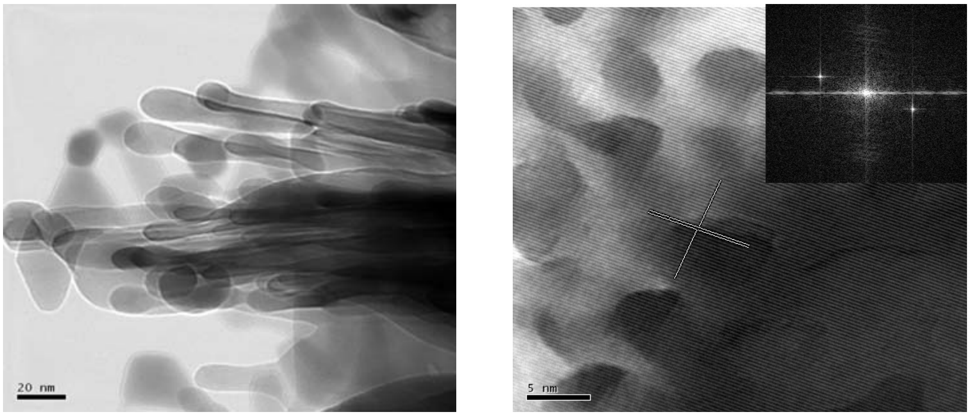

Fig. 4. Low magnification TEM image of the grown ZnO nanosheets (a) and HRTEM image showing the difference between two lattice fringes (b), which is about 0.281 nm. Corresponding FT pattern (inset) is consistent with the HRTEM observation

Figure 4a shows a low magnification TEM image of the ZnO nanosheets grown in the sphere-shaped structures. The ZnO nanosheets are clearly evident from this image. The corresponding FFT pattern obtained from the shown nanosheets confirmed that the synthesized products are single crystalline and grew in the [100] direction. Figure 4b shows a high resolution transmission electron microscopy (HRTEM) image of a nanosheet. The lattice fringe between two adjacent planes is about 0.28 nm, which is equal to the lattice constant of ZnO, indicating that the obtained structure has a wurtzite hexagonal phase and is predominantly grown in the *a* axis [100] direction. The corresponding FFT pattern (inset in Fig. 4b) is consistent with the HRTEM observation.

The composition and quality of the product was analyzed by the IR spectroscopy. Figure 5 (lower curve) shows the IR spectrum of A_1 in the range of 400–4000 cm^{-1}. The band at 571 cm^{-1} is correlated with zinc oxide [21]. The bands at 3200–3600 cm^{-1} correspond to the O–H vibration and the stretching vibration of C=O is observed at 1430 cm^{-1}. The IR spectrum of A_2 in the range of 400–4000 cm^{-1} is also shown in Fig. 5 (upper curve). The band at 560 cm^{-1} is correlated with zinc oxide. The bands at 3200–3600 cm^{-1} correspond to the O–H vibration and the stretching vibration of C=O is observed at 1437 cm^{-1}.

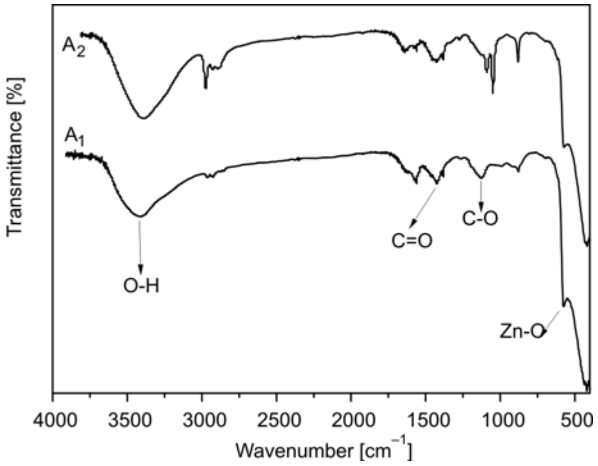

Fig. 5. Typical IR spectra of the synthesized nanostructures

3.2. Optical properties of the sphere-shaped ZnO nanostructures

The optical properties of the synthesized sphere-shaped ZnO nanostructure were investigated by Raman scattering. The Raman spectra are sensitive to the crystal quality, structural defects and disorders of the grown products. With the wurtzite hexagonal structure, ZnO belongs to the C_{6V}^{4} with two formula units per a primitive cell. The primitive cell includes two formula units in which all the atoms occupy the 2b sites of the C_{3V} symmetry. The group theory predicts, the existence of the following optical modes at the Γ point of the Brillouin zone: $\Gamma = A_1 + 2B_1 + E_1 + 2E_2$. The A_1, E_1 and E_2 modes are Raman active. Furthermore, the A_1 and E_1 are infrared active and split into

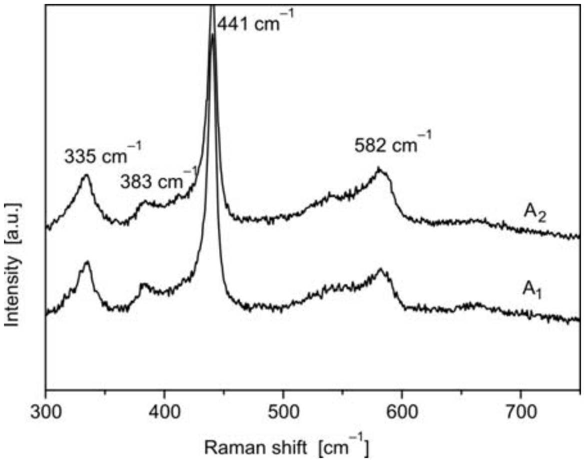

Fig. 6. Typical Raman spectra of the synthesized nanostructures

longitudinal optical (OP) components and transverse optical (TO) components [22]. Figure 6 shows the Raman spectrum of the synthesized powder. A sharp and strong peak observed at 441 cm^{-1} is attributed to the optical phonon E_2 mode of the ZnO and a characteristic Raman active peak for the wurtzite hexagonal phase of ZnO [23]. Two very small peaks at 335 and 383 cm^{-1} observed in the spectrum are assigned as E_{2H}–E_{2L} (multiphonon process) and A_{1T} modes, respectively. Additionally, a very suppressed peak at 582 cm^{-1} the spectrum was assigned as E_{1L} mode [24, 25]. The origin of the E_{1L} mode in the Raman scattering is explained by the impurities and structural defects (oxygen vacancies and Zn interstitials) of the synthesized products. The presence of the high intensity E_2 mode with the suppressed and very weak E_{1L} peak in the Raman scattering indicated that the synthesized sphere-shaped ZnO nanostructures have good crystal quality and possess the wurtzite hexagonal crystal structure.

4. Conclusion

Synthesis of sphere-shaped ZnO nanostructures composed of ZnO nanosheets and synthesis of flower-shaped ZnO nanostructures composed of ZnO nanorods were successfully achieved by reacting zinc acetate dihydrate, sodium hydroxide and PEG-20000 at 180 °C for 4 h in solution. Detailed structural characterizations demonstrated that the synthesized products are single crystalline with the wurtzite hexagonal phase, the obvious differences are clearly evident from the SEM and TEM data.

Acknowledgement

We gratefully acknowledge the financial support of this research by the Key Technology R&D program of Heilongjiang Province (No. TB06A05), basic research fund of Harbin Engineering University (No. mzj07076) and Science Fund for Young Scholar of Harbin City (No. 2008RFQXG028).

References

[1] Alivisatos A.P., Science, 271 (1996), 933.
[2] Beek W.J.E., Wienk M.M., Janssen R.A.J., Adv. Mater., 16 (2004), 1009.
[3] Beek W.J.E., Wienk M.M., Emerink M.K., Yang X., Janssen R.A.J., J. Phys. Chem. B, 109 (2005), 9505.
[4] Xia Y., Yang P., Sun Y., Wu Y., Mare B., Gates B., Yin Y., Kim F., Yan H., Adv. Mater., 15 (2003), 323.
[5] Wang Z.L., Mater. Today, 7 (2004), 26.
[6] Sekar A., Kim S.H., Umar A., Hahn Y.B., J. Cryst. Growth, 277 (2005), 471.
[7] Umar A., Ra H.W., Jeong J.P., Suh E.K., Hahn Y.B., Korean J. Chem. Eng., 23 (2006), 499.
[8] Umar A., Kim S.H., Lee Y.S., Nahm K.S., Hahn Y.B., J. Cryst. Growth, 282 (2005), 131.
[9] Umar A., Karunagaran B., Suh E.K., Hahn Y.B., Nanotechn., 17 (2006), 4072.
[10] Hughes W.L., Wang Z.L., Appl. Phys. Lett., 82 (2003), 2886.
[11] Zhang B.P., Binh N.T., Wakatsuki K., Segawa Y., Yamada Y., Usami N., Koinuma H., Appl. Phys. Lett., 84 (2004), 4098.
[12] Umar A., Hahn Y.B., Appl. Phys. Lett., 88 (2006), 17312.

[13] HUGHES W.L., WANG Z.L., J. Am. Chem. Soc., 126 (2004), 6703.
[14] GAO P.X., WANG Z.L., J. Appl. Phys., 97 (2005), 44304.
[15] UMAR A., LEE S., LEE Y.S., NAHM K.S., HAHN Y.B., J. Crystal Growth., 277 (2005), 479.
[16] UMAR A., LEE S., IM Y.H., HAHN Y.B., Nanotechn., 16 (2005), 2462.
[17] UMAR A., KIM S.H., IM Y.H., HAHN Y.B., Superlatt. Microstruct., 39 (2006), 238.
[18] SHEN G., BANDO Y., IU B., GOLBERG D., LEE C.J., Adv. Func. Mater., 16 (2006), 410.
[19] UMAR A., HAHN Y.B., Nanotechn., 17 (2006), 2174.
[20] WAHAB R., ANSARI S.G., KIM Y.S., SEO H.K., KIM G.S., KHANG G., SHIN H.-S., Mater. Res. Bull., 42 (2007), 1640.
[21] LILI W., YOUSHI W., YUANCHANG S., HUIYING W., Rare Metals, 25 (2006), 68.
[22] DAMEN T.C., PORTO S.P.S., TELL B., Phys. Rev., 142 (1966), 142.
[23] XING Y.J., XI Z.H., XUE Z.Q., ZHANG X.D., SONG J.H., WANG R.M., XU J., SONG Y., ZHANG S.L., YU D.P., Appl. Phys. Lett., 83 (2003), 1689.
[24] RAJALAKSHMI M., ARORA A.K., BENDRE B.S., MAHAMUNI S., J. Appl. Phys., 87 (2000), 2445.
[25] VANHEUSDEN K., SEAGER C.H., WARREN W.L., TALLANT D.R., VOIGT J.A., J. Appl. Phys., 79 (1996), 7983.

Received 11 August 2008
Revised 9 January 2009

Materials Science-Poland, Vol. 27, No. 2, 2009

Deposition of Au, Au–V and Au–VO$_x$ on Si wafers by co-sputtering technique

S. NARKSITIPAN[1], T. BANNURU[2], W.L. BROWN[2], R.P. VINCI[2], S. THONGTEM[3*]

[1]Department of Physics, Faculty of Science, Maejo University, Chiang Mai 50290, Thailand

[2]Department of Materials Science and Engineering, Lehigh University, Bethlehem, PA 18015, U.S.A

[3]Department of Physics and Materials Science, Faculty of Science,
Chiang Mai University, Chiang Mai 50200, Thailand

Au, Au–V and Au–VO$_x$ thin films were deposited on Si wafers by a co-sputtering technique. A four-point probe shows that the electrical resistivity of pure Au thin film on Si wafer without annealing is 7.2 mΩ·cm. The resistivities of thin films deposited on Si wafers, with or without annealing, tended to increase with the increase in the V and VO$_x$ concentrations, and were attributable to the inhibited drift mobility of charge carriers within the films. By using the nanoindentation technique, the hardness in all cases also tended to increase with the increase in the V and VO$_x$ concentrations. The hardness of pure Au, without annealing, was 2.52 GPa. It decreased to 1.80 GPa and 1.75 GPa after annealing at 200 °C and 400 °C, respectively. SEM and TEM analyses revealed the presence of nanosized particles on the surfaces of the thin films. XRD analysis of Au–4.00% VO$_x$ film deposited on Si wafer detected the presence of Au, VO and Si. However, SAED analysis only detected the presence of Au on the film.

Key words: *Au, Au–V, Au–VO$_x$ thin films; electrical resistivity; hardness*

1. Introduction

The development of biological and microelectromechanical systems (MEMS), microelectronics and optoelectronics has been increasingly important, inspiring a number of researchers to investigate new materials for use as thin films [1–3]. Low electrical resistivity, good resistance to wear, and biological compatibility are the prime features of such materials [1, 2]. Among various thin films, Au/Si is widely used due to its chemical stability, low resistivity, good reliability and other factors. These properties, influenced by microstructures and processing temperatures [4], deserve further investigation. Au and its alloys are very attractive for use in many MEMS devices due to

---

[*] Corresponding author: schthongtem@yahoo.com; sthongtem@hotmail.com

their low electrical resistivity and good corrosion resistance [1, 2]. Au thin films were deposited on substrates using various methods, such as Au films deposited on glass by ion beam-induced enhanced adhesion [5], nanoparticle Au films by pulsed laser deposition [6], uniform Au film on glass by microwave-assisted deposition [7], Au thin films by Ar sputtering [8] and by thermal evaporation [9], Pt and Au thin films by filtered vacuum arc [10] and Au films by electrodeposition [1]. V is a promising element which can be used as an alloying element of Au [2]. The electrical properties of VO_x are also very attractive. They change between metallic and insulating behaviours, termed metal–insulator transition (MIT) [11, 12]. VO has metallic conductivity due to the overlapping of 3d orbitals of the metal [12]. VO_2 exhibits phase change from insulator to metallic state at 68 °C, and V_2O_5 does so at 250 °C [11]. V_2O_3 undergoes phase transition from semiconductor to metal at –123 °C [13]. It has a low noise property due to its low resistivity at room temperature [13]. Therefore, VO_x film can be used for many applications such as electronic switches, sensors and memory units [11]. The purpose of the research was to deposit Au, Au–V and Au–VO_x thin films on Si wafers by the co-sputtering technique and to investigate their properties.

2. Experimental

Au, Au–V and Au–VO_x thin films were deposited on Si wafers by dc magnetron sputtering under the pressure of 4×10^{-3} torr Ar pressure. To deposit the Au–V and Au –VO_x films, two guns were used to control the Au and V compositions. The pressure of O_2 equal to 10^{-4} Torr was also applied to the Au–VO_x film depositions. Each film was deposited until it was 500 nm thick. A part of the deposited films were subject to annealing at 200 °C and 400 °C for 1 h. In order to characterize the resistivity, hardness, morphology and phase compositions of the deposited films, the following techniques were employed: a four-point probe method, a nanoindentation technique, X-ray diffractometry (XRD), scanning electron microscopy (SEM), transmission electron microscopy (TEM) and selected area electron diffraction (SAED).

3. Results and discussion

The electrical resistivities of Au and Au–V thin films deposited on Si wafers (Fig. 1a) increased with the increase in the V concentrations. These observations show that the additional V atoms hindered charged carriers from drifting in the films. The resistivities of pure Au thin films, with or without annealing at 200 °C and 400 °C, share the same values, namely 7.2 mΩ·cm. For the same V concentrations, their resistivities tended to decrease after high temperature annealing, especially at 400 °C. During the annealing, Au and V atoms were arranged in a systematic array, leading to a decrease in resistivity. The resistivities of Au, Au–2.30% VO_x and Au–4.00% VO_x (Fig. 1b), with or without annealing, slowly increased with the increase in the VO_x

content, and tended to decrease after the annealing. For each of the annealing temperatures, the resistivity of Au–VO$_x$ is not as great as that of Au–V. The resistivities of Au–4.00% VO$_x$ are almost equivalent to those of the corresponding VO$_x$ –free matrix. They are 17.3 mΩ·cm if the sample is not subject to annealing (T_R), whereas it measures 17.7 and 10.2 mΩ·cm if subjected to annealing at 200 °C and 400 °C, respectively.

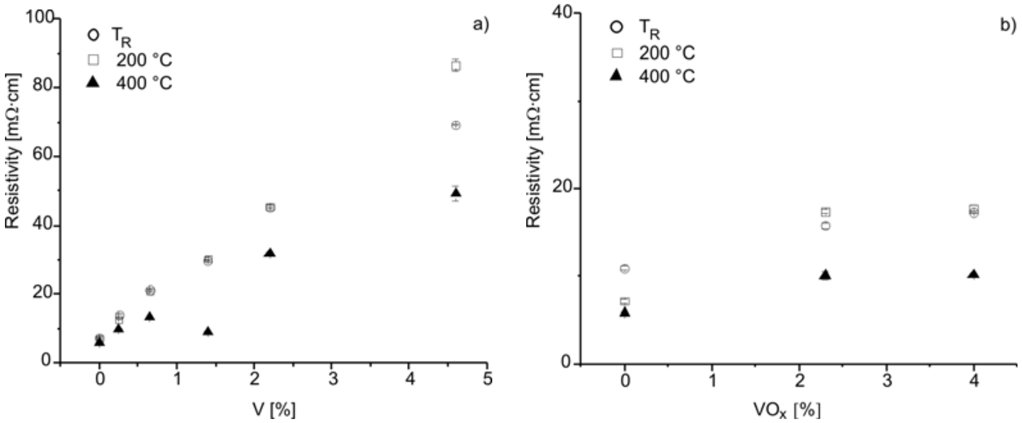

Fig. 1. Resistivities of Au, Au–V (a), and Au–VO$_x$ (b) thin films deposited on Si wafers before (room temperature, T_R), and after annealing at 200 °C and 400 °C for 1 h

The hardness of each thin film deposited on Si wafer was measured ten times. Averages and standard deviations have been calculated (Fig. 2). The hardness of various Au and Au–V thin films (Fig 2), with or without annealing, tended to increase with the increase in the V concentrations. The hardness of pure Au not subject to annealing amounted 2.52 GPa, whereas after annealing at 200 °C and 400 °C it was

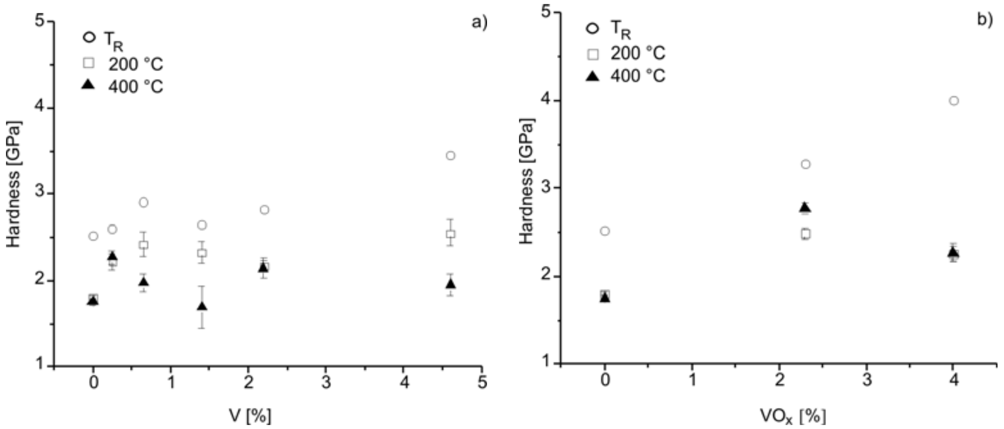

Fig. 2. Hardness values of Au, Au–V (a) and Au–VO$_x$ (b) thin films deposited on Si wafers before and after annealing at 200 °C and 400 °C for 1 h

1.80 GPa and 1.75 GPa, respectively. In comparison with the values obtained for non-annealed films, the hardness of the corresponding thin films deposited on Si wafers became lower after annealing, due to the grain growth and phase change processes. In general, the lowest hardness corresponds to the highest annealing temperature. In the case of Au, Au–2.30% VO_x and Au–4.00% VO_x (Fig. 2b), the hardness also tended to increase with the increase in the VO_x concentration. The greatest hardness, equal to 4.00 GPa, was found in non-annealed Au–4.00% VO_x. The higher hardness implies that VO_x particles have the effect of hindering plastic deformation of thin films, by trapping dislocations. The hardness became lower when the films were subject to annealing.

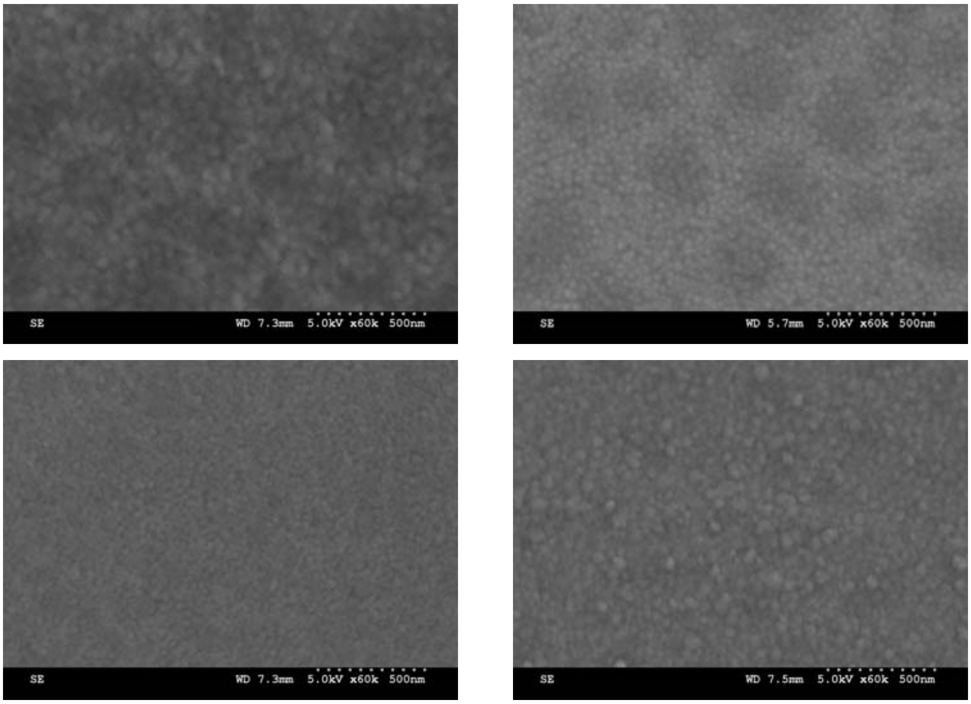

Fig. 3. SEM images of: a) Au, b) Au–0.65% V, c) Au–4.60% V and d) Au–4.00% VO_x thin films deposited on Si wafers after annealing at 200 °C for 1 h

SEM images show general morphologies of the films. After annealing at 200 °C, the Au, Au–0.65% V and Au–4.60% V surfaces (Figs. 3a–c) were composed of a number of nanodots or nanoparticles, although the films did contain a variety of V concentrations. The average size of pure Au particles was 56 nm. The addition of V to Au led to the reduction in their sizes by hindering grain boundary mobility. For the Au–4.00% VO_x surface (Fig. 3d), a number of nanoparticles were also detected. This reflects their properties such as electrical resistivity, surface roughness and hardness.

TEM image data (Fig. 4a) show that the thin film was composed of a number of dispersed, nanosized particles. Different colours (dark, white and gray) appear on the

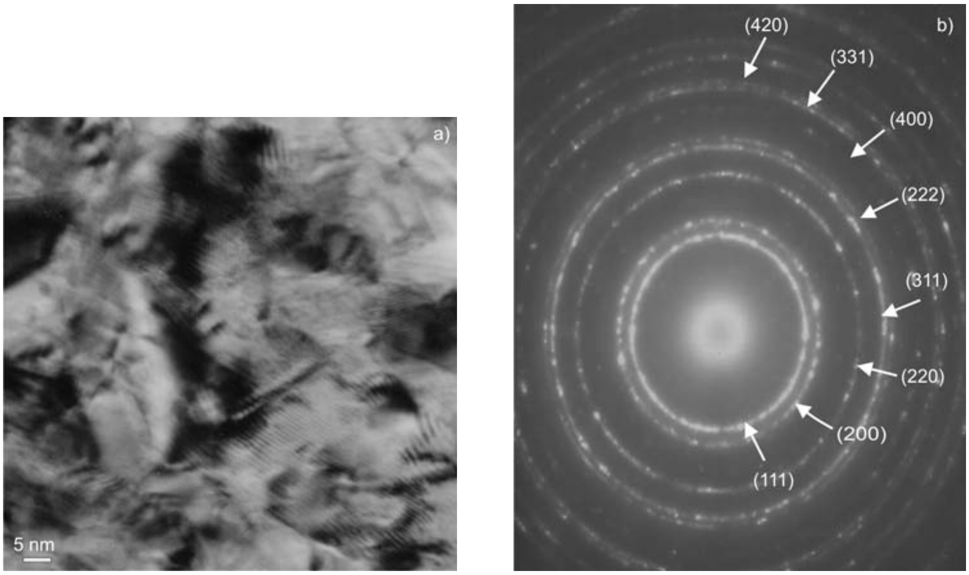

Fig. 4. TEM image (a) and SAED pattern (b) of Au–4.00% VO$_x$ thin film without annealing at a high temperature

image, showing that a rough surface had been produced on the wafer. Moiré fringes were detected. They are the interference patterns of two crystallographic phases with slightly different lattice parameters [14–16]. A SAED pattern (Fig 4b) appears as several concentric rings, due to the diffraction of electrons through the polycrystals. The rings are diffuse and hollow, showing that the thin film was composed of nanosized crystals. Interplanar spaces of the diffraction planes were calculated [17–19] and compared with those computed by the JCPDS software [20]. The pattern corresponds to (111), (200), (220), (311), (222), (400), (331) and (420) planes of the polycrystals, specified as Au (cubic) with *Fm*3*m* space group. The (111) ring has the strongest intensity. No VO$_x$ was detected in the research presented here. Its concentration could have been too low to be detected.

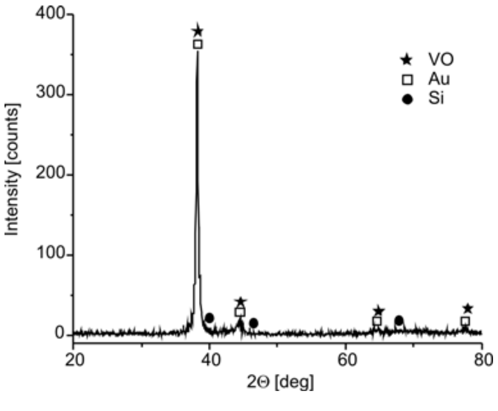

Fig. 5. XRD spectrum of Au–4.00% VO$_x$ thin film deposited on Si wafer without annealing at a high temperature

The XRD spectrum (Fig. 5) was indexed using Bragg's law for diffraction, and was compared with that provided by the JCPDS software [20]. The spectrum is consistent with the deposition of Au and VO_x on Si wafer. It is very sharp, showing that the deposited film was composed of crystals. The strongest intensity peak is at $2\theta = 38.1°$. It mainly diffracted from the (111) plane of Au. VO played a relatively minor role in the diffraction, due to its low concentration (Au–4.00% VO_x).

4. Conclusions

Au, Au–V and Au–VO_x thin films were successfully deposited on Si wafers using a DC magnetron sputtering technique. The resistivities and hardness of thin films deposited on Si wafer increased with the increase in the V and VO_x concentrations decreased after high temperature annealing. The properties were influenced by the number of nanosized particles and different phases of the thin films.

Acknowledgement

We are extremely grateful to the Thailand Research Fund, Thailand, for supporting the research.

References

[1] KAL S., BAGOLINI A., MARGESIN B., ZEN M., Microelectron. J., 37 (2006), 1329.
[2] LIN M.T., CHROMIK R.R., BARBOSA N. III, EL-DEIRY P., HYUN S., BROWN W.L., VINCI R.P., DELPH T.J., Thin Solid Films, 515 (2007), 7919.
[3] PATRIARCHE G., LE BOURHIS E., FAURIE D., RENAULT P.O., Thin Solid Films 460 (2004), 150.
[4] LEE W.S., FONG F.J., Mater. Sci. Eng. A, 475 (2008), 319.
[5] GUZMAN L., MIOTELLO A., CHECCHETTO R., ADAMI M., Surf. Coat. Tech., 158–159 (2002), 558.
[6] DONNELLY T., KRISHNAMURTHY S., CARNEY K., MCEVOY N., LUNNEY J.G., Appl. Surf. Sci., 254 (2007), 1303.
[7] HUANG H., ZHANG S., QI L., YU X., CHEN Y., Surf. Coat. Tech., 200 (2006), 4389.
[8] DELGADO J.M., ORTS J.M., PÉREZ J.M., RODES A., J. Electroanalyt. Chem., 617 (2008), 130.
[9] ZHANG S., BERGUIGA L., ELEZGARAY J., ROLAND T., FAIVRE-MOSKALENKO C., ARGOUL F., Surf. Sci., 601 (2007), 5445.
[10] SALVADORI M.C., MELO L.L., VAZ A.R., WIEDERKEHR R.S., TEIXEIRA F.S., CATTANI M., Surf. Coat. Tech., 200 (2006), 2965.
[11] LEE J.W., MIN S.R., CHO H.N., CHUNG C.W., Thin Solid Films, 515 (2007), 7740.
[12] RATA A.D., CHEZAN A.R., PRESURA C., HIBMA T., Surf. Sci., 532–535 (2003), 341.
[13] HAN Y.H., CHOI I.H., KANG H.K., PARK J.Y., KIM K.T., SHIN H.J., MOON S., Thin Solid Films, 425 (2003), 260.
[14] THONGTEM T., PHURUANGRAT A., THONGTEM S., Mater. Lett., 60 (2006), 3776.

[15] GNANASEKAR K.I., CATHRINO H.A., JIANG J.C., MRSE A.A., NAGASUBRAHMANIAN G., DOUGHTY D.H., RAMBABU B., Solid State Ion. ,148 (2002), 299.
[16] YU K., ZHAO J., GUO Y., DING X., BALA H., LIU Y., WANG Z., Mater. Lett., 59 (2005), 2515.
[17] ANDREWS K.W., DYSON D.J., KEOWN S.R., *Interpretation of Electron Diffraction Patterns*, Plenum Press, New York, 1971, p. 14.
[18] THONGTEM T., KAOWPHONG S., THONGTEM S., J. Mater. Sci., 42 (2007), 3923.
[19] THONGTEM T., PHURUANGRAT A., THONGTEM S., J. Mater. Sci., 42 (2007), 9316.
[20] Powder Diffract. File, JCPDS Internat. Centre for Diffract. Data, PA 19073-3273, U.S.A., (2001).

Received 18 August 2008

Materials Science-Poland, Vol. 27, No. 2, 2009

Influence of WO_3 content on the optical properties of Eu^{3+}-doped $Bi_2O_3–B_2O_3–WO_3$ glasses

Z. WANG[*], R. TONG, H. LIN, D. YANG

School of Chemical Material, Dalian Polytechnic University, Dalian 116034, P.R. China

Eu^{3+}-doped bismuth borate based glasses with various contents of WO_3 were fabricated by melt quenching. Optical properties of Eu^{3+} ions in these ternary systems and their dependence on the WO_3 content were investigated: absorption and emission spectra were studied as the WO_3 molar ratio was adjusted from 1 to 5 mol %. The Judd–Ofelt parameters were calculated from the emission spectra and expressed in terms of reduced matrix U^t (t = 2, 4, 6) characters for optical transitions. The influence of WO_3 content on the Judd–Ofelt intensity parameter Ω_2 was also investigated. Experimental results lead us to conclude that the optimum luminescence of Eu^{3+}-doped bismuth borate based glasses is achieved if the WO_3 content is 3 mol %.

Key words: *$Bi_2O_3–B_2O_3–WO_3$ system glasses; Eu^{3+} ions; Emission spectrum, Judd-Ofelt parameters*

1. Introduction

Rare-earth doped glasses have attracted considerable attention owing to their applications in optical communications, bulk lasers and sensors, etc. [1–4]. Among conventional glasses, borate glasses are known to be excellent host matrices of rare earth oxides. Bismuth oxide glass has a high refractive index and a low phonon energy system, which enhances the radiative transitions of rare earth ions and is expected to have high fluorescence quantum efficiency. Besides, adding a low quantity of WO_3 improves luminescence, a fact which has been confirmed by optical measurements in $TeO_2–WO_3–Tm_2O_3$ systems [5, 6]. Therefore, we expect that the introduction of WO_3 into the bismuth borate matrix will influence the spectral properties of rare earth ions. Additionally, doping with suitable rare earth ions is important for studying the structure and bonding characteristics of different material: thus Eu^{3+} ions have been chosen due to their unsplit $^7F_0$ ground state and relatively simple system of electronic levels [7–12].

---

[*] Corresponding author, e-mail: wangzhiqiang_dlpu@hotmail.com

The Judd–Ofelt theory is used to estimate the local structure and bonding states of rare-earth ions in host materials. Some important optical parameters such as the oscillator strength, radiative transition probability, fluorescence branching ratio and radiative lifetime can be calculated by the parameter Ω_λ. Up to now, the Judd–Ofelt parameters have been calculated from absorption and emission spectra of Eu^{3+}-doped glasses. However, Gao Tang et al. [9] have shown that the Ω_λ parameters obtained from the emission spectrum is more reliable than that obtained from the absorption spectrum in the case of Eu^{3+}-doped GaF_3–InF_3–CdF_2–ZnF_2–PbF_2–SnF_2 glasses.

In this paper, we report the optical properties of Bi_2O_3–B_2O_3–WO_3 glasses doped with Eu^{3+} ions. The Judd–Ofelt parameters were calculated from the emission spectrum. The influence of WO_3 on the change of Ω_2 was also analyzed.

2. Experimental

A series of glass samples in molar composition: $(99 - x)[Bi_2O_3 \cdot B_2O_3]xWO_3 \cdot Eu_2O_3$ (x =1, 3, 5 mol %) were prepared. The starting materials were Bi_2O_3 (99.0%), H_3BO_3 (99.5%), WO_3 (99.0%), Eu_2O_3 (99.9%). A batch of 15 g in a platinum crucible was melted at 850 °C for 30 min in an electrical furnace. The melt was then quickly poured onto a preheated steel block, and the transparent samples were annealed at approximately the glass transition temperature T_g. Then the glass samples were polished in order to facilitate subsequent test measurements. The samples had a typical thickness of approximately 0.5 cm.

The density of the glasses was measured according to Archimedes' principle. The refractive indices of the glass samples were measured according to Brewster's law [13, 14] with an FGY 201 spectrometer. The absorption spectrum of each sample was recorded with a Perkin-Elmer Lambda 35 UV-VIS double-beam spectrophotometer. The emission spectrum of each sample was obtained with a P-E LS 55 spectrofluorimeter. All the spectra were measured at room temperature.

3. Results and discussion

3.1. Absorption spectrum

Figure 1 shows the absorption spectra of the samples. Three absorption peaks are observed in the Eu^{3+}-doped Bi_2O_3–B_2O_3–WO_3 glasses at 462, 526 and 579 nm. The first excited state, ${}^7F_1$, is very close in energy to the ground state ${}^7F_0$. The absorption transitions from ${}^7F_1$ cannot be ignored at room temperature [15]. In view of this, the absorption peaks corresponding to the following transitions: ${}^7F_0 \rightarrow {}^5D_2$, ${}^7F_{0,1} \rightarrow {}^5D_1$ and ${}^7F_1 \rightarrow {}^5D_0$. As can be seen in Fig. 1, the absorption edge wavelength shifts towards the longer wavelengths as the WO_3 content increases because the content of Bi_2O_3 with intense absorption at UV relatively decreases. However, several absorption bands of Eu^{3+} ions in the ultraviolet range were covered with strong absorption bands of the host glasses, especially Bi_2O_3. Only three weak absorption peaks were observed, ranging from 460 to 600 nm.

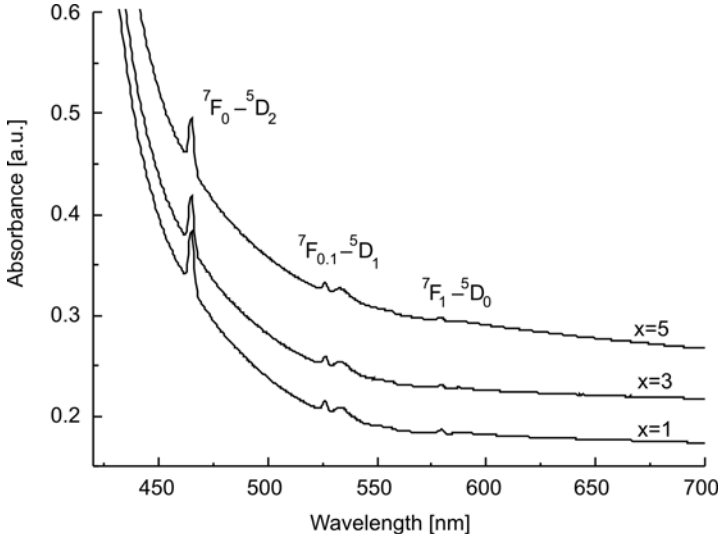

Fig. 1. Absorption spectra of Eu^{3+}-doped Bi_2O_3–B_2O_3–WO_3 glasses

3.2. Emission spectrum and the Judd–Ofelt theory

Figure 2 shows the emission spectra of Eu^{3+}-doped Bi_2O_3–B_2O_3–WO_3 glasses in the 550–750 nm region. From the figure, it is clear that there are four peaks at around 590, 615, 650 and 698 nm in the spectrum corresponding to $^5D_0 \to {}^7F_1$, $^5D_0 \to {}^7F_2$, $^5D_0 \to {}^7F_3$ and $^5D_0 \to {}^7F_4$ transitions, respectively. As seen in Fig. 2, the band around 615 nm is most intense, thus Eu^{3+}-doped Bi_2O_3–B_2O_3–WO_3 glasses emit bright red light under UV light excitations. Furthermore, the intensity of the transitions initially increases and then subsequently decreases as the of WO_3 content increases: the most intense light emitted by the glasses appears when the WO_3 content is 3 mol %.

The Judd–Ofelt theory [16, 17] provides a very useful method for analyzing the local structure around rare-earth ions. As in this glass system some absorption peaks of Eu^{3+} ions at the ultraviolet range could not be observed and other peaks were very weak, we are unable to accurately calculate the Judd–Ofelt parameters from the absorption spectra. More recently, some scholars have extended the Judd–Ofelt theory by calculating the optical parameters from the emission spectrum [14, 18].

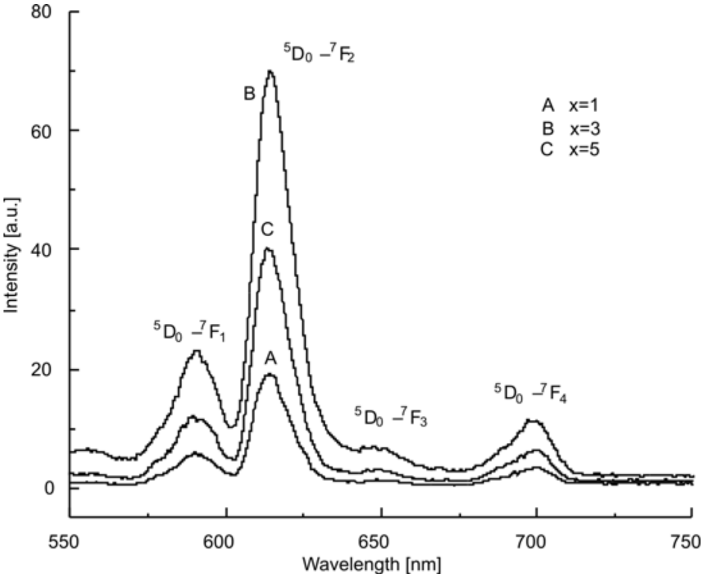

Fig. 2. Emission spectra of Eu^{3+}-doped Bi_2O_3–B_2O_3–WO_3 glasses (λ_{exc} = 465 nm)

Based on the optical transition law of rare-earth ions [19], the $^5D_0 \to {}^7F_J\,(J=2,4,6)$ transition is allowed by the electric dipole, and electric dipole radiative transition probability A_{ed} can be calculated from the formula:

$$A_{ed}=\frac{64\pi^4e^2}{3h}\frac{\bar{v}^3}{2J'+1}\frac{n\left(n^2+2\right)^2}{9}\times\sum_{t=2,4,6}\Omega_t\left\langle\psi J\left\|U^t\right\|\psi'J'\right\rangle^2 \tag{1}$$

where e, c and n are the charge of electron, velocity of light and refractive index of the glasses, respectively; h is the Planck constant, $\bar{v}$ is the average wavenumber of the transition, J is the quantum number of angular momentum of the initial state and J' is that of the final state. $\left\langle\psi J\left\|U^t\right\|\psi'J'\right\rangle^2$ represents the square of the matrix elements of the unit tensor operation U^t connecting the initial and final states and the its value for the Eu^{3+} ion is given in Table 1. The $^5D_0 \to {}^7F_1$ transition is allowed by the magnetic dipole, and the magnetic dipole radiative transition probability A_{md} is given by:

$$A_{md}=\frac{64\pi^4}{3h}\frac{\bar{v}^3}{2J'+1}n^3S_{md} \tag{2}$$

where S_{md} is the line strength for magnetic dipole transition. The local rare earth environment does not affect S_{md}, thus it is generally accepted as a constant. The value of S_{md} can be obtained from

$$S_{md}=\frac{e^2h^2}{16\pi^2m^2c^2}\left\langle\psi J\left\|U^t\right\|\psi'J'\right\rangle^2 \tag{3}$$

Table 1. Square of the matrix elements for $^5D_0 \to {}^7F_J\ (J = 2, 4, 6)$ of Eu^{3+} ions

Parameter	Transition		
	$^5D_0 \to {}^7F_2$	$^5D_0 \to {}^7F_4$	$^5D_0 \to {}^7F_6$
$U^{(2)2}$	0.0032	0	0
$U^{(4)2}$	0	0.0023	0
$U^{(6)2}$	0	0	0.0002

Neglecting the fact that the different transition wavelengths of $^5D_0 \to {}^7F_1$ and $^5D_0 \to {}^7F_J\ (J = 2,4,6)$ should result in a difference in the refractive index, the transition intensity ratio of the electric dipole to the magnetic dipole is as follows:

$$\frac{\int I_J(v)\,dv}{\int I_{md}(v)\,dv} = \frac{e^2}{S_{md}} \frac{v_J^3}{v_{md}^3} \frac{\left(n^2+2\right)^2}{9n^2} \Omega_J \times \left\langle \psi J \left\| U^t \right\| \psi' J' \right\rangle^2 \tag{4}$$

Thus the optical transition intensity parameter Ω_J can be calculated from Eqs. (1)–(4). Since the emission band for the $^5D_0 \to {}^7F_6$ transition centres at around 810 nm could not be detected, due to measurement limitations, we can only determine the value of Ω_2 and Ω_4. As a matter of fact, the parameter Ω_6 can be negligibly small compared with Ω_2 and Ω_4, because $U^{(6)2}$ is comparatively small. The value of Ω_J (J = 2, 4) is given in Table 2.

Table 2. Transition intensity parameter Ω_J (J = 2, 4) and refractive index n

x	Ω_2 (10^{-20}cm^2)	Ω_4 (10^{-20}cm^2)	n
1	3.83	1.70	2.3790
3	3.37	1.39	2.3751
5	3.75	1.44	2.3711

According to previous studies, Ω_2 is a useful parameter, because it is sensitive to the local symmetry of the ligand field and bond covalency [19–21]. The value of Ω_2 increases as the local symmetry of the ligand field decreases and as the bond covalency increases. It is necessary to consider these two aspects. The structure units ($[WO_4]$ or $[WO_6]$) of WO_3 gradually participate in the glass network as the WO_3 content increases, these then lower the symmetry of the glass network, thus leading to an increase in the value of Ω_2. On the other hand, the electric field of W^{6+} has a strong attraction to the O^{2-} ion, the W^{6+} ion decreases the covalency of Eu–O by means of increasing the Eu–O distance, because the attractive function of W^{6+} to the O^{2-} ion is higher than to the Eu^{3+} ion. From Table 2, we can see that Ω_2 shows a minimum when the WO_3 content is 3 mol %, Ω_2 tends to decrease initially and then to increase subsequently. When the content of WO_3 is lower than 3 mol %, the influence of WO_3 on the covalency of Eu–O plays a dominant role in changing Ω_2 compared with the local symmetry of the ligand field, so the value of Ω_2 initially decreases. However, the value of Ω_2 increases as the WO_3 content increases beyond a critical level, thus the influence of the WO_3 content on the symmetry of the ligand field plays a dominant role in changing Ω_2 compared with the covalency of Eu–O.

4. Conclusions

Eu^{3+}-doped Bi_2O_3–B_2O_3–WO_3 glasses having different WO_3 contents were prepared. The Judd–Ofelt parameters Ω_2, Ω_4 for Eu^{3+} were calculated from the emission spectra. The bright red emission is observed in Eu^{3+}-doped glasses under UV light excitations. It is found that the glass with 3 mol % WO_3 content has the best optical properties in this system. The effect of WO_3 on the change of Ω_2 was also analyzed. When the content of WO_3 is lower than 3 mol %, the influence of WO_3 on the covalency of Eu–O plays a dominant role in changing Ω_2, compared with the local symmetry of the ligand field, thus the value of Ω_2 initially decreases. However, the value of Ω_2 increases as the WO_3 content increases beyond a critical level; this is due to the influence of WO_3 on the symmetry of the ligand field, which plays a dominant role in changing Ω_2, compared with the covalency of Eu–O.

Acknowledgements

The authors gratefully acknowledge the financial support of the Science and Technology Foundation of Liaoning Province (20041067) and the Technology Foundation of Dalian City (2004166)

References

[1] SAMSON B.N., MEDEIROS NETO J.A., LAMING R.I., HEWAK D.W., Electron. Lett., 30 (1994), 1617.
[2] JACKSON S.D., Appl. Phys. Lett., 83 (2003), 1316.
[3] CHIODINI N., PALEARI A., BRAMBILLA G., TAYLOR E.R., Appl. Phys. Lett., 80 (2000), 4449.
[4] TRIPATHI G., RAI V.K., RAI S.B., Optics Comm., 264 (2006), 116.
[5] CENK S., DEMIRATA B., ÖVEÇOGLU M.L., ÖZEN G., Spectrochim. Acta Part A., 57 (2001), 2367.
[6] ÖZEN G., AYDINLI A., CENK S., SENNAROĞLU A., J. Lumin., 101 (2003), 293.
[7] PISARSKI W.A., PISARSKA J., DOMINIAK DZIK G., MĄCZKA M., RYBA ROMANOWSKI W., J. Phys. Chem. Solids., 67 (2006), 2452.
[8] CHAKRABARTI R., DAS M., KARMAKAR B., ANNAPURNA K., BUDDHUDU S., J. Non-Cryst. Solids., 353 (2007), 1422.
[9] TANG G., ZHU J.Q., ZHU Y.M., BAI C.Y., J. Alloys Compd., 453 (2008), 487.
[10] LIM K.S., LEE S., TRIN M.T., KIM S.H., LEE M., HAMILTON D.G., GIBSON G.N., J. Lumin., 122–123 (2007), 14.
[11] NOGAMI M., J. Lumin., 92 (2001), 329.
[12] RAMI REDDY B., J. Non-Cryst. Solids., 352 (2006), 483.
[13] KAPLAN S.G., HANSSEN L.M., Opt. Eng., 239 (1998), 3425.
[14] RUTT H.N., Infrared Phys. Technol., 38 (1997), 31.

[15] DEJNEKA M., SNITZER E., RIMAN R.E., J. Lumin., 65 (1995), 227.
[16] JUDD B.R., Phys. Rev., 127 (1962), 750.
[17] OFELT G.S., J. Chem. Phys., 37 (1962), 511.
[18] EPPENDORFF-HEIDEPRIEM H., EHRT D., J. Non-Cryst. Solids., 208 (1996), 205.
[19] RIBEIRO S.J.L., DINIZ R.E.O., MESSADDEQ Y., NUNES L.A., AEGERTER M.A., Chem. Phys. Lett., 1994 (220), 214.
[20] TANABE S., J. Non-Cryst. Solids., 259 (1999), 1.
[21] AHRENS H., WOLLENHAUPT M., FRÖBEL P., JUN LIN, BARNER K., SUN G.S., BRAUNSTEIN R., J. Lumin., 82 (1999), 177.

Received 22 August 2008
Revised 12 November 2008

Materials Science-Poland, Vol. 27, No. 2, 2009

Synthesis of claw-like CuO and its catalytic activity in the thermal decomposition of ammonium perchlorate

J. WANG[*], S. HE, Z. LI, X. JING, M. ZHANG

School of Material Science and Chemical Engineering,
Harbin Engineering University, Harbin 150001, P. R. China

Claw-like CuO was prepared by solution process at 100 °C simply by using copper nitrate and hexamethylenetetramine for 3 h. The structure and morphology of resulting CuO powders were characterized by X-ray diffraction, scanning electron microscopy and transmission electron microscopy. CuO nanocrystals were studied as an additive for promoting the thermal decomposition of ammonium perchlorate. With the addition of the claw-like CuO nanocrystals, thermal decomposition temperature of ammonium perchlorate decreased. CuO nanocrystals showed catalytic activity on the decomposition of ammonium perchlorate.

Key words: *nanostructure; crystal growth; chemical synthesis; catalytic activity*

1. Introduction

In recent years, the research into the shape control of various nanostructures has been widely developed because of their morphology dependent properties. Such research concentrated not only on metal and semiconductor nanostructures but also on transitional metal oxide nanostructures. Copper oxide (CuO), as an important oxide of transitional metal with a narrow band gap ($E_g = 1.2$ eV), has been extensively studied because of its importance for fundamental investigations and practical applications such as heterogeneous catalysts [1–3], gas sensors [4], and electrode materials [5, 6]. It is also a promising material for fabricating solar cells [7], due to its photoconductive and photochemical properties. Because of the practical reasons mentioned above, the synthesis of nanostructured CuO has also attracted considerable attention. To this end, various techniques have been used including precursor thermal decomposition [8], hydrothermal methods [9–11], solid-phase methods [12], wet-chemical methods

---

[*] Corresponding author, e-mail: junwang@hrbeu.edu.cn

[7, 13], hydrolysis route [14], electrochemical methods [15], template-free solution route [16], and chemical deposition method [17].

Up to now, there have been many reports about the preparation of CuO nanostructures such as nanorods [6, 7, 13], nanowires [12, 18], nanosheets [19] nanoparticles [20], nanoplatelets [11], nanowhiskers [21], nanoribbons [13], Other than morphologies of CuO structures, some complex structures of CuO have also been reported in the literature, such as flower-like [14, 17], sheaf-like [22], dendrite-like [9], doughnut-like [8], and sphere-like structures [4, 23]. However, the obtained morphology (claw, flower,) in these reports is limited.

In this paper, a simple chemical precipitation method is employed to synthesize CuO nanostructures in the presence of aqueous solution of hexamethylenetetramine. Without using templates, surfactants or additives, this route is capable of synthesizing a variety of complex CuO structures, including claw-like structures, and multilayer flower-like ones. These structures consist of nanometer-sized CuO crystals self-organized into micrometer-sized flower-like with a hierarchical architecture. The influence of reaction time on morphology of the CuO nanostructure is examined. In addition, the catalytic effect of the as-synthesized CuO was studied in this paper. The claw-like CuO nanostructures showed effective catalytic activity on the decomposition of ammonium perchlorate.

2. Experimental

Synthesis of samples. Copper nitrate ($Cu(NO_3)_2\cdot 3H_2O$), hexamethylenetetramine (HMTA, $C_6H_{12}N_4$) were all analytical reagents. In a typical procedure, 3.62 g of $Cu(NO_3)_2\cdot 3H_2O$ was dissolved in 150 cm^3 of deionized water under stirring. Then, 0.05 M aqueous solution of hexamethylenetetramine was added into the above solution under constant stirring at room temperature, forming a blue aqueous solution with pH equal to 5.0. The obtained solution was then heated and refluxed with continuous stirring at 100 °C for 3 h in a three-necked refluxing pot. During refluxing, the temperature of the solution was controlled by manually adjustable thermocouple. After cooling to room temperature, the products were filtered, washed with deionized water and ethanol for several times, and finally dried in ambient environment. The product was labelled as sample A. Reaction time extended to 5 h, other conditions kept unchanged, the product was labelled as sample B.

Characterization of samples. The morphologies of products were determined by scanning electron microscopy (SEM, JSM-6480A), equipped with EDS (energy dispersive spectroscopy), and transmission electron microscopy (TEM, Philips CM 200 FEG, 160 kV). The structure and crystal phases were characterized by power X-ray diffraction (XRD) with CuK_α radiation, wavelength λ = 1.54178 Å (Rigaku D/Max-IIIA).The study of the thermal behaviour of the CuO nanocrystals was carried out with an STA 409 PC thermal analyzer at the heating rate of 10 °C·min^{-1} from 35 °C to 450 °C under argon atmosphere and under ambient atmospheric pressure. The quality and composition of the synthesized flower-shaped CuO nanostructures were characterized by the Fourier transform infrared (FT-IR) spectroscopy in the range of 400–4000 cm^{-1}.

Catalytic activity measurements. The catalytic activities of claw-like CuO nanostructures in the thermal decomposition of AP were studied by TG technique using the STA 409 PC thermal analyzer at the heating rate of 10 °C·min^{-1} in an Argon atmosphere over the temperature range of 35–450 °C. In this experiment, the CuO powders and NH_4ClO_4 were thoroughly mixed in the mass proportion of 2:98 to prepare the target samples for thermal decomposition analyses. A total sample mass of 3.0 mg was used in all runs. In this work, open alumina crucibles were employed for all runs in order to eliminate possible catalytic impacts from noble metals.

3. Results and discussion

In Figure 1, typical XRD patterns for the sample series are shown. XRD patterns of the samples thus obtained matched well the standard data for bulk CuO, while no impurity peaks from secondary phase of Cu_2O or Cu were detected. In addition, the EDS (Fig. 2c) spectrum reveals that the atomic ratio of Cu to O is equal to 1:1. Therefore, it is obvious that the sample is composed of pure monoclinic phase CuO which is consistent with the XRD pattern.

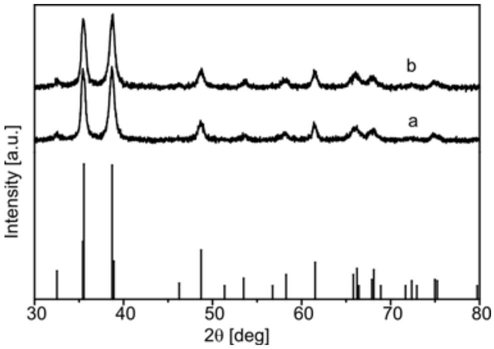

Fig. 1. XRD pattern of the CuO nanostructures; with reaction time 3 h (curve a) and 5 h (curve b); vertical lines represent the standard diffraction data of CuO from JPCDS file

The particle size and morphology of CuO nanocrystals were investigated using SEM (Fig. 2) and TEM (Fig. 3).

First, we briefly summarized the preparation conditions that yielded pure phase CuO nanocrystals with various reaction times. When CuO nanocrystals were prepared in solution at 100 °C simply by using copper nitrate and hexamethylenetetramine (HMTA) for 3 h, the morphologies of claw-like CuO nanocrystals with uniform shape and size were obtained on a large scale (Fig. 2a).

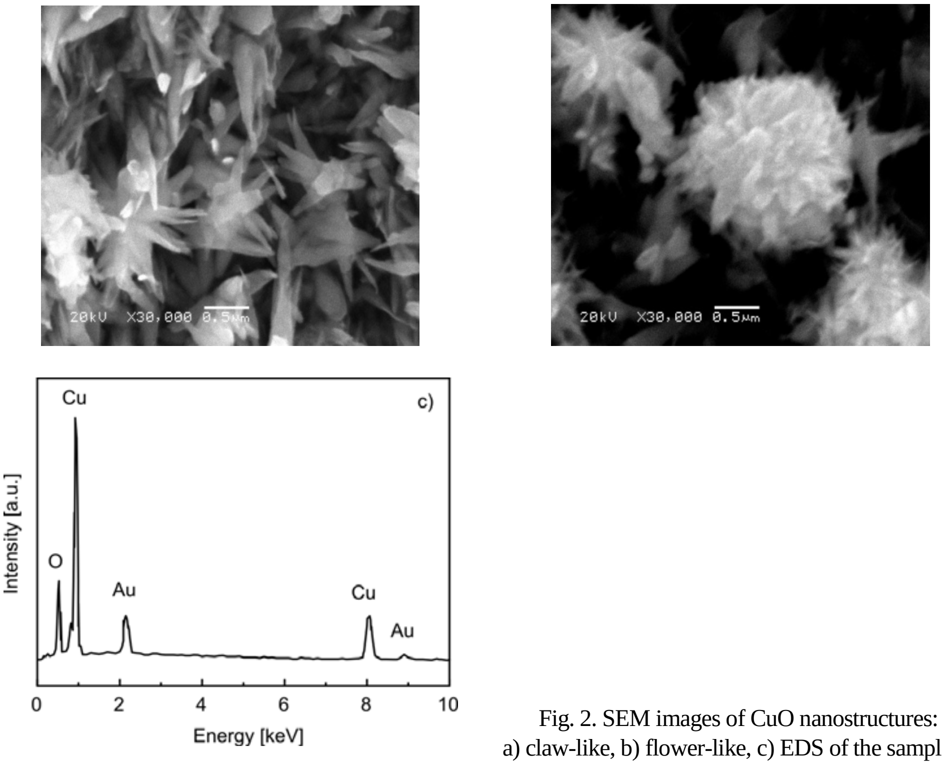

Fig. 2. SEM images of CuO nanostructures:
a) claw-like, b) flower-like, c) EDS of the sample A

When the reaction time extended to 5 h, the morphologies of CuO flower-like structures were investigated (Fig. 2b). Further structure characterization was carried out by the TEM equipped with the FFT setup. Figures 3a–c show the low magnification TEM images of the claw-like CuO nanocrystals, flower-like structures and building blocks. The lattice fringes can be easily observed from the HRTEM image. The lattice fringe corresponding to (110) ($d = 0.25$ nm) crystallographic planes of CuO is presented in Fig. 3d, which is consistent with the Fourier diffractogram shown in the inset. In addition, the crystal plane spacing ($d = 0.25$ nm) was calculated in the Gatan Digital Micrograph and the photos were disposed by the Adobe Photoshop Image.

The quality and compositions of the synthesized CuO structures, shown in Fig. 4, were characterized by the Fourier transform infrared (FTIR) spectroscopy in the range of 400–4000 cm^{-1}. Several bands appeared in the FTIR spectrum of the as-grown sample. The presence of a weak absorption at 3444 cm^{-1} is caused by the stretching vibration of the adsorbed water and surface hydroxyls. No infrared active modes from Cu_2O were detected. The absorption bands at 1673 cm^{-1} are bending vibrational modes of combined water molecules. The appearance of a weak and small absorption peak at 2339 cm^{-1} could be ascribed to CO_2 present in air. Absorption bands observed at 490, 433 cm^{-1} are characteristic of Cu–O vibrational modes. The absorption band at 1412 cm^{-1} was also found in the spectrum which was attributed to the presence of CH plane bending vibrations.

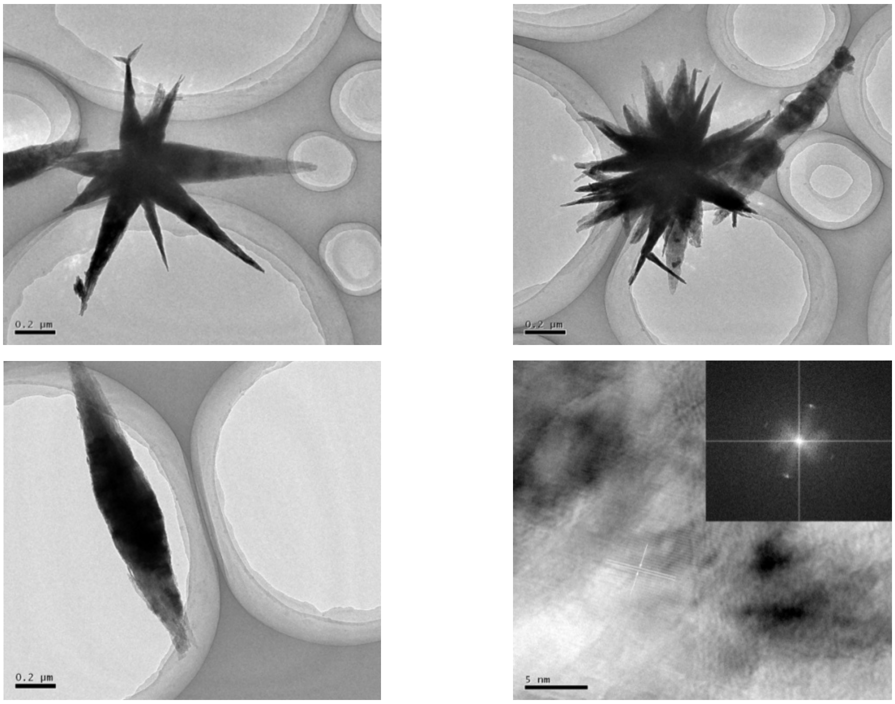

Fig. 3. Low magnification TEM image of CuO nanostructures: a) claw-like, b) flower-like, c) low magnification TEM image of primary building units, d) HRTEM image of sample A showing the difference between two lattice fringes being ca. 0.252 nm using a Gatan Digital Micrograph. Corresponding FFT pattern (inset) is consistent with the HRTEM observation

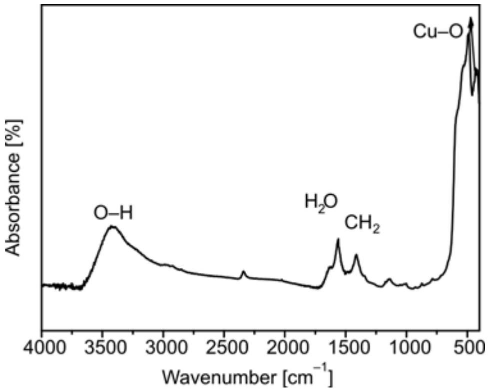

Fig. 4. FT–IR spectrum of the as-obtained final product A

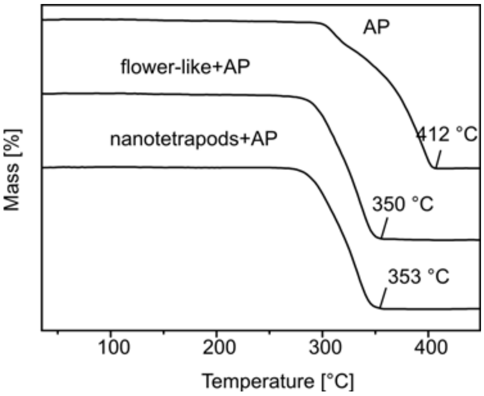

Fig. 5. TG curves for pure AP, mixtures of AP with addition of CuO nancrystals by the solution process in reaction times of 3 h and 5 h

To study the catalytic properties of the as-prepared CuO nanocrystals, the thermal-decomposition of the mixture of as-prepared CuO and NH_4ClO_4 was studied. Figure 5 shows TG curves for pure AP and mixtures of AP with CuO nanostructures. The decomposition of pure AP generally extends from 322 to 412 °C. Addition of CuO nanostructures in AP led to a significant reduction of the ending decomposition temperature, to 350 °C and 353 °C, respectively.

4. Conclusion

Claw-like or flower-like morphologies of CuO have been synthesized in a large-quantity via simple solution process at low temperature of 100 °C without the use of any complex instruments and reagents. The morphologies and crystallization of the as-prepared CuO were mainly determined by the molar ratio of hexamethylenetetramine ($C_6H_{12}N_4$) to $Cu(NO_3)_2$, reaction temperature and reaction time. The detailed structural investigations revealed that the as-grown products are nanocrystalline pure CuO possessing a monoclinic structure. The products show an effective catalytic activity on the decomposition of NH_4ClO_4. With the addition of nanocrystalline CuO, the temperature of thermal decomposition of AP decreased.

Acknowledgement

We gratefully acknowledge the support of this research by the Key Technology R&D Program of Heilongjiang Province (No. TB06A05), Science Fund for Young Scholar of Harbin City (No. 2004AFQXJ038) and basic research fund for Harbin Engineering University (No. mzj07076).

References

[1] LAKSHMI KANTAM M., RAMANI T., CHAKRAPANI L., VIJAY KUMAR K., Tetrahedron Lett., 49 (2008), 1498.
[2] ROUT L., JAMMI S., PUNNIYAMURTHY T., Organic Lett., 17 (2007), 3397.
[3] SUN Q., ALTARAWNEH M., DLUGOGORSKI B.Z., KENNEDY E.M., MACKIE J.C., Environ. Sci. Technol., 41 (2007), 5708.
[4] ZHANG J.T., LIU J.F., PENG Q., WANG X., LI Y.D., Chem. Mater., 18 (2006), 867.
[5] WANG S.Q., ZHANG J.Y., CHEN C.H., Scripta Mater., 57 (2007), 337.
[6] GAO X.P., BAO J.L., PAN G.L., ZHU H.Y., HUANG P.X., WU F., SONG D.Y., J. Phys. Chem. B., 108 (2004), 5547.
[7] ANANDAN S., WEN X.G., YANG S.H., Mater. Chem. Phys., 93 (2005), 35.
[8] CAO A.M., MONNELL J.D., MATRANGA C., WU J.M., CAO L.L., GAO D., J. Phys. Chem. C., 111 (2007), 18624.
[9] ZHANG H., LI S.Z., MA X.Y., YANG D.R., Mater. Res. Bull., 43 (2008), 1291.
[10] ZHANG Y.G., WANG S.T., LI X.B., CHEN L.Y., QIAN Y.T., ZHANG Z.D., J. Crystal Growth, 291 (2006), 196.
[11] ZOU G.F., LI H., ZHANG D.W., XIONG K., DONG C., QIAN Y.T., J. Phys. Chem. B., 110 (2006), 1632.
[12] WANG W.Z., ZHUANG Y., LI L., Mater. Lett., 62 (2008), 1724.
[13] CHANG Y., ZENG H.C., Crystal Growth Des., 4 (2004), 397.

[14] ZHU J.W., BI H.P., WANG Y.P., WANG X., YANG X.J., LU L.D., Mater. Lett., 61 (2007), 5236.
[15] YUAN G.Q., JIANG H.F., LIN C., LIAO S.J., J. Crystal Growth, 303 (2007), 400.
[16] LU C.H., QI L.M., YANG J.H., ZHANG D.Y., WU N.Z., MA J.M., J. Phys. Chem. B., 108 (2004), 17825.
[17] ZHANG H.X., ZHANG M.L., Mater. Chem. Phys., 108 (2008), 184.
[18] JIANG X.C., HERRICHS T., XIA Y.N., Nanolett., 2 (2002), 1333.
[19] ZHENG L.K., LIU X.J., Mater. Lett., 61 (2007), 2222.
[20] PREMKUMAR T., GECKELER K.E., J. Phys. Chem. Solids, 67 (2006), 1451.
[21] SARAVAN P., ALAM S., MATHUR G.N., Thin Solid Films, 491 (2005), 168.
[22] ZHANG M., XU X.D., ZHANG M.L., Mater. Lett., 62 (2008), 385.
[23] ZHANG Y.G., WANG S.T., QIAN Y.T., ZHANG Z.D., Solid State Sci., 8 (2006), 462.

Received 24 August 2008

Materials Science-Poland, Vol. 27, No. 2, 2009

Fabrication of MWNTs–PANI composite – a chemiresistive sensor material for the detection of explosive gases

C.-L. YUAN[1], C.-P. CHANG[2*], Y.-S. HONG[2], Y. SUNG[3]

[1]Graduate School of Defense Science, Chung Cheng Institute of Technology,
National Defense University, Tao-Yuan, Taiwan 335, ROC

[2] Department of Applied Chemistry & Materials Science, Chung Cheng Institute of Technology,
National Defense University, Tao-Yuan, Taiwan 335, ROC

[3]Chemical System Research Division, Chung Shan Institute of Science and Technology,
Tao-Yuan, Taiwan 325, ROC

A chemiresistive sensor was fabricated by the chemical modification of multi-walled carbon nanotubes (MWNTs) and chemical oxidation of polyaniline (PANI). The resistances of the sensing film samples against 100, 250, 500, 1000 ppm explosives (picric acid (PA), 2,6-dinitrotoluene (2,6-DNT) and 2,4,6-trinitrotoluene(TNT)) agents were investigated. The MWNTs with various wt. % PANI agents were characterized by TGA, SEM, FTIR and Raman spectroscopy, respectively. The experimental results showed that 1wt. % MWNTs and 10, 5, 1wt. % PANI sensor samples provided high sensitivity, excellent selectivity and good reproducibility to PA and 2,6-DNT vapours. In addition, principal component analysis (PCA) was applied to distinguish the performance of PA, 2,6-DNT and TNT agents. Our results indicate that the electric detection of explosive agents is possible with simply fabricated MWNTs–PANI devices.

Key words: *multi-walled carbon nanotubes; polyaniline; explosive; PCA*

1. Introduction

During recent years, explosives-based terrorism has grown enormously because explosive-based weapons are simple to make, easy to deploy, and can cause extremely large damage. Detecting explosives is a challenging task, because of a number of factors such as the low mass of explosives, frequent introduction of novel explosive compositions, and variety of concealment techniques [1]. Recently, many researchers have

---

[*] Corresponding author, e-mail: junelong@mail2000.com.tw

attempted to detect explosive gases using various methods, including electrical conductivity of metal oxide semiconductors, quadrupole resonance, X-ray diffraction, electron capture detection and ion mobility spectrometry. Those techniques, however, are expensive and require frequent calibration [2]. Therefore, the fabrication of a more reliable and inexpensive technique with stable sensors, and the ability to adjust the pattern recognition routine according to the variation in the explosives adsorptive matrix such as electrochemical/chemical polymer and nanostructure sensors is needed. Chemical sensors for the rapid detection of explosives are important because they have potential applications, such as tactical and humanitarian demining, remediation of explosives manufacturing sites and forensic and criminal investigations [3].

Since fast and accurate detection of explosives is essential to protect human beings, many researchers have already attempted to detect nitro-aromatic explosive gases using various kinds of sensors. The explosives are mainly classified into four specific types such as trinitrotoluene (TNT), tetryl, picric acid and dinitrotoluene (DNT). Investigations using MEMS explosive sensors based on piezoresistive silicon microcantilevers to the desorption of explosive TNT, PETN and RDX vapours from under ambient air have also been carried out [4].

Carbon nanostructures show unique properties and morphological flexibility which makes them multifunctional and compatible with organic and inorganic systems. In other words, the gas sensor fabricated with multi-walled nanotubes (MWNTs) may work at room temperature [5]. But it did not receive much attention due to its low sensitivity.

At present, analyses of this kind are possible exclusively within the confines of sophisticated research laboratories. “Nanostructure–polymer” detectors of explosives have to be portable, fast-acting, cheap, simple to operate, and they have to be very sensitive and selective to gases under detection. The sensor array described consists of various highly sensitive electrode carbon nanotube based sensors with metal assemblies, and carbon nanotubes coated with polymers. The viability has been established of semiconductor metal oxides (SMO) thick-film gas sensors prepared using cheap commercial sensor platforms and a very simple drop-coating technique accompanied with *in situ* annealing of the deposited films by integrated heaters [6]. In addition, MWNTs and polyaniline films deposited on glassy carbon (GC) electrodes by the layer-by-layer method and have shown to be excellent amperometric sensors for H_2O_2 [7].

Conducting polymers are an important and interesting class of organic conductors for molecular electronic devices. Polyaniline (PANI) is regarded as one of the most technologically promising conducting polymers because of its ease of preparation, low cost, high environmental stability and relatively stable electrical conductivity [8–10].

The aim of this study is to analyze the suitability of multi-walled carbon nanotubes (MWNTs)–PANI sensor arrays for the identification of certain gases, which swell reversibly and cause changes of resistance with a wide variety of chemical explosives in the gas/vapour concentrations at 1000, 500, 250, 100 ppm levels. Thereafter, the responses are examined to simulate the gases of trinitrotoluene (TNT), 2,6-dinitrotoluene (2,6-DNT) and picric acid (PA). Principal component analysis (PCA), one of the statistical classification methods, was performed, in order to classify these three test gases [11].

2. Experimental

Materials. Multi-walled carbon nanotubes were produced by the chemical vapour deposition (CVD) method, with the nominal outside diameter (OD) of 10–20 nm. All chemicals (aniline, acetonitrile, methanol, 1-methyl-2-pyrrolidone) used were AR grade, The explosive agents (Cerilliant) were fabricated in our laboratory. Ammonium persulphate was used as an oxidizing agent for the preparation of the polyaniline.

Preparation of polyaniline. 2.0 moles of dodecylbenzenesulfonate were dissolved in 1 cm^3 of aniline and allowed to stand at room temperature for 1 h. The ammonium persulphate ($(NH_4)_2S_2O_8$) solution was then added to 20 cm^3 of deionized water, with constant stirring, over a period of 30 min. The resulting deep-blue solution was removed and allowed to stand at room temperature for 12 h, then it was vacuum filtered and rinsed several times with deionized water (1.0 dm^3) followed by rinsing with methanol (1.0 dm^3). Polyaniline (Scheme 1) was allowed to remain under vacuum until it became a dark blue powder.

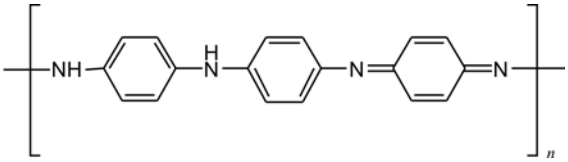

Scheme 1. Polyaniline (PANI)

Preparation of thin film (layer-by-layer), The first MWNTs (1 wt. %) layer-modified electrode was prepared by casting 5mg/cm^3 methylethylketone (MEK) of the dispersion on the surface of an interdigitated microelectrode device, which was air-dried at room temperature. When the methylethylketone had volatilized, an MWNTs film was formed. The PANI layer was then formed from the PANI solution (5 mg/cm^3, 1 M NMP) ultrasonicated for 10 min and deposited on the MWNT-modified microelectrode, which was vacuum-dried to form the sensing film.

Sensor measurements and characterization. Sensor response was measured using a customized interdigitated microelectrode (IME) device, having 12 pairs of gold electrodes 1 mm wide with the 1 mm spacing on an SiO_2 wafer substrate. A computer-interfaced multi-channel home-made multimeter was used to measure the lateral resistance of the nanostructured coating on IME. The resistance and frequency measurements were performed simultaneously under a computer control. All experiments were performed at room temperature. The gas flow was controlled by a calibrated Aalborg mass-flow controller (GFM-17), and the flow rates of the vapour stream were 100 cm^3/min. The vapour generating system followed the gas standard generator (KIN-TEK, Laboratories Inc. 670C). The vapour stream was produced by bubbling dry gas through a bubbler of the vapour solvent using a controller to manipulate vapour concentration. We measured the resistance percentage, and used the relative differential resistance change $\Delta R/R_0$ for the evaluation of the vapour sorption responses. ΔR is the difference of the maximum and minimum values in the resistance response, and R_0 is the initial resistance of the film. The gas devices were housed_in a Teflon chamber (inner diameter of 1/8 inch) with tubing connections to vapour and air pump sources. The setup of the vapour generating system followed the standard protocol. The vapour concentration in the unit was calculated from the weight loss and the volume of the analyte in the air.

The resistance measurement apparatus. An air pump was used for supplying/removing the carrier gas. Various concentrations of vapours were generated using an impingement system. At the beginning of the experiment, the test chamber was purged with air for 30 min to ensure the absence of air and also to establish the baseline. During the experiments, the test chamber was purged with air for 10 min and then with test vapour for 5 min at the desired vapour concentration.

The functionalized MWNTs–PANI samples were characterized using several techniques. A Fourier-transform infrared (FTIR, Brucher VECTOR22 spectrometer of Varian) spectrometer was used to examine the types of functional groups present in those samples. Raman spectra, with the excitation in the visible range of a HeNe 633 nm laser, were captured on a Renishaw inVia Reflex Raman microscope using an objective of the 50× magnification and 10 s accumulation time. The power was always kept low to avoid destruction of the samples. A thermo-gravimetric analyzer (TGA), manufactured by the TA Co. of America, was used to determine the content of MWNTs–PANI under air flow at the heating rate of 10 °C/min. The observation of polyaniline morphology was performed by a JSM-6500F scanning electron microscope (SEM).

3. Results and discussion

The TGA analyses have been carried out on carbon nanotubes to investigate the content of PANI on the MWNTs surface. Figure 1 shows the TGA curves of MWNTs–PANI and of pure PANI samples. In curve a, the weight loss of 18.72% can be attributed to the decomposition of PANI in the MWNTs–PANI. In contrast, the 57% weight loss of pure PANI occurred at 972 °C, resulting from thermal decomposition of the PANI sample (Fig. 1, curve b). The weight loss of the MWNTs–PANI is mainly due to the depolymerization of PANI chains; we can therefore assume that, the weight percentage of PANI on the MWNTs surface can be estimated to be 18.72%.

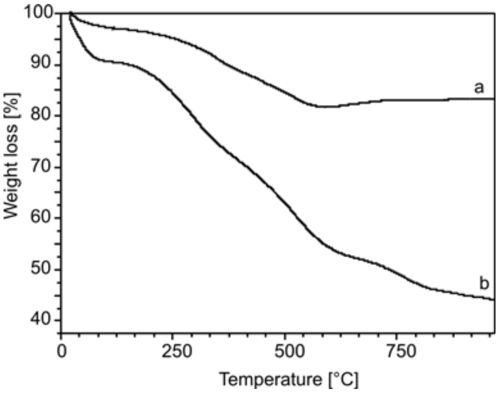

Fig. 1. TGA traces of 1 wt. % MWNTs –10 wt. % PANI (a) and pure PANI (b)

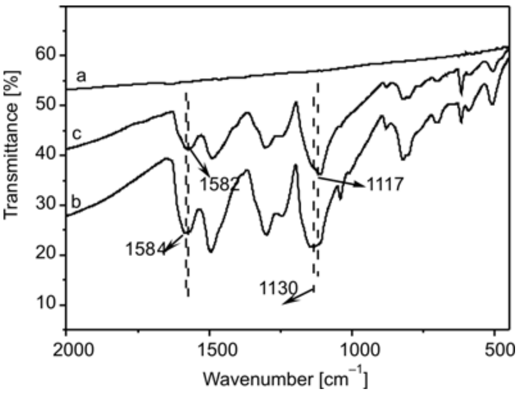

Fig. 2. FTIR spectra of MWNTs (a), MWNTs–PANI (b), pure PANI (c)

While the TGA data allows one to determine shows the concentration of PANI on the MWNTs surface, it does not provide any significant evidence as to the chemical bonding of the PANI onto the MWNT surface. Fortunately, it can be shown from FTIR spectra that the PANI was attached to the MWNTs. Figure 2 depicts the FTIR spectra of MWNTs, PANI and MWNTs–PANI. The characteristic absorption band of PANI is 1582 cm^{-1} (N=Q=N) and 1117 cm^{-1} (C–N) (Fig. 2, curve c), while the absorption peaks of MWNTs–PANI composite shift to 1584 cm^{-1} and 1130 cm^{-1} (Fig. 2, curve b). The absorption peak of the MWNTs–PANI composite is thus shifted by ca. 2 cm^{-1} and 13 cm^{-1} when compared to that of the pure PANI. These results indicate that intermolecular interactions exist between MWNTs and PANI. As shown in Fig. 2, curve a, pure MWNTs has no peak between 2000 cm^{-1} and 600 cm^{-1}.

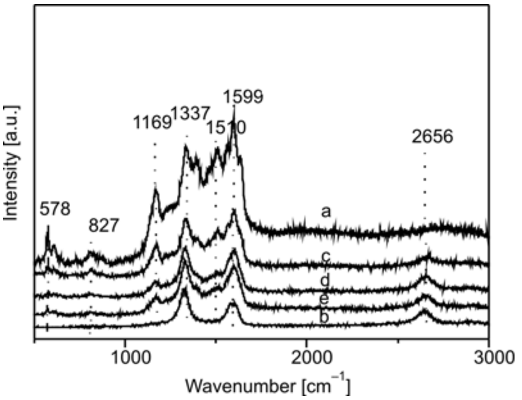

Fig. 3. Raman spectra of carbon nanotubes covered with PANI: pure PANI (a), pure MWNTs (b), 5 wt. % PANI–1 wt. % MWNTs (c), 10 wt. % PANI–1 wt. % MWNTs (d), 1 wt. % PANI–1 wt. % MWNTs (e)

Figure 3 shows that Raman spectroscopy is a useful tool for the characterization of PANI and MWNTs composite materials. A typical G-band (derived from the graphite-like mode) is situated at 1599 cm^{-1} in the spectrum of neat CNT. In contrast with the graphite G-band, which exhibits a single Lorentzian peak, the band for CNT has a shoulder extending to higher wavenumbers. The disorder-induced D-band is situated at 1337 cm^{-1} and its second-order harmonic D$_0$ band is found at 2656 cm^{-1} (Fig. 3, curve b). After coating of CNT with PANI, the spectrum of this polymer is dominant in all samples. This observation confirms that good coverage of CNT with PANI has been achieved. The peaks in the spectra are typical of protonated PANI and are located at 1599, 1510, 1337, 1169, 827 and 578 cm^{-1} (Fig. 3, curve a). Their positions remain practically unchanged for all contents of CNT. We have observed a relative decrease and a shift of the second-order of the disorder-induced band D$_0$ which indicates a less perfect structure for the nanotubes embedded in the polymer (Fig. 3, curves c–e) [12].

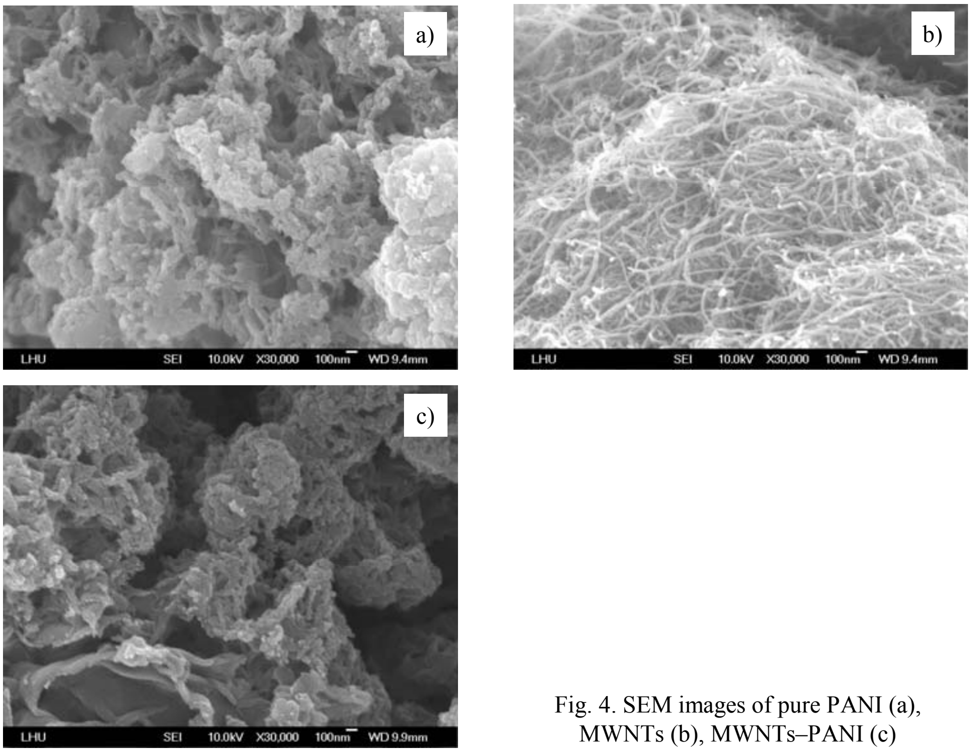

Fig. 4. SEM images of pure PANI (a), MWNTs (b), MWNTs–PANI (c)

Scanning electron micrographs (SEM) of the MWNTs and PANI are shown in Fig. 4. In these micrographs, PANI can be seen as an amorphous region. The surface of the particles is not smooth; lumps and holes (about 100 nm) in the material are visible (Fig. 4a). This uneven surface is a good property for gas adsorption. As shown in Fig. 4b, the SEM images also reveal that the MWNTs, with the diameter ranging from 30 to 80 nm, are well distributed on the surface and that most of the MWNTs are in the form of small bundles or single tubes. Such small bundles and single tubes assembled homogeneously on the substrate are believed to improve sensor performance because most of well-dispersed MWNTs are electrochemically accessible. In contrast,

Fig. 4c shows that depositing PANI on MWNTs film produces a layer-by-layer morphology : agglomeration and holes on the surface of the film were also observed. The larger diameter of PANI covered MWNTs compared with the neat MWNTs is visible.

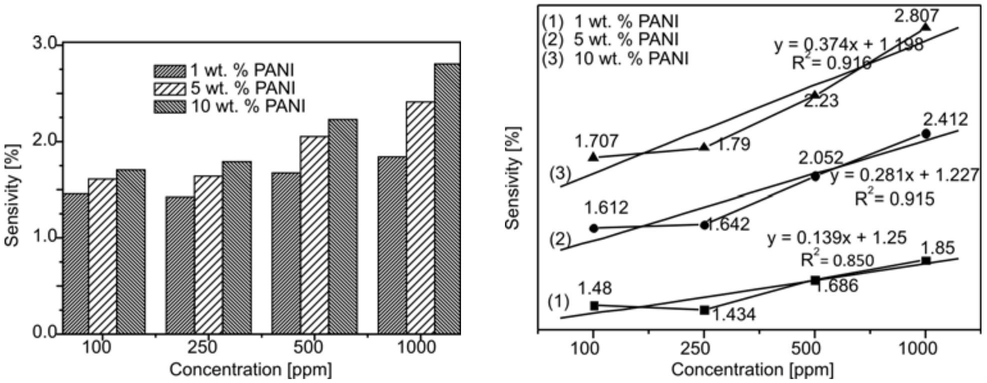

Fig. 5. Sensor response patterns (left) and fit-linear values (right) to TNT with an array of three weight percentages MWNTs/PANI sensing films

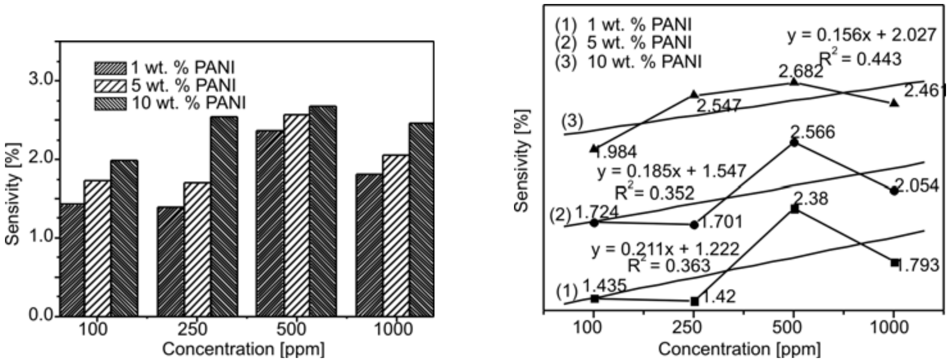

Fig. 6. Sensor response patterns (left) and fit-linear values (right) to 2,6-DNT with an array of three weight percentages MWNTs/PANI sensing films

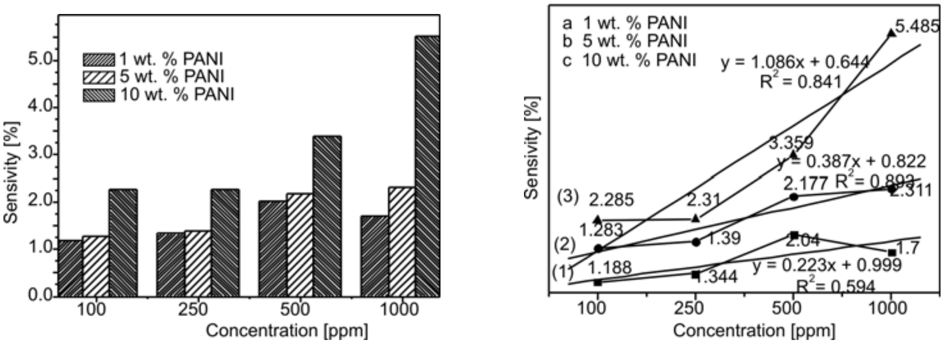

Fig. 7. Sensor response patterns (left) and fit-linear values (right) to picric acid with an array of three weight percentages MWNTs/PANI sensing films

The anchoring of PANI covering the MWNTs surface can impart its compatibility and transfer the electron, which greatly improves the responsiveness and reversibility of the materials. The response of the MWNTs–PANI composite film to three explosive vapours has been examined, as shown Figs. 5–7. Herein, the relative resistance responsivity is defined as $S = ((\Delta R)/R_0)\times 100\%$, where R_0 and R are the original resistance and the maximum resistance of the film upon exposure to the above explosive vapours, respectively. The resistance of the sensors was in the range of 20–100 kΩ.

As shown in Figs. 5–7, the responsivities of the MWNTs- PANI systems to TNT, 2,6-DNT, PA are about 1.18 and ca. 5.51, respectively. However, only very small responsivities to any other explosive vapours were observed, for example to TNT. All these facts mean that the 10 wt. % MWNTs–PANI sensor has a stronger anti-jamming capacity and high sensitivity to PA vapour, and is therefore considered to be an ideal candidate for potential selective sensor applications.

The phenomenon may be associated with the differences in physical properties of MWNTs and polyaniline (PANI) conductive polymers. A high polar surface energy component was found for multi-walled carbon nanotubes, which significantly differs from that of carbon black particles [13], leading to different interaction of MWNTs and PANI sensing films. Moreover, the MWNTs–PANI film with centrally hollow core structures enables the analytes to permeate both the inner-layer and the outer-layer of the polymer nanotube, thus swelling the polymers rapidly. Additionally, it is likely that when the interlayer interactions of nanotubes were introduced, MWNTs –PANI could induce changes from metal to semiconductor, resulting in an increase in resistance. Of course, whether PA can definitively induce a change in conductive performances by adsorption on the MWNTs–PANI surface needs further investigation.

In fact, the PANI chain consisting of aniline anion and $C_{18}H_{29}$ SO_3 cation units may be responsible for the unique characteristics of the composite samples. This structure allows the formation of inter- and intramolecular hydrogen bonds [14], and the electronic transitions from the valence band into the mid-band gap states occur through the polaron state, containing one electron; the bipolaron state (i.e., containing two holes) is completely empty. In this case, the polymer material appears to "swell" and "dissolve" so that the original structure or configuration of the film will be destroyed. At the same time, the polymer volume increases under swelling and the interlayer distance between MWNTs is enlarged, which breaks the conducting network, leading to a large increase in the electrical resistance of the film.

It is worth noting that the swelling behaviour of PANI chains wrapped around MWNTs is very different from that of a pure PANI matrix. The former is concerned with the influence of interactions on the surface of MWNTs–PANI. The interactions among polymer differ from the latter that is easy to aggregate. Thus, only the dissolution ability to polymer is not a sufficient criterion to throw light on the aforementioned phenomenon. Up to now, there has been no extensive theoretical investigation into the interaction between polymer and MWNTs [15]. One viewpoint suggests that the polymer molecular structure and atomic interactions at CNT interfaces are likely to significantly influence the properties of sensor systems [16]. The other viewpoint is that weak electrostatic or noncovalent interactions between highly delocalized electron system of nanotubes and polymer may affect the molecular recognition of PANI to solvent molecules. For covalently functionalized MWNTs, the polymer is individually anchored onto the tube surface, forming a nanoscale layer of coating, especially in the case of higher conducting polymer proportions. A hopping mechanism is responsible for intertube charge transfer between CNTs and an intertube modulation of the CNTs network *in lieu* of a conductivity change [17]. This leads one to conclude that PANI molecules form an assembly domain around MWNTs with a large radius (Fig. 8) being a plausible structure model, suggested to explain the response mechanism.

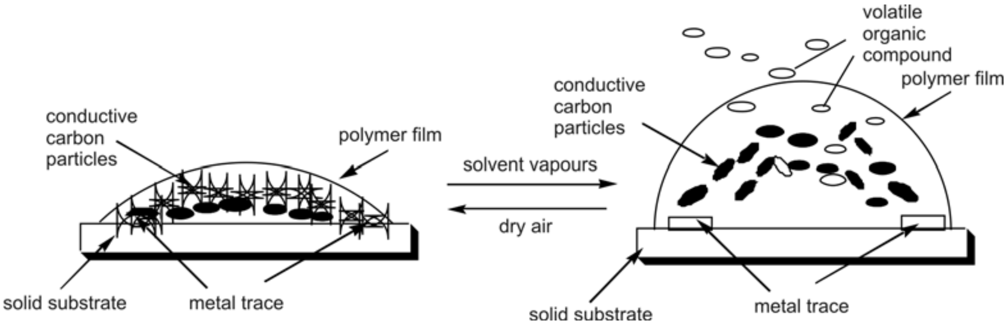

Fig. 8. Schematic representation of a possible structural model of MWNTs–PANI for explaining the response mechanism

In our study, explosive nitroaromatic compounds possess multiple basic sites at the nitro group oxygen atoms and the hydrogen-bond acidity of the polymer group is complimentary to these basic sites oriented to interact with electron rich oxygen atoms of the nitro groups on the nitro aromatic analytes. Here, hydrogen bonds may play an important role, and 2,6-DNT molecules act as good agents of MWNTs–PANI film. On the other hand, explosive agents such as TNT and PA, clearly induce an excellent response. Especially, PA vapour molecules act as a good agent of MWNTs–PANI film.

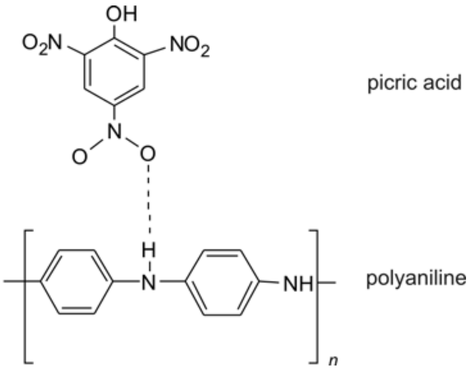

Scheme 2. Possible scheme of MWNTs–PANI interactions

Because the PA structure has –NO and –OH groups with strong electron donor properties, the sensor adsorption of a PA agent results in a partial charge transfer between the analyte and MWNTs–PANI that changes its electrical resistance, and speeds the motion and swelling of the polymer chains; it thereby breaks the conductive path and leads to an increase in resistance. The possible interaction is presented in Scheme 2.

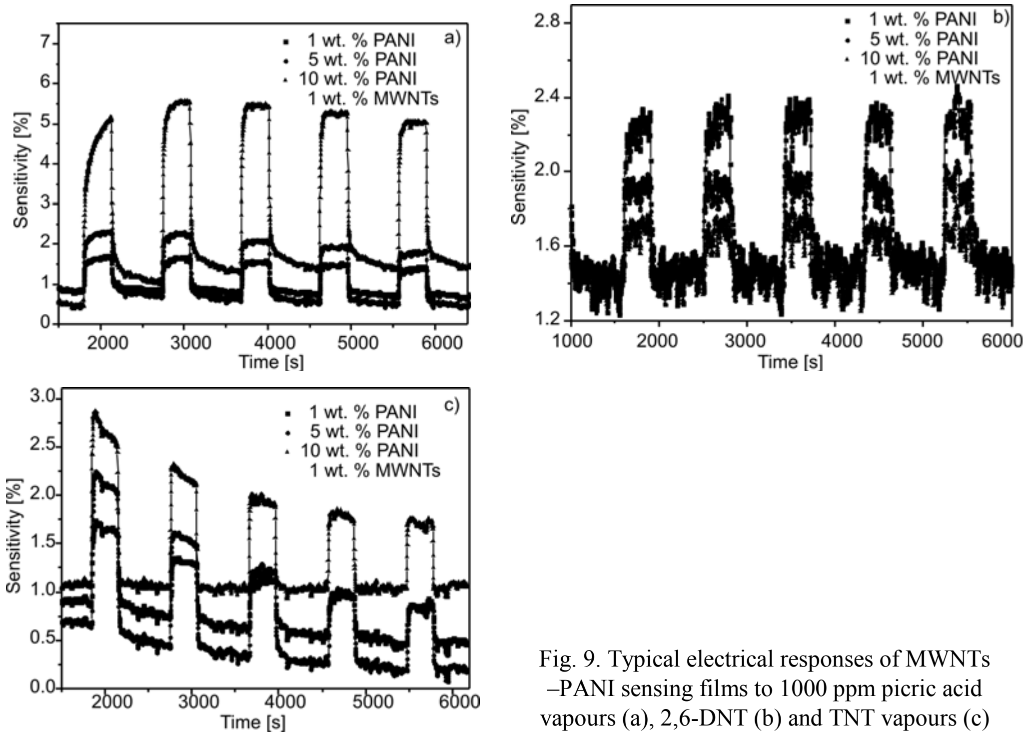

Fig. 9. Typical electrical responses of MWNTs –PANI sensing films to 1000 ppm picric acid vapours (a), 2,6-DNT (b) and TNT vapours (c)

We have contrasted the response patterns of the sensors in Figs. 5–7, based on the MWNTs–PANI materials. The resistance of the MWNTs–PANI (10 wt. %) sensing film drastically increased to over 5.5 of % within 1 s upon exposure to PA vapour (Fig. 9a). When it was transferred from the solvent vapour into dry air, the electrical resistance returned to the original value rapidly, showing a significant improvement in the restoring performance. This is also attributed to the weak hydrogen bond interaction between 2,6-DNT vapour and a polymer, which results in an abrupt adsorption of analyte molecules in a short time. The TNT adsorption resistance increased by about 1.73 of magnitude and the resistance could return to the original value (see also Fig. 9b). This further suggests that the rate of reversible response of the former is apparently superior to the latter. Therefore, a highly selective explosive gas sensor based on the MWNTs–PANI can be obtained. Figure 9 shows that the sensor developed from various weight ratios of MWNTs–PANI conductive material exhibits a better resistance reproducibility and stability five-fold exposure to the explosive vapours and dry air. Over a 6000 s period, the maximized variation in the baseline resistivity is less than 0.6 %. Such minor shifts did not significantly affect the response patterns and therefore do not affect sensor functionality. And the sensor film can be reused at least 12 times in this way. These results imply that the MWNTs–PANI material is a highly promising vapour sensor candidate, with excellent stability.

In the principle component analysis (PCA) study [18], the input data of the primary matrix are the normalized responses, chosen as the relative MWNTs–PANI resistance change ($\Delta R/R_0$), and processed by the correlation matrix (centred and standardized data). The response of the three MWNTs–PANI sensors array is normalized by the sum of all the sensor response values towards a given analyte. Such a normalization process reduces the dependence of the array response to the PA, 2,6-DNT and TNT concentrations, and also reduces slightly the effects of sensor drifts.

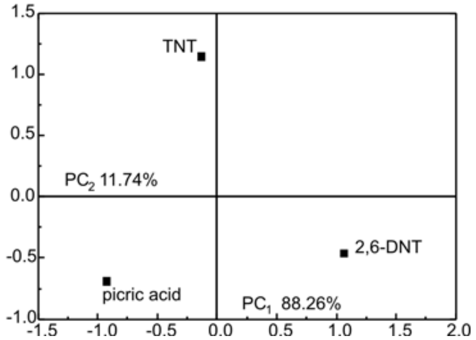

Fig. 10. PCA scores plot of the TNT, 2,6-DNT and PA in the PC_1–PC_2 plane of the original dataset obtained from the normalized responses of the all three deferent concentration MWNTs –PANI sensors of the IME

Figure 10 shows the scores plot in the PC_1–PC_2 class plane of two distinct clusters of PA, DNT and TNT with a spread of data points related to explosive agents with various graduated mixing ratios. The separate regions including the measurements of single simulantes indicate that the two different simulantes under test can be clearly discriminated from each other, and the first PCA value, 88.26, indicates the importance of the specific axis from the whole axis. In other words, if the sum of a whole axis importance was assumed to be 100, 88.26 means that the *X*-axis occupies about 88._As shown in Fig. 10, test gases can be easily distinguished by using a sensor array. The second principal component provides less information (11.74%), while the third principal component the lowest amount of information, by summing the overall information content of 100%. The results obtained indicate that the MWNTs–polymer composite sensors are the most appropriate option for the detection of a low concentration of an explosive.

4. Conclusion

We have demonstrated that chemical polymerization of PANI to the surface of MWNTs could endow devices with remarkable gas sensing properties with regard to both PA and DNT. The MWNTs–PANI sensor samples were afforded high sensitivity, excellent selectivity and good reproducibility or long stability. Thus the modification of the electronic structure of MWNTs–PANI by chemical functionalization provided a valuable route for the development of advanced sensor materials. To explain the selective responsiveness, we suggest swelling of PANI chains covering MWNTs. The interaction among PANI chains, MWNTs–PANI and analytes may also play an important role in gas sensing. The change in resistance of the film is caused by the interlayer distance change induced by the polymer swelling via gas absorption. On the other hand, the response on the MWNTs–PANI film to PA and 2,6-DNT differed from that to TNT, which is attributed to hydrogen bond interaction between explosive molecules and PANI chains. This interaction greatly affects the properties of MWNTs. In summary, we have developed a simple MWNTs, functionalized with a PANI sensor platform, for detecting explosive vapours at room temperature. The application of the PCA can be used to distinguish between the performance of PA, 2,6-DNT and TNT agents. The progress made here could be used as the basis for developing MWNTs –PANI sensors for highly sensitive and specific molecular detection.

References

[1] SENESAC L., THUNDAT T.G., Mater. Today, 11 (2008), 28.

[2] BYALL E.B., *Explosives report 1998–2001detection and characterization of explosives and explosive residue. A review*, 13th INTERPOL Forensic Science Symposium, Lyon, France, October 2001, pp. 16–19.

[3] TOAL S.J., TROGLER W.C., J. Mater. Chem.,16 (2006), 2871.

[4] PINNADUWAGEA L.A., THUNDATA T., GEHLA A., WILSONA S.D., HEDDENA D.L., LAREAUB R.T., Ultramicr., 100 (2004), 211.

[5] DOHN S., KJELSTRUP-HANSEN J., MADSEN D.N., MOLHAVE K., BOGGILD P., Ultramicr., 105 (2005), 209.

[6] TOMCHENKO A.A., HARMER G.P., MARQUIS B.T., Sens. Actuators B., 108 (2005), 41.

[7] QU F., YANG M., JIANG J., SHEN G.AND YU R., Anal. Biochem., 344 (2005), 108.

[8] SHIMANO J.Y., MACDIARMID A.G., Synth. Met., 123 (2001), 251.

[9] DHAWAN S.K., KUMAR D., RAM M.K., CHANDRA S., TRIVEDI D.C., Sens. Actuators B., 40 (1997), 99.

[10] GOSPODINOVA N., TERLEMEZYAN L., Prog. Polym. Sci., 23 (1998), 1443.

[11] LEEA D.-S., JUNGA H.-Y., LIMA J.-W., LEEB M., BANB S.-W., HUHC J.-S., LEE D.-D., Sens. Actuators B., 71 (2000), 90.

[12] BAIBARAC M., BALTOG I., LEFRANT S., MEVELLER J.Y., CHAUVER G., Chem Mater., 15 (2003), 4149.

[13] FREDERICH J..HARRIS P., *Carbon Nanotubes and Related Structures. New Materials for the Twenty-First Century*, Cambridge University Press, Cambridge, 1999.

[14] MATSUGUCHI M., UMEDA S., SADAOKA Y., SAKAI Y., Sens. Actuators B., 49 (1998), 179.

[15] BLAU W.J., PANHUIS M., MAITI A., DALTON A.B., VAN DEN NOORT A., COLEMAN J.N., MCCARTHY B., J. Phys. Chem. B., 107 (2003), 478.

[16] WEI C., Nano Lett., 6 (2006), 1627.

[17] VALENTINI L., BAVASTRELLO V., STURA E., ARMENTANO I., NICOLINI C., KENNY J.M., Chem. Phys. Lett., 383 (2004), 617.

[18] CHOI N.-J., KWAK J.-H., LIM Y.-T., BAHN T.-H., YUN K.-Y., KIM J.-CH., HUHD J.-S., LEE D.-D., Sens. Actuators B., 108 (2005), 298.

Received 5 May 2008
Revised 3 November 2008

Materials Science-Poland, Vol. 27, No. 2, 2009

Carbon supported Pt–Ni nanoparticles as catalysts in direct methanol fuel cells

S. S. DIPTI[1*], U.C. CHUNG[2], W.S. CHUNG[1]

[1]School of Materials Science and Engineering, Pusan National University, Busan 609-735, Korea

[2]Busan R&D Center, Korea Institute of Industrial Technology, Busan 609-735, Korea

Two types of carbon supported Pt–Ni nanoparticles were fabricated as catalysts for the cathode part of a direct methanol fuel cell, and were characterized by X-ray diffraction, transmission electron microscopy and cyclic voltammetry analyses. TEM and XRD analyses pointed to a good dispersion of the catalysts with carbon black and carbon nanotubes (CNTs) having sizes of ca. 2–6 nm, which is very important for supporting catalysts of the methanol fuel cell. CV analysis showed that the catalytic activity of a Pt–Ni/CNTs catalyst is more efficient than that of other catalysts. We also noticed that it is more appropriate to use a glassy carbon electrode rather than carbon paper as the working electrode for the methanol electrooxidation of Pt Ni/CNTs catalysts.

Key words: *carbon nanotubes; carbon black; direct methanol fuel cell*

1. Introduction

Fuel cells are efficient, silent and clean energy conversion systems producing electricity via electrochemical reactions. Direct methanol fuel cells (DMFC) are expected to be the first fuel cells to provide a power source for portable electronic devices, such as mobile phones, laptop computers and advanced mobile electronic devices [1]. A successful commercialization of DMFC is very much dependent, however, on the activity of their electrocatalysts. Nowadays, all pre-commercial, low-temperature fuel cells use supported Pt and Pt alloys as electrocatalysts. Critical properties to consider when choosing an electrocatalyst support include its electrical conductivity, surface area, microstructure, macromorphology, corrosion resistance and cost. carbon nanotubes (CNTs) have been shown to be more corrosion-resistant under operational conditions than carbon black (CB) in a simulated fuel cell [2–6]. Ever since their discovery in 1991 [7], CNTs have shown a highly electrochemically accessible surface area and offered a remarkable electronic conductivity in comparison with the vulcan carbon black.

---

[*] Corresponding author, e-mail: diptiru@yahoo.com

In the present study, we pretreated CNTs, CB and prepared electrocatalysts, then characterized these supporting Pt–Ni electocatalysts in order to find out better catalysts for DMFC, and finally we observed the performance of two types of working electrodes for Pt–Ni/CNTs.

2. Experimental

CNTs of diameters ranging from 10 nm to 20 nm were treated separately with 30% HCI and HNO_3 step by step at 120 °C with 300 rpm on a hot plate. Then they were washed twice and dried in an oven at 120 °C. CB was refluxed with 30% HNO_3 at 60 °C at 80 rpm. It was also finally filtrated, washed twice and dried in an oven at 120 °C. 20 wt. % of Pt–Ni nanoparticles were loaded separately onto CNTs and CB by the impregnation method. These catalysts were refluxed at room temperature and stirred for 12 h. The solutions were then evaporated by heating, rotating and drying at 100 °C. The impregnated samples were finally reduced with hydrogen at 350 °C. Before the hydrogen gas reduction, nitrogen was purged for 35 min to prevent reoxidation. For TEM investigations, catalysts were ultrasonicated in ethyl alcohol for 30 min and then deposited on Cu grids.

X-ray diffraction measurements of catalysts were accomplished using a CuK_α source. Scans were recorded at 5 deg·min^{-1} for 2θ in the range of 30–90°. Electrochemical measurements were performed with a computer-controlled voltammetric analyzer EGG 273 potentiostat/galvanostat.

A three electrode cell composed of an Ag/AgCl reference electrode, Pt wire as a counter electrode and a glassy carbon electrode (GCE) was used as the working electrode. The working electrode was polished with 0.5 mg alumina powder on a polishing cloth prior to each electrochemical measurement. Then, it was thoroughly rinsed with methanol and rinsed twice in distilled water, and then gently dried with tissue paper. The Nafion-impregnated Pt–Ni catalysts ink were prepared by mixing carbon material with 5% of Nafion (Aldrich Inc.) solution and electrocatalysts was applied on it. 1 M CH_3OH in 1 M H_2SO_4 solution was used as the electrolyte. To record another current –potential curve for Pt–Ni/CNTs, another three electrode cell was used, made of an Ag/AgCl reference electrode, Pt wire as a counter electrode and the sample pasted on carbon paper, used as working electrode. The working electrode was made of a paste of 5% Nafion and a catalyst sample (4 mg per square inch with catalysts). Voltammograms were recorded after fifty activation cycles for each measurement.

3. Results and discussion

Figure 1 presents a schematic diagram of fabrication of Pt–Ni nanoparticles with CNTs and CB. From Figure 2, one may conclude that the methanol oxidation on the two catalysts commenced in the potential range 0.7–0.9 V. The peak corresponding to full oxidation was found at 0.81V for Pt–Ni/CNTs catalysts; the peak is much higher and wider than the corresponding one for Pt–Ni/CB. This fact is very important for improving DMFC catalysts, and is probably due to a higher electrical conductivity of multiwall CNTs.

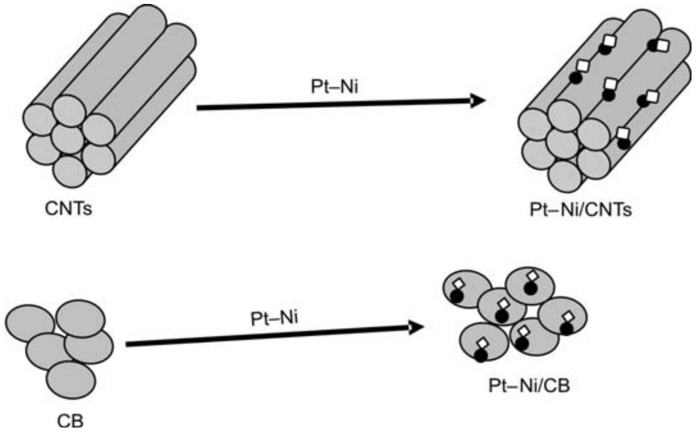

Fig. 1. Schematic diagram of fabrication of Pt–Ni/CNTs and Pt–Ni/CB catalysts

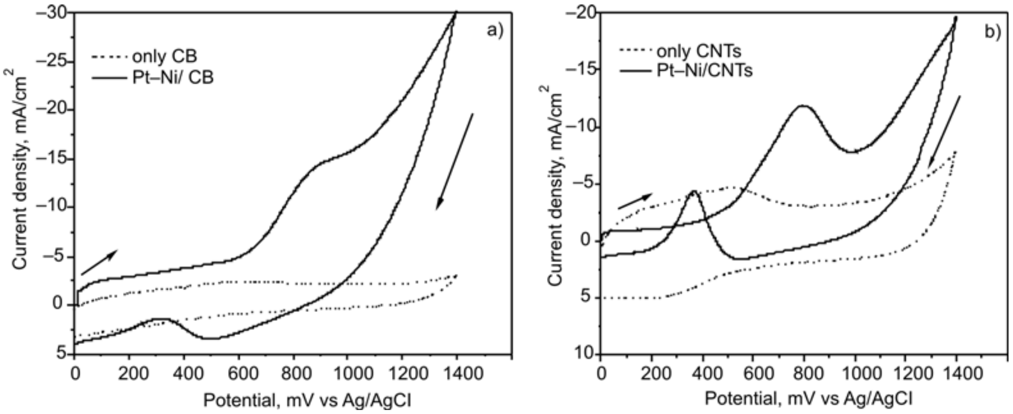

Fig. 2. Cyclic voltammetry of the catalysts: a) Pt–Ni/CB, b) Pt–Ni/CNTs

In fact, CNTs with Pt–Ni nanoparticles attached showed much more electroactivity. The change of the potential toward more positive values proved that the catalysts have high electrocatalytical activity. The peaks in the current were also protected from the methanol crossover voltages. The peak current densities associated with methanol oxidation at the forward scan were –12.0 and –12.7 mA/cm^2 for Pt–Ni/CNTs and Pt–Ni/CB, respectively. Moreover, CNTs are promising materials for improving the catalytic activity supporting fuel cell electrode reactions. Previous studies have also shown that Pt (or Pt alloys) supported on CNTs exhibits a better performance for the electrooxidation of methanol and oxygen reduction than that on vulcan XC-72 [8–11].

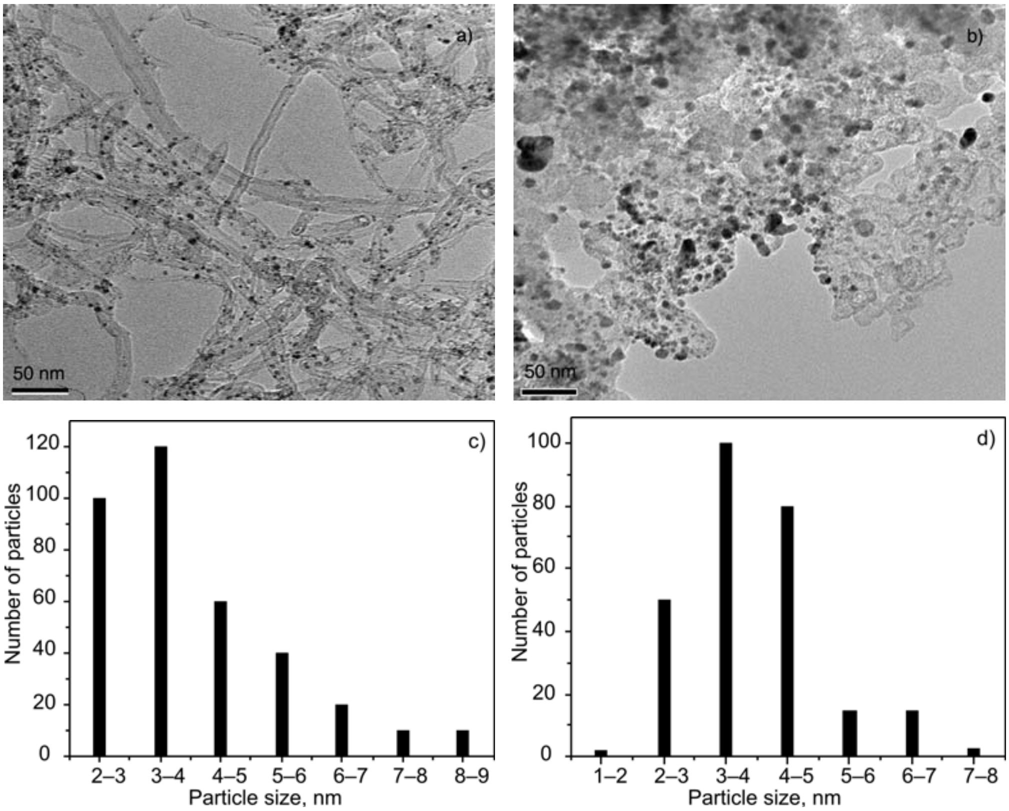

Fig. 3. TEM images of CNTs and CB supported catalysts: a) Pt–Ni/CNTs, b) Pt–Ni/CB taken at 50 nm wavelength and particle sizes shown in (c) for Pt–Ni/CNTs and (d) for Pt–Ni/CB

Figure 3 presents the TEM images of two types of catalysts. TEM was used to confirm the dispersion of the nanoparticles in the support, and the histograms for particle size distribution of each catalyst were obtained. The average sizes of each sample were respectively 2.12 nm (Pt–Ni/CNTs) and 3.26 nm (Pt–Ni/CB). The dependence of electroactivity on the particle size of the catalytically active component is well known. It is known that metal–support interactions can significantly affect supported catalysts. On the TEM image, Pt–Ni/CNTs catalysts indicated that the small black particles are better dispersed on the carbon support than that of Pt–Ni/CB catalysts. TEM images also confirmed that metal catalysts were uniformly and finely deposited on to CNTs.

In Figure 4, the TEM images are shown of the two catalysts taken at 20 nm wavelength. From these photographs, we can see that the CNTs surface acted as a stabilizer for the nanoparticles, to inhibit agglomeration. A high stability of Pt–Ni/CNT is probably due to a specific interaction between Pt–Ni and the support.

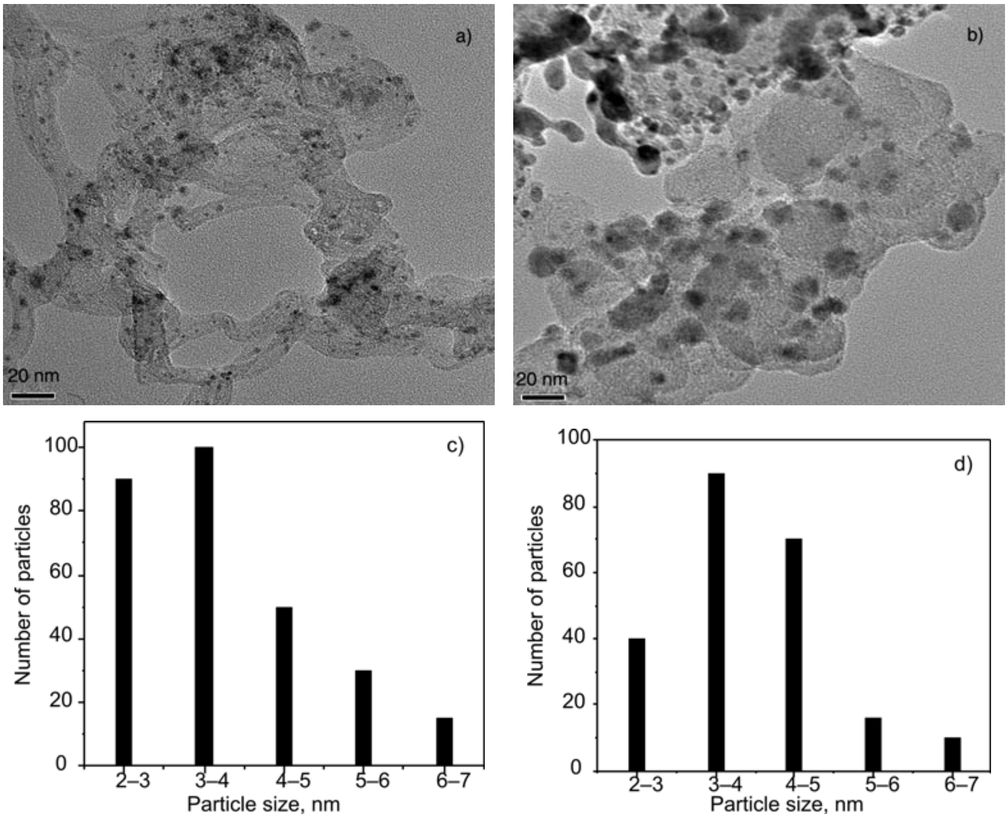

Fig. 4. TEM images of CNTs and CB supported catalysts: a) Pt–Ni/CNTs, b) Pt–Ni/CB at 20 nm wavelength and particle sizes shown in (c) for Pt–Ni/CNTs and (d) for Pt–Ni/CB

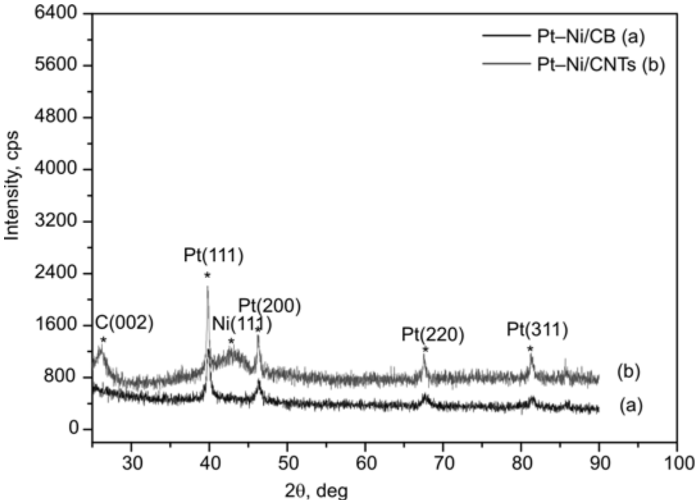

Fig. 5. XRD pattern of CNTs and CB supported Pt–Ni catalysts

The XRD patterns of Pt–Ni/CNTs and Pt–Ni/CB catalysts are shown in Fig. 5. In the case of Pt–Ni/CNTs and Pt–Ni/CB catalysts, Pt peaks are identifiable in the (111), (200), (220), (311) planes, and Ni peaks in the Ni (111) plane for specific 2θ values. The width of all peaks in Pt–Ni/CNTs is quite sharp and well localised, which is necessary for supporting catalysts of DMFC. It can be seen that the Pt–Ni/CNTs catalysts have the most intense diffraction peak in the (111) plane, among the supporting catalysts. This may indicate that the crystallization of the (111) plane has improved the Pt–Ni/CNTs catalyst activity.

The Pt–Ni/CNTs catalysts displayed the diffraction peaks characteristic of the *fcc* structure of Pt. The broader diffraction peaks for the two catalysts also led to smaller average particle size as calculates from Scherrer's equation:

$$L = \frac{0.9\lambda_{k\alpha 1}}{B_{2\theta}\cos\theta_B}$$

Here, L is the average particle size, $\lambda_{k\alpha 1}$ is the X-ray wavelength (1.54056 Å for $\mathrm{CuK}_{\alpha 1}$ radiation), $B_{2\theta}$ is the half-peak width for Pt (111), and θ_B is the maximum angle of the (111) peak. The calculated values of the average Pt particle sizes are 6.7±0.6 nm and 6.7 ±0.6 nm for CNTs and CB, respectively. The negligible differences between the particle sizes obtained by XRD with TEM are probably due to the fact that Scherrer's equation is only approximate. Another important detail is that the average particle sizes obtained from TEM are generally smaller than those for crystallites of XRD, but in most cases TEM results confirm the average values obtained from XRD when the standard deviation is considered. It has to be taken into account that only a fraction of particles were measured by TEM. TEM and XRD analyses consistently showed that the Pt–Ni/CNTs catalyst has a smaller particle size and more uniform distribution than Pt–Ni/CB.

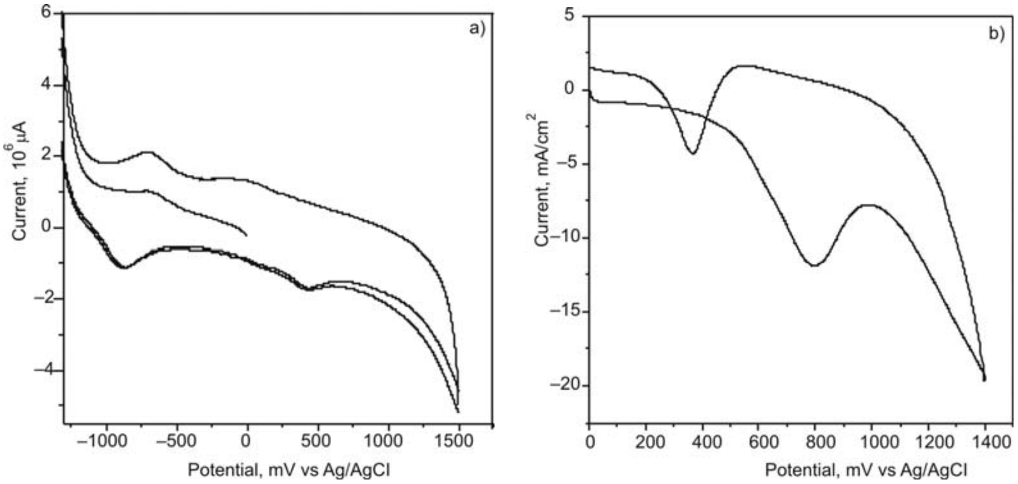

Fig. 6. Cyclic voltammogram of Pt–Ni/CNTs catalysts with:
a) carbon paper, b) GCE as a working electrode

Figure 6a shows the voltammogram of Pt–Ni/CNTs with carbon paper used as a working electrode. The oxidation-reduction peaks are observed in the potential region of –0.12 V to 0.4 V, demonstrating an electrochemically active surface area of the catalysts. However, upon comparison of the glassy carbon electrode (GCE) with the carbon paper electrode (Fig. 6b), it can be confirmed that the methanol oxidation peak for the Pt–Ni/CNTs catalysts appears in a more suitable potential range in the case of GCE: the peak appears at higher positive voltages thus allowing a higher methanol tolerance. For the Pt–Ni/CNTs, a very large cathodic current was detected between 0.7~0.9 V thus indicating a high electro-catalytic activity of the Pt–Ni/CNTs with GCE.

Figure 6b confirms that the peak is protected and very far from methanol crossover voltage because the methanol crossover drop voltage is from 0.2 to 0.3 V [8]. However, in the case of 20 wt. % Pt–Ni/CNTs (with GCE), the thickness of the catalyst layer is reduced and methanol can penetrate more easily into the electrode, even if the current is high. Probably due to that the current-potential curve for Pt–Ni/CNTs catalysts with GCE, better methanol electrooxidation occurs through electro-catalytic activity.

4. Conclusions

The performances of the two types of electrocatalysts were distinct with impregnation method for DMFC under similar conditions. The experimental results of methanol electrooxidation showed that the catalysts prepared on CNTs as supporting catalysts for cathodes produce better performance and have stronger resistance compared with those prepared on CB. However Pt–Ni/CNTs catalysts also have good particle sizes, according to morphological tests. Pt–Ni/CNTs will be efficient catalysts due to their particle size, adhesion, uniformity and electro-activeness for DMFC.

On the other hand, GCE for Pt–Ni/CNTs catalysts showed better electrochemical activity for methanol oxidation, compared with carbon paper as the working electrode. Thus the method is useful for direct methanol fuel cell applications and can be used as a general method for the preparation of other carbon supporting catalysts for methanol fuel cells.

Acknowledgements

This work was supported by a grant awarded to the National Core Research Center Program from the Ministry of Science and Technology and the Korea Science and Engineering Foundation (No. R15-2006-022-01001-0).

References

[1] CHEN C.Y., LIU D.H., HUANG C.L., CHANG C.L., J. Power Sources, 167 (2007), 442.
[2] SHAO Y., YIN G., GAO Y., SHI P., J. Electrochem. Soc., 153 (2006), A1093.
[3] NODA S., TSUJI Y., MURAKAMI Y., MARUYAMA S., Appl. Phys.Lett., 86 (2005), 173106.
[4] YE F., CHEN S., DONG X., LIN W., J. Natl. Gas. Chem., 16 (2007), 162.

[5] PRABHURAM J., ZHAO T.S., WONG C.W., GUO J.W., J. Power Sources, 134 (2004), 1.
[6] WANG Z.B., YIN G.P., SHI P.F., SUN Y.C., Electrochem. Solid State Lett., 9 (2006), A13.
[7] IIJIMA S., Nature, 354 (1991), 56.
[8] SEO Y.K., KIM Y.H., CHUNG U.C., CHUNG W.S., Solid State.Phen., 119 (2007), 247.
[9] DIPTI S.S., CHUNG U.C., CHUNG W.S., Met. Mater. Int., 13 (2007), 257.
[10] DIPTI S.S., CHUNG U.C., CHUNG W.S., Met. Mater. Int., 13 (2007), 417.
[11] DIPTI S.S., CHUNG U.C., CHUNG W.S., Phys. Stat. Sol. A, 204 (2007),4174.

Received 31 July 2008
Revised 18 November 2008

Materials Science-Poland, Vol. 27, No. 2, 2009

Composition and magnetic properties of M-Ba ferrite powders fabricated via sugar-nitrates process

X. TANG[*], Y.G. YANG

State Key Laboratory of OGRGE, Southwest Petroleum University,
No. 8 Xindu Road, Chengdu 610500, P.R. China

Fine M-type hexagonal barium ferrite (M-Ba ferrite) powders were synthesized by a novel sugar-based process. The effects of synthesis variables such as the molar ratio of Fe/Ba, the calcination temperature and the pH value of the precursor solution on the phase component of the obtained powder and the magnetic properties of M-Ba ferrite were studied by the thermogravimetric analysis, differential thermal analysis, X-ray diffraction, scanning electron microscopy and a physical properties measurement system. The results of this study showed that magnetic properties and formation of M-Ba ferrite were significantly influenced by the Fe/Ba molar ratio, the heat treatment temperature and pH of the precursor solution. Single phase M-Ba ferrite powders with the specific saturation magnetization of 63.6 emu/g and the coercivity of 1849 Oe could be obtained when the Fe/Ba molar ratio was 11.5 and the pH value of precursor solution was 6.5.

Key words: *sugar-nitrates process; M-Ba ferrite powder; X-ray diffraction; magnetic properties*

1. Introduction

Barium ferrite with a hexagonal molecular structure is a well-known permanent magnet. It is widely used in magnetic recording media, in microwave devices and as an absorber [1]. The conventional way of producing ferrite is by solid-state reaction of a mixture of $BaCO_3$ and Fe_2O_3, and then calcination at high temperature (higher than 1200 °C). The solid-state reaction method has some inherent disadvantages such as chemical inhomogeneity, coarser particle size, and the contamination with impurities during ball milling. In the last few years, alternative methods, such as chemical co-precipitation [2], precursor technique [3], salt-melt technique [4, 5], hydrolysis of metal-organic complexes [6], etc., have been proposed in order to overcome the limitations of the solid-state reaction method and improve the properties of barium ferrites. As is well known, the method of synthesis strongly affects homogeneity of the product, particle size distribution, shape, and magnetic characteristics [7]. Moreover, the

---

[*] E-mail: tungqin@126.com

synthesis parameters are interrelated in a complex way which, in turn, determines the material performance. In the current research, we present a novel, sugar-based process to prepare barium ferrite. Sugar (saccharose) is a carbohydrate, which yields two monosaccharides upon hydrolysis, and the product can easily be further oxidized into carboxylic acid in the presence of an oxidizer. Carboxylic acid is a kind of ligand and forms chelate complexes with many multivalent ions. Therefore, we used white granulated sugar as a chelating agent. A metal nitrates–white granulated sugar solution was used to prepare the precursor of the product, and then the precursor was thermally decomposed and transformed into fine powder of $BaFe_{12}O_{19}$. In this paper, we report on the synthesis, phase evolution, microstructure, and magnetic properties of barium ferrite. In particular, we discuss the effects of processing parameters such as pH, the molar ratio of Fe/Ba and the calcination temperature on the phase composition and magnetic properties of the resultant barium ferrites powders.

2. Experimental

Synthesis of samples. The chemicals used in this study were of reagent purity and were used without further purification. The starting materials were $Fe(NO_3)_3 \cdot 9H_2O$ (99.9% purity), $Ba(NO_3)_2$ (99.5% purity), white granulated sugar (Shanghai Sugar and Tobacco Industry Limited Company, China, GB317, saccharose >98%) and ammonium hydroxide (concentration: 30 wt. %). For studies on the effect of various Fe/Ba molar ratios, the molar ratio of Fe/Ba was set to 10.9, 11.5, and 12.0 which are denoted as A1, A2 and A3, respectively. The chemicals were weighed and dissolved in a minimum quantity of water (120 cm^3 for 0.1 mol of Fe^{3+}). Ferric nitrate and sugar solutions were mixed according to a prespecified proportion (for all the samples, the molar ratio of sugar to metal ions was set to 3/2) and barium nitrate was added with continuous stirring for 2 h. Then the mixed solution was evaporated slowly at 90 °C, during which the Fe^{3+} and nitrate ions provided an in situ oxidizing environment for the sugar to be hydrolyzed and converted into carboxylic acids. The nitrates themselves were decomposed with the evolution of brown fumes of nitrogen dioxide. Then the obtained solution was cooled. Solutions with various pH values can be obtained by introducing appropriate amounts of ammonia solution. The precursors were precipitated and separated from the reaction medium by adding ethanol. The shallow green precipitate was then filtered and dried at 80 °C for 24 h to become a dry precursor. Finally, powders of the dried precursors were heat treated in air at various temperatures at the heating rate of 10 °C/min to obtain barium ferrite phase.

Characterization. The thermal decomposition of the dried powders was examined by the DTA/TGA in air using a TA Instruments TGA2050 thermo-gravimetric analyzer with the heating rate of 20 $°C \cdot min^{-1}$. The X-ray powder diffraction pattern data of the samples were collected by an X-ray diffractometer (Philips X’pert Pro PW3040) set to a wavelength of 1.54051 Å of CuKα radiation in the 2θ range 20–80°. The morphology of particles was examined with a Philips Siron 200 field emission type scanning electron microscope (FE-SEM). The magnetic properties of some selected specimens were measured by means of a physical properties measurement system (PPMS-9, USA) at a maximum applied field of 30 kOe at room temperature.

3. Results and discussion

The TGA and DTA curves recorded in air for the dried precursor with the Fe/Ba molar ratio of 11.5 and a pH of 6.5 are shown in Fig. 1, as a typical example. All other samples show a similar thermal behaviour. The TGA pattern exhibits three distinct weight loss steps corresponding to an endothermic peak and two exothermic peaks in the DTA curve.

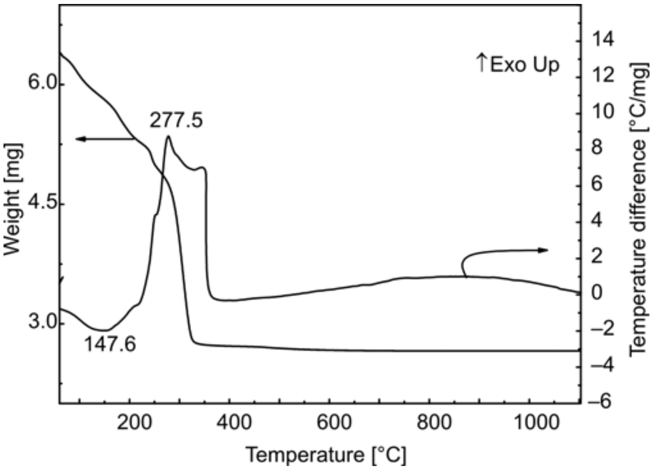

Fig. 1. DTA/TG curves of the dried precursor with the Fe/Ba molar ratio of 11.5 and pH value of 6.5

On heating we observe a continuous mass loss in the TG curve between room temperature and 250 °C which is accompanied by a distinct endothermic peak around 147.6 °C in the DTA curve, ascribed to the vaporization of residual water molecules; a more pronounced mass loss between 250 °C and 350 °C is associated with the release of large quantities of gas, the DTA analysis indicated a large exothermic double peak at 250–350 °C, which is caused by the release of a large amounts of heat due to vigorous oxidation reaction or combustion reaction of carbonaceous residue. The whole thermal process is accompanied by the evolution of large amounts of gas that is manifested in the weight loss in the TG curve. The exothermic temperature in the DTA pattern is consistent with the major weight loss temperature in the TGA pattern. No further distinguishable weight change above 350 °C is observed, though there is a broad exothermic peak around 800 °C, due to the crystallization process of phase transformation.

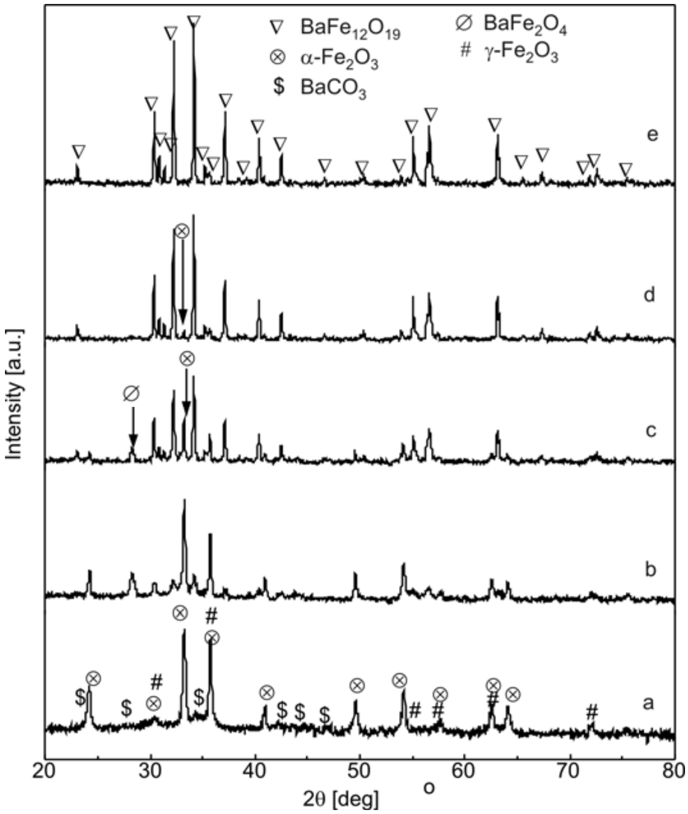

Fig. 2. XRD patterns of calcination powders at:
a) 400 °C, b) 650 °C, c) 850 °C, d) 1000 °C, e) 1100 °C

Figure 2 shows the X-ray powder diffraction patterns of the specimens with the molar ratio of Fe/Ba = 11.5 annealed at various temperatures. It is evident that the powder annealed at 400 °C mainly shows a mixture of phase α-Fe_2O_3, γ-Fe_2O_3 and $BaCO_3$. As temperature reached 650 °C, the intensity of γ-Fe_2O_3 decreases markedly, and $BaCO_3$ phase disappeared, the $BaFe_{12}O_{19}$ (JCPDS No. 74-1121) and intermediate phase identified as barium iron oxide ($BaFe_2O_4$) were formed. In the 850–1000 °C temperature range, $BaFe_{12}O_{19}$ was the major phase with a small amount of residual α-Fe_2O_3. Pure $BaFe_{12}O_{19}$ was formed at 1100 °C. It is in disagreement with the results by Pullar et al. [8] where the single phase barium ferrite can be easily formed directly in sol-gel systems, where no $BaCO_3$ is involved, and without formation of an intermediate phase. In this study, α- and γ-Fe_2O_3 co-exist in the intermediate phase in pattern (a), α-Fe_2O_3 has $FeTiO_3$-type structure, which belongs to the trigonal crystal system difficult to transform into the $BaFe_{12}O_{19}$ phase, a complete conversion of the mixture into single $BaFe_{12}O_{19}$ phase requires a high temperature.

Figure 3 shows the SEM micrograph of the specimens synthesized with the Fe/Ba molar ratio of 11.5 and calcined at 1100 °C for 2 h. From the image it can be seen that the sample consists of various morphologies, i.e., it shows small amounts of spherical particles and a greater number of platelets, aggregated and joined by weak bonding. As shown in the SEM micrograph, barium ferrite powders annealed at 1100 °C exhibit aggregates with an irregular shape and particle coarsening and sintering.

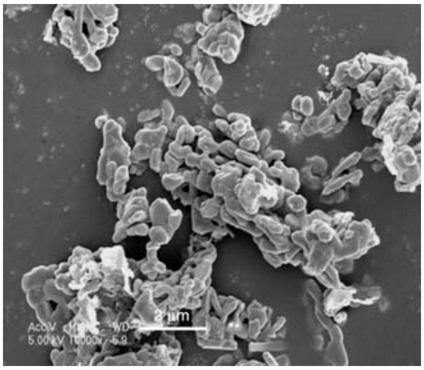

Fig. 3. SEM micrograph of the sample with the Fe/Ba molar ratio of 11.5, calcined at 1100 °C for 2 h

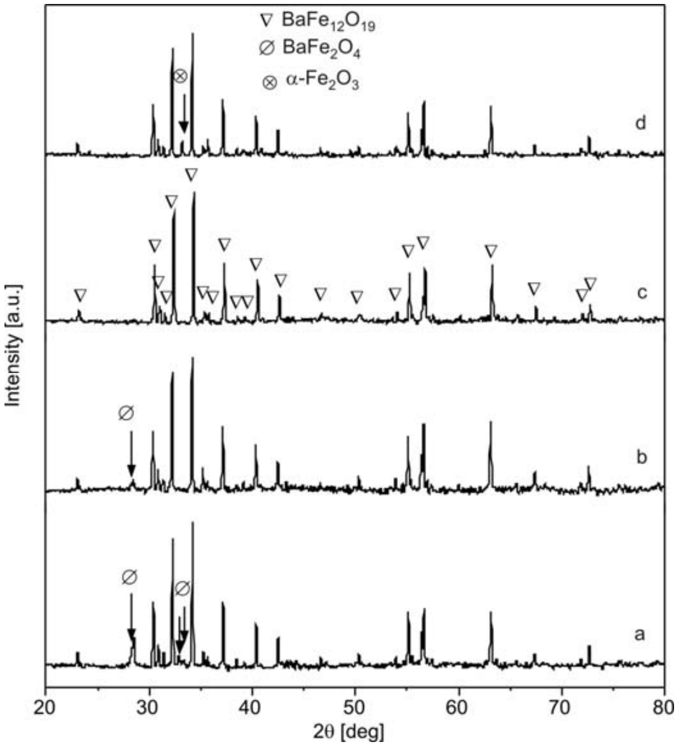

Fig. 4. X-ray diffraction patterns of powders derived from the sugar-nitrate process with various pH values of the precursor solution: a) 1.2, b) 4.0, c) 6.5, d) 9.0

The influence of pH of the precursor solution on the chemical composition of the sugar-based derived barium ferrite powders can been seen in Fig. 4, which shows the

XRD patterns of the specimens after having been thermally treated at 1100 °C for 2 h. The heated specimens with a Fe/Ba ratio of 11.5 were prepared using precursor solution of different pH values (i.e., pH = 1.2 (without any NH_4OH addition), 4.0, 6.5 and 9.0, respectively). Barium ferrite was the major phase in all specimens, however, pure barium ferrite was obtained at pH = 6.5. Small amounts of α-Fe_2O_3 or $BaFe_2O_4$ crystallites were detected at pH of 1.2, 4.0 and 9.0. As previously indicated, sugar yields two monosaccharides upon hydrolysis, and the product can easily be further oxidized to carboxylic acid in the presence of an oxidizer. Carboxylic acid is a kind of ligand and complexes with many multivalent ions to form chelates. Bechtold et al. [9] described the complexation of Ca^{2+} ions by the Fe–D-gluconate system, and the species distribution calculated for the system $Ca^{2+}Fe^{3+}$DGI is shown in Fig. 5.

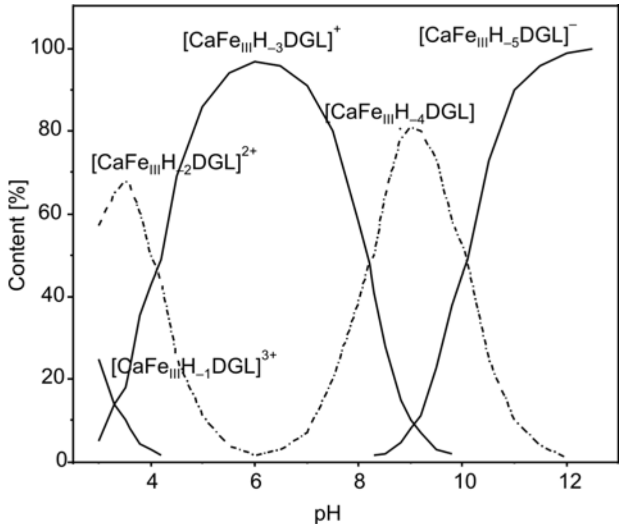

Fig. 5. Species distribution calculated for the system $Ca^{2+}Fe^{3+}$DGI [9]

In this case, gluconic acid molecules, with a carboxylic acid group at one end and five linear hydroxyl groups, easily form metal ion complexes in the complex system of Ba-Fe-gluconic acid. As described in the literature, the formation constants, species distribution and stoichiometry of the complexes are dependent on pH of the solution. It is believed that the complex species resulting from chelation of metallic ions in the solution is responsible for the phase composition of the resultant powders. Upon heating, the specimen prepared from the solution of pH = 6.5 can easily and completely convert to hexagonal barium ferrite.

The saturation magnetization (M_s), remanent magnetization (M_r) and coercivity (H_c) of barium ferrite particles at various pH are shown in Table 1. When the pH of the precursor solution is 6.5, the particles are single phase $BaFe_{12}O_{19}$, exhibiting better magnetic properties than those obtained at other pH values. It is believed that chemical phases present in the specimens are the main reason for small differences in the values of saturation magnetization. Magnetic data are in good agreement with the results obtained from XRD.

Table 1. Magnetic properties of calcined powders
for various pH values of the precursor solution

pH	M_s [emu/g]	M_r [emu/g]	H_c [Oe]
1.2	52.8	27.5	2476.3
4.0	58.4	30.8	2502.8
6.5	62.2	31.5	2546.5
9.0	55.5	28.6	2396.3

It is worthwhile to point out that these values of magnetic saturation are high, although they are lower than the theoretical one (72 emu/g). On the other hand, the coercivity values for the products are lower than those obtained for barium ferrite powders produced by coprecipitation [10]. It is unlikely that the lower coercivity were a result of the presence of small amounts of amorphous impurities, undetectable by XRD: it is far more likely that the intrinsic properties of the prepared powders are responsible. The higher saturation magnetization and the lower coercivity have potential applications in microwave absorption and in high-density magnetic recording. As is well known, the magnetic properties are influenced by many factors such as the grain size and particle size distribution, morphology and microstructure of particles, the method of synthesis, etc. According to our SEM image (Fig. 3), the particle shape was not an ideal hexagon and plate-like. Also, evident agglomeration occurred. In our opinion, the non-equilibrium microstructure and the uniform size of the particles should be the main reasons for those low coercivity values, and, in addition, the method of synthesis might be another reason. More evidence may be required to understand the present results of measurements.

Figure 6 shows the XRD patterns of the specimens obtained at various Fe/Ba molar ratios. Table 2 shows their magnetic properties. Single phase M-type $BaFe_{12}O_{19}$ powders with better magnetic properties were obtained at the Fe/Ba ratio of 11.5. On the other hand, the XRD patterns showed that formation of the mono-ferrite $BaFe_2O_4$ took place at the Fe/Ba molar ratio of 10.9 and of α-Fe_2O_3 at the Fe/Ba molar ratio of 12.0. Owing to their antiferromagnetic character, the α-Fe_2O_3 or $BaFe_2O_4$ intermediate phases deteriorate the magnetic properties. The appropriate molar ratio of Fe/Ba may vary with the fabrication method used and the starting materials. Liu et al. [11] suggested that the Fe/Ba molar ratio of 8 is a favourable one in order to obtain single phase M-type $BaFe_{12}O_{19}$. An investigation of the synthesis of barium ferrite by coprecipitation showed that the M-type phase only forms as a pure product in a non-stoichiometric mixture with a Fe/Ba =11 [12]. On the other hand, single phase barium ferrite can be obtained from a stoichiometric mixture of Fe/Ba = 12 via a sol-gel route [13]. Usually, an iron deficient non-stoichiometric mixture with the excess barium is needed to form the single-phase product.

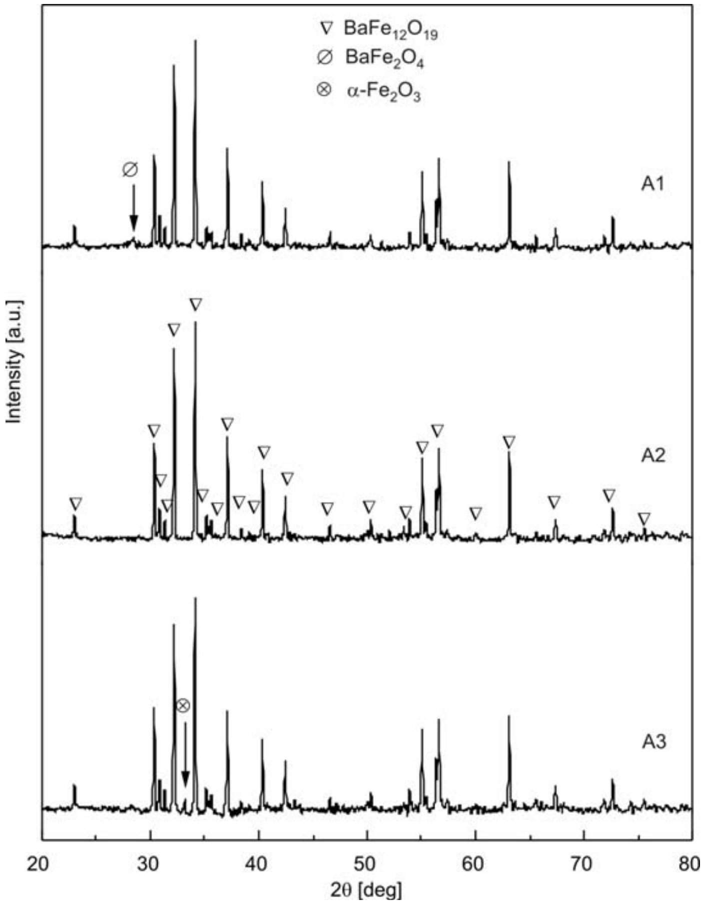

Fig. 6. XRD patterns of powders calcined at 1100 °C
for 2 h at various starting Fe/Ba molar ratios

Table 2. Magnetic properties of calcined powders for various Fe/Ba molar ratios

Fe/Ba molar ratio	M_s [emu/g]	M_r [emu/g]	H_c [Oe]
10.9	56.3	30.6	1649.5
11.5	64.5	33.8	1848.9
12.0	54.5	26.9	1785.2

In our study, it seems that the Fe/Ba molar ratio of 11.5 is more favourable than other ratios for the formation of single phase barium ferrite. In the case of chemical synthesis routes, it has been proposed that a deviation from $BaFe_{12}O_{19}$ stoichiometry should be considered due to variations in the solubility of the Fe^{3+} and Ba^{2+} cation sources. This can be accounted for by the fact that the solubility of Ba nitrate in water is poor, and the coordinative ability of carboxylic acid to the Fe^{3+} cation is much stronger than that of carboxylic acid to the Ba^{2+} cation. Ba nitrate can crystallize from precursor solution during evaporation [14]. The other reason is attributed to enhanced diffusion rates among various ions in the non-stoichiometric mixtures due to induced lattice defects permitting single-phase formation at a lower temperature [15]. Similar to the other synthesis routes, it is noticeable that an excess amount of barium ions is required in order to keep the stoichiometry for barium ferrite in the sugar-nitrates process.

4. Conclusions

Using $Fe(NO_3)_3\cdot 9H_2O$, $Ba(NO_3)_2$ and white granulated sugar as the starting materials, fine M-type barium ferrite powders were synthesized successfully by the sugar nitrates process. The crystal structure and magnetic properties of the prepared powders were investigated. The results show that the annealing temperature, the molar ratio of Fe/Ba and pH of the precursor solution affected greatly the phase composition and magnetic properties of M-Ba ferrite powders. Single phase M-type barium ferrite powders with superior magnetic properties were obtained at the Fe/Ba molar ratio of 11.5 and pH = 6.5. The powders exhibited higher values of saturation magnetization and lower coercivity. These features of the prepared powders point to their potential applications in microwave absorbing and in high-density magnetic recording.

Acknowledgements

The author thanks Prof. Hu Keao (School of Materials Science and Engineering, Shanghai Jiao Tong University, China) for helpful discussions on this research.

References

[1] MESHRAM M.R., NAWAL K.A., MISRA P.S., J. Magn. Magn. Mater., 271 (2004), 207.
[2] WANG C.S., QI X.W., LI L.T., Mater. Sci. Eng., B 99 (2003), 270.
[3] DA ROCHA CAFFARENA V., OGASAWARA T., PINHO M.S., LEIXAS CAPITANEO J.L., Mater. Sci.-Poland, 25 (2007), 875.
[4] TOPII U., OZKAN H., SOZRI H., J. Magn. Magn. Mater., 284 (2004), 416.
[5] YU X.J., ZHANG L.P., DONG Y.H., J. Rare Earths, 24 (2006), 129.
[6] HANEDA K., MIYAKAWA C., GOTO K., IEEE Trans. Magn., 23 (1987), 3134.
[7] BENITO G., MORALES M.P., REQUENA J., J. Magn. Magn. Mater., 234 (2001), 65.
[8] PULLAR R.C., BHATTACHARYA A.K., Mater. Lett., 57 (2002), 537.
[9] BECHTOLD T., BURTSCHER E., TURCANU A., J. Chem. Dalton Trans., (2002), 2683.
[10] HANEDA K., MORRISH A.H., IEEE Trans. Magn., 25 (1989), 2597.
[11] LIU X., WANG J., GAN L.M., NG S.C., J. Magn. Magn. Mater., 195 (1999), 452.
[12] CHEN D.H., CHEN Y.Y., J. Coll. Inter. Sci., 235 (2001), 9.
[13] PULLAR R.C., TAYOR M.D., J. Europ. Ceram. Soc., 22 (2002), 2039.
[14] ZHONG W., DING W., JIAN Y., J. Am. Ceram. Soc., 80 (1997), 3258.
[15] RANE M.V., BAHADUR D., J. Magn. Magn. Mater., 195 (1999), 256.

Received 8 September 2008
Revised 24 November 2008

Materials Science-Poland, Vol. 27, No. 2, 2009

Amorphous phase formation of Zr–Cu thin films fabricated by magnetron co-sputtering

L.X. LI[*], D.T. ZHANG, M. LI, H.X. WANG

College of Physics and Chemistry, Henan Polytechnic University, Jiaozuo, 454000 China

Zr_xCu_{1-x} amorphous films were prepared on Si(111) substrates by magnetron co-sputtering of pure Zr and Cu targets. It was found that the amorphous forming ability of the films increased with x when x was smaller than 65. It was therefore different from their bulk counterparts, which only for $x = 35$ and 50 were reported to have high glass forming ability during casting. The structures of the films were sensitive to the substrate temperature and the sputtering pressure of argon. X-ray diffraction and atomic force microscopic analyses of the $Zr_{65}Cu_{35}$ amorphous films annealed at various temperatures confirmed that the crystallization temperature was approximately 573 K.

Key words: *Zr–Cu thin film; magnetron sputtering; amorphous film; crystallization*

1. Introduction

Amorphous alloys have been researched intensively since the 1960s [1, 2] due to their special properties, which result from the long-range disorder arrangement of atoms. Two main ways to obtain new amorphous alloy systems are: (i) enhancing the cooling rate during casting, and; (ii) finding appropriate chemical composition for a given alloy. A high cooling rate could be obtained easily during film preparation. In 1929, Kramer fabricated for the first time an amorphous alloy by electrodepositing Au–Si films [3]. In recent decades, amorphous alloy films have been the subject to intense research, due to the progress of preparation technology (deposited by sputtering or evaporation, solid-state reactions, ion beam mixing, etc.), and its excellent potential for direct or indirect exploitation in applications such as superconducting [4], ultra-high density magnetic recording [5], shape memory [6], etc. Although much progress has been achieved in research on bulk metallic glasses (BMGs), most of them developed so far have been complex multi-component alloys. Consequently, it is difficult to examine glass forming ability (GFA) with these alloy systems. As amorphous

---

[*] Corresponding author, e-mail: lilixin@hpu.edu.cn

films can be prepared with relative simple alloy systems, they are, therefore, best candidates to understand GFA of alloys.

Zr–Cu alloy is an important amorphous alloy [7–10]. Several studies on the structure, mechanical properties [11–14] and superconductivity [15] of Zr–Cu amorphous alloy films have been reported in recent years. Dudonis et al. [16] fabricated Zr_xCu_{1-x} amorphous films in a wide composition range of ($5 \leq x \leq 95$) by using high working power (490–1380 W) in a relatively high vacuum ($p \leq 3\times10^{-2}$ Pa) during magnetron sputtering deposition. As the structure of the deposited films depends on the deposition parameters, the aim of this study was to acquire detailed understanding of how conditions of film deposition influence the formation of amorphous Zr-Cu films.

2. Experimental

Zr_xCu_{1-x} alloy films were prepared by magnetron sputtering deposition in an argon atmosphere. Two targets, pure Cu (purity, 99.999%) and pure Zr (purity, 99.999%), were used for co-deposition of the alloy films. Through altering the sputtering power for the two targets, films with various compositions were obtained. In the present experiments, the power used for the Zr target was 40–85 W, and the power for the Cu target was 80–130 W. The target–substrate distance was 130 mm. The target dimension was ∅80 mm. Single crystal Si(111) substrates, ultrasonically cleaned before deposition, were placed on a rotating holder which could be electrically heated. Before deposition, the targets were sputtered for 20 min in order to remove contaminants and oxides on the surfaces. Samples of the prepared films were annealed at various temperatures for 30 min in a furnace having the base vacuum of 5×10^{-4} Pa.

The compositions of the alloy films were measured by the Kevex-Sigma level4 energy dispersive spectroscopy (EDS) and the percentage error of measurements was lower than ±1%. Small angle X-ray diffraction was used to investigate the structures of the films. To observe the surface morphology of the samples, a Solver P47 atomic force microscope was employed.

3. Results and discussion

3.1. Influence of chemical composition on the amorphous film formation

In order to investigate the influence of composition on the amorphous formation ability, the Zr_xCu_{1-x} films were deposited under the same processing parameters except the sputtering power. A series of film samples with various compositions were prepared at room temperature (substrates), under the argon pressure of 0.5 Pa; the voltage bias was –30 V, and the sputtering lasted 15 min. Results of the small angle X-ray diffraction experiments of the films are shown in Fig. 1. The $Zr_{35}Cu_{65}$ film sample clearly displays a crystalline characteristics of separated Cu- and Zr-based solid solution phases rather than a single solid solution phase or any Zr–Cu compound.

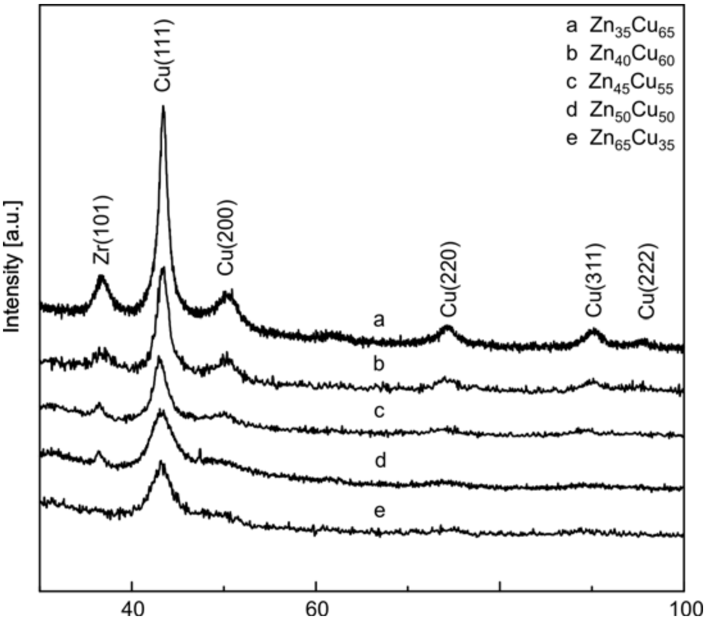

Fig. 1. XRD patterns of Zr_xCu_{1-x} films of several compositions

As the content of Zr in the composition increases in the $35 \leq x \leq 65$ range, both the phase separation tendency and the crystalline characteristics weaken. When $x = 65$, just one broad, diffuse peak was left, indicating a fully amorphous structure had been obtained. Beyond this composition range, the amorphous formation ability was decreased. Thus it can be concluded that the amorphous forming ability of Zr_xCu_{1-x} films increases continuously with the increase of Zr content. This result is apparently different from the bulk counterparts which have been reported that only with particular compositions did the amorphous structure form easily [7, 8, 11]. During casting, $Zr_{35}Cu_{65}$ alloy was proved to be a good glass former because it was around the eutectic composition and the liquid had a high stability which was beneficial for glass formation [17–20]. During the film deposition, this composition exhibited, however, rather low amorphous formation ability. In sputtering, the atoms or clusters were continuously deposited onto the surface of the substrates. Typically, deposited atoms had higher diffusion ability than the atoms in the liquid being quenched during casting. As reported [21, 22], the diffusivity was approximately by one order of magnitude higher during deposition. This was possibly why separated Zr- and Cu-based crystal phases were formed during deposition as only a limited solubility range was found in Zr-Cu alloy system from the phase diagram. Diffusion ability of the atoms, therefore, determines to some extent the formation ability of the amorphous film. As to the higher amorphous formation ability with increasing Zr content from 35 to 65 at. %, the most possible reason was also the atomic diffusion. Typically, atoms with smaller atomic diameters exhibit higher diffusion ability. Because the atom diameters of Cu and Zr are 0.256 nm and 0.320 nm, respectively, it is reasonable to conclude that Cu atoms have higher diffusion ability compared with that of Zr atoms. Therefore higher Cu content is not conducive for preparing amorphous film in Zr-Cu system.

3.2. Influence of the substrate temperature on the amorphous film formation

Substrate temperature is an important parameter influencing the structure of the alloy films. $Zr_{65}Cu_{35}$ films were sputtered at room temperature, 373 K and 573 K. According to the XRD patterns shown in Fig. 2, the film deposited at room temperature was fully amorphous. When the substrate temperature was, however, elevated to 373 K, the film showed crystalline characteristics. And when the temperature was further increased to 573 K, the crystalline peaks of Zr- and Cu-based phases were rather sharp.

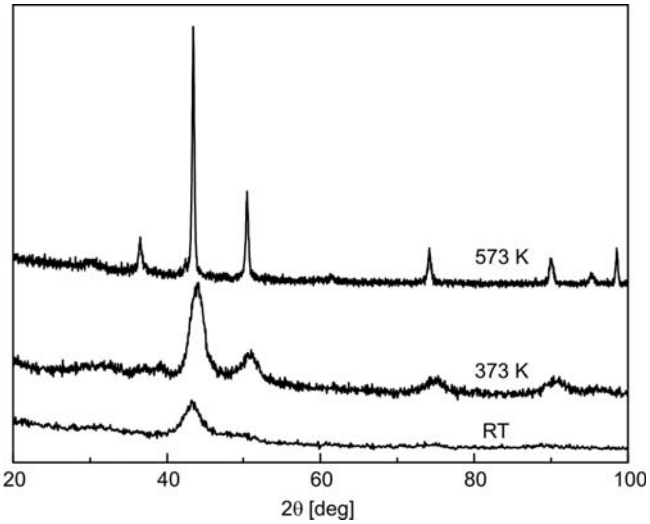

Fig. 2. XRD patterns of $Zr_{65}Cu_{35}$ films sputtered at various substrate temperatures

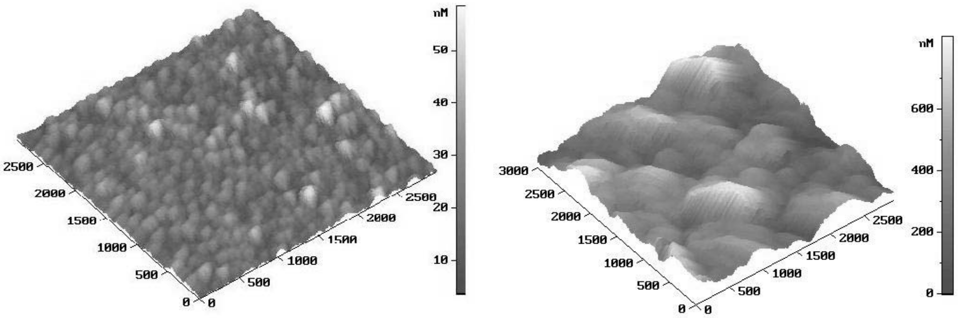

Fig. 3. AFM images of surfaces of $Zr_{65}Cu_{35}$ films sputtered at various temperatures of the substrate: 373 K (left) and 573 K (right)

AFM images of the morphologies formed at various substrate temperatures, as shown in Fig. 3, reveal that the higher substrate temperature was conducive to the crystalline formation. At a higher substrate temperature the atoms reaching the substrate had higher mobility and diffused more easily. Consequently higher substrate temperature was not conducive to the formation of the amorphous structure as pointed out above.

3.3. Influence of argon pressure on the formation of amorphous films

Appropriate argon pressure is necessary to deposit amorphous films. A relatively high pressure (≥ 2 Pa) decreases the quality of the films. On the other hand, if an ultra low argon pressure is employed, the plasma cannot be inducted, thus the deposition cannot take place. A pressure scale of 0.1–0.5 Pa was imposed in order to investigate the effect of working pressure on the amorphous formation of the films. For the composition of $Zr_{65}Cu_{35}$, obvious crystalline structure formed at the argon pressure of 0.5 Pa, as shown in Fig. 4.

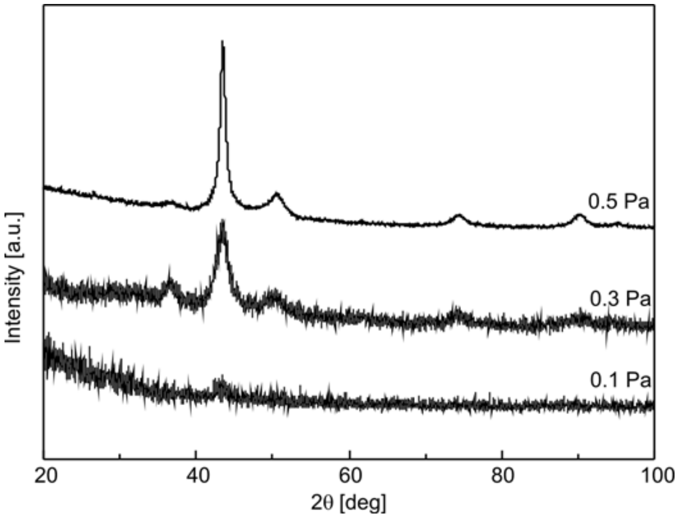

Fig. 4. XRD patterns of $Zr_{65}Cu_{35}$ films sputtered at various argon pressures

By decreasing the argon pressure, the amorphous formation ability was increased, and the pressure of 0.1 Pa was the optimum pressure for the formation of amorphous structure, assuming that the method of deposition satisfies all the conditions described earlier. When the pressure was smaller than 0.1 Pa, the deposition was too slow. The mechanism of the influence of pressure on the formation of amorphous films is hard to be explained. When the argon pressure was high, the atoms and the clusters sputtered from the Zr and Cu targets had higher energy and, and this consequently led to a higher diffusivity on the substrates. As pointed out above, separate Zr- and Cu-based crystalline phases formed more easily.

3.4. Annealing and crystallization of the $Zr_{65}Cu_{35}$ amorphous films

$Zr_{65}Cu_{35}$ amorphous film samples were annealed for 30 min at 373, 473, 573, 623, 673, and 773 K, respectively. The XRD results of the annealed samples as well as of the as-sputtered one are shown in Fig. 5.

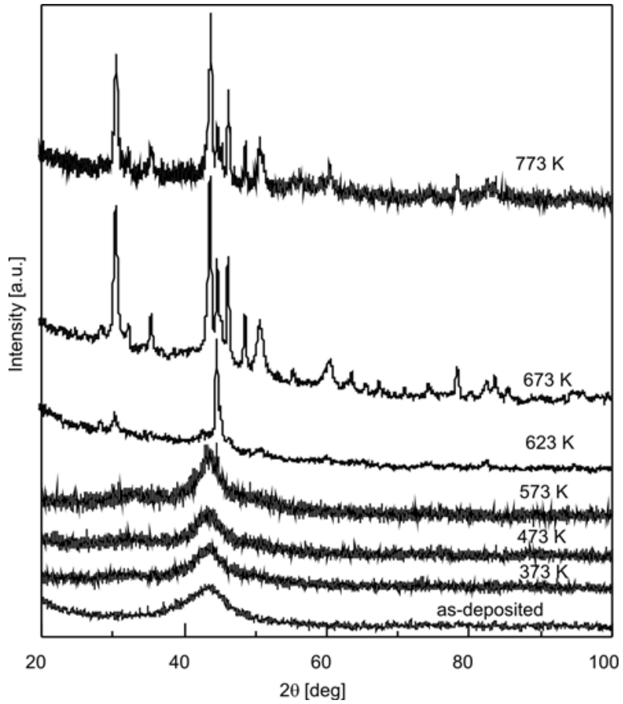

Fig. 5. XRD patterns of as-sputtered and annealed $Zr_{65}Cu_{35}$ films

It can be seen that the crystallization of the films did not occur when the temperature was lower than 473 K. However, some small crystal peaks can be seen in the XRD pattern of the sample annealed at 573 K. When the annealing temperature increased to 623 K, obvious crystalline peaks could be found in the XRD pattern. The film crystallized even further when annealed at 673 K. Thus, the onset temperature (T_x) of crystallization was at about 573 K.

4. Conclusions

In the range $35 \leq x \leq 65$, the amorphous forming ability of Zr_xCu_{1-x} films increased continuously with x. The amorphous formation ability was sensitive to the deposition parameters. If the argon pressure ranged between 0.1~0.5 Pa, a lower pressure was conducive to the formation of amorphous film. A high substrate temperature was unfavorable to the formation of the amorphous structure. The effect of the parameters investigated in this paper on the formation of the amorphous phase is probably due to their influence on the diffusivity of atoms or clusters deposited on the substrates.

Acknowledgement

This work was supported by the Natural Science Research Program, Foundation of Education Department of Henan Province (2008A430009).

References

[1] Clement W., Willens R.H., Duwez P., Nature, 187 (1960), 869.
[2] Wang W.H., Dong C., Shek C.H., Mater. Sci. Eng. R, 44 (2004), 45.
[3] Kramer J., Physics, 106 (1937), 675.
[4] Amato J.C., Appl. Phys. Lett., 85 (2004),103.
[5] Wang Y.T., Xi X.K., Fang Y.K., Zhao D.Q., Pan M.X., Han B.S., Wang W.H., Wang W.L., Appl. Phys. Lett., 85 (2004), 5989.
[6] Lee H.J., Ramirez A.G., Appl. Phys. Lett., 85 (2004), 1146.
[7] Tang M.B., Zhao D.Q., Pan M.X., Wang W.H., Chin. Phys. Lett., 21 (2004), 901.
[8] Wang D., Li Y., Sun B., Appl. Phys. Let., 84 (2004), 4029.
[9] Yu P., Bai H., Wang W., J. Mater. Res., 21 (2006), 1674.
[10] Kenoufi A., Bailey N.P., Schiotz J., Adv.Eng. Mater., 9 (2007), 505.
[11] Xu D.H., Lohwongwatana B., Duan G., Johnson W.L., Garland C., Acta Mater., 52 (2004), 2621.
[12] Das J., Tang M.B., Kim K.B., Theissmann R., Baier F., Wang W.H., J. Phys. Rev. Lett., 94 (2005), 205501.
[13] Musil J., Zeman P., Vacuum, 52 (1999), 269.
[14] Musil J., Daniel R., Surf. Coat. Techn., 166 (2003), 243.
[15] Karpe N., Bttiger J., Krog J.P., Nordström A., Rapp Ö., Thin Solid Films, 275 (1996), 82.
[16] Dudonis J., Brucas R., Miniotas A., Thin Solid Films, 275 (1996), 164.
[17] Lu Z.P. , Liu C.T., Intermetall., 12 (2004),1035.
[18] Turnbull D., Contemp. Phys., 10 (1969), 473.
[19] Ma D., Tan H., Zhang Y., Li Y., Mater Trans., 44 (2003), 2007.
[20] Wang D., Li Y., Sun B.B., Sui M.L., Lu K., Ma E., Appl. Phys. Lett., 84 (2004), 4029.
[21] Vauth S., Mayr S.G., Appl. Phys. Lett., 86 (2005), 061913.
[22] Faupel F., Frank W., Macht M.P., Mehrer H., Naundorf V., Ratzke K., Sochober H.R., Sharma S.K., Teichler H., Rev. Mod. Phys., 75 (2003), 237.

Received 19 October 2008
Revised 10 December 2008

Materials Science-Poland, Vol. 27, No. 2, 2009

Effects of substrate temperature on crystallite orientation of HfO_2 thin films

L. WANG[1,2*], B. FAN[1,3], Z. WANG [1], X. CHENG[1], Y. WU[1], L. CHEN[1]

[1]Institute of Precision Optical Engineering, Department of Physics,
Tongji University, Shanghai, 200092, China

[2]School of Media and Communications Technology, Liaocheng University,
Shandong Province, 252059, China

Optorun Co. Ltd. Kawagoe Shi, Saitama 350-0801 Japan

Hafnium dioxide thin films were deposited on fused silica substrates by reactive electron beam evaporation at three different substrate temperatures. After deposition, hafnium dioxide thin films were annealed in the ambient atmosphere for two hours at 500 °C and 1000 °C, respectively. X-ray diffractometry was used to study physical characterizations of as-deposited and annealed hafnium dioxide. The experimental results showed that hafnium dioxide fabricated at various substrate temperatures had different crystallite orientations after annealing at 500 °C or 1000 °C. These facts suggest that substrate temperature influences not only the crystallization state of as-deposited hafnium dioxide but also crystallite re-orientation after annealing.

Key words: *hafnium dioxide; reactive electron-beam evaporation; crystallite re-orientation*

1. Introduction

Hafnium oxide (HfO_2) has been extensively studied during the last few years due to its relatively high values of the refractive index, bulk modulus, melting point and chemical stability. In particular, it is being considered as a suitable high-*k* material candidate for replacing the gate dielectrics in field effect transistors and dynamic random access memories [1]. HfO_2 is well known as one of the most important oxide thin film materials for interference multilayer coatings down to 250 nm [2, 3]. In general, the dielectric properties of high-*k* materials can be affected by the degree of crystallinity, crystal structure, and crystallographic orientation, in addition to their stoichiometric composition. There have been several reports on the dependences of the dielectric constant upon the crystal structure or crystallographic orientation in high-*k* materials

---

[*] Corresponding author, e-mail: wangyleee@hotmail.com

[4, 5]. HfO_2 may form four crystalline phases (monoclinic, tetragonal, cubic, and orthorhombic) having different dielectric constants [6, 7]. Amorphous layers are generally preferable to gate oxides, but a polycrystalline layer may also be acceptable [8]. Tetragonal and cubic phases can be transformed thermodynamically at approximately 1720 °C and 2600 °C, respectively, whereas the monoclinic phase appears at room temperature [9].

It is therefore important to understand the crystallization kinetics of pure HfO_2 films deposited under various conditions and by various methods and when they are subject to high temperatures. Jiang et al. have demonstrated that the orientation of HfO_2 films is determined by the competition between the surface energy and strain energy by changing fabrication parameters [10]. The morphology and crystallization kinetics of HfO_2 films in function of annealing time or temperature have been previously reported [8, 11, 12]. Until now, however, little work has been done to study the relationship between deposition parameters and annealed HfO_2 crystallization state. In this paper, we report on the solid phase crystallization of HfO_2 films fabricated at various substrate temperatures and on the changes of crystallite orientation after annealing.

2. Experimental

HfO_2 films were prepared by using a box type electron-beam gun coating system (OTFC-1300DBI, Optorun.co., Ltd) at three deposition temperatures, i.e., 100 °C, 200 °C, and 300 °C, on fused silica substrates. The vacuum chamber was baked out prior to deposition for a minimum of 2 h. A programmable temperature controller was used to monitor and control the chamber temperature. Before evaporation, the chamber was evacuated to the pressure lower than 3.0×10^{-4} Pa. Ultrahigh purity O_2 was used to backfill the chamber to the pressure of 1.5×10^{-2} Pa for the deposition. The pressure was monitored by a hot cathode ionization gauge, and it was automatically controlled with a variable leak valve. The evaporation material for HfO_2 films was granular hafnium (of 99.9% purity). The rate approximately of 1 Å/s was maintained for all depositions. Film thickness and deposition rate were monitored by both a crystal monitor and an optical monitor. The crystal monitor was primarily used to control deposition rate, and the optical monitor was used to control film thickness. Table 1 shows the substrate temperatures and the film thicknesses.

Table 1. Films deposited at various substrate temperatures

Sample	Substrate temperature [°C]	Physical thickness [nm]
A	100	756
B	200	739
C	300	735

After deposition, HfO_2 samples were annealed in the ambient atmosphere for 2 h at 500 °C and 1000 °C. The crystal structures of HfO_2 films were investigated using an X-ray diffractometer (XRD Rigaku) in θ–2θ configuration with CuK_α radiation.

3. Results and discussion

The X-ray diffraction diagrams in Fig. 1 demonstrate that HfO_2 films deposited at 100 °C are amorphous, while other samples are polycrystalline.

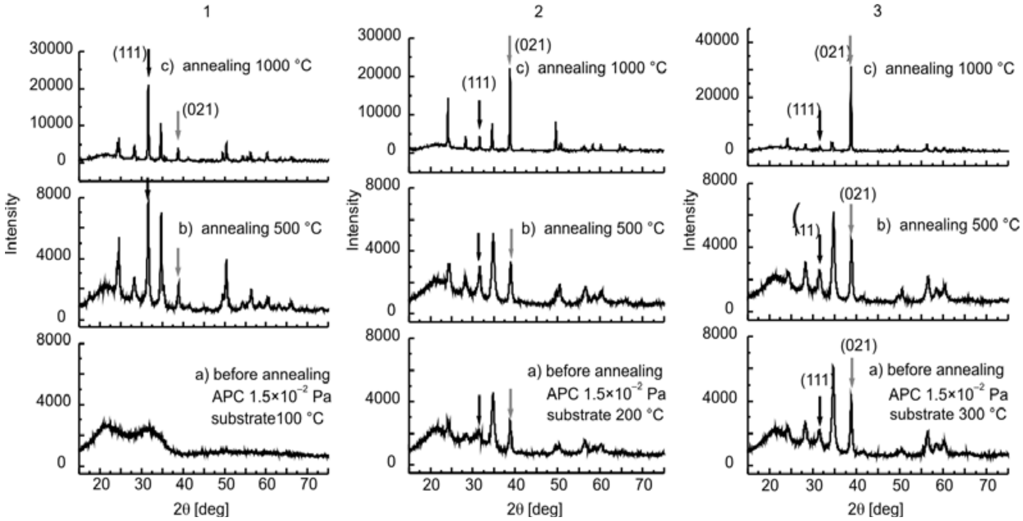

Fig. 1. The influence of substrate temperature to HfO_2 film crystallization state after annealing at: 1) 100 °C, 2) 200 °C, 3) 300 °C

The peak positions and intensities for monoclinic HfO_2 and Hf films from the powder diffraction ICDD card files are shown in Fig. 2.

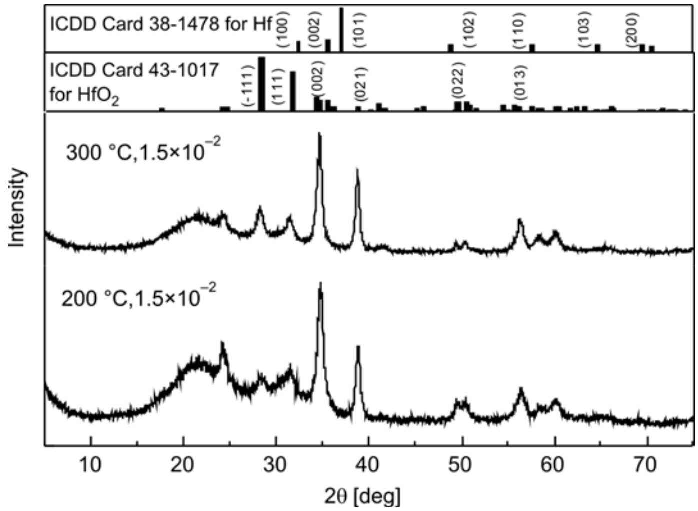

Fig. 2. ICDD card for hafnium and monoclinic hafnia

Each of the resolved peaks in Fig. 1 corresponds to the monoclinic crystal standard and there is no obvious Hf film peak. Around $2\theta = 35°$, there is a strong peak in Fig. 1 (curves 2a and 3a, respectively), which may be enhanced by the superimposed effects of (002), (020) and (200) orientations. The orientations of all the samples changed after annealing and showed different characteristics. After annealing at 500 °C, HfO_2 films deposited at 100 °C follow the transition from amorphous to polycrystalline with strong (111) peak and weak (021) peak, as shown in Fig. 1 (curves 1). As the deposition temperature increases, the (111) peak becomes weak and the (021) peak becomes gradually higher. After being annealed at 1000 °C, the re-orientation of HfO_2 proceeds and the films show the same orientation with stronger (021) peak compared with HfO_2 films annealed at 500 °C. It is obvious that HfO_2 films show preferred orientation during the annealing process. The degree of crystallinity depends strongly on the annealing and deposition temperature, indicating that grain growth in this system is thermally activated.

4. Conclusions

HfO_2 films were deposited at four substrate temperatures and annealed at 500 °C and 1000 °C. The results demonstrate that substrate temperature has great influence on the crystalline state of bpth, as-deposited and annealed HfO_2 films. Sample structure also has important consequences for their optical properties.

Acknowledgement

This work is supported by the National Natural Science Foundation of China (60508018), Committee of Science and Technology Shanghai Municipality (07dz22302) and 863 Project of China.

References

[1] ROBERTSON J., Rep. Prog. Phys., 69 (2006), 327.

[2] TORCHIO P., GATTO A., ALVISI M., ALBRAND G., KAISER N., AMRA C., Appl. Opt., 41 (2002), 3256.

[3] DAVID R., PAUL B., KENNETH J., Appl. Opt., 39 (2000), 1589.

[4] JOSHI P., COLE M., J. Appl. Phys., 86 (1999), 871.

[5] ZHAO X., VANDERBILT D., Phys. Rev. B, 65 (2002), 075105.

[6] LEGER J., ATOUF A., TOMASZEWSKI P., PEREIRA A., Phys. Rev. B, 48 (1993), 93.

[7] PARK P., KANG S., Appl. Phys. Lett., 89 (2006), 192905.

[8] HO M., GONG H., WILK G., BUSCH B., GREEN M., VOYLES P., MULLER D., BUDE M., LIN W., SEE A., J. Appl. Phys., 93 (2003), 1477.

[9] WANG J., LI H., STEVENS R., J. Mater. Sci., 27 (1992), 5397.

[10] JIANG B., REN C., ZHENG Z., LIU X., FAN H., YAO L., LI Y., SU X., Nucl. Instr. Meth. B, 215 (2004), 413.

[11] BOHRA F., JIANG B., ZUO J., Appl. Phys. Lett., 90 (2007), 161917.

[12] MODREANU M., PARRAMON J., CONNELL D., JUSTICE J., DURAND O., SERVET B., Mater. Sci. Eng., 118 (2005), 127.

Received 30 October 2008
Revised 25 March 2008

Materials Science-Poland, Vol. 27, No. 2, 2009

Hydrothermal synthesis and characterization of tube-structured ZnO needles

Y. Li[*], H. Feng, N. Zhang, C. Liu

College of Science, Civil Aviation University of China, Tianjin, 300300, P.R. China

Tube-structured ZnO needles were successfully synthesized hydrothermally, using H_2O_2 as the solvent, Zn $(NO_3)_2{\cdot}6H_2O$ and NaOH as the starting materials and $C_{19}H_{42}BrN$ as the additive. The samples were characterized by scanning electron microscopy, X-ray diffraction and room temperature photoluminescence measurements. The as-synthesized ZnO needle possesses a tube structure coiled by multilayer along the [0001] direction and a wurtzite structure. The intensity of the (0002) diffraction peak is obviously lower than the $(10\overline{1}0)$ and $(10\overline{1}1)$ peaks. Photoluminescence results reveal that the UV emission is restrained as hydrothermal temperature increases, and that the concentration of H_2O_2 has no influence on the photoluminesence when the concentration of H_2O_2 is higher than 10%.

Key words: *zinc oxide; hydrothermal synthesis; photoluminescence; morphology; tube*

1. Introduction

Zinc oxide (ZnO) is one of the important prospective short wavelength emitters owing to its large excitation binding energy and a wide energy gap of 3.3 eV at room temperature. It is also a material suitable for generating ultraviolet (UV) light [1]. Furthermore, high exciton binding energy of about 60 meV in ZnO, which is significantly larger than the thermal energy at room temperature (26 meV), can ensure an efficient exciton emission at room temperature [2, 3]. Owing to these properties, zinc oxide is widely used in various applications such as photonic devices [4], solar cell windows [5], plasma display panels [6], surface acoustic wave devices [7], and gas sensors [8]. It is well-known that the optical, electrical and magnetic properties of zinc oxide are markedly influenced by its microstructure and morphology [9]. Therefore, various morphological crystallites of zinc oxide, such as nanorods [10], and microflowers

---

[*] Corresponding author, e-mail address: liyan01898@163.com

[11], nanorings [12], nanowires [13] have been synthesized via different methods. Needle-shaped nano zinc oxide has been synthesized by the wet chemical method [14] and solid-vapour method [15]. In this paper, a novel tube-structured ZnO needles were successfully synthesized hydrothermally. The morphologies and photoluminescence of ZnO needles were characterized by XRD, SEM and PL methods. A multilayer structure, namely a spiral growth line and a honeycomb structure, not reported in the above references, have been found in our experiment.

2. Experimental

Nitrate hexahydrate ($Zn(NO_3)_2{\cdot}6H_2O$), sodium hydroxyl (NaOH), hydrogen peroxide (H_2O_2, 30%) and N,N,N-trimethyl-1-hexadecanaminium bromide (CTABr, $C_{19}H_{42}BrN$) were analytical grade reagents, purchased commercially and used without further purification.

The ZnO needles were prepared according to the following process. 0.1 M aqueous solution of $Zn(NO_3)_2{\cdot}6H_2O$ and 0.2 M solution of NaOH were all prepared with deionized water. NaOH solution was added to zinc nitrate solution drop by drop at room temperature under vigorous stirring which resulted in formation of a white suspension. The suspension was then separated with a centrifuge and washed three times with distilled water, and then finally washed with absolute alcohol. The separated powder was dried at 70 °C for 24 h in an oven to obtain the precursor. Subsequently, 2 g of precursor materials and CTABr were added to 30 cm^3 of H_2O_2 solution and the mixture was stirred and then sealed into a Teflon-lined autoclave with a filling capacity of about 35%. The autoclave was treated by hydrothermal method. Two batches of ZnO samples were obtained under different conditions. The first batch was synthesized at 70 °C, 90 °C, 120 °C, 150 °C and 180 °C for 12 h in a mixture of 30 cm^2 H_2O_2 (30%) and 0.1 g CTABr. The other batch was synthesized at 120 °C for 12 h in 30%, 25% and 10% H_2O_2 solutions. The resulting white precipitates were collected and washed with distilled water and alcohol for several times to obtain ZnO crystallites.

The morphology of ZnO particles was observed with a 1530VP model field emission scanning electron microscope (SEM) and Axioskop 40 Pol optical microscope. X-ray diffraction (XRD) with CuK_α radiation (λ = 0.1542 nm) on DX-2000 X-ray diffractometer was used for checking the formation and identification of compounds present in the obtained particles. Photoluminescence (PL) spectra of ZnO nanocrystals were recorded with a WGY-10 fluorescence spectrophotometer equipped with a Xe lamp (150 mW). The excitation wavelength was 325 nm. The emission spectrum of solid zinc oxide powder samples at room temperature was observed in the wavelength range of 350–650 nm.

3. Results and discussion

3.1. Powder X-ray diffraction analysis

Figure 1 shows the X-ray diffraction (XRD) patterns of as-obtained ZnO crystallites synthesized hydrothermally at various temperatures. In Figure 1, curves c–e, the the ZnO crystals possess a wurtzite structure and the diffraction peaks can be well indexed to hexagonal ZnO with the lattice parameters a = 0.324982 nm and c = 0.520661 nm. Although the peaks of $(10\bar{1}0)$ and $(10\bar{1}1)$ planes in Fig. 1, curves a, b are uniform with that in Fig. 1c–1e (0002), $(10\bar{1}2)$ and $(11\bar{2}0)$ peaks are not visible due to small sizes and lower dimension of the samples synthesized at lower temperature. Meanwhile, the intensity of the (0002) peak in Fig. 1 is obviously lower those of the peaks $(10\bar{1}0)$ and $(10\bar{1}1)$. This result seems to be in conflict with the long needle shaped morphology (Fig. 2) grown quickly along the [0001] direction. In fact, the low intensity of the (0002) peak is caused by a small area of (0001) cross section and a thin multilayer wall of the tube-structured needle. Upon increasing hydrothermal temperature, the diffraction peaks intensities of five polar planes increase substantially, because the growth rate of ZnO increases when the temperature is raised.

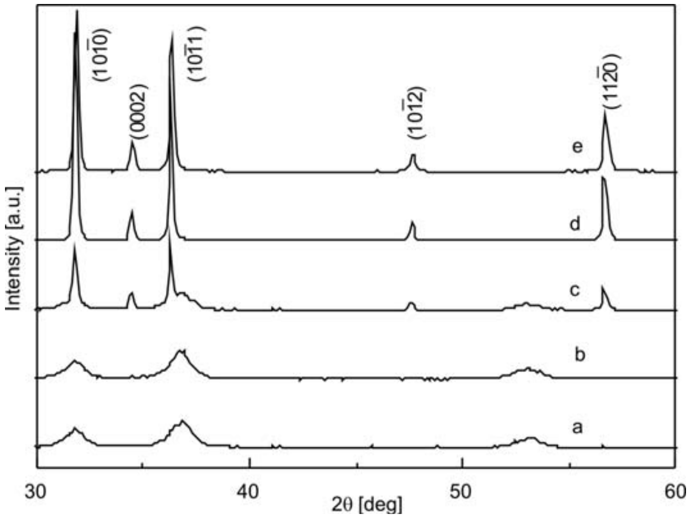

Fig. 1. XRD patterns of ZnO needles synthesized at: a) 70 °C, b) 90 °C, c) 120 °C, d) 150°C, e) 180°C

3.2. Morphology of ZnO samples

Figure 2 shows the morphology of the synthesized ZnO. Samples synthesized at various temperatures have similar morphologies to that in Fig. 2 besides having larger dimensions at higher temperatures.

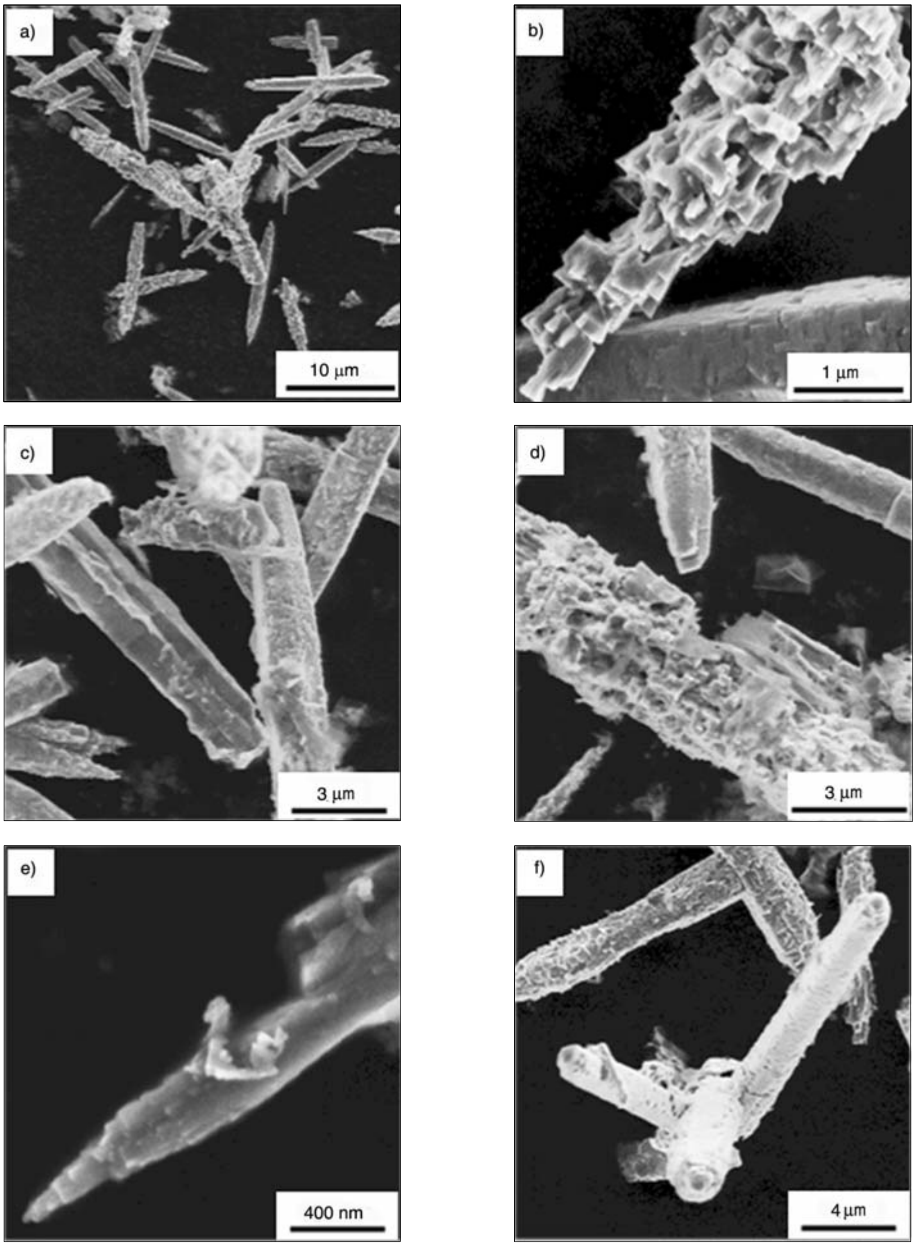

Fig. 2. SEM images of tube-structured ZnO needles synthesized at 180 °C for 48 h

The tube-structured ZnO needles in Fig. 2, with a thin (up to 50 nm) and long (up to 1 μm) tips (Figs. 2a, e), are 5–10 μm long, 500–1000 nm in external diameter and 100–200 nm (Fig. 2f) in inner diameter. The local wall thickness of the tube is ca.

100–150 nm. A random honeycomb structure, decorticated needles resulting from experimental processing, coiled by belts or layers with the width of about 200 nm and 50–100 nm thick are observed in Fig. 2b, d, and the remains of the surface layers can be seen in Fig. 2d. The top (0001) and bottom $(000\overline{1})$ surfaces are partly or completely opened (Fig. 2f) and some cracks and holes are observed in the side surface wall as shown in Figs. 2c, f. Interestingly, for some needles, the inner layer and outer layer and the interstice between the layers can be clearly observed (cf. Fig. 2c). Furthermore, some tubes derived from layer coiling along the [0001] direction with a multilayer wall were found, the hatch and some cracks could be seen in the tube end in the middle of Fig. 2f. The spiral lines formed by the layer coiling approach during the growth of ZnO needles could be clearly observed in Fig.2e. It is reasonable to suggest that these needle-shaped ZnO tubes with polycrystalline walls consist of wurtzite-type ZnO layers. It is implied that the supersaturation near the side surface of the growing crystal is higher than that at the centre, leading to preferential stronger nucleation and growth along the [0001] direction of the side surface. Furthermore, hydrogen peroxide could support the growth along the [0001] direction and the side-face by providing enough oxygen. The most likely growth mechanism is that described in the references [16]: an initially grown sheet turns into a roll and the cone-shaped roll transforms into a cylindrical tube, presumably via a dislocation “zipper” mechanism. Finally, a hollow tube transforms into a needle.

3.3. Photoluminescence

Figure 3 presents the photoluminescence (PL) spectra of the as-prepared ZnO crystallites fabricated at various temperatures, excited with 325 nm UV light from a He-Cd laser at room temperature. A typical emission spectrum consists of a peak at ca. 400 nm, a broad blue emission at ca. 410–470 nm, and a narrow green one at ca. 550 nm. The visible emission is usually considered to be related to various intrinsic defects produced during preparation of ZnO and post-treatment. Normally, these defects are located at the surface of the ZnO structure. The blue emission corresponds to the zinc vacancy and oxygen vacancy; the zinc vacancy forms a shallow acceptor level and the oxygen vacancy forma a shallow donor level [17]. There are two kinds of transitions for blue emission: one is electron transition from conduction band to the shallow acceptor level formed by zinc vacancy, the other is an electron transition from the shallow donor level formed by oxygen vacancy to the valence band. The UV emission corresponds to the near band-edge emission resulting from the recombination of free excitons.

Figure 3 shows that the UV emission gradually diminishes, while the blue emission intensity increases and the UV peaks cannot be observed in Fig. 3, curves d and e. It implies that the blue emission probability is higher than that of the UV emission due to the concentration of zinc vacancies and oxygen vacancies increasing as the hydrothermal temperature increases. The green emission is commonly referred to as the singly ionized oxygen vacancy and the emission results from the radiative recombination of photo generated holes with electrons occupying oxygen vacancies [18].

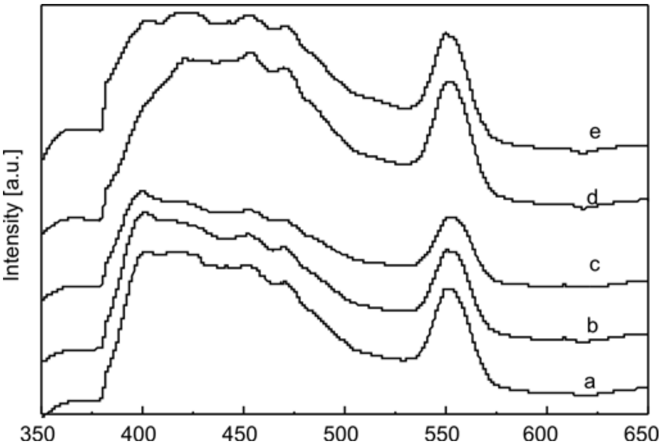

Fig. 3. Room temperature photoluminescence spectrum of ZnO needles hydrothermally synthesized at: a) 70 °C, b) 90 °C, c) 120 °C, d) 150 °C, e) 180 °C

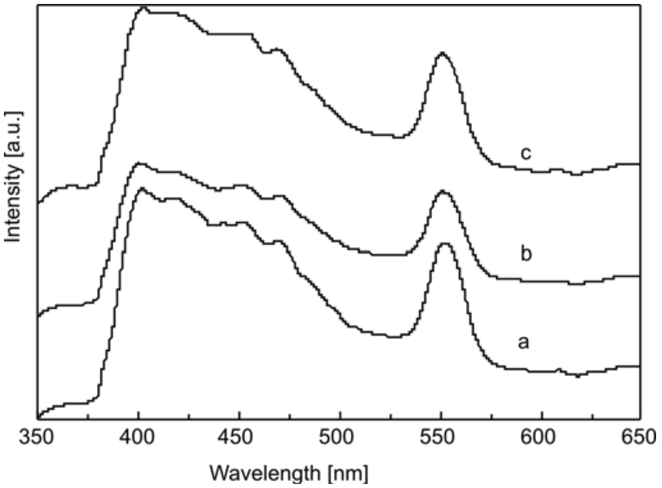

Fig. 4. Room temperature photoluminescence spectrum of ZnO needles synthesized in: a) 30%, b) 25%, c) 10% H_2O_2 solution

The room temperature PL spectra of the ZnO nanoneedles (batch 2) fabricated for three different quantities of H_2O_2 were recorded as shown in Fig. 4. A broad UV-blue emission peak scatters at around 400 to 470 nm and a green emission peak centred at about 550 nm are observed in Fig. 4. It is found that concentration of H_2O_2 has no influence on the PL properties when the concentration of H_2O_2 is higher than 10%.

4. Conclusion

Tube-structured ZnO needles were successfully synthesized via a hydrothermal method in H_2O_2 solution. It was found that ZnO needles possess a tube structure encircled by multilayer along the *c*-axis. Hydrogen peroxide could support the growth along *c*-axis and the side-face by providing enough oxygen. The XRD spectroscopy results show that each ZnO needle has a wurtzite structure, and the weak intensity of the (0002) peak is caused by the small area of (0001) cross section and a thin multilayer wall of the tube-structured needle. PL results reveal that the blue emission probability is greater than that of the UV emission as increasing the hydrothermal temperature or the concentration of H_2O_2 has no influence on the PL properties when the concentration of H_2O_2 is higher than 10%.

Acknowledgements

We thank the Tianjin Natural Science Foundation (05yfJMTC 12900) for financial support.

References

[1] KIM D.K., MANOR U., Scripta Mater., 54 (2006), 807.
[2] CHEN Z., GAO Q.M., ROAN M., SHI J.L., Appl. Phys. Lett., 87 (2005), 93113.
[3] VOROB'EV V.A., J. Opt. Techn., 72 (2005), 47.
[4] YATSUI T., SANGU S., KAWAZOE T., OHTSU M., AN S.J., YOO J., YI G.C., Appl. Phys. Lett., 90 (2007), 223110.
[5] BHOSLE V., PRATER J.T., YANG F., BURK D., FORREST S.R., NARAYAN J., J. Appl. Phys., 102 (2007), 023501.
[6] YOON S.H., YANG H., KIM Y.S., J. Ceram. Process. Res., 8 (2007), 261.
[7] SHIH W.C., WANG M.J., LIN I.N., Diamond Relat. Mater., 17 (2008), 390.
[8] LIAO L., LU H.B., SHUI M., LI Y.L., LIU C., SHEN Z.X., YU T., Nanotechn., 19 (2008), 175501.
[9] ANDELMAN T., GONG Y.Y., POLKING M., KUSKOVSKY I., NEUMARK G., O’BRIEN S., J. Phys. Chem., 109 (2005), 14314.
[10] TEKI R., PARKER T.C., LI H.F., KORATKAR N., LU T.M., LEE S., Thin Solid Films., 516 (2008), 4993.
[11] LIU J.P., HUANG X.T., LI Y.Y., DUAN J.X., AI H.H., REN L., Mater. Sci. Eng. B., 127 (2006), 85.
[12] PENG Y., BAO L., Chem. J. Chin. Univ., 29 (2008), 28.
[13] WANG Z.L., J. Nanosci. Nanotechnol., 8 (2008), 27.
[14] YADAV R.S., PANDEY A.C., Physica E., 40 (2008), 660.
[15] FAN H.J., LOTNYK A., SCHOLZ R., YANG Y., KIM D.S., PIPPEL E., SENZ S., HESSE D., ZACHARIAS M., J. Phys. Chem., 112 (2008), 6770.
[16] POKROPIVNY V.V., KASUMOV M.M., Techn. Phys. Lett., 33 (2007), 44.
[17] WANG Q.P., ZHANG X.J., WANG G.Q., CHEN S.H., WU X.H., MA H.L., Appl. Surf. Sci., 254 (2008), 5100.
[18] DAI Y., ZHANG Y., BAI Y.Q., WANG Z.L., Chem. Phys. Lett., 375 (2003), 96.

Received 24 June 2008
Revised 22 December 2008

Materials Science-Poland, Vol. 27, No. 2, 2009

Study of hydrogen passivation in SiN$_x$:H films using Fourier transform infrared and photoluminescence spectroscopy

S. CHOPRA[1], R.P. GUPTA[2], B.C. JOSHI[2], G. ERANNA[2], S. BANERJEE[3*]

[1]Department of Physics, Birla Institute of Technology and Science,
Pilani, Rajasthan-333031, India

[2]Semiconductor Device Fabrication, Central Electronics Engineering Research Institute,
Pilani, Rajasthan-333031, India

[3]Department of Physics, Birla Institute of Technology and Science Pilani,
Hyderabad Campus, Andhra Pradesh, India

Amorphous silicon nitride (a-SiN$_x$:H) films were deposited at 300 °C by plasma-enhanced chemical vapour deposition. Silane/ammonia (SiH_4/NH_3) and silane/nitrogen (SiH_4/N_2) gas compositions were used at various flow rates to study the effect of hydrogen passivation of the films using the photoluminescence (PL) spectroscopy. Fourier transform infrared (FTIR) spectroscopy was employed to derive the relative changes in the total bonded hydrogen (TBH) concentration with increasing flow rates. The composition and the refractive indices of the as-deposited films were also extracted using the bond density calculations from FTIR spectra. The calculated refractive indices of the silicon nitride films were consistent with the ellipsometry measurements. The PL spectra were observed to be free from any interference effect and this was attributed to the nitrogen related defects in all the a-SiN$_x$:H films. The films deposited using SiH_4/NH_3 showed a higher PL intensity than those deposited in a SiH_4/N_2 environment. A direct relation between the PL intensity and TBH content of the films was found.

Key words: *silicon nitride; PECVD; FTIR; photoluminescence; hydrogen passivation*

1. Introduction

Since the discovery of visible light emission in porous Si [1], intense research activity has been focused on Si nanostructures for their potential application in Si-based light-emitting devices (LED), which is compatible with the current electronic ultra large scale integration technologies [2]. Several prototype devices have been demon-

---

[*]Corresponding author, e-mail: souri@bits-hyderabad.ac.in

strated recently in silicon dioxide (SiO_2) embedded with Si nanostructures, revealing a bright future for Si-based photonics [3, 4]. However, a too large band gap of SiO_2 hinders the injection of carriers, reducing the efficiency and reliability of the devices. In this context, silicon nitride embedded with Si nanoclusters has received great attention due to its smaller band gap and lower tunnelling barrier in comparison with SiO_2 [5]. This makes it more advantageous for carrier injection in electroluminescent devices, often showing intense light emission in the full visible light range in photoluminescence (PL) spectroscopy studies [6, 7]. Thus, Si-rich nitride structures emerge as potential candidates for the development of tunable and highly efficient Si-based LEDs [8, 9]. However, the origin of PL from Si-rich nitride films (hereafter referred as SRN) is still a subject of debate. Though it has been related to the quantum confinement effect of Si nanoclusters in SRN films [10], the radiative lifetime of this SRN structure was found to be much shorter than that of Si nanocrystals [11–13]. Thus there was an apparent ambiguity whether the light emission comes from the defect centres or Si nanoclusters or even from the interface states in the SRN films [14, 15]. Moreover, a thin hydrogenated silicon nitride film on a polished substrate has optical properties similar to those of Fabry–Perot etalon so that it can exhibit interference effect, which may affect the shape of PL spectra substantially [16]. Hence further investigation of the origin of photoluminescence, particularly in light of the interference effect, is of utmost importance.

The present study aims to clarify and classify the origin of PL in amorphous silicon nitride (a-SiN_x:H) films, deposited under identical conditions, using plasma enhanced chemical vapour deposition (PECVD) technique in ammonia (NH_3) and nitrogen (N_2) ambience in the presence of silane (SiH_4). Though there were several reports which showed that there existed a substantial difference in the hydrogen passivation of SiN_x:H films deposited in NH_3 and N_2 atmosphere [10, 17], there have been very few works that related the dependence of PL intensity on the hydrogen passivation of those SRN films [18]. In this paper, we present a comparative study of hydrogen passivation in a-SiN_x:H films deposited using the two gas systems mentioned above. Chemical bonds in the films were examined with the aid of a Fourier transform infrared (FTIR) spectrometry, and room temperature photoluminescence spectroscopy was employed to investigate the dependence of PL intensity on the hydrogen passivation of the SRN films, and from which a direct relation was found between the PL intensity and the hydrogen content of the films.

2. Experimental

The silicon nitride films were prepared using argon-diluted 3% silane with ammonia and argon-diluted 3% silane with nitrogen at the purity in excess of 99.9999%, as the reactant gas sources. Hereafter the SiH_4/NH_3 and SiH_4/N_2 deposited samples will be referred as samples A1, A2 and A3 and samples B1, B2 and B3, respectively. The depositions were carried out on RCA cleaned Si(100) wafers kept at 300 °C. The operating frequency, the RF power and the pressure were maintained at 13.56 MHz, 120 W and 0.3 Torr, respectively. Whereas only the gas flow rate ratios $R(NH_3/SiH_4)$ and $R(N_2/SiH_4)$ were set to 6.76, 10.14, 13.52 for samples A1, A2 and A3 and set to 27.8, 37, 46.3 for samples B1, B2 and B3, respectively, the flow rate of SiH_4 was kept at a fixed value of 10.8 sccm for both kinds of samples. The thicknesses t of the samples A1, A2 and A3 and samples B1, B2 and B3 were around 120 nm and 150 nm, respectively, as measured by a Stylus profilometer. An ellipsometer using 632.8 nm light (Sentech, Laserpro-37-001) was employed to determine the refractive indices of all the samples. Absorption spectra of the samples were obtained using a Shimadzu IR-Prestige-21 FTIR spectrometer at the resolution of 4.0 cm^{-1}. The IR scanning range was from 400 cm^{-1} to 4000 cm^{-1}. PL measurements were performed using a Shimadzu RF-5301PC spectrofluorophotometer under the excitation of the 450 nm line of a 150 W Xe lamp at room temperature. The amorphous nature of the as-deposited silicon nitride films was confirmed from the broad hump-like feature exhibited in X-ray diffraction studies.

3. Results and discussion

3.1. FTIR Analysis

Figure 1a shows the FTIR spectra of nitride films deposited using NH_3 and Fig. 1b shows the corresponding spectra for the films deposited using N_2. The figure exhibits the presence of N–H and Si–H bonds responsible for the hydrogen content present in these films. In samples A1, A2 and A3, the peaks for the stretching modes of Si–H and N–H bonds appear in the range 2330–2357 cm^{-1} and 3330 cm^{-1}, respectively, with a broad Si–N stretching peak centred at 854 cm^{-1}.

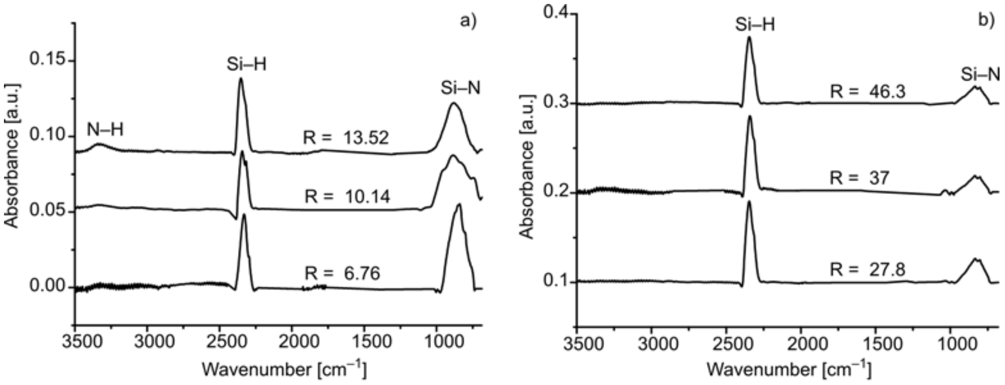

Fig. 1. FTIR absorption spectra for SRN films deposited using: a) NH_3/SiH_4, b) N_2/SiH_4 gas systems exhibiting N–H, Si–H and Si–N stretching bonds. It is to be noted that N–H bonds are absent in b)

The absorbance peaks obtained in the samples B1, B2 and B3 are at 2345 cm^{-1} for the stretching mode of the Si–H bond with a broad Si–N stretching peak around 840 cm^{-1}. The peak positions obtained in the FTIR spectra of our samples are very similar to that reported by several groups in FTIR studies of SRN films [18]. It is also to be noted that there is a relative change in the concentration of Si–H and N–H bonds in the silicon nitride films.

The Si–H and N–H bond concentrations were estimated by the integration of the absorbance peaks centred around 2340 and 3330 cm^{-1}, respectively, using the following equations [19]:

$$[\text{Si–H}] = \beta_{\text{Si}-\text{H}} I_{2340} \tag{1}$$

$$[\text{N–H}] = \beta_{\text{N}-\text{H}} I_{3330} \tag{2}$$

where I is the integrated absorption and β represents the absorption cross sections with $\beta_{\text{Si–H}} = 7.4\times10^{-18}$ cm^2 and $\beta_{\text{N–H}} = 5.3\times10^{-18}$ cm^2 [20], thus

$$\frac{\beta_{\text{N}-\text{H}}}{\beta_{\text{Si}-\text{H}}} = \frac{1}{1.4} \tag{3}$$

The total concentration of bonded hydrogen (TBH) in the silicon nitride film equals:

$$[\text{H}_{\text{total}}] = [\text{Si–H}] + [\text{N–H}] = \text{const}\left[I_{2340} + 1.4 I_{3330}\right] \tag{4}$$

Since, in this study, we are primarily interested in the relative change in TBH content under various gas flow rates, it is permissible to ignore the constant and use the sum of the two integrals (total area under the Si–H and N–H peaks) in the FTIR spectrum as a measure of the concentration of TBH (in arbitrary units) in the film as prescribed by Cai et al. [19].

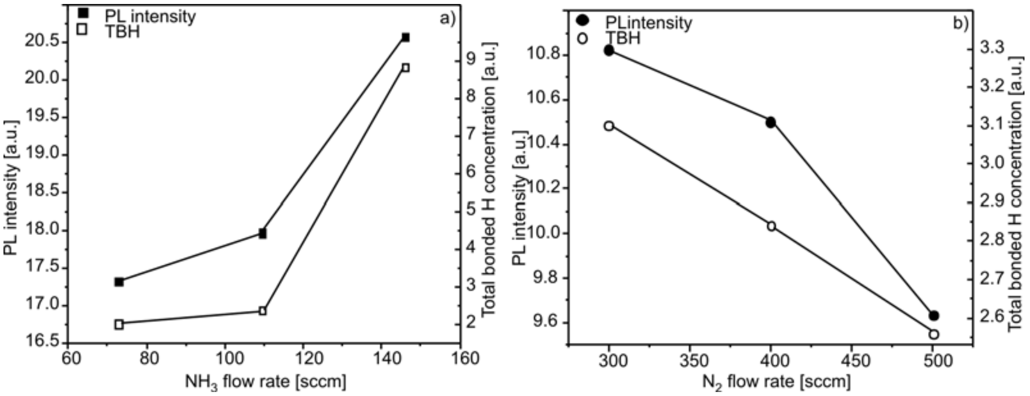

Fig. 2. PL intensity and TBH contents of the SRN films in function of: a) NH_3, b) N_2 flow rates. The figure clearly indicates a direct correspondence between PL intensity and TBH contents of the SRN films

The value of TBH for samples A1, A2 and A3 was found to increase as the gas flow rate ratio $R(NH_3/SiH_4)$ increases, as shown in Fig. 2a. This increase in TBH is attributed to the formation of more N–H bonds as R increases [18]. A close look at the FTIR spectra (Fig. 1) would reveal that samples B1, B2 and B3 contain more Si–H bonds and a negligible amount of N–H bonds. This can be attributed to the choice of improper plasma deposition parameters, namely, RF power and the gas flow rate ratio (N_2/SiH_4) in our study as predicted by Smith et al. [21, 22]. Hence TBH in this case would equal the integral area of Si–H bond only. Unlike the value of TBH for samples A1, A2 and A3, here it was found to decrease as the gas flow rate ratio $R(N_2/SiH_4)$ increased, as depicted in Fig. 2b. This is consistent with a corresponding decrease in Si–H bond area as the gas flow rate ratio R (N_2/SiH_4) increases. Reduction of Si–H bond area can be explained by the displacement of hydrogen atoms from the adsorbing silane radicals as the N_2 flow rate is increased [22].

It is customary to determine the composition x and the refractive index n of the as-deposited SRN films. Though, ellipsometry is generally used to estimate the refractive indices of the silicon nitride films [23], there are several techniques to calculate the composition of the film. Zambom et al. [24] used Rutherford back scattering spectroscopy to extract the composition of their nitride films, whereas Mackel et al. [25] calculated the same composition using the data on the bond densities available from the FTIR spectra of the films through the following equation

$$\frac{[\mathrm{Si}]}{[\mathrm{N}]} = \frac{1}{x} = 0.084\,\frac{[\mathrm{Si-H}]}{[\mathrm{N-H}]} + 0.70 \tag{5}$$

where [Si–H] and [N–H] correspond to the respective bond densities determined from the FTIR spectra. As we have carried out extensive analysis of FTIR spectra of the SRN films, it prompted us to adopt Eq. (5) for estimating the N/Si ratio of those films. Mackel et al. [25] also asserted that there is a relation between x and n such that

$$\frac{[\mathrm{N}]}{[\mathrm{Si}]} = x = \frac{3}{4}\frac{3.3-n}{n-0.5} \tag{6}$$

The composition x and the refractive indices for the samples A1, A2 and A3 are estimated using Eqs. (5) and (6), respectively. The variation of the same data as a function of NH_3 flow rate is plotted in Fig. 3. The values of the refractive indices were also obtained from the ellipsometry measurements, which show a variation from 2.20 to 1.98 with the increase in the NH_3 flow rate. It is clear from Fig. 3 that the calculated values of the refractive indices are in close agreement with the ellipsometry-derived values. The increase in the N/Si ratio with the increase in the NH_3 flow rate is attributed to the increase in [N–H] bonds, as is evident from the FTIR spectra (Fig. 1a). Similar correlations between the composition and [N–H] bond densities were also reported by Zhang et al. [23] in silicon nitride films. However, we avoided direct estimation of the composition for samples B1, B2 and B3 using Eq. (5) as it would lead to erroneous result due to the negligible presence of [N–H] bonds in those samples. Instead, Eq. (6) was used to estimate the N/Si ratio from the knowledge of *n*, extracted from the ellipsometry data. Since the refractive indices for samples B1, B2 and B3 vary nominally between 2.0 and 1.95 as obtained from the ellipsometry measurements, the values of *x* turn out to vary only between 0.65 to 0.70, respectively.

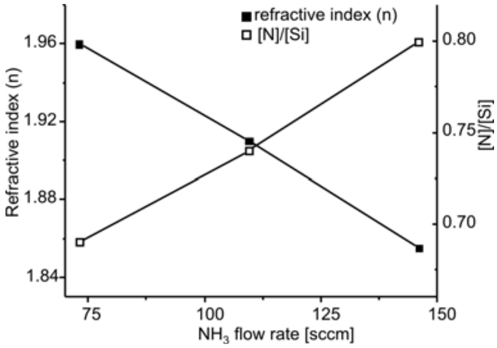

Fig. 3. Refractive index and [N]/[Si] vs. NH_3 flow rate as calculated from Eqs. (5) and (6)

3.2. Analysis of photoluminescence

Figure 4 shows the room temperature PL spectra of samples A1–A3 and B1–B3. A comparison between PL intensities of two typical SRN films, namely, sample A1 and sample B1 is shown in Fig. 5, indicating a stronger visible photoluminescence response for the sample A1 than for the sample B1. A similar trend is also seen for the other sets of samples. The PL intensity in the former case was found to be nearly 1.3 times higher than that in the latter case. This increase is attributed to a better hydrogen passivation in samples A1, A2 and A3, as more N–H bonds contribute to the TBH content [18].

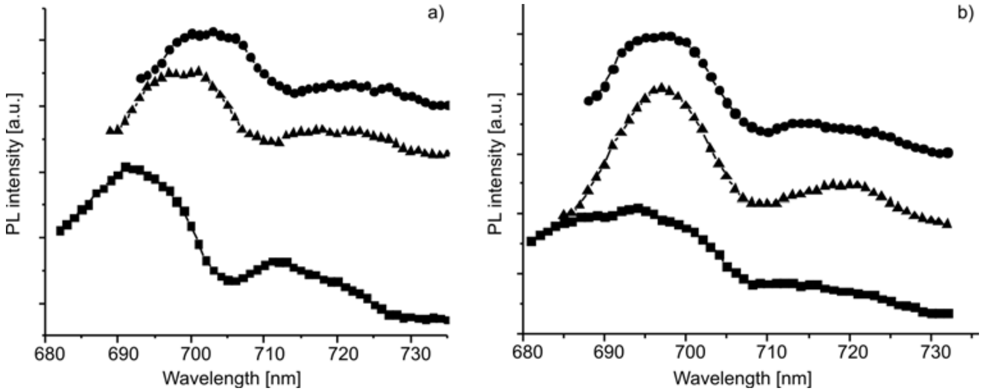

Fig. 4. PL spectra of samples: a) A1 (■), A2 (▲), A3 (●) and b) B1 (●), B2 (▲), B3 (■). The figures show an insignificant shift in the emission wavelengths both in a) and b)

The PL intensity for these samples was also found to increase as the NH_3/SiH_4 ratio increases, as shown in Fig. 2a. This observation is consistent with the increase in the N/Si ratio as the NH_3 flow rate increases (Fig. 3). On the other hand, Fig. 2b shows a small decrease in PL intensity with the increase in the N_2/SiH_4 ratio for the samples B1–B3. This can be explained by a slight decrease in TBH content if there is an increase in the N_2/SiH_4 ratio, where the bonds S–H between the hydrogen and the silicon atoms start breaking as the N_2/SiH_4 ratio increases as mentioned earlier [22]. It is interesting to note that in both kinds of the samples we found a one-to-one correspondence between the TBH concentration and the PL intensity, as clearly exhibited in Fig. 2, though the variations were nominal in samples deposited using N_2. The enhancement of PL in the case of NH_3 deposited samples is clearly due to a greater hydrogen content, as given by the value of TBH, exhibiting a direct dependence of PL intensity on the extent of nonradiative defect passivation of the films, as recently proposed by Kim et al. [18].

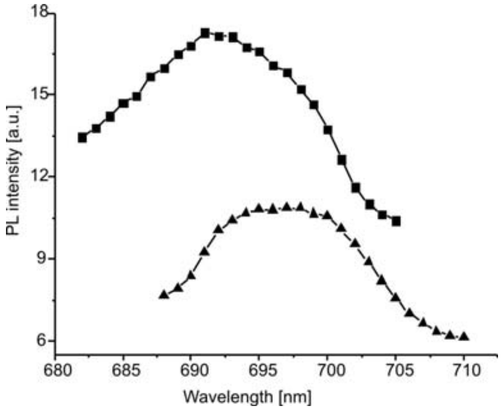

Fig. 5. PL spectra for two typical SRN films, namely, samples A1 (■) and B1 (▲)

It is now important to investigate the luminescence mechanisms in the samples. Generally, luminescence mechanisms have been classified into two types, namely due to radiative defects in the film and due to the quantum confinement effect (QCE) in Si quantum dots [26]. In this context, three main radiative defect energy levels around 1.8, 2.4, and 3.0 eV have been reported for a-SiN$_x$:H films [15]. Pundur et al. [27] also observed two peaks, around 1.75 and 2.0 eV in SRN films using cathodoluminescence, which were also attributed to defect levels.

Before analyzing the emission properties of SRN films to understand the origin of the PL spectra, it is essential to check if there is any interference effect that might have masked the true spectra or have resulted in any additional peak in the PL spectra. Two typical PL spectra corresponding to samples A1 and B2 (Fig. 4a, b) were thoroughly investigated in view of the interference effects by studying how the PL spectra are modified by changing the angle of incidence of light, as prescribed by Marra et al. [28]. The incidence angle with respect to the surface normal was intentionally varied by a small amount from the measurement angle θ and the corresponding PL spectra were recorded. When the original PL spectra (Fig. 4a) are compared with the new ones, as shown in Fig. 6, it is evident that: an additional peak appears around 596 nm, which was previously absent for these samples, and two broad peaks mask the original peaks, which were situated around 696 nm (ca. 1.78 eV) and 718 nm (ca. 1.73 eV). Moreover, the PL intensity of the samples under investigation is much higher than that for the original PL spectra. These observations closely match the PL spectra resulting from the interference effect in a thin amorphous nanocrystalline silicon film as reported by Golubev et al. [16]. It is to be noted that as the true luminescence spectrum in a film–transparent substrate system can always be reconstructed by straightforward division of the PL spectrum by the experimental transmission spectrum, it was suggested that a sample showing comparatively lower PL intensity will not indicate the interference effect, unlike as observed in our SRN films [16]. It is clear from Fig. 6 that there is no shift in the peak positions compared with those obtained in the original PL spectra. This also supports our conclusion that the original PL spectra of SRN samples are free from interference effects [28].

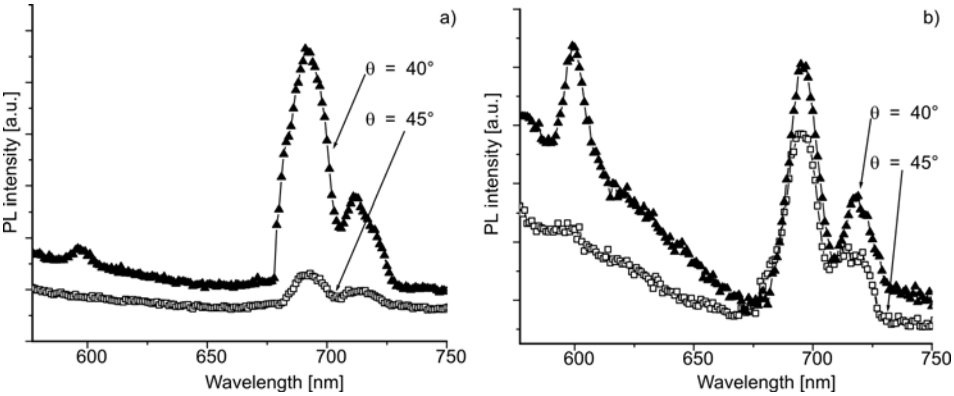

Fig. 6. Combined plot of the original PL spectra (□) and the PL spectra obtained by changing the measurement angle (θ) of light (▲) for the samples: a) A1, b) B2 with thicknesses ca. 120 nm (a) and 150 nm (b)

In the PL spectra of SiN$_x$:H films (Fig. 4) one can observe two peaks, around 697 nm (ca. 1.78 eV) and 718 nm (ca. 1.73 eV) for samples A1–A3 whereas in samples B1–B3, they were found around 696 nm (ca. 1.78 eV) and 718 nm (ca. 1.73 eV). Along with it, an insignificant shift in the emission wavelengths has also been apparent in both kinds of films. This eliminates the possibility that photoluminescence in the as-deposited nitride films was due to any QCE, which is generally associated with a blue shift [18]. The emission peaks obtained near 1.78 eV and 1.73 eV in all samples could be associated with the recombination between nitrogen defect states N_4^+ and N_2^0 which are mostly present in a-SiN$_x$:H films as suggested by several groups [15, 23]. The absence of other defect related peaks, namely around 2.4 eV and 3.0 eV, could be due to the choice of excitation wavelength (450 nm = 2.76 eV) which may not be sufficiently high to excite those defects, as claimed by Wang et al. [29].

4. Conclusion

Silicon nitride films have been fabricated by PECVD using SiH_4/NH_3 and SiH_4/N_2 gas compositions. The composition ratio (N/Si) of the SRN films deposited using NH_3 was found to increase with the NH_3 flow rate, whereas the analogous ratio for N_2 deposited films showed a nominal increase with the N_2 flow rate. The refractive indices of the SRN films vary between 2.20 to 1.98 and 2.0 to 1.95 for samples deposited using NH_3 and N_2, respectively. The PL in both kinds of films is found to be free of any interference effect: this was attributed to the recombination between the nitrogen defect states N_4^+ and N_2^0. The absence of signatures of other defects around 2.4 eV and 3 eV in the films could be related to the inadequacy of the excitation wavelength (450 nm). On changing the gas flow rates, improved PL was observed when using NH_3 as the reactive gas, instead of conventional N_2. This enhancement/suppression of PL intensity in the case of the NH_3/N_2 deposited samples is due to the presence of greater/less hydrogen content, as given by the value of TBH, resulting in a direct correlation between the PL intensity and the TBH content of the films. It is also concluded that the existence of Si–H and N–H bonds could effectively passivate the non-radiative defects in the films. However, to ascertain the role played by the defect states in tuning the PL spectra, it is crucial to investigate how the PL intensity is modified after the samples are annealed at various temperatures. Such investigations are already underway.

Acknowledgements

This work was supported by the Central Electronics Engineering Research Institute (CEERI), Pilani, Rajasthan. We extend our thanks to the Director of CEERI for his encouragement and appreciation of this work.

References

[1] CANHAM L.T., Appl. Phys. Lett., 57 (1990), 1046.

[2] FAUCHET P.M., RUAN J., CHEN H., PAVESI L., NEGRO L.D., CAZZANELI M., ELLIMAN R.G., SMITH N., SAMOC M., LUTHER-DAVIES B., Opt. Mater., 27 (2005), 745.

[3] CHEN M.J., YEN J.L., LI J.Y., CHANG J.F., TSAI S.C., TSAI C.S., Appl. Phys. Lett., 84 (2004), 2163.

[4] WALTERS R.J., BOURIANOFF G.I., ATWATER H.A., Nat. Mater., 4 (2005), 143.

[5] PARK N.M., JEON S.H., YANG H.D., HWANG H. PARK S.J., Appl. Phys. Lett., 83 (2003), 1014.

[6] WANG Y.Q., WANG Y.G., CAO L., CAO Z.X., Appl. Phys. Lett., 83 (2003), 3474.

[7] YANG M.S., CHO K.S., JHE J.H., SEO S.Y., SHIN J.H., KIM K.J., MOON D.W., Appl. Phys. Lett., 85 (2004), 3408.

[8] CHEN L.Y., CHEN W.H., HONG F.C.N., Appl. Phys. Lett., 86 (2005), 193506.

[9] CHO K.S., PARK N.M., KIM T.Y., KIM K.H., SUNG G.Y., Appl. Phys. Lett., 86 (2005), 071909.

[10] PARK N.M., CHOI C.J., SEONG T.Y., PARK S.J., Phys. Rev. Lett., 86 (2001), 1355.

[11] NEGRO L.D., YI J.H., KIMERLING L.C., HAMEL S., WILLIAMSON A., GALLIB G., Appl. Phys. Lett., 88 (2006), 183103.

[12] MA L.B., SONG R., MIAO Y.M., LI C.R., WANG Y.Q., CAO Z.X., Appl. Phys. Lett., 88 (2006), 093102.

[13] GARCIA C., GARRIDO B., PELLEGRINO P., FERRE R., MORENO J.A., MORANTE J.R., PAVESI L., CAZZANELLI M., Appl. Phys. Lett., 82 (2003), 1595.
[14] WARREN W.L., ROBERTSON J., KANICKI J., Appl. Phys. Lett., 63 (1993), 2685.
[15] DESHPANDE S.V., GULARI E., BROWN S.W., RAND S.C., J. Appl. Phys., 77 (1995), 6534.
[16] GOLUBEV V.G., MEDVEDEV A.V., PEVTSOV A.B., SEL'KIN A.V. FEOKTISTOV N.A., Phys. Sol. St., 41 (1999), 137.
[17] CHO C.H., KIM B.H., KIM T.W., PARK S.J., PARK N.M., SUNG G.Y., Appl. Phys. Lett., 86 (2005), 143107.
[18] KIM B.H., CHO C.H., KIM T.W., PARK N.M., SUNG G.Y., PARK S.J., Appl. Phys. Lett., 86 (2005), 091908.
[19] CAI L., ROHATGI A., YANG D. EL-SAYED M.A., J. Appl. Phys., 80 (1996), 9.
[20] LANDFORD W.M. RAND M.J., J. Appl. Phys., 49 (1978), 2473.
[21] SMITH D.L., J. Vac. Sci. Technol. A, 11 (1993), 1843.
[22] SMITH D.L., ALIMONDA A.S. VONPREISSIG F.J., J. Vac. Sci. Technol. B, 8 (1990), 3.
[23] ZHANG X., SHI G., YANG A. SHAO D., Thin Solid Films, 215 (1992), 134.
[24] ZAMBOM L.S., MANSANO R.D., FURLAN R., Vacuum, 65 (2002), 213.
[25] MACKEL H., LUDEMANN R., J. Appl. Phys., 92 (2002), 2602.
[26] SUNG G.Y., PARK N.M., SHIN J.H., KIM K.H., KIM T.Y., CHO K.S. HUH C., IEEE J. Sel. Topics Quant. El., 12 (2006), 6.
[27] PUNDUR P.A., SHAVALGIN J.G. GRITSENKO V.A., Phys. Stat. Sol. A, 94 (1986), K107.
[28] MARRA D.C., AYDIL E.S., JOO S.J., YOON E., SRDANOV V.I., Appl. Phys. Lett., 77 (2000), 3346.
[29] WANG M., LI D., YUAN Z., YANG D. QUE D., Appl. Phys. Lett., 90 (2007), 131903.

Received 30 June 2008
Revised 12 December 2008

Materials Science-Poland, Vol. 27, No. 2, 2009

The van der Pauw method of measurements in high-T_c superconductors

M. S. DA LUZ[*], C. A. M. DOS SANTOS, C. Y. SHIGUE,
F. J. H. DE CARVALHO JR., A. J. S. MACHADO

Escola de Engenharia de Lorena - USP, P. O. Box 116, Lorena, SP 12602-810, Brazil

Details on the transport measurements of high-T_c superconductors have been presented using the van der Pauw technique. Basic procedures to obtain good and reliable results in polycrystalline samples were discussed. The influence of heating rates and the direction of the applied magnetic field on the results of measurements has been examined. An unexpected nonzero transverse voltage at zero magnetic field was observed in the vicinity of the superconducting temperature transition (T_c). Measurements in two different magnetic field directions allowed one to calculate the symmetric and the asymmetric components of the Hall resistance. Those components were calculated for two different superconductor systems and analyzed in the framework of the recent theory about the longitudinal and transverse voltages in high-T_c superconductors.

1. Introduction

The measurement of electrical resistivity and the Hall effect in high-T_c superconductors (HTSC) remains a subject of great interest [1–5]. In particular, the unusual behaviour of the Hall effect in many high-temperature superconductors and in some conventional superconductors has become a persistent problem in understanding the flux motion in superconductors. To measure resistivity and the Hall effect employing standard methods, the samples need to be processed into a bar structure with two end contacts, for passing electrical current, and two pairs of thin protruding leads on each side of the bar, where the longitudinal and Hall voltages can be measured. In an ideal case, the Hall contacts should be correctly placed to avoid longitudinal contributions to the Hall voltage. Since the superconductor samples are usually very small and have no regular geometry, the fabrication of such contacts is more difficult.

In a normal state, the Hall effect in superconductors is antisymmetric in an external magnetic field, and should be zero at zero magnetic field. However, for real sam-

---

[*] Corresponding author, e-mail: luz@physics.montana.edu

ples we usually find a finite voltage at zero field which can superimpose on the Hall signal when a magnetic field is applied. This undesired contribution can result from either a geometrical mismatch in voltage contacts, a misalignment of the magnetic field and current directions, or the inhomogeneity of the sample. Several methods are used to eliminate or reduce that undesired contribution. One of them is the technique elaborated by van der Pauw (vdP) [6, 7]. The van der Pauw technique enables the measurement of resistivities on thin samples with arbitrary shapes. In contrast to Hall-bar measurements, the vdP technique requires only four sufficiently small contacts placed at the circumference of an arbitrarily shaped (but simply connected) sample [6, 7]. The methods of reversing magnetic field and without reversing its direction may be used.

The method of reversing magnetic field is based on the fact that the Hall potential changes its sign (but not the absolute value) after reversing the magnetic field while the longitudinal potential remains the same. The non-Hall potentials can be thus eliminated after two measurements in both field directions (H, $-H$). Here, we have to keep in mind that the polarity of the injected current should be kept the same. So, the longitudinal and Hall voltages can be calculated by:

$$V_{XY} = \left(\frac{V_{AC,BD}(H) - V_{AC,BD}(-H)}{2} \right) \tag{1}$$

$$V_{XX} = \left(\frac{V_{AC,BD}(H) + V_{AC,BD}(-H)}{2} \right) \tag{2}$$

where the $V_{AC,BD}$ is defined as the voltage between points A and C when an applied current flows through contacts B and D (see Fig. 1).

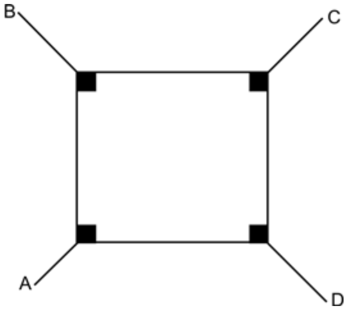

Fig. 1. Schematic view of the electrical contacts in the sample

In the method without reversing the applied magnetic field, the voltage due to the transversal electric field can be detected by permutation of voltage and current contacts (see Fig. 2). Any pair of contacts can be used as current contacts and the remaining pair as voltage contacts. From the reciprocity theorem it follows that $V_{AC,BD}(-H) = V_{BD,AC}(H)$ [8, 9]. Thus, the Hall and longitudinal voltages can now be reformulated as:

$$V_{XY} = \left(\frac{V_{AC,BD}(H) - V_{BD,AC}(-H)}{2} \right) \tag{3}$$

$$V_{XX} = \left(\frac{V_{AC,BD}(H) + V_{CD,AB}(-H)}{2} \right) \tag{4}$$

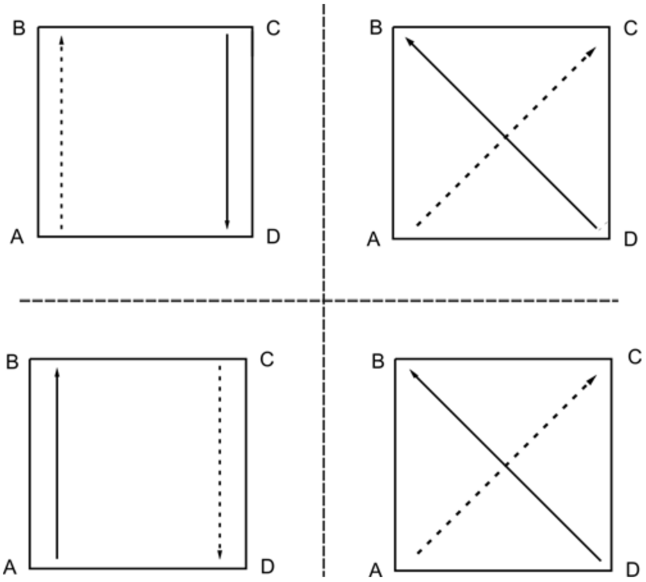

Fig. 2. Scheme of a four probe configuration used for the longitudinal (left) and Hall voltages (right) measurements. The solid and dashed arrows represent current and potential pairs of the contacts, respectively. In the top, the two configurations denote $V_{AB,CD}$ and $V_{AC,BD}$ and the other two below $V_{AB,CD}$ and $V_{BD,AC}$ voltages, respectively

Based on the methods described above, this work reports an important dc technique which uses the van der Pauw method for measurements HTSC polycrystalline sample. Firstly, a modified method has been presented. Basic procedures to obtain good and reliable results have been discussed. The influence of heating rates and of the direction of the applied magnetic field is described. The results are analyzed in the framework of the recent theory of the longitudinal and transverse voltages in high-T_c superconductors.

2. Experimental

Polycrystalline samples of $YBa_2Cu_3O_{7-\delta}$ were prepared by a solid state reaction. Samples of the $Bi_2Sr_2Ca_{1-X}Pr_XCu_2O_{8+\delta}$ superconducting system were also prepared with $x = 0.2$ and 0.3. X-ray powder diffractometry showed that all the samples are single phase. For more details about sample preparation and characterization see the references [10, 11].

In order to obtain a good voltage signal, the sample was mechanically polished until very thin square prism had been obtained. The contacts were placed in the corners as shown schematically in the Fig. 1. The electrical terminals were prepared using low resistance sputtered Au contacts (~ 0.1 Ω). Magneto-transport properties were studied using a Maglab Oxford system of 9T. The magnetic field was applied perpendicular to the sample surface. A constant current was applied using a programmable current source Keithley model 220, and the corresponding voltage was measured using a nanovoltmeter Keithley model 181. V_{XX} and V_{XY} were measured by means of the van der Pauw technique, with permutation of the voltage and current contacts. The contacts were appropriately switched using a computer-controlled relay circuit (Fig. 3). In this method, the Hall and longitudinal voltages were measured simultaneously at each temperature and each applied magnetic field. Data acquisition and calculation of V_{XX} and V_{XY} were done in real time using the LabVIEW software [12].

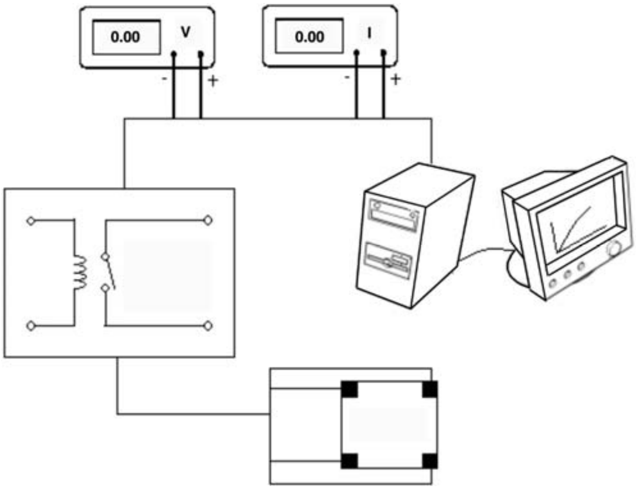

Fig. 3. Measurement setup for the modified switching contacts exploiting the van der Pauw technique. The contacts are switched using four different relays

Noise (thermopower effects, etc.) was eliminated by reversing the transport current polarity (I) in the samples under measurement. Thus, to obtain longitudinal (V_{XX}) and transverse (V_{XY}) voltages, eight voltage signals were measured. The V_{XX} and V_{XY} components were calculated based on the combination of eight records, which can be expressed as

$$V_{XX} = \frac{\left(V_{AB,CD}(I) - V_{AB,CD}(-I)\right)\left(V_{BC,AD}(I) - V_{BC,AD}(-I)\right)}{4} \tag{5}$$

and

$$V_{XY} = \frac{\left(V_{AC,BD}(I) - V_{AC,BD}(-I)\right)\left(V_{BD,AC}(I) - V_{BD,AC}(-I)\right)}{4} \tag{6}$$

By the method without field reversal, all voltages may be detected due to the transversal electric field. However, using Eq. (6), we can only partially compensate for those voltages added to the Hall effect. In this case we should also revert the magnetic field to separate the asymmetric and symmetric part of the Hall effect.

3. Results and discussion

Separating the Hall effect signal from its resistive offset signal is hard enough under normal circumstances, but it becomes even more challenging when the resistivity is drifting rapidly, as happens in materials transforming from metallic to superconductor behaviour. An important prerequisite for the validity of Eqs. (5) and (6) is that the measurements of the eight components are made under the same conditions, especially at the same temperature. Thus, the van der Pauw measurement of high-T_c superconductors requires consideration of some additional factors such as the influence of heating conditions of the sample during the measurement.

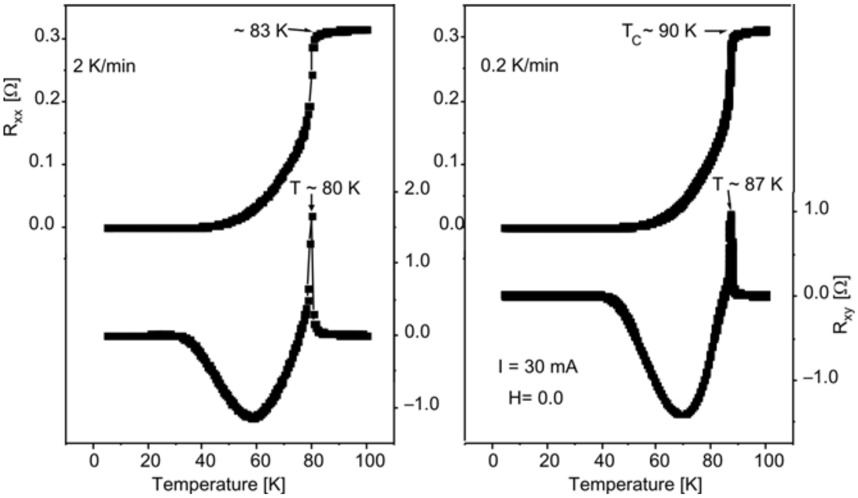

Fig. 4. Longitudinal resistance (upper curves) and transverse resistance of $YBa_2Cu_3O_{7-\delta}$ (lower curves) in function of the temperature measured for the various heating rates at $B = 0$, and $I = 30$ mA

We have performed a number of tests focused on the temperature stabilization of the sample. Figure 4 presents longitudinal (R_{XX}) and transverse (R_{XY}) resistances in function of temperature for the sample of $YBa_2Cu_3O_{7-\delta}$ measured at various heating rates under zero applied magnetic field. Measurements were taken during heating at the rates of 0.2 K/min and 2 K/min. At 2.0 K/min, the onset of the superconducting transition is far from the well-reported critical temperature for $YBa_2Cu_3O_{7-\delta}$ ($T_{ci} \approx 90$ K). However, at 0.2 K/min, T_{ci} is ca. 89 K which suggests that the measurement was performed under thermal equilibrium. Note that R_{XX} is essentially independent of the heating rate but the longitudinal resistance moves towards lower temperatures for higher heating rates. However, in the R_{XY} signal, both the intensity and the temperature dependence are altered with the change in the heating rate. The peak intensity (positive) at T_c increases while the second peak intensity (negative), at lower temperatures, decreases as the heating rate increases. Also both peaks move towards lower temperatures at 2 K/min. Based on these results, we conclude that lower heating rates are crucial for reliable transport measurements in superconductor materials, especially for Hall effect measurements.

The fact of occurrence of the Hall resistance at zero magnetic field is worth noting. In the mixed state, the Hall resistance in superconductors results from hydrodynamics vortices produced by the current flowing through the sample in an external magnetic field [1–5]. Then, in zero magnetic field we should not observe the appearance of a transverse voltage. However, transverse voltages in zero magnetic field have been observed in various HTSC materials [1, 5, 13–17]. Near T_c, a free vortex in the mixed state was observed which can be generated without the application of an external magnetic field. In this case, vortex–antivortex pairs may be excited by thermal fluctuations in the superconducting state, or induced by transport current passing through the sample on the opposite sides of the sample [13–17]. From Fig. 4, we can clearly see nonzero longitudinal transverse voltage close to T_c at zero magnetic field. The V_{XY} curves are non-zero close to the critical temperature with the maximum value approximately in the middle of the longitudinal superconducting transition, which has been reported in the literature [14, 15]. Moreover, a sign change from positive to negative is observed as the temperature decreases. In a true superconducting state ($R = 0$ in the longitudinal resistance) and in the normal state ($T > T_c$), no finite transversal voltage was detected. These results can be explained based on induced vortex–antivortex pairs applying the guiding vortex model [15]. The theory of the guiding vortex was proposed to explain the even effect in superconductors which assumes the existence of a new force acting on the vortex. This force (the guiding force) impels the vortex to move only in a given direction that is determined by the direction of the pinning potential valley. However, the nature of this pinning potential has not been completely solved. One of the promising models is the intrinsic pinning model, which assumes that the origin of the guiding forces is due to the layered structure of the HTSC [18]. Other mechanisms such as grain boundary guiding in polycrystalline materials for example, should be kept in mind. This model seems to offer a consistent explanation of our results.

In general, transverse voltage consists of three components: a component coming from the geometrical misalignment of the contacts, a Hall voltage component, and a component originating from the guided motion of vortex and antivortex. The geometrical misalignment can be detected by normal state measurements in zero magnetic field. In our case, in the normal state, no transverse voltage was detected at zero applied magnetic field. Therefore, the transverse voltage in zero magnetic field cannot originate from a geometrical misalignment of the contacts. The other two components can be distinguished by comparing the voltages measured in two opposite magnetic field directions: while in the Hall voltage, the sign of the measured voltage depends on the applied magnetic field direction because the vortex motion is only governed by the Lorentz force: in the case of the guided vortex–antivortex motion, it is independent of the field direction. This difference gives us the chance to distinguish between generation mechanisms of these two voltages. Figure 5a shows the transverse voltage in function of the temperature measured in the same sample that was presented in Fig. 4 under magnetic field in positive ($H = 9$ T) and negative ($H = -9$ T) directions.

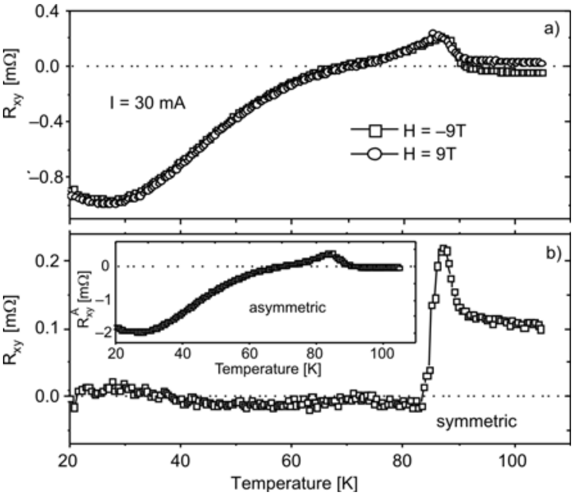

Fig. 5. Transverse resistance in function of the temperature measured in the sample of YBa$_2$Cu$_3$O$_{7-\delta}$ at the applied magnetic field in positive ($H = 9$ T) and negative ($H = -9$ T) directions (a); and symmetric and asymmetric transverse resistances calculated from the data of Fig. 4a (b)

From Figure 5a we can observe two distinct behaviours: above T_c (ca. 90 K), R_{XY} is dependent on the direction of the applied magnetic field; below T_c, the transverse resistance is independent of its direction. Using R_{XY} measurements in both directions of the magnetic field, we can calculate the symmetric (R^S_{XY}) and asymmetric (R^A_{XY}) resistance components. To obtain the symmetric transverse resistance which is due to the applied magnetic field, we should calculate $R^S_{XY} = (R_{XY}(H) - R_{XY}(-H))/2$, where $R_{XY}(H)$ and $R_{XY}(-H)$ are measured under magnetic field applied in positive and negative directions, respectively. The asymmetric transverse resistance was calculated as $R^A_{XY} = (R_{XY}(H) + R_{XY}(-H))/2$. The results for both components are presented in Fig. 5b. In the normal state ($T > T_c$), the symmetric component presents a positive signal, as observed for several superconductor materials. In the superconducting state ($T < T_c$) no transverse voltage was detected for this value of magnetic field. Thus, we can say that this component presents the true Hall resistance effect. The inset (Fig. 5b) shows the asymmetric component which can be due to guided motion of vortex and anti-vortex, similar to Hall measurements in zero applied magnetic field.

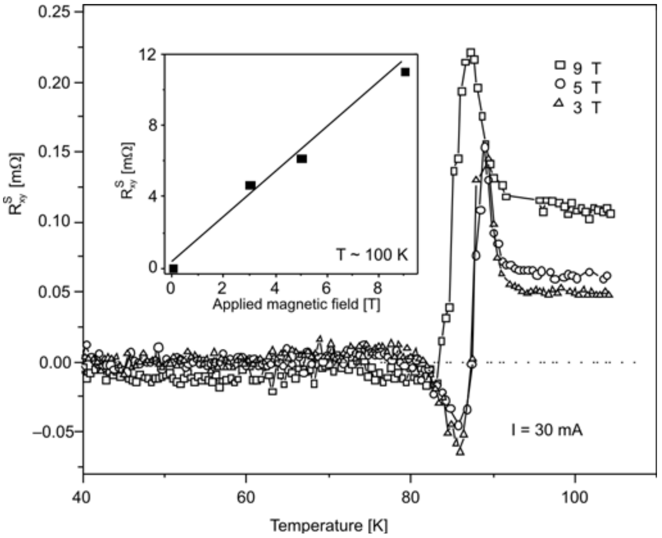

Fig. 6. R^S_{XY} in function of temperature for the same sample $YBa_2Cu_3O_{7-\delta}$ for various magnetic fields. The inset shows the transverse resistance in function of magnetic field at ca. 100 K

In Figure 6, we show other results for R^S_{XY} in function of temperature for the sample $YBa_2Cu_3O_{7+\delta}$ for various magnetic fields. In the normal state (see inset), the transverse voltage is positive and increases linearly as the strength of the applied magnetic field increases, as is expected of hole-doped high-T_c superconductors [19, 20]. The resistance changes from positive to negative below T_c for low and moderate magnetic fields. Higher fields suppress this sign reversal and restore $R_{XY} > 0$ near T_c, while at low temperatures R_{XY} tends to zero. There are several models to explain this effect, but common agreement has not been achieved up to now [3, 5]. In addition to the sign reversal near T_c, the R^S_{XY} measured for the sample $Bi_2Sr_2Ca_{0.8}Pr_{0.2}Cu_3O_{8+\delta}$ suggest the occurrence of a second sign reversal which has been observed in most high-T_c superconductors (see inset of Fig. 7) [21, 22]. The error is about 5%. Figure 7 shows longitudinal resistance (upper) and symmetric transverse resistance (lower), calculated from the results of the van der Pauw measurements at 5 T. In the R_{XX} we can see a broad superconducting transition which can be related to granular superconductivity. The R^S_{XY} is positive in the normal state and changes to negative around T_c. These sign reversals in the transverse component are believed to be related to the quasiparticle or vortex-core contributions which are associated with the normal state excitation, superconducting dissipation resulting from vortex hydrodynamics and superconducting fluctuations [22].

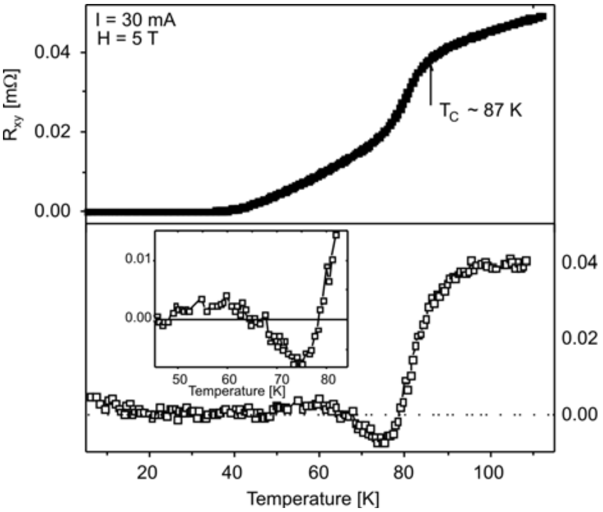

Fig. 7. Longitudinal resistance (upper) and symmetric transverse (lower) resistances calculated from the results of the van der Pauw measurements at 5 T, for the sample of $Bi_2Sr_2Ca_{0.8}Pr_{0.2}Cu_3O_{8+\delta}$. In the inset, the results suggest a double sign reversal of the R^S_{XY} in the vicinity of T_c

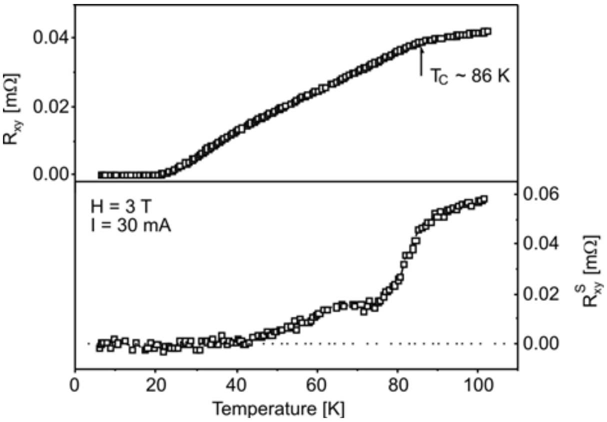

Fig. 8. Longitudinal resistance (upper) and symmetric transverse (lower) resistances calculated from results of the van der Pauw measurements at 3 T, for the sample of $Bi_2Sr_2Ca_{0.7}Pr_{0.3}Cu_3O_{8+\delta}$

Finally, the longitudinal resistance and symmetric transverse resistance, calculated from results of the van der Pauw measurements at 3 T for $Bi_2Sr_2Ca_{0.7}Pr_{0.3}Cu_3O_{8+\delta}$ are shown in Fig. 8. We have noted a very wide superconducting transition in the temperature dependence of R_{XX}. In contrast with that observed for $Bi_2Sr_2Ca_{0.8}Pr_{0.2}Cu_3O_{8+\delta}$

(see Fig. 7), no sign inversion was observed in the transverse component. This difference in behaviour probably reflects the difference in the flux dynamics and the nature of the pinning mechanism between these two superconductor materials. Similar behaviour is observed in some of the conventional high-T_c superconductors in the mixed state, but is not fully understood yet [23].

4. Conclusion

A modified van der Pauw technique has been presented to measure transport properties of HTSC superconductors. It was observed that a low heating rate is crucial for obtaining reliable transport measurements in high-T_c superconducting materials. It is necessary to carry out measurements in two opposite magnetic field directions in order to separate the transverse resistance components. We believe that this technique makes real-time Hall and longitudinal measurements practical in undergoing superconducting transitions.

Acknowledgements

This work has been supported by the FAPESP (97/11113-6, 00/03610-4) and CNPq.

References

[1] DA LUZ M.S., DE CARVALHO F.J.H. JRDOS SANTOS C.A.M., SHIGUE C.Y., MACHADO A.J.S., Physica C, 419 (2005), 71, and references therein.
[2] JANEČEK I., VAŠEK P., Physica C, 468 (2008), 17.
[3] RICHTER H., PUICA I., LANG W., PERUZZI L.M., DURRELL J.H., STURM H., PEDARNIG J.D., BÄUERLE D., Phys. Rev. B, 73 (2006), 184506.
[4] WÖRDENWEBER R., SANKARRAJ J.S.K., DYMASHEVSKI P., HOLLMANN E., Physica C, 434 (2006) 101.
[5] PUICA I., LANG W., GÖB W., Phys. Rev. B, 69 (2004), 104513.
[6] VAN DER PAUW L.J., Philips Res. Rep., 13 (1958), 1.
[7] VAN DER PAUW L.J., Philips Tech. Rev., 20 (1959), 220.
[8] JANEČEK I., VAŠEK P., Physica C, 390 (2003), 330.
[9] JANEČEK I., VAŠEK P., Physica C, 402 (2004), 199.
[10] DOS SANTOS C.A.M., MACHADO A.J.S., Physica C, 354 (2001), 213.
[11] DOS SANTOS C.A.M., MOEHLECKE S., KOPELEVIC Y., MACHADO A.J.S., Physica C, 390 (2003), 21.
[12] National Instruments LabVIEW Graphical Programming for Instrumentation, Austin, TX, Version 5.0, 1998.
[13] VAŠEK P., Supercond. Sci. Technol., 20 (2007), 67.
[14] FRANCAVILLA T.L., HEIN R.A., IEEE Trans. Mag., 27 (1991), 1039.
[15] VAŠEK P., SHIMAKAGE H., WANG Z., Physica C, 411 (2004), 164.
[16] FRANCAVILLA T.L., CUKAUSKAS E.J., ALLEN L.H., BROUSSARD P.R., IEEE Appl. Sup., 5 (1995), 1717.
[17] VAŠEK P., Physica C, 364–365 (2001), 194.

[18] Vašek P., Janeček I., Plecháček V., Physica C, 247 (1995), 381.
[19] Chien T.R., Jing T.W., Ong N.P., Wang Z.Z., Phys. Rev. Lett., 66 (1991), 3075.
[20] Malinowski A., Cieplak M.Z., Guha S., Wu Q., Kim B., Krickser A., Perali A., Karpinska K., Berkowski M., Shang C.H., Lindenfeld P., Phys. Rev. B, 66 (2002), 104512, and references therein.
[21] Lang W., Göb W., Pedarnig J.D., Rössler R., Bäuerle D., Physica C, 364-365 (2001), 518.
[22] Göb W., Liebich W., Lang W., Puica I., Sobolewski R., Rössler R., Pedarnig J.D., Bäuerle D., Phys. Rev. B, 62 (2000), 9780.
[23] Iye Y., Nakamura S., Tamegai T., Physica C, 159 (1989), 616.

Received 2 August 2008
Revised 28 October 2008

Materials Science-Poland, Vol. 27, No. 2, 2009

Dielectric properties of lignocellulosic materials–polypropylene composites

E. MARKIEWICZ[1*], D. PAUKSZTA[2], S. BORYSIAK[2]

[1]Institute of Molecular Physics, Polish Academy of Sciences,
Smoluchowskiego 17, 60-179 Poznań, Poland

[2]Institute of Chemical Technology and Engineering, Poznań University of Technology,
M. Skłodowskiej-Curie 2, 60-965 Poznań, Poland

Composites were made from isotactic polypropylene and lignocellulosic materials derived from hemp and flax plants using moulding and hydraulic pressing techniques. Frequency dependences of the electric permittivity ε' and the ac conductivity σ_{ac} of the composite samples were measured in the frequency range from 100 Hz to 13 MHz at room temperature. The linear relationship between the reciprocal relative permittivity ($1/\varepsilon'$) and the volume fraction of the lignocellulosic material was established. The loading of the polypropylene with the lignocellulosic materials increases the electric permittivity ε' and improves the electrical conductivity σ_{ac}. The effect of temperature (150–450 K) on the dielectric spectrum of polypropylene and the composites was investigated in the frequency range from 100 Hz to 1 MHz. Four dielectric relaxation processes were found in the spectra of the composites: β – ascribed to the local motion of the main polymer chain, β_{wet} – associated with the presence of water, δ – related to the motion of the end groups in the branched polymers and σ – due to the conductivity effect. The dielectric spectrum of polypropylene does not exhibit anomalies.

Key words: *polymer matrix composites; lignocellulosic material; electrical properties*

1. Introduction

Composites of thermoplastic polymers based on lignocellulosic fillers are widely used in several branches of industry, e.g. automotive and building engineering [1], aviation and the packaging industry [2]. Mechanical and physical properties of a polymer can be improved by addition of a lignocellulosic filler [3–5]. Composites made from polypropylene (PP) and wood fibre are known to exhibit significantly higher stiffness than unreinforced polypropylene [6]. The loading of the polypropylene

---

[*] Corresponding author, e-mail: ewamar@ifmpan.poznan.pl

with rice husk powder increases Young's modulus and the flexural modulus of the composite, compared with those of the polypropylene [7]. Cellulose fibres incorporated into the polyethylene matrix also enhance the mechanical performance of the composite [8–10]. The most interesting feature of the biocomposites is their partial biodegradability as the filler materials come from a natural resource. The addition of lignocellulosic materials results in a significant decrease of such essential parameters as heat release rate (HRR) peak and mass loss rate (MLR) [11, 12] which are very important in terms of the resistance against the fire expansion. The nonabrasive nature of lignocellulosic fillers allows one to treat biocomposites as an ecological alternative [1] to composites reinforced with glass fibre and other mineral fillers. An additional advantage of the polymer composite based on the lignocellulosic filler is their sound absorption capacity due to the anatomic structure of the tubiform lignocellulosic components [13–16]. The hollow structure is responsible for the insulation against heat and noise.

Combination of the polymer and the lignocellulosic materials results in new dielectric properties of the composite. The possibility of designing new materials with predictable properties is very promising from the application point of view. The materials characterized by a low electric permittivity are applied as insulators to cut off the energy flow in alternating and direct electric current circuits. However, to achieve good energy accumulation in the presence of an electric field, materials having high electric permittivity are particularly suitable. In the latter application, the temperature insensitivity and the dispersion of the electric permittivity are of great importance because the materials are often used for thermal compensation of the electric circuits as well as they work in high frequency range [17]. Recently, new composite materials with non-standard dielectric properties were designed. The composites containing hollow keratin fibres are characterized by unusually low value of electric permittivity due to air present inside [18]. They can replace dielectrics in microchips and printed circuit boards used in the electronic industry. Some composites were designed with the aim of application as antistatic materials to dissipate static charges. They show typical behaviour which can be concluded: the electric permittivity, the dissipation factor and the electrical conductivity increase steadily with increasing fibre loading whereas the volume resistivity decreases with increase of fibre content. Sisal fibre reinforced LDPE [19, 20], sisal–oil palm hybrid biofibre reinforced natural rubber [18] and epoxy resin reinforced with sisal fibre [21] belong to this kind of biocomposites.

In recent years, the composites of polypropylene reinforced with hemp [22] and flax [23] were developed. The thermal behaviours and thermal decompositions of both composites were examined by the differential scanning calorimetry (DSC) and thermogravimetry (TGA), in addition to microscopy analyses. The mechanical properties (tensile modulus, stress and elongation at break) of polypropylene–hemp composites were also determined [22]. However, dielectric properties of polypropylene composites reinforced with hemp and flax have not been investigated to date. The aim of this work is to show the influence of the lignocellulosic material loading on the electric permittivity ε' and on the ac conductivity σ_{ac} of the composites. The temperature dependences of the electric permittivity ε' and the loss factor ε'' have also been studied.

2. Experimental

Materials. Isotactic polypropylene Malen F-401 (Melt Flow Index 230/2.16 = 2.4 –3.2 g/10 min, isotacticity 95%), produced by Orlen Płock (Poland) was used as a matrix for fabrication of the composites. Lignocellulosic materials: long and short flax fibres, long and short hemp fibres as well as flax and hemp shivers were used as filling materials.

Sample preparation. The composites were made by two different methods. The former one consisted in mixing crumble lignocellulosic materials with polypropylene granulate in proportion of 25 wt. % of natural component. After that, the extrusion was carried out using a "Fairex" (McNell Akron Repiquetn, France) single-screw extruder, L/D = 25. The composite material was obtained in a granulate form [24]. To obtain samples for investigations, the granulate of the composite was melted in a mould between heating plates at 200 °C under the load of 3000 kG. The composites containing long fibres of hemp and flax (40 wt. %) were fabricated using only the technique of hydraulic pressing at 200 °C under the load of 3000 kG, described elsewhere [25]. Finally, all the samples assumed the shapes of disks, typically having the diameter of 10 mm and the thickness of 1.5 mm. In Table 1, all the fabricated samples are specified.

Table 1. Specification of the investigated samples

No.	Material	Density [kg/m^3]	Volume fraction of the lignocellulosic material
1	Polypropylene (PP)	881.8	0
2	PP+25% of short hemp fibres	862.5	0.27
3	PP+25% of hemp shivers	911.3	0.28
4	PP+40% of long hemp fibres	927.9	0.37
5	PP+25% of short flax fibres	883.0	0.25
6	PP+25% of flax shivers	943.1	0.20
7	PP+40% of long flax fibres	934.6	0.37

Measurement. The plane surfaces of the samples (Table 1) were covered with gold electrodes using the BALTEC SCD 050 sputter coater and fixed to the sample holder of the measurement device. Frequency dependences of the electric permittivity ε' and the ac conductivity σ_{ac} of the samples were measured by means of a computer aided (program WinDETA V4.0) HP 4192 LF impedance analyzer operating in the frequency range from 100 Hz to 13 MHz at room temperature.

The effect of temperature variation on the dielectric spectrum of PP as well as the of the composites was investigated in the frequency range from 100 Hz to 1 MHz using a computer-aided (program HP VEE) HP-4284A precision LCR meter. The samples were mounted in a CF 1204 Oxford Instruments cryostat equipped with an ITC 4 temperature controller. The measurements were performed during heating from 150 K to 450 K at the rate of 1 K/min.

The relative electric permittivity ε' was calculated from the expression:

$$\varepsilon' = \frac{Cd}{\varepsilon_0 S} \tag{1}$$

where: C is the capacitance of the condenser with the dielectric, S stands for the area of the sample covered by the electrode, d means the thickness of the sample and ε_0 equal to $8.85 \cdot 10^{-12}$ F/m is the electric permittivity of the vacuum.

The ac conductivity σ_{ac} was determined by using the following equation:

$$\sigma_{ac} = \varepsilon_0 \omega \varepsilon' \tan\delta \tag{2}$$

where $\tan\delta$ denotes the dielectric dissipation factor and ω stands for the angular frequency.

3. Results and discussion

The frequency dependences of the electric permittivity ε' measured at room temperature for the polypropylene composites reinforced with various lignocellulosic materials derived from hemp and flax are presented in Figs. 1 and 2. The effect of loading with the lignocellulosic material consists in the increase of the electric permittivity ε' over the whole measurement frequency range. The effect is predominant at lower frequencies. This result is very similar to that obtained by Paul et al. [19] for sisal fibre–LDPE composites.

Pure polypropylene is a non-polar hydrophobic material which shows only instantaneous ionic and electronic polarization. Its electric permittivity ε' remains nearly constant over the whole frequency range with a slender increase below 10^3 Hz. The addition of a hydrophilic lignocellulose material to the polypropylene entails the insertion of polar groups into the non-polar material, explaining why the polarization, dependent of the dipole reorientation, increases. Moreover, the presence of the hydroxyl groups –OH in the cellulose, the hemicellulose and the lignin extends the moisture absorption, due to the interaction of –OH groups and water molecules. The overall polarization of the composite, being the sum of three contributions: electronic, ionic and dipole reorientation-related ones, exhibits the maximum values at low frequencies and decreases with increasing frequency. The same behaviour shows the electric permittivity of the composites ε’.

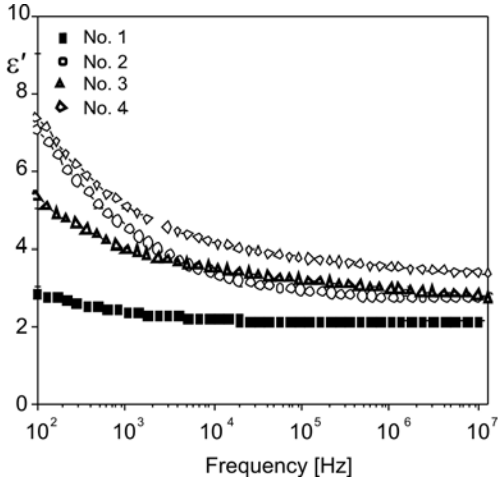

Fig. 1. Frequency dependences of electric permittivity ε' obtained for PP and the composites with hemp: No. 1 – PP, No. 2 – PP + 25 wt. % of short hemp fibres, No. 3 – PP + 25 wt. % of hemp shivers, No. 4 – PP + 40 wt. % of long hemp fibres

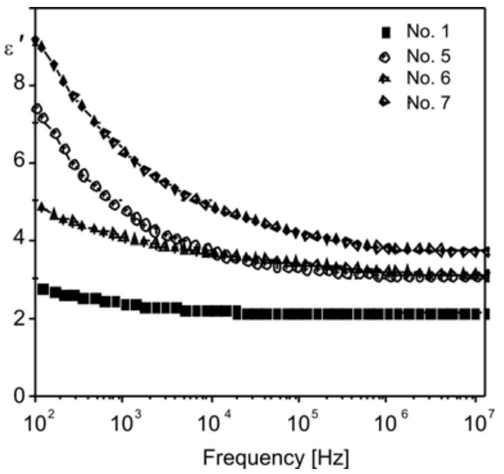

Fig. 2. Frequency dependences of electric permittivity ε' obtained for PP and the composites with flax: No. 1 – PP, No. 5 – PP + 25 wt. % of short flax fibres, No. 6 – PP + 25 wt. % of flax shivers, No. 7 – PP + 40 wt. % of long flax fibres

The relative electric permittivity ε' increases as the content of the lignocellulosic material increases. In the higher frequency range, i.e. above 10^6 Hz, the value of the relative electric permittivity ε' tends to the constant value fixed by squared refractive index. Moreover, the values for composites with the same content (25 wt. %) of different lignocellulosic materials converge. In the case of hemp–polypropylene composites (Fig. 1), one can notice that the values of ε' for PP + 25 wt. % of short hemp fibres (No. 2) and for PP + 25 wt. % of hemp shivers (No. 3) are ca. 2.7. For the flax –polypropylene composites it can be seen (Fig. 2) that the values of ε' obtained for PP + 25 wt. % of short flax fibres (No. 5) and for PP + 25 wt. % of flax shivers (No. 6) tend to 2.8 as the frequency increases. In the frequency range between 10^3 and 10^4 Hz, one can notice a characteristic point below which the crucial modification in the frequency dependences of the relative permittivity ε' appears. Thus, the differences in the electric permittivity ε' are most significant in the low frequency range, and they are observed also for the composites having the same content of lignocellulosic materials derived from different parts of hemp and flax. The composites containing the shivers derived from hemp as well as from flax (25 wt. %) exhibit lower ε' than the ones comprising short fibres (also 25 wt. %). The shivers are the lignified parts of stems, separated from the fibres, and they show lower capacity of moisture absorption. This fact can be indicative of a smaller number of polar groups and lower polarization related to dipole reorientation.

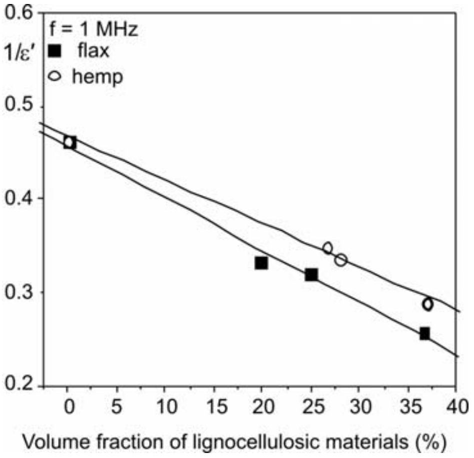

Fig. 3. Reciprocal electric permittivity $1/\varepsilon'$ in function of volume fraction of lignocellulosic material derived from hemp and flax

Figure 3 displays the plots of the reciprocal relative electric permittivity $1/\varepsilon'$ vs. the volume fraction of lingocellulosic material derived from hemp and flax at the frequency of 1 MHz. The obtained results are in agreement with the theoretical model of the electric permittivity for natural rubber biocomposites reinforced with sisal oil palm hybrid biofibre, as presented by Jacob et al. [18]. The relationship between the reciprocal of the relative electric permittivity ε' and the volume fraction of the lignocellulosic material is linear for the applied contents of the filler. The dielectric impermeability of the composite decreases as the filler content increases.

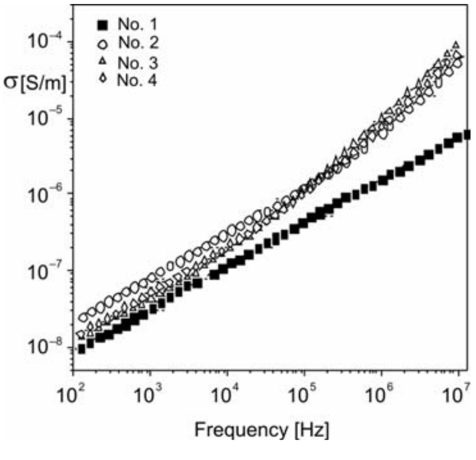

Fig. 4. Frequency dependences of ac conductivity for the samples: No. 1 – PP, No. 2 – PP + 25 wt. % of short hemp fibres, No. 3 – PP + 25 wt. % of hemp shivers, No. 4 – PP + 40 wt. % of long hemp fibres

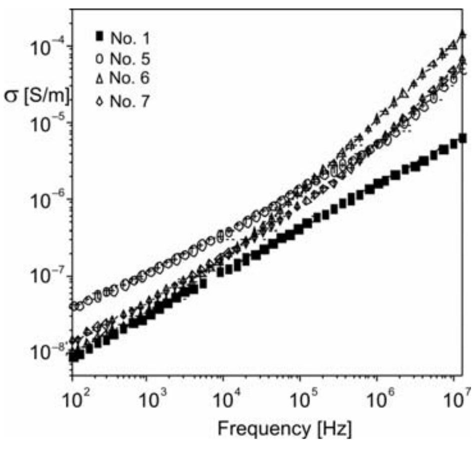

Fig. 5. Frequency dependences of ac conductivity obtained for the samples: No. 1 – PP, No. 5 – PP + 25 wt. % of short flax fibres, No. 6 – PP + 25 wt. % of flax shivers, No. 7 – PP + 40 wt. % of long flax fibres

The variations of the ac conductivity in function of the frequency measured for the polypropylene and all composite samples at room temperature are shown in Figs. 4

and 5. The reinforcement of the polypropylene with the lignocellulosic material increases the conductivity. The frequency dependence of the electrical conductivity is described by the expression [26]:

$$\sigma(\omega) \propto \omega^n \tag{3}$$

The exponent n is close to 0.5 for pure polypropylene and points to diffusive carrier transport. For the composites, n changes from ca. 0.5 at low frequencies to ca. 1 at high frequencies. This fact proves the existence of diffusive as well as hopping carrier transport. The lack of any frequency-independent conductivity at low frequencies indicates that no ohmic conduction occurs at room temperature in any of the samples under investigation.

One can state the influence of the distribution of the lignocellulosic fillers in the matrix on the frequency dependence of ac conductivity. The incorporation of the shivers (No. 3 Fig. 4, and No. 6, Fig. 5) as well as long fibres (No. 4, Fig. 4, and No. 7, Fig. 5) in the polypropylene causes a relatively small increase in the conductivity at lower frequencies. A comparatively high increase in the conductivity at lower frequencies is shown by the composites with the short fibres derived from hemp (No. 2, Fig. 4) as well as from flax (No. 5, Fig. 5). This fact is probably due to the different distribution of the filler. Short fibres are randomly distributed in the matrix, and the electric field is applied at different angles with respect to the axes of the fibres. The random distribution enables rearrangement of the short fibres in a chain structure which ensures better carrier mobility in the presence of electric field. However, the manufacturing method of the composites with long fibres implies the perpendicular orientation of the electric field with respect to the fibre axis. It is difficult to arrange the fibres so that they form a chain structure. These results demonstrate that the composites having short, randomly distributed fibres provide the best conductivity among the investigated samples.

The variations of the relative electric permittivity ε' with the temperature investigated for the polypropylene as well as the composites with hemp and flax are presented in Figs. 6 and 7. The value of ε' measured for polypropylene is almost independent of temperature, up to the melting point at 438 K [27]. The dielectric response of the composites is dominated by the relaxation ascribed to an orientational motion of mixed phase of both lignocellulosic material and water. This phenomenon, characteristic of cellulose and its derivatives, has been reported by many authors [28–31]. The electric permittivity ε' of the composites increases with the temperature up to the maximum associated with traces of water, and then decreases. The position of the maximum is determined by the contents of chemically bound water which cannot be removed during the preparation. The maximum is shifted towards higher temperatures in the case of higher water contents [21]. In the vicinity of the melting point of the polypropylene, a steep fall is visible. The relative electric permittivity ε' decreases as the frequency increases, as is seen for two frequencies: 100 Hz and 1 MHz.

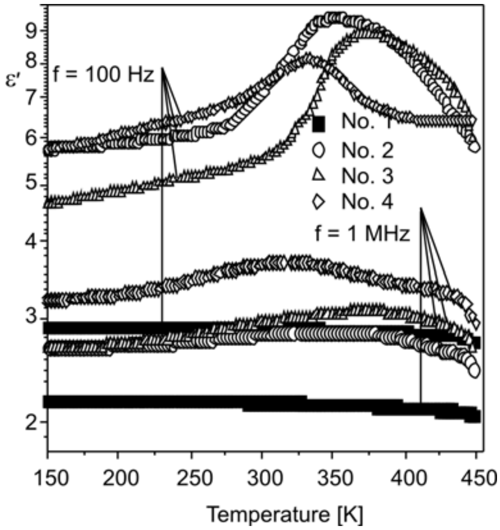

Fig. 6. Temperature dependences of electric permittivity ε' obtained at frequencies 100 kHz and 1 MHz for the samples: No. 1 – PP, No. 2 – PP + 25 wt. % of short hemp fibres, No. 3 – PP + 25 wt. % of hemp shivers, No. 4 – PP + 40 wt. % of long hemp fibres

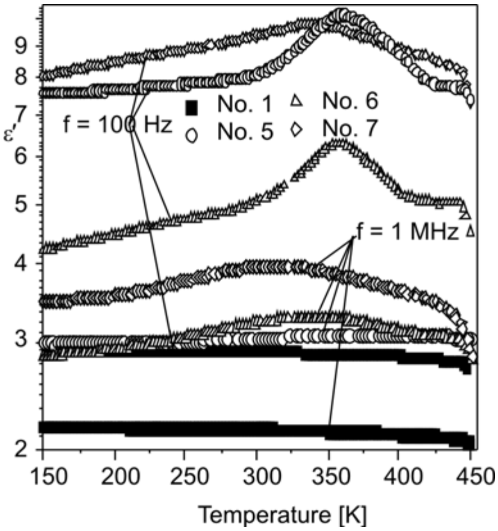

Fig. 7. Temperature dependences of electric permittivity ε' obtained at the frequencies 100 kHz and 1 MHz for the samples: No. 1 – PP, No. 5 – PP + 25% of short flax fibres, No. 6 – PP + 25% of flax shivers, No. 7 – PP + 40% of long flax fibres

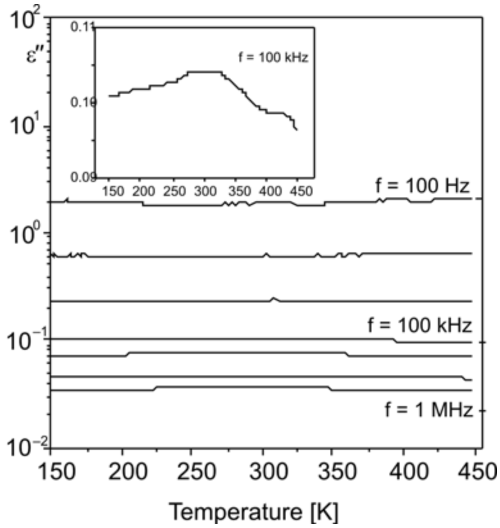

Fig. 8. Temperature dependence of dielectric loss factor ε'' for polypropylene. Inset: the dependence at the frequency of 100 kHz. Note an expanded ε'' scale

The temperature dependence of dielectric losses of the composites is strongly influenced by the contribution of the lignocellulosic materials. The dielectric loss factor ε'' of pure PP in function of temperature is presented in Fig. 8. Pure PP is known to exhibit two characteristic features [32]: a glass relaxation peak around 263 K, and a high-temperature (ca. 323 K) shoulder associated with chain relaxation in the crystalline phase. These features cannot be exactly detected by the dielectric relaxation spectroscopy (DRS) method without special modification of the polymer structure or introducing polar groups in the structure [33] because of the non-polarity of the polypropylene. The absence of polar groups is the reason why the temperature dependence of the dielectric losses does not show any anomalies (Fig. 8). In the inset, the two shoulders are hardly visible. The former one starts to increase above 263 K and is ascribed to the glass transition. The other one appears around 314 K and is caused by the chain relaxation in the crystalline α-phase. These trace relaxation processes in the spectrum of pure polypropylene result from the presence of a small number of polar groups, due to undesired phenomena (thermal degradation of chains and oxidation) during processing of the polymer.

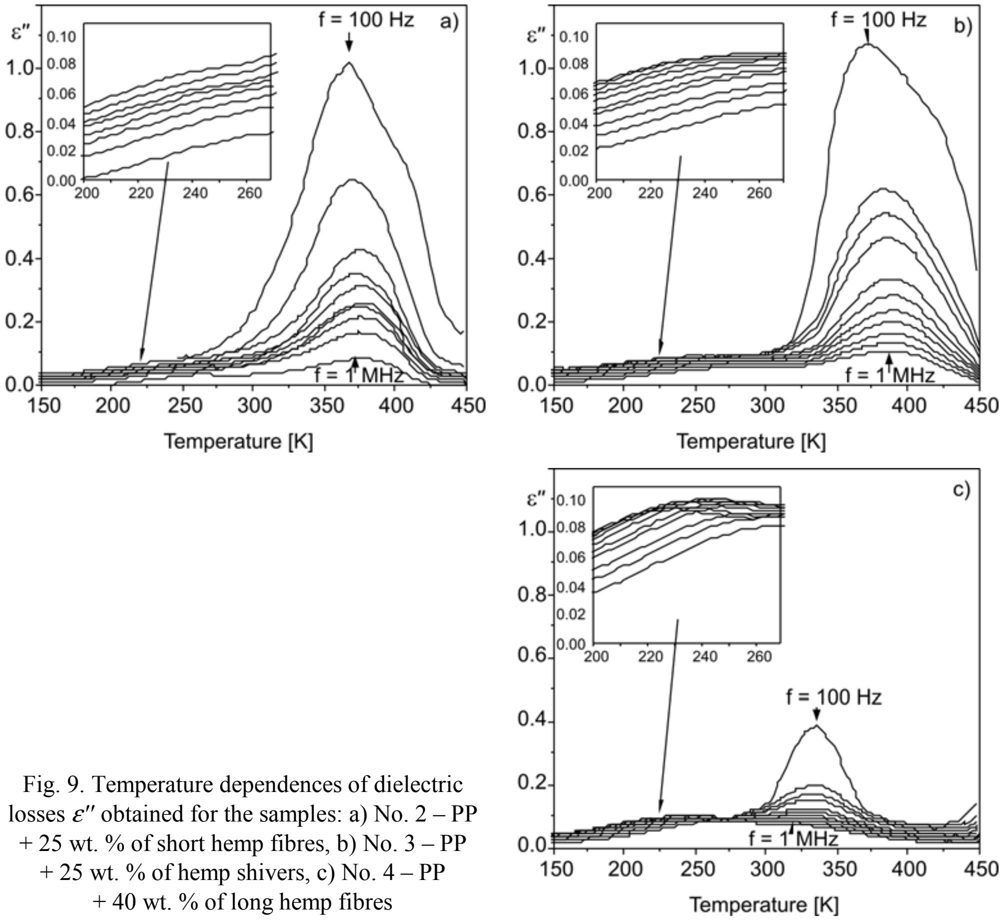

Fig. 9. Temperature dependences of dielectric losses ε'' obtained for the samples: a) No. 2 – PP + 25 wt. % of short hemp fibres, b) No. 3 – PP + 25 wt. % of hemp shivers, c) No. 4 – PP + 40 wt. % of long hemp fibres

Figures 9 and 10 show the dielectric loss factor ε'' in function of temperature measured for the polypropylene composites reinforced with the lignocellulosic material derived from hemp and flax, respectively. Both kinds of fillers modify the dielectric absorption spectrum in the same way. The anomalies due to polar groups present in the lignocellulosic material can be easily detected by means of DRS.

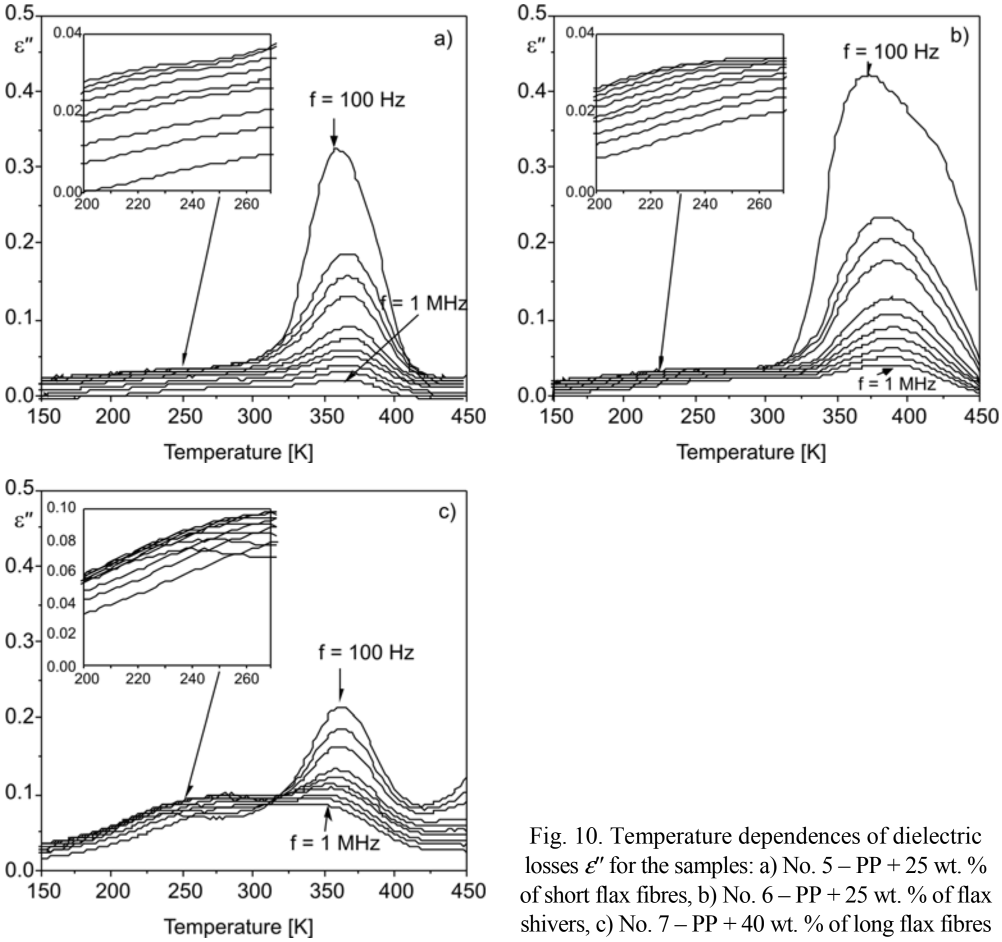

Fig. 10. Temperature dependences of dielectric losses ε'' for the samples: a) No. 5 – PP + 25 wt. % of short flax fibres, b) No. 6 – PP + 25 wt. % of flax shivers, c) No. 7 – PP + 40 wt. % of long flax fibres

In the low-temperature range (from 200 to 270 K) one can observe the maxima of ε'' ascribed to the β relaxation in cellulose, which is the main component of each lignocellulosic filler (71 wt. % in flax, and 75 wt. % in hemp fibres [3]). The β relaxation is interpreted as a local motion of chain segments via the glucosidic linkages [28]. Above room temperature (330–400 K) one can notice high relaxation peaks. From their shape, it can be deduced that two relaxation processes overlap in this temperature and frequency range: β_{wet} – the relaxation associated with the orientational motion of both cellulose and water [28, 29] and δ – the relaxation ascribed to the motion of the end groups in branched polymers [28] present in the lignocellulosic material (hemicellulose, pectin, lignin). Because the intensity of the δ relaxation is significantly lower than that of β_{wet} relaxation [28], one can state that in the polypropylene–lignocellulose material composites the β_{wet} relaxation is disturbed by the δ process. In the case of composites with long fibres derived from flax as well as hemp (Figs. 9c and 10c), higher dielectric losses were observed in the highest temperature range (above 420 K). This effect results from the electric conductivity and is called σ relaxation [28]. The losses due to the electric conductivity are ascribed to charge carrier hopping between localized sites in amorphous solids. The fact that the σ relaxation was observed only for the composites with long fibres confirms the conclusion [28] that the activation energy for the carrier hopping increases when the amount of water is reduced. The technique of hydraulic pressing, applied for fabrication of composite samples with long fibres implied low contents of water. The intensity of β_{wet} relaxation is proportional to the contents of water. The low intensity of β_{wet} relaxation in the composites with long fibres is a reason for a relatively high strength of β relaxation in comparison with that observed for other investigated samples where the β process is suppressed by β_{wet} relaxation.

The temperature dependence of the β relaxation time $\tau(T)$ follows an Arrhenius type behaviour, characterized by the activation energy E_a and a pre-exponential factor τ_0:

$$\tau(T) = \tau_0 \exp\left(\frac{E_a}{kT}\right) \tag{4}$$

where k is the Boltzmann constant. The activation energy is interpreted as the height of the potential barrier between two orientational conformation states which can be reached during the molecular motion [28]. The pre-exponential factor τ_0 represents the inverse oscillation frequency of the molecular group in a conformational potential minimum [28]. According to the Eyring rate theory [34], the factor τ_0 is an indicator of the cooperativity of the orientational motion within polar groups. A smaller value of τ_0 means higher cooperativity of the motion.

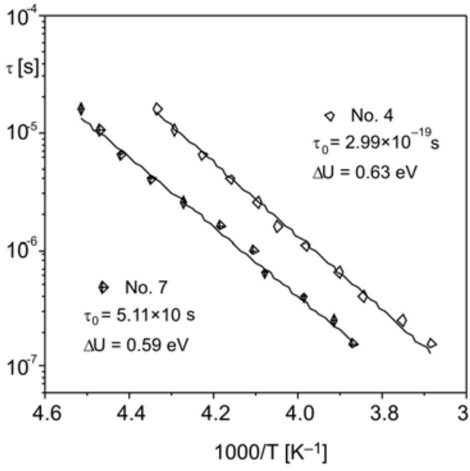

Fig. 11. β -relaxation time vs. reciprocal of temperature for the composite samples: No. 4 – PP + 40 wt. % of long hemp fibres and No. 7 – PP + 40 wt. % of long flax fibres

The Arrhenius plots of the relaxation times for the polypropylene composites with long fibres are presented in Fig. 11. The values of the activation energy E_a and the pre-exponential factor τ_0 resulting from fitting indicate better cooperativity of the motion than that of cellulose, which is usually characterized by the activation energy below 0.5 eV and pre-exponential factor of the order of 10^{-16} s [28]. The origin of the improved cooperativity might be the presence of branched polymers (hemicellulose, pectin, lignin) in the lignocellulosic materials. Branched polymers are known to have the capacity to form interchain hydrogen bonds, due to their high dimensions. In this manner, the local chain motion can be involved not only in the nearest repeating unit of the same chain but also in motion of another chains [35].

4. Conclusions

The dielectric properties (relative electric permittivity ε' and ac conductivity σ_{ac}) of polypropylene–lignocellulosic material composites were evaluated in function of frequency, filler contents and temperature. The relative electric permittivity ε' increases with loading of the polypropylene with the lignocellulosic material. In all the filler types considered, the relative permittivity ε' is inversely proportional to the volume fraction of the lignocellulosic material. The increase in the electric permittivity ε' is attributed to the increase in the orientation polarization of polar groups present in the lignocellulosic material. The effect is more predominant in the low frequency range. The incorporation of the lignocellulosic materials in the polypropylene matrix improves ac conductivity σ_{ac}.

The effect of temperature variation (150–450 K) on the dielectric spectrum of polypropylene and the composites was investigated in the frequency range from 100 Hz to 1 MHz. Four dielectric relaxation processes were found in the spectra of the composites: β – ascribed to the local motion of the main polymer chain, β_{wet} – associated with the presence of water, δ – related to the motion of the end groups in the branched polymers and σ – due to the conductivity effect. The dielectric spectrum of polypropylene does not show anomalies. The temperature dependence of dielectric losses of the composites is strongly influenced by the contribution of the lignocellulosic materials.

The obtained results point to the possibilities of practical application of the investigated composites. The increased electric permittivity, in comparison with the polypropylene, is preferable in the application for accumulation of the energy in electric field. The constant value of ε' at frequencies above 1 MHz is evidence that the composites can be used in the high frequency range. The temperature measurements reveal that the composites with short fibres show the best thermal stability of the relative electric permittivity ε' in the vicinity of the room temperature. The other investigated samples exhibit more pronounced maxima in the temperature dependence profile of the relative electric permittivity because of the contents of water. Moreover, the polypropylene composites reinforced with short fibres assure the best antistatic properties, because of their improved electrical conductivity over the whole measurement frequency range. The results presented point to the possibility of exploiting polypropylene composites reinforced with flax and hemp lignocellulosic material in the furniture, building and automotive industry in modern wood–plastic composite (WPC) designs [36]. Not only these materials have better antistatic properties in comparison with the polypropylene, but they also have good sound absorption [36]. Composites containing lignocellulosic fibres [13–15] will improve the quality of human life.

Acknowledgements

This research was supported by the University Grant of Poznań University of Technology 32-171/08-DS.

References

[1] Peijs T., Mater. Today, 6 (2003), 30.
[2] Błędzki A.K., Gassan J., Prog. Polym. Sci., 24 (1999), 221.
[3] Averous L., Le Digabel F., Carbohydr. Polym., 66 (2006), 480.
[4] Mohanty A.K., Misra M., Hinrichsen G., Macrom. Mater. Eng., 276/277 (2000), 1.
[5] Saheb D.N., Jog J.P., Adv. Polym. Techn., 18(4) (1999), 351.
[6] Bhattacharyya D., Bowis M., Jayaraman K., Comp. Sci. Techn., 63 (2003), 353.
[7] Hattotuwa G.B. Premalal, Ismail H., Baharin A., Polym. Test., 21 (2002), 833.
[8] Kuruvilla J., Siby V., Kalaprasad G., Sabu T., Prasannakumari L., Koshy P., Pavithran C., Europ. Polym. J., 32 (1996), 1243.
[9] Abdelmouleh M., Boufi S., Belgacem M.N., Dufresne A., Comp. Sci. Techn., 67 (2007), 1627.
[10] Herrera-Franco P.J., Valadez-Gonzalez A., Comp., Part B, 36 (2005), 597.
[11] Borysiak S., Paukszta D., Helwig M., Polym. Degr. Stab., 91 (2006), 3339.
[12] Helwig M., Paukszta D., Mol. Cryst. Liq. Cryst., 354 (2000), 373.
[13] Yang H.-S., Kim D.-J., Lee Y.-K., Kim H.-J., Jeon J.-Y., Kang Ch.-W., Biores. Techn., 95 (2004), 61.
[14] Yang H.-S., Kim D.-J., Lee Y.-K., Kim H.-J., Biores. Techn., 86 (2003), 117.
[15] Zhou H., Li B., Huang G., He J., J. Sound Vibr., 304 (2007), 400.
[16] Markiewicz E., Borysiak S., Paukszta D., Polimery, 54 (2009), 430.
[17] Uchino K., *Ferroelectric Devices*, Marcel Dekker, New York, 2000.
[18] Jacob M., Varughese K.T., Thomas S., J. Mater. Sci., 41 (2006), 5538.
[19] Paul A., Joseph K., Sabu T., Comp. Sci. Techn., 57 (1997), 67.
[20] Li Y., Mai Y.-W., Ye L., Comp. Sci. Techn., 60 (2000), 2037.
[21] Chand N., Jain D., Comp., Part A, 36 (2005), 594.
[22] Pracella M., Chionna D., Anguillesi I., Kuliński Z., Piorkowska E., Comp. Sci. Techn., 66 (2006), 2218.
[23] Arbelaiz A., Fernandez B., Ramos J.A., Mondragon I., Thermochim. Acta, 440 (2006), 111.
[24] Garbarczyk J., Helwig M., Kozłowski R., Mankowski J., Paukszta D., Polish Patent No. 186577, (2004).
[25] Borysiak S., Dolata T., Garbarczyk J., Koppe M., Lagocki G., Paukszta D., Pawlinski R., Sterzynski T., Zamroczynski Z., Polish Patent No. 190405, (2005).
[26] Jonscher A.K., Nature, 267 (1977), 673.
[27] Doh G.-H., Lee S.-Y., Kang I.-A., Kong Y.-T., Comp. Struct., 68 (2005), 103.
[28] Einfeldt J., Meissner D., Kwasniewski A., Prog. Polym. Sci., 26 (2001), 1419.

[29] BARANOV A.I., ANISIMOVA V.N., KIRIPUNOV A.K., BAKLAGINA Y.U., Ferroelectrics, 286 (2003), 141.
[30] EINFELD J., KWASNIEWSKI A., Cellulose, 9 (2002), 225.
[31] MARKIEWICZ E., HILCZER B., PAWLACZYK CZ., Ferroelectrics, 304 (2004), 39.
[32] KOTEK J., KELNAR I., STUDENOWSKY M., BALDRIAN J., Polymer, 46 (2005) 4876.
[33] SENGERS W.G.F., VAN DEN BERG O., WUEBBENHORST M., GOTSIS A.D., PICKEN S.J., Polymer, 46 (2005), 6064.
[34] GLASSTONE S., LAIDER K.J., EYRING H., *Theory of Rate Processes*, McGraw-Hill, New York, 1941.
[35] RACHOCKI A., MARKIEWICZ E., TRITT-GOC J., Acta Phys. Polon. A, 108 (2005), 137.
[36] ASHORI A., Biores. Techn., 99 (2008), 4661.

Received 29 May 2008
Revised 24 September 2008

Materials Science-Poland, Vol. 27, No. 2, 2009

A computational study of hydrogen embrittlement phenomena in an iron nickel based alloy

S. I. SIMONETTI[1, 2*], G. P. BRIZUELA[2], A. JUAN[2]

[1]Centro de Investigaciones en Mecánica Teórica y Aplicada, Universidad Tecnológica Nacional,
11 de Abril 461, 8000 Bahía Blanca, Argentina

[2]Departamento de Física, Universidad Nacional del Sur,
Av. Alem 1253, 8000 Bahía Blanca, Argentina

The interaction between H atoms and a $Fe_{50}Ni_{50}$ alloy containing vacancies was studied. The energy of the system was calculated by the atom superposition and electron delocalization molecular orbital (ASED-MO) method. The electronic structure was studied using the concept of density of states (DOS) and crystal orbital overlap population (COOP) curves. The minimum energy position for the H atom in the vacancy region was found at 1.32 Å from the vacancy centre. The changes in the electronic structure of Fe and Ni atoms near the vacancies were analyzed. The interactions mainly involve Fe and Ni metal 4s and 4p atomic orbitals, the most important being the contribution of Fe orbitals. Fe–Fe, Fe–Ni and Ni–Ni bonds weakened as new Fe–H ones were formed. The effect of H atoms is limited to its first neighbours. The detrimental effect of H atoms on the metallic bonds can be related to the mechanism for H embrittlement.

Key words: *vacancy; alloy; hydrogen; embrittlement*

1. Introduction

The presence of hydrogen atoms in a solid metal absorbed in a metal matrix and accumulated in defect regions can result in the reduction of its ductility by decreasing the energy of cohesion and consequently in the increase of the probability of brittle fracture. Dissolved hydrogen atoms in metals tend to concentrate in defects of the crystal structure such as vacancies. Vacancy contributions to hydrogen embrittlement and hydrogen-induced degradation of mechanical properties are very important in steel and Fe based alloys. Hydrogen may degrade the mechanical performance of metallic materials and lead to operational failure [1–4]. A review of H embrittlement in steels was

---

[*] Corresponding author, e-mail: ssimonet@uns.edu.ar

reported by Oriani [5]. The author describes there important properties and effects of H in iron and steel that are relevant to understanding the embrittlement phenomena.

Liang and Sofronis investigated the hydrogen embrittlement in nickel-based alloys. In general, hydrogen was found to decrease both the macroscopic stress and strain at which void initiation starts, and reduce the energies expended on bulk deformation and interfacial separation [6]. The mechanical behaviour of very high purity nickel based alloys, charged with hydrogen and deformed in tension was investigated by Cornet et al. [7].

Molecular dynamics simulation was applied to study hydrogen embrittlement in Ni–Cr–Fe alloys. The results of this study were discussed in terms of the influence of the simulation method on the grain boundary fracture of the alloys in function of the boundary type, boundary structure and hydrogen content [8].

Hydrogen entrapment in lattice defects in nickel was studied by Angelo et al. The authors concluded that the embrittlement process is most likely associated with the trapping of hydrogen on/at grain boundaries and in Lomer–Cottrell locks [9]. H embrittlement is not completely understood at the microscopic level. A better understanding of the environmental factors affecting hydrogen embrittlement is critical for the development of alloys as engineering materials for industrial use. Experimental approaches are quite limited owing to the extremely low solubility of hydrogen. In this context, a computational approach would seem to be a suitable way to address the problem.

In this paper, we used the atom superposition and electron delocalization molecular orbital (ASED-MO) method and the YAeHMOP software to study the hydrogen absorption near a γ-FeNi based alloy containing vacancies and the effect of the impurity in the electronic structure of the solid. Ni–H and Fe–H bonding were also analyzed.

2. Computational method

The calculations were performed using the ASED-MO method [10–13]. The modification of the extended Hückel molecular orbital method (EHMO) was implemented with the YAeHMOP software [14]. Double zeta expansions of metal d orbitals were employed. The ASED-MO method is a semi-empirical method which makes a reasonable prediction of molecular and electronic structure. The EHMO method in its original form is not able to optimize geometries correctly, as it lacks repulsive electrostatic interactions. This deficiency can be overcome by introducing a two-body electrostatic correction term [15]. ASED theory is based on a physical model of molecular and solid electronic charge density distribution functions [13–16].

The adiabatic total energy values were computed as the difference between the electronic energy (E) of the system when the impurity atom is at a finite distance within the bulk and the same energy when that atom is far away from the solid surface. The hydrogen absorption energy can be expressed as:

$$\Delta E_{\text{total}} = E\left(\text{Fe}_{50}\text{Ni}_{50}-\text{H}\right) - E\left(\text{Fe}_{50}\text{Ni}_{50}\right) - E\left(H\right) + E_{\text{repulsion}} \tag{1}$$

The repulsive energy was computed taking into account all atom–atom interactions. To understand the interactions, we used the concept of density of states (DOS) and crystal orbital overlap population (COOP) curves. The DOS curve is a plot of the number of orbitals per unit volume per unit energy. The COOP curve is a plot of the overlap population weighted DOS vs. energy. The integration of the COOP curve up to the Fermi level (E_f) gives the total overlap population of the bond specified and it is a measure of the bond strength.

3. The FeNi vacancy cluster model

In order to simulate a FeNi alloy containing vacancies, it is necessary to consider the interaction between the extended nature of a solid and the local character of the defect. This requirement can be satisfied with a cluster of a reasonable size. A conventional FCC cell of chemically ordered FeNi is simulated [17]. A cluster consisting of 179, Fe and Ni, metal atoms (50:50) distributed in five close packed FCC (111) planes is used to represent the alloy containing the defect and its environment. The selected geometry for each plane is an equilateral triangle with the interplanar distance of 2.074 Å. The reference plane is the central one which contains the vacancy.

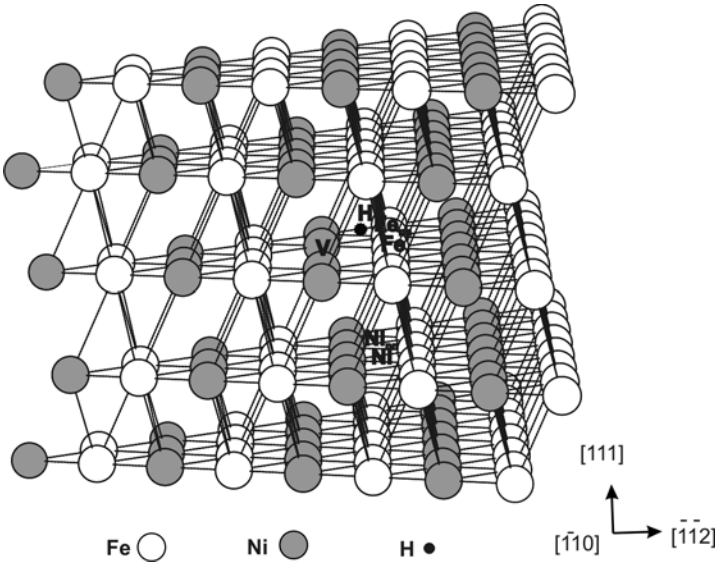

Fig. 1. The $\text{Fe}_{50}\text{Ni}_{50}$–H cluster containing the vacancy (V)
Metallic bonds close to the H atom are indicated

The cluster used in the calculations is shown in Fig. 1. All calculations were performed at the central section of the cluster in order to avoid border effects. The analysis of the results was made based on the energy contour corresponding to FeNi–H interaction mainly at the vacancy zone, covering all the (111) plane at steps of 0.05 Å. The predictions were made from the energy contour corresponding to FeNi–H interaction occurring mostly near the vacancy site: numerical computations were made by discretizing the (111) plane in a rectangular mesh having the step size of 0.05 Å. After determining the most stable position for the H atom inside the cluster, the electronic structure of the FeNi–H system was computed.

3. Results and discussion

The energy analysis is made from the energy contour plots corresponding to FeNi–H interaction in the vacancy region (see Fig. 2). The energy of the system has a relative minimum value of –5.98 eV at the H–vacancy distance of 1.32Å. We can notice the presence of a minimum energy zone when the vacancy is present. The positions of lower energy for the H atom result to be the zone close to the vacancy (V), according to the knowledge that vacancies act as traps for impurities.

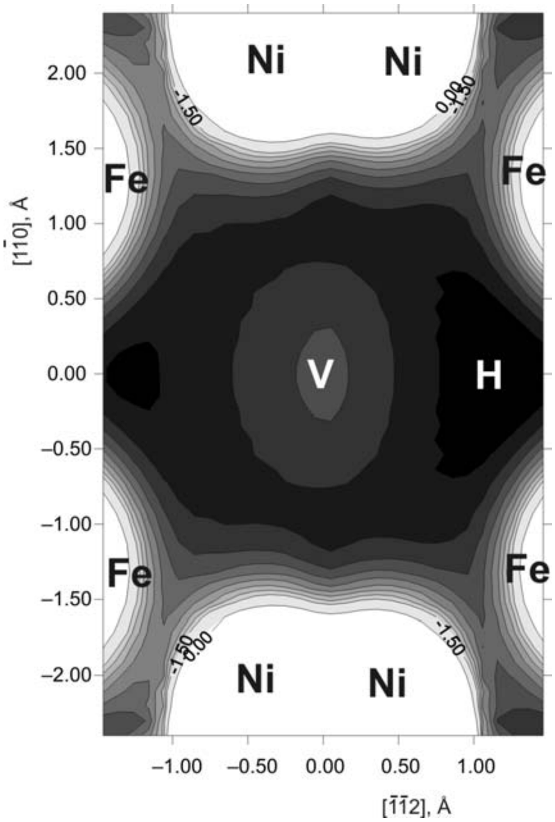

Fig. 2. Contour lines corresponding to the energy (eV) for the FeNi–H system at the vacancy region

An interaction diagram was analyzed (see Fig. 3). Comparing, the total DOS curve for the isolated FeNi system with the total DOS curve for FeNi–H system, the last one presents a small peak appearing below the d metal band corresponding to H based states. A small contribution of H to the DOS is due to its low concentration. The value of the Fermi energy changes slightly with respect to the isolated alloy.

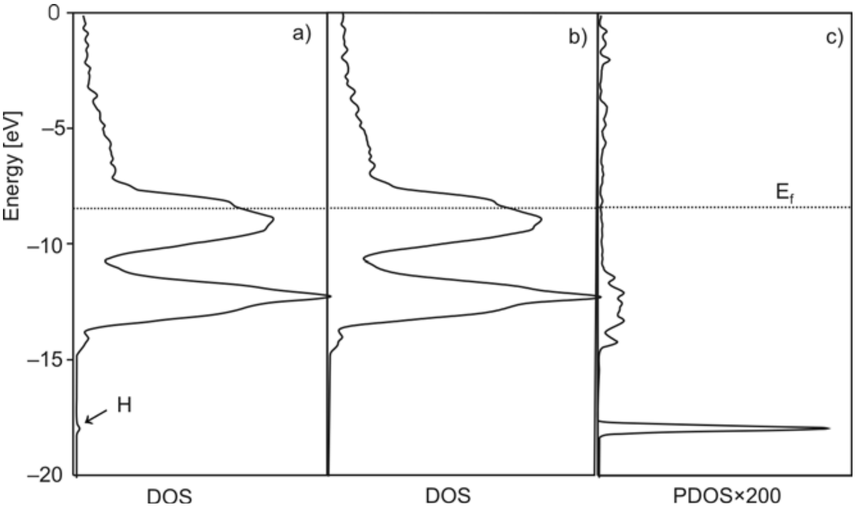

Fig. 3. Total DOS for the FeNi–H cluster (a), total DOS for the FeNi cluster (b) and projected DOS for the H atom (c)

The hydrogen atom affects the states of its surrounding Fe and Ni atoms, causing a change in their electronic densities. As a consequence, the orbital population (OP) between the metallic atoms nearest neighbouring to the hydrogen decreases (Table 1).

Table 1. Atomic orbital occupations and net charges for the H atom and their neighbouring Fe and Ni atoms[a]

Atom	s	p	d	Charge	Bond	Distance [Å]	OP	
H	1.195			–0.195	H–Fe	1.623		0.165
					H–Ni	2.830		
							H	free of H
Fe*	0.511	0.055	4.928	2.506	Fe–Fe$_{nn}$	2.540	0.096	0.239
Fe$_{nn}$	0.510	0.051	4.913	2.526				
Ni*	0.827	0.954	9.433	–1.213	Ni–Ni$_{nn}$	2.540	0.264	0.329
Ni$_{nn}$	0.822	0.949	9.442	–1.214				
					Fe–Ni	2.540	0.148	0.222

[a] The major overlaps population values for these atoms are indicated. An asterisk means a metallic atom (Fe or Ni), first neighbour to H, nn – a nearest neighbour.

These metal–metal bonds are then weakened. The Fe–Fe bond is the most affected after H location, its strength diminishes to about 60%. The Fe–Ni and Ni–Ni OPs decrease to about 33% and 20%, respectively, when an H atom is present. The Fe–H bond is formed and the bonding is achieved at the expense of the metallic nearest neighbours. Our results show how decohesion of metallic bonds contributes to the embrittlement process.

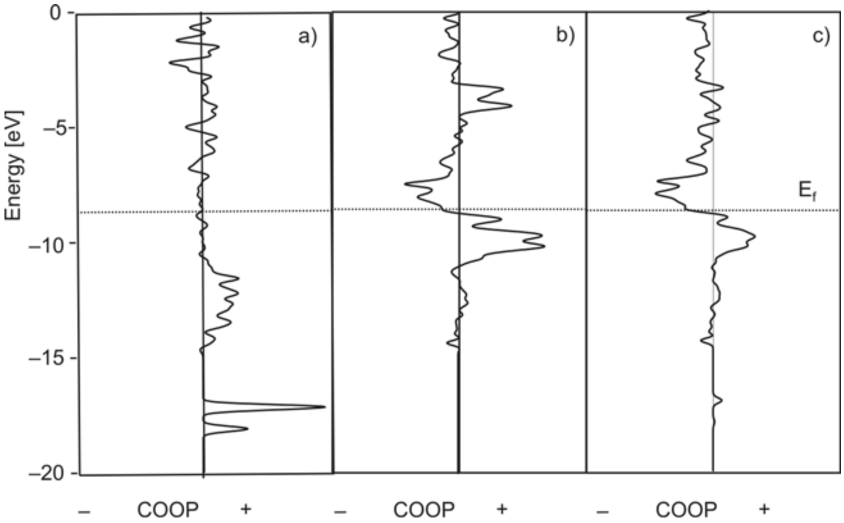

Fig. 4. COOP curves for the Fe–H interaction (a), Fe-Fe$_{nn}$ before H location (b) and Fe-Fe$_{nn}$ after H location(c)

The Fe–H COOP curve is plotted in Fig. 4a. The interaction is bonding, the Fe–H interaction mainly involves Fe 4s and Fe 4p atomic orbitals. The contribution of Fe 3d orbitals is much less important. The contribution of Fe 4s and Fe 4p populations decreases to about 15% and 40%, respectively, with respect to the cluster without H impurity. The Fe 3d population diminishes to about 7% when the hydrogen is present. In Figure 4b, c one can see the Fe–Fe interaction before and after H location. On the other hand, the Ni–H interaction is almost null, it mainly involves Ni 4s and Ni 4p atomic orbitals but the populations decrease only to about 5% and 4%, respectively, when the H atom is located in the vacancy zone.

The contribution of Ni 3d orbitals is lower than 1%. The Fe–H interaction presents an OP value of 0.165 at the distance of 1.623 Å. The Ni–H bond is much longer than the Fe–H one, thus the Ni–H bond is almost negligible. As predicted by the electronegativity differences, there is an electron transfer to the H atom from its nearest Fe neighbours. Atomic orbital occupations and net charges for the H atom and their neighbouring Fe and Ni atoms are summarized in Table 1.

4. Conclusions

The interaction between a hydrogen atom and a γ-FeNi structure having vacancies was studied. The most stable positions for the H absorption atom in the region near the vacancy were found. The Fe–H is formed and their bondings are achieved at the expense of their Fe–Fe, Fe–Ni and Ni–Ni first neighbour bonds. The interactions mainly involve Fe 4s and Fe 4p metal atomic orbitals. The greatest decrease in the metal overlap population is approximately 60%. The detrimental effect of the H atom on the metallic bonds can be associated with hydrogen embrittlement by the decohesion mechanism.

Acknowledgements

Our work was supported by the SGCyT-PGI Universidad Nacional del Sur, Departamento de Ingeniería Mecánica-Universidad Tecnológica Nacional and PIP CONICET. A. Juan, G. Brizuela and S. Simonetti are members of CONICET.

References

[1] CHENE J., BRASS A., Scrip. Mater., 40 (1999), 537.
[2] BRASS A., CHEME J., J. Phys. IV, 9 (1999), 165.
[3] BRASS A., CHEME J., Mater. Sci & Eng. A, 242 (1998), 210.
[4] KROM A., KOERS R., BAKKER A., J. Mech. & Phys. Solids, 47 (1999), 971.
[5] ORIANI R. A., Annu. Rev. Mater. Sci. 8 (1978), 327.
[6] LIANG Y., SOFRONIS P., Modelling Simul. Mater. Sci. Eng., 11 (2003), 523.
[7] CORNET M., BERTRAND C., DA CUNHA BELO M., Metall. and Mater. Trans. A, 13 (1982), 141.
[8] SMITH R., WAS G., Phys. Rev. B, 40 (1989), 10322.
[9] ANGELO J. E., MOODY N. R., BASKESET M. I., Model. Simul. Mater. Sci. Eng., 3 (1995), 289.
[10] HOFFMANN R., LIPSCOM W. N., J. Chem. Phys., 36 (1962), 2179.
[11] HOFFMANN R., J. Chem. Phys., 39 (1963), 1397.
[12] WHANGBO M. H., HOFFMANN R., J. Amer. Chem. Soc., 100 (1978), 6093.
[13] ANDERSON A., J. Chem. Phys., 62 (1975), 1187.
[14] LANDRUM G., GLASSEY W., *Yet Another extended Hückel Molecular Orbital Package (YAeHMOP*) Cornell University, Ithaca, NY, 2004.
[15] ANDERSON A., HOFFMANN R., J. Chem. Phys., 60 (1974), 4271.
[16] ANDERSON A., J. Electroanal. Chem. Interfacial Electrochem., 280(1) (1990), 37.
[17] DANG M., RANCOURT D., Phys. Rev. B, 53 (1995), 2291.

Received 25 October 2008

Materials Science-Poland, Vol. 27, No. 2, 2009

A study of the gas specificity of porous silicon sensors for organic vapours

S.-H. CHOI, H. CHENG, S.-H. PARK, H.-J. KIM, Y.-Y. KIM, K.-W. LEE*

Department of Physics, Kongju National University, 314-701 Chungnam, Republic of Korea

A porous silicon sensor was investigated as a means to determine the response specificity for organic vapours. Porous silicon layers were fabricated by electrochemical anodization of p-type crystalline silicon in an HF ethanol solution under various conditions. The porous silicon sensors were placed in a gas chamber with various organic vapours, and the changes in electrical resistance under constant voltage of each sensor were used as detection signals. The sensors recorded various changes in resistivity for various organic vapours.

Key words: *porous silicon; response pattern; gas sensor; gas specificity*

1. Introduction

Porous silicon has been widely studied since the discovery of its strong visible photoluminescence [1]. The early research focused on fabrication methods, mechanical structures, electronic band structures, optical constants, and luminescence mechanisms, to name a few [2, 3]. Recent research focus has shifted to applications involving porous silicon based LEDs [4, 5] and various sensors [6–9]. Porous silicon is thought to be an ideal sensor material because of its large specific surface area of approximately 200–800 m^2/cm^3 [10].

To detect various substances including organic gases [11], NO_2 [9], L-glutamine [12], and humidity [13], changes in physical properties of the porous silicon layer, such as electrical resistance [11], photoluminescence intensity [7], capacitance [14], and optical reflectance [15], are used as response signals. Research thus far has focused on porous silicon capacity to detect gas and the properties of the response signal with respect to single gases. Such research has demonstrated porous silicon to be a good candidate for gas sensors. However, there is a paucity of research into the use of porous silicon for detecting gas mixtures. Due to differences in gas properties such

---

*Corresponding author, e-mail: ga992205@kongju.ac.kr as molecular weight, dipole moment, adsorption mechanisms on porous silicon surfaces, we can expect differences in electrical response for each gas, and that the intensity of these signals is proportional to the gas densities. Gas specificity of porous silicon sensors is taken from signal intensities specific to a certain gas. It seems more natural to say that different sensors have different specificities. Improvements in specificity can be obtained by using several different porous silicon samples. The results thus obtained are compared. Hence, gas specificity for one gas is acquired if a number of samples used thus allows obtaining precise gas fingerprints.

The acquired gas fingerprints can be incorporated into electronic sniffer systems, and gas composition can then be obtained through data processing. First, however, one should determine if porous silicon could indeed be used to detect a particular gas.

In this paper, we examine gas specificity of electrical signals obtained from the reaction of porous silicon samples prepared under various fabrication conditions, to specific organic vapours. Different electrical signal patterns thus obtained highlight the differences between the sample gasses.

2. Experimental

Porous silicon samples were prepared by the electrochemical anodization process in 10% ethanolic solution of HF using a (100)-oriented p-type single crystal silicon wafer of 0.06–0.12 Ω·cm. Table 1 presents the detailed fabrication conditions for the samples, and the labels given to each sample. The samples were fabricated at various current densities and anodization times with no change in the HF solution concentration. Porous silicon layers of various thicknesses and pore sizes were thus produced. These differences are expected to produce different responses of the porous silicon layers when brought into contact with the target organic gases.

Table 1. Fabrication conditions of porous silicon samples

Sample	HF concentration	Current density [mA/cm^2]	Anodization time [s]
A1	10%	5	1000 s
A2			2000 s
A3			4000 s
B1		10	200 s
B2			500 s
B3			1000 s
B4			2000 s
B5			4000 s
C1		20	100 s

A schematic diagram of our experimental set-up, showing only one sensor for simplicity sake, is shown in Fig. 1. Each sensor unit was biased with a constant 5 V dc between the top surface of the porous silicon layer and the bottom surface of the silicon substrate under the porous silicon layer. A tungsten tipped probe 600 μm in diameter served as a negative electrode (direct contact with the surface of the porous silicon layer), and Al conducting wire served as a positive electrode (attached to the back-side of the Si wafer). The movement of the probe tip over the porous silicon layer surface was precisely controlled by a micrometer to prevent surface damage.

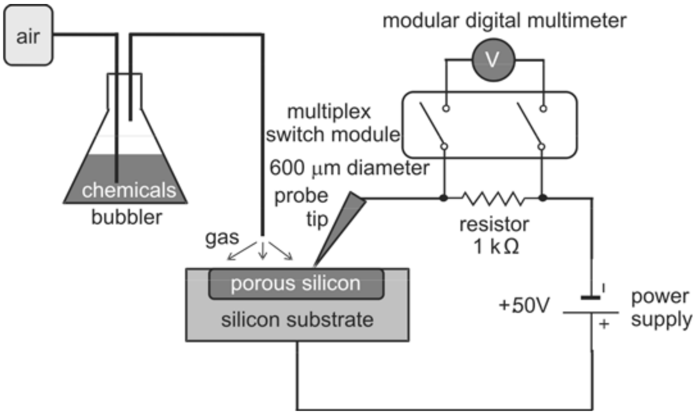

Fig. 1. Schematic diagram of the experimental equipment

The sensors were exposed to an organic gas under gas saturation conditions. Air was used as a carrier gas for the organic vapour, which was generated at room temperature in a vessel containing a liquid solvent such as isopropyl alcohol, ethanol, methanol, acetone, or xylene. The flow of the air introduced into the sample chamber was kept constant during the process and measurement stages. Under these experimental conditions, the gas concentration the samples were exposed to was considered to be nearly constant. The electrical response induced by the reaction between the porous silicon and the organic gas was recorded by measuring the voltage drop across a 1 kΩ resistor connected in a series circuit. The intensity of the measured response voltage increased as the resistance of a sample decreased, and vice-versa. To do this, a digital multimeter (National Instruments, PXI-4072) and a multiplex switch module (National Instruments, PXI-2503) were used.

3. Results and discussion

Cross-sectional scanning electron microscope (SEM) images of the porous silicon layers made with a current density of 10 mA/cm^2 for 100 s and 500 s show many pores between the silicon skeletons in the porous silicon layer (Fig. 2). Target organic vapours can penetrate into these pores. The ensuing interaction, under a constant bias voltage, results in an electrical response signal.

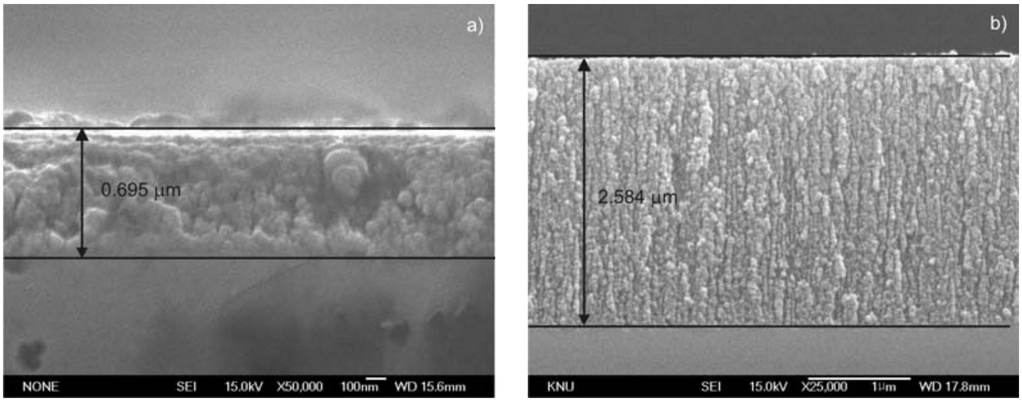

Fig. 2. Cross-sectional images of the porous silicon layers obtained with a 10 HF solution with the current density of 10 mA/cm^2 for: a) 100 s, b) 500 s

There are active studies on the change of the electrical signal when porous silicon is introduced by gas. For example, the conductivity of porous silicon layers increases for both NO_2 and ethanol gases. Measurements indicate that molecules of NO_2 act as acceptor centres [9]. Free carrier (hole) concentration in the porous silicon layers increases, thus increasing conductivity. Increasing conductivity for ethanol gas case is known to be correlated with oxidation of porous silicon layers [16]. Harper and Sailor have shown that reversible photoluminescence quenching of porous silicon is related to layer (molecular oxygen) oxidation [17]. Since O_2 molecules are absorbed into porous silicon layers by either physisorption or weakly chemisorption processes, photoluminescence quenching is due to transient nonradiative electron transfer from the luminescent chromophore in porous silicon by that same oxygen. From this point of view, the phenomenon of enhanced conductivity when porous silicon comes into contact with organic vapours is due to activation of the surface state via layer oxidation.

A typical time evolution of the electrical response signals (sample B5 for five types of organic gases) is shown in Fig. 3. All response signals were normalized to a base voltage in order to compare the signal intensities from various measurements. All response signals were higher than the base voltage during exposure to the gas; this effect indicates that the resistance of the porous silicon layer decreased and correspondingly its conductivity increased; this is consistent with the results of Baratto et al. [16]. Additionally, the response time or the time required to reach 90% of the steady state of the response curve ranged from 0.5 to 6.1 s depending on the organic gas type. These short response times indicate that the porous silicon sample could be used as a sensor, since the minimum response time required for a general sensor is within 20 s [18].

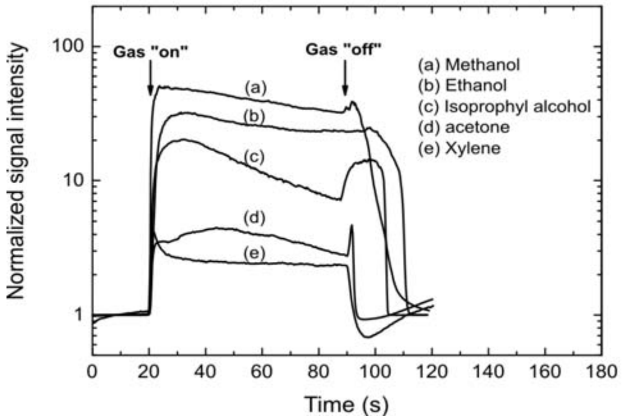

Fig. 3. Time evolution of the response signal
of sample B5 for various organic gases

The normalized intensity of the response signal from the porous silicon sensor differed for each of the gases (Fig. 3). It was the highest for methanol and the lowest for xylene vapour. This result indicates that porous silicon is capable of differentiating gases – an important factor for practical sensor applications using porous silicon. Note that gradual changes in the signals during exposure to the gases, as well as irregular signals that appeared soon after the gas was shut off, were observed. These phenomena, especially the change in signal intensity over time, have been previously reported [7, 9]. They must be resolved if porous silicon is to be used in practical sensing applications. Nevertheless, despite these limitations, the discovery of the gas selectivity of porous silicon is an important finding. For a given gas, electric signals obtained using different fabricated porous silicon samples can produce total specificity. In addition, comparison of electric signal patterns under specific instances can differentiate various organic gases.

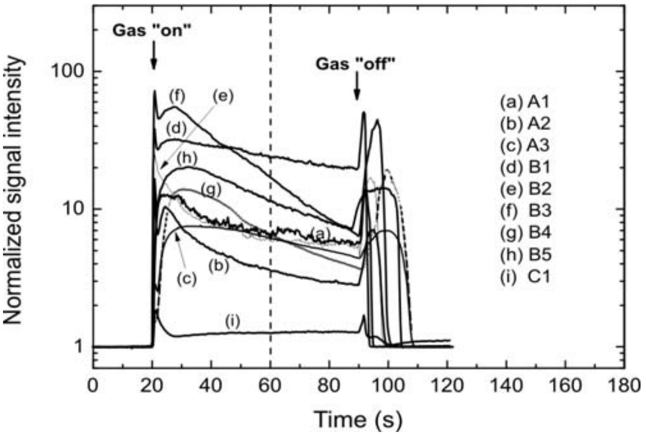

Fig. 4. Time evolution of the response signals measured
from the porous silicon samples for gaseous isopropyl alcohol

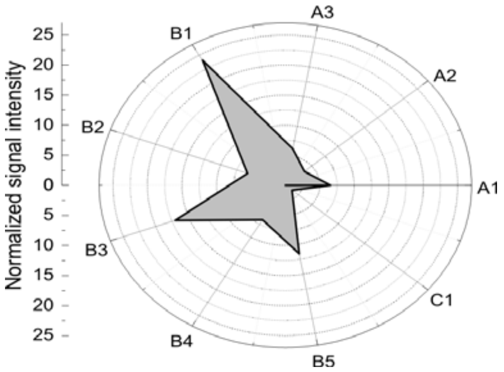

Fig. 5. Polar plot at the time of 60 s under conditions as in Fig. 4

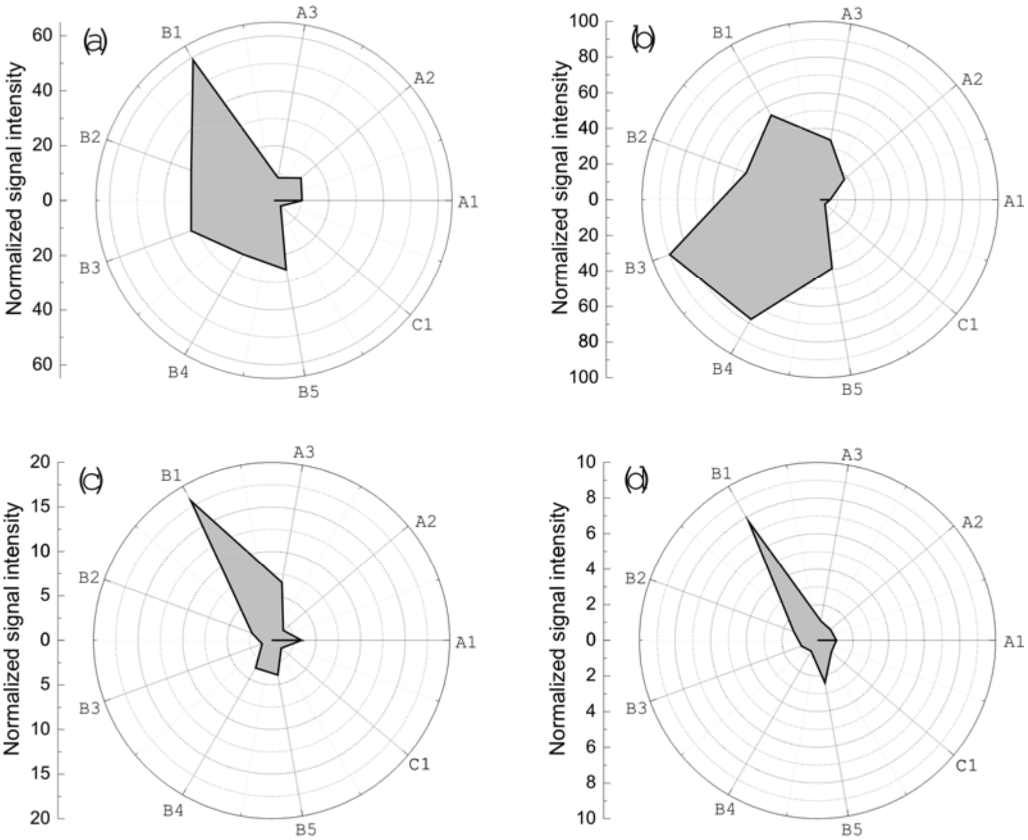

Fig. 6. The response patterns of various organic gases: a) ethanol, b) methanol, c) acetone, d) xylene

The time dependence of the measured response signals using porous silicon, made under various fabrication conditions (Table 1) and an isopropyl alcohol gas, was investigated (Fig. 4). As expected, different response signals were observed for different sensors. For example, at 60 s, the intensity of the response signal is highest for B1 and lowest for C1. We visualized the gas specificity of sensors through the detection signals patterns. The pattern expressions of the gases are generally expressed in polar coordinates. The resulting image is typically referred to as the gas 'fingerprint'.

Figure 5 shows the results after 60 s under conditions as in Fig. 4. The electrical response signal in Fig. 4 changes in time while it is in contact with the gas, thus it is important to compare the pattern of each gas at the same time. Patterns for various organic gases used in this experiment are different (Fig. 6). These results indicate that porous silicon sensors have gas specificity.

4. Conclusions

The electrical detection specificity of porous silicon sensors have been investigated for various organic vapours. The porous silicon sensors, which were made under various fabrication conditions, were operated under a constant voltage without any modifications of sensing efficiency such as surface modification or heaters. The results indicate that the sensors produce different response signals and patterns for different gasses, indicating a gas specificity. However, an unstable nature of the response signals is an issue that should be addressed in future research.

Acknowledgement

This work was supported by the Korea Research Foundation Grant funded by the Korean Government (MOEHRD) (No. KRF-2007-331-D00245).

References

[1] CANHAM L.T., Appl. Phys. Lett., 57 (1990), 1046.
[2] CANHAM L.T., *Properties of Porous Silicon*, INSPEC, London, 1997.
[3] VIAL J.C., DERRIEN J., *Porous Silicon Science and Technology*, Springer-Verlag, Berlin, 1995.
[4] HIRSCHMAN K.D., TSYBESKOV L., DUTTAGUPTA S.P., FAUCHET P.M., Nature, 384 (1996), 338.
[5] SZENTPÁLI B., NOHÁCSY T., BÁRSONY I., Curr. Appl. Phys., 6 (2006), 174.
[6] RAVI KUMAR REDDY R., BASU I., BHATTACHARYA E., CHADHA A., Curr. Appl. Phys., 3 (2003), 155.
[7] BARATTO C., FAGLIA G., SBERVEGLIERI G., GABURRO Z., PANCHERI L., OTON C., PAVESI L., Sensors, 2 (2002), 121.
[8] OUYANG H., STRIEMER C.C., FAUCHET P.M., Appl. Phys. Lett., 88 (2006), 163108.
[9] PANCHERI L., OTON C.J., GABURRO Z., SONCINI G., PAVESI L., Sens. Actuators B, 89 (2003), 237.
[10] SALEM M.S., SAILOR M.J., HARRAZ F.A., SAKKA T., OGATA Y.H., J. Appl. Phys., 100 (2006), 083520.
[11] SALGADO G.G., BECERRIL T.D., SANTIESTEBAN H.J., ANDRÉS E.R., Opt. Mater., 29 (2006), 51.
[12] STEFANO L.D., ROTIROTI L., RENDINA I., MORETTI L., SCOGNAMIGLIO V., ROSSI M., D'AURIA S., Biosens. Bioelectron., 21 (2006), 1664.
[13] PÉREZ E.X., MARSAL L.F., FERRÉ-BORRULL J., TRIFONOV T., PALLARÈS J., Physica E, 38 (2007), 172.

[14] XU Y.Y., LI X.J., HE J.T., HU X., WANG H.Y., Sens. Actuators B, 105 (2005), 219.

[15] MARTÍN-PALMA R.J., TORRES-COSTA V., ARROYO-HERNÁNDEZ M., MANSO M., PÉREZ-RIGUEIRO J., MARTÍNEZ-DUART J.M., Microelectron. J., 35 (2004), 45.

[16] BARATTO C., COMINI E., FAGLIA G., SBERVEGLIERI G., FRANCIA G.D., FILIPPO F.D., FERRARA V.L., QUERCIA L., LANCELLOTTI L., Sens. Actuators. B, 65 (2000), 257.

[17] HARPER J., SAILOR M.J., Langmuir, 13 (1997), 4652.

[18] Standard Committee on Sensors, Standard of Electronic Industries Association of Korea EIAK GC-6220 (2000), p. 6.

Received 23 April 2008
Revised 29 November 2008

Contents

GUIDELINES FOR AUTHORS

Manuscripts can be sent by conventional mail or by e-mail. Submission of a manuscript to *Materials Science-Poland* implies that it is not being considered for the publication elsewhere, and the authors have a necessary authorization to publish the material contained in the paper. **The manuscripts should conform to the formal standards of the Journal which may be found in the first issue of each volume and on the web page.**

Authors are encouraged to submit electronic versions of the manuscript by e-mail, to the address of the Journal. A single PDF file should be sent, containing text, references, figures, tables etc. Alternatively, the authors can submit the manuscript by conventional mail, sending a CD with the PDF file mentioned above, to the Editor-in-Chief at his address given below.

Each submitted manuscript will be reviewed, the final decision concerning its acceptance resting with the editors. Upon acceptance, the corresponding author will be requested to submit the following material (via e-mail or by conventional mail, on CD)

- A DOC or RTF file containing the final version of the text, references, tables and figure captions. The content of the file should be identical with that of the hard copy, and should exactly match the version seen and accepted be the referee(s).
- File(s) in appropriate formats containing figures. The required formats of the drawings (plots, schemes of technological processes) must be vector files such as XLS, OPJ, cdr (Excel, Origin, CorelDraw) which may also be exported as EPS, EMF or WMF files. Drawings submitted in tiff or jpg formats (bitmaps, raster graphics), even if exported as EPS, EMF or WMF files, will not be accepted. **Bitmaps are acceptable only in the case of photographs**. The photographs (only in grayscale) should have the resolution not lower than 300 dpi (estimated for the size in which they are expected to be reproduced).
- A PDF file containing the complete manuscript (text, literature, tables, figures, etc). The file should be carefully checked as it will serve as a hard copy in case of doubts. **The contents of the PDF file should exactly match the material in other files.**

Irrespective of whether the final version is submitted by e-mail or by conventional mail, the authors should also send **via conventional mail** a signed copy of the Copyright Transfer Agreement (available on the web page of the Journal).

For detailed information consult the first issue of each volume or the web page of the Journal.

The mail should be addressed to:

Professor Juliusz Sworakowski
Editor-in-Chief, Materials Science-Poland
Politechnika Wrocławska, W-3
Wybrzeże Wyspiańskiego 27
50-370 Wrocław, Poland

Electronic correspondence should be sent to: MatSci@pwr.wroc.pl
Web page of Materials Science-Poland: www.MaterialsScience.pwr.wroc.pl

The Publisher reserves the right to make necessary alterations to the text. Each corresponding author will be supplied with one free copy of the journal. Orders for additional offprints can be placed with the Publisher.